Geometric and Electronic Properties of Size-Selected Metal Clusters on Surfaces

Dissertation

Zur Erlangung des Doktorgrades der Naturwissenschaften

vorgelegt von

Thomas Christoph Eng Fuk Irawan

angefertigt am
Lehrstuhl Experimentelle Physik I
des Fachbereichs Physik
der
Universität Dortmund

August 2006

Erster Gutachter: Priv. Doz. Dr. H. Hövel

Zweiter Gutachter: Prof. Dr. T. Weis

Tag der mündlichen Prüfung: 20.09.2006

DEDICATION

This thesis is dedicated to my wife Katrin.

ABSTRACT

Within this thesis, we present a project regarding metallic clusters on surfaces. We use scanning tunneling microscopy to investigate their geometric structure and scanning tunneling spectroscopy and ultraviolet photoelectron spectroscopy to study their electronic properties. A new cluster deposition machine built within a priority program of the German Research Foundation (DFG)[1] allows the investigation of size-selected clusters on surfaces.

In a first set of experiments, we produced clusters by metal island growth on rare-gas multi-layers and investigated several combinations of different cluster materials on various rare gases on miscellaneous substrates. On a rare gas film of 60-monolayer thickness, the clusters are electronically decoupled from the substrate. This leads to a change of the reference energy, which is no longer the FERMI energy but the vacuum energy of the substrate. In this sense, we use the term *free clusters on substrate*.

In a second part, after the successful setup and initial operation of the cluster deposition machine, we use a magnetron sputter gas aggregation cluster source[2] and a semi-continuous time-of-flight mass selector[3] to deposit mass-selected silver clusters (number of atoms n = 40, 55, 80,…, 923, and 2130) onto different substrates.

In particular, mass-selected silver clusters with closed icosahedral shells deposited on a gold surface functionalized with a C_{60} monolayer show very interesting results. Despite of using five different silver cluster sizes between 55 and 923 atoms, we observed for all samples clusters with almost the same average cluster height of 1.7 nm. In addition, for Ag_{561} and Ag_{923} clusters we observed also larger clusters that roughly agree with the expected cluster sizes. Our present hypothesis is that the clusters deposited at room temperature, exhibit rather a metastable than an equilibrium shape.

---

[1] DFG priority program SPP 1153: *Clusters in Contact with Surfaces – Electronic Structure and Magnetism*, website: http://www.ieap.uni-kiel.de/surface/ag-berndt/spp/index.html.

[2] H. HABERLAND, M. MALL, M. MOSELER, Y. QIANG, Th. REINERS, and Y. THURNER: *Filling of micron-sized contact holes with copper by energetic cluster impact*, J. Vac. Sci. Technol. A **12**, 2925 (1994).

[3] B. v. ISSENDORFF and R. E. PALMER: *A new high transmission infinite range mass selector for cluster and nanoparticle beams*, Review of Scientific Instruments **70**, 4497 (1999).

TABLE OF CONTENTS

LIST OF FIGURES

LIST OF TABLES

LIST OF ABBREVIATIONS

Ag	Silver
Ag(111)	(111)-oriented silver single crystal
Ag_n	Silver cluster consisting of n atoms
AP	**A**cceleration **P**late
AR	**A**cceleration **R**egion
Ar	Argon
Au	Gold
Au(111)	(111)-oriented gold single crystal
A_x	x^{th} Acceleration electrodes (in CCH)
BLAG	**B**uffer **L**ayer **A**ssisted **G**rowth
BN	Boron Nitride
C	Carbon
CCH	**C**ryo Pumping **Ch**amber
C_n	Carbon cluster consisting of n atoms
CPU	**C**entral **P**rocessing **U**nit
CT_I	Channeltron I
CT_{II}	Channeltron II
Cu	Copper
DOS	**D**ensity **o**f **S**tates
DP	**D**eceleration **P**late
DR	**D**eceleration **R**egion
d_{Target}	Distance between target and iris
D_X	X^{th} electrode of the deposition optics
$D_{x/y}$	x-y-deflector plates (in CCH)
ECS	**E**quilibrium **C**rystal **S**hape
E_F	Focus electrode
EFM	**E**vaporator with **I**ntegrated **F**lux **M**onitor
ERH	**E**vaporator with **R**esistive **H**eating
e_t	Exit tube (of the mass-selector)
FBN	Boron Nitride Foil
FC_I	FARADAY Cup I (MCH)
FC_I	Faraday Cup I
FC_{II}	FARADAY Cup II PCH)
HOPG	**H**ighly **O**riented **P**yrolytic **G**raphite
i	Iris
Ir	Iridium
L	Laser
LDOS	**L**ocal **D**ensity of **S**tates
LHe	**L**iquid **H**elium
Li	**Li**thium
LN_2	**L**iquid **N**itrogen
LT	**L**ow **T**emperature
m	**M**agnetron Sputter Discharge Head

m ……..Magnetron-Sputter-Discharge head
MCH ……..**M**ass Selector **Ch**amber
ML ……..**M**ono**l**ayer
MS ……..**M**ass **S**elector
nanopits ……Nanometer-sized defect
Ni ……**Ni**ckel
PAX ……**P**hotoemission of **A**dsorbed **X**enon
Pb(111) ……(111)-oriented lead single crystal
PCH ……Preparation Chamber
Pd ……**Pa**lla**d**ium
PES ……**P**hoto**e**lectron **S**pectroscopy
Pt ……**Pl**a**t**inum
RT ……..**R**oom **T**emperature
s ……..Skimmer
SC ……S**ample** C**arrier**
SCH ……**S**ource **Ch**amber
SH_H ……Heatable Sample Holder
SH_{LT} ……Low Temperature Sample Holder
Si ……**Si**licon
Si(111) ……..(111)-oriented silicon crystal
SO ……**O**uter **S**hielding of the cryo pump
SPS ……**S**tandard **P**icture **S**ize of STM images (100 nm x 100 nm)
SSF ……**S**urface **S**cience **F**acility
St_I ……..First (outer) stage of the cool head
St_{II} ……Second (inner) stage of the cool head
STM ……..**S**canning **T**unneling **M**icroscopy / **M**icroscope
STS ……..**S**canning **T**unneling **S**pectroscopy
TEM ……**T**ransmission **E**lectron **M**icroscopy / **M**icroscope
TF ……**T**antalum **F**oil
TiO_2 ……..Titanium Dioxide
t_m ……..Movable tube
TPC ……..Turbo pump in the cryo chamber
TPM ……..**T**urbo **P**ump in the **M**ass Selector Chamber
TPS ……..Turbo pump in the source chamber
T_{STI} ……Temperature of the first (outer) stage of the cool head
T_{STII} ……Temperature of the second (inner) stage of the cool head
UHV ……..**U**ltra **H**igh **V**acuum
UPS ……**U**ltraviolet **P**hotoelectron **S**pectroscopy
U_{tm} ……High voltage connector of the movable tube
VCP ……..Connection valve between cluster depostion
V_f ……..Floating voltage
Xe(100) ……(100)-oriented Xenon crystal
y^+/y^- ……y-deflector plate
ZnO ……Zinc Oxide

Chapter 1

INTRODUCTION

The Milky Way is nothing else but a mass of innumerable stars planted together in ***clusters****.*

GALILEO GALILEI (1564 – 1642)

In this quotation the famous Italian physicist GALILEO GALILEI summarizes his observation that our galaxy is nothing else than stars accumulated in *clusters*.

In contrast to large scaled objects such as the universe, with its unimaginable number of 10^{22} stars, small objects consist of an unimaginable number of atoms. For example, one could fill the volume of a large raindrop with approximately 10^{22} silver atoms. In such dimensions, the accumulations of a few up to ten thousand atoms are also named *clusters*.

The continuous progress in nano-science raises new challenges. For example, the constant increase of memory requirements leads to structures of extremely small sizes. Today, common computers use 100-nanometer-sized structures in their central processing unit (CPU). In regions of that scale, we reach the limit of the bulk material properties approach. Since the size of devices getting smaller and smaller, it is becoming more and more important to understand the physics of clusters. The study of properties of small metal particles is of fundamental importance due to their applications in catalysis and surface nano-structuring [1, 2, and 3].

Therefore, we have to build new and innovative concepts on a scientific and technological basis using the bottom-up approach. We have to build structures from atoms (*bottom-up*), instead shrinking the macroscopic elements (*top-down approach*). This will become possible with clusters. One can characterize these objects by quantum effects, which are interesting and promising as well.

Several experiments for clusters in a free beam show, that free clusters behave drastically different compared to solids [4]. In contrast to the well-understood and already well-investigated case of free clusters, there is only rudimentary knowledge of clusters on solid-state surfaces. The geometric, magnetic, and chemical properties of clusters on surfaces are particularily interesting to study. Depending on the combination of substrate and cluster material, their properties differ in some cases only slightly and in other cases extremely compared to their corresponding free properties.

For this reason, the German Research Foundation (Deutsche Forschungsgemeinschaft - DFG) supports the activities in surface science and cluster physics, and combines both within the DFG priority program SPP 1153: *Clusters in Contact with Surfaces – Electronic Structure and Magnetism* [5].

In the next section, we briefly introduce the general aims and topics of the SPP 1153 and describe our collaboration with V. ISSENDORFF *et al.* in the context of this priority program.

1.1 Priority Program

The DFG priority program SPP 1153 deals with the most important questions concerning the electronic structure, charge transfer processes, and magnetism of clusters. The aim is to answer these questions from different point of views. Therefore, the SPP 1153 is interested in the manipulation of single atoms, the specific nature of the resulting nano-particle and the dependency of electronic and magnetic effects on the exact number and position of the atoms. These aspects are not only interesting from the scientific point of view, but also promising regarding technological applications. One long-term aim is to produce new materials, using the specific geometric structures and the resulting electronic properties of clusters.

Before thinking of a concrete application, we have to bring the clusters onto a surface. In this case, the coupling to the surface and the environment will definitely change the properties of theses clusters. The new system - consisting of cluster, substrate, and the environment - represents a new element of the nanometer-size scale and will be used in the future for several interesting applications.

The SPP 1153 is an interdisciplinary priority program, in which the combination of theoretical and experimental investigations of clusters on surfaces, as well as collaborations between several theoretical and experimental groups leads to interesting new results.

1.2 State of the Art

The following state of the art examples depict today's status of this kind of research. FURCHE *et al*. investigate the structure determination of gas phase clusters determining the structure of gold clusters via ion mobility measurements [.6]. KIRILYUK *et al.* investigate the structure of niobium clusters via the measurement of infrared absorption spectra [.7]. Moreover, BONZEL *et al.* describe the structure of larger particles on surfaces within a

recent review article. He studies the direction and temperature dependent surface energy of µm-sized faceted crystallites [8]. It is interesting to compare the behavior in these rather bulk-like sizes with our results.

Our collaborators V. ISSENDORFF *et al.* study among other systems noble metal clusters. The results (*see* figure 1.1) clearly demonstrate that copper (Cu) and silver (Ag) clusters exhibit strongly perturbed electron shell structures (see 2.4.2, pp 62), except Cu_{55}^- and Ag_{55}^- (nomenclature of clusters explained in chapter 2, p. 29), which have a highly discretized DOS due to their icosahedral symmetry. These clusters therefore are ideal candidates to study possible changes of the electronic DOS of clusters close to a surface. Gold clusters behave completely different and exhibit a tendency to amorphous structures [9].

A similar determination of the geometric structure of sodium clusters recently solved the old problem of the origin of the strong size dependence of the melting properties of sodium clusters [10].

Moreover, V. ISSENDORFF *et al.* investigated large Aluminum clusters with photoelectron spectroscopy and observed so-called *COULOMB Staircases* (*see* figure 1.2) [11]. The steps appear due to multiple ionizations. The negatively charged cluster absorbs a photon and emits an electron. The resulting neutral cluster is able to absorb again a photon and emit another electron, *etc*. Due to this process, the positively charged cluster attracts the emitted electron. The attraction results in a shift of the kinetic energy of the emitted electron and, consequently, in a shift of the cluster FERMI edge. The FERMI edge shift comes from the COULOMB interaction between positively charged cluster and emitted electron. The shift of the FERMI edge for each additional charge amounts to e^2/R (*see* figure 1.2).

Therefore, the ionization potential increases with increasing positive charge. With this, one is able to measure the capacity of a cluster or nano-particle.

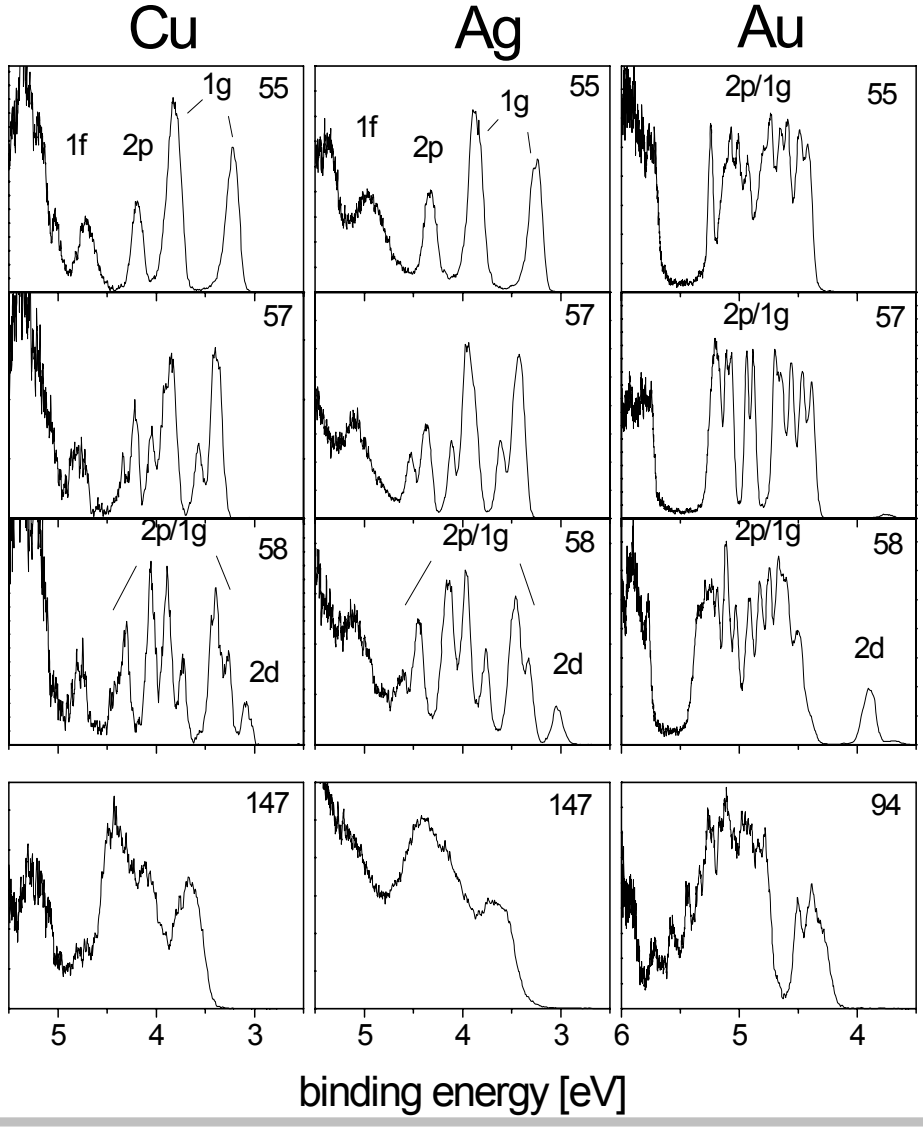

Figure 1.1 Photoelectron spectra of noble metal cluster anions, measured at a photon energy of 6.42 eV (based on figure 1 from ref. [9]).

The clusters exhibit a strongly perturbed electron shell structure. For all three systems at size 58 the expected onset of the 2d-shell is visible; nevertheless the overall DOS is more complex than a simple shell structure. Only the icosahedral clusters Ag_{55}^- and Cu_{55}^- exhibit highly degenerate states due to their symmetry. Gold shows a different behavior; it seems to prefer geometries of low symmetry [2].

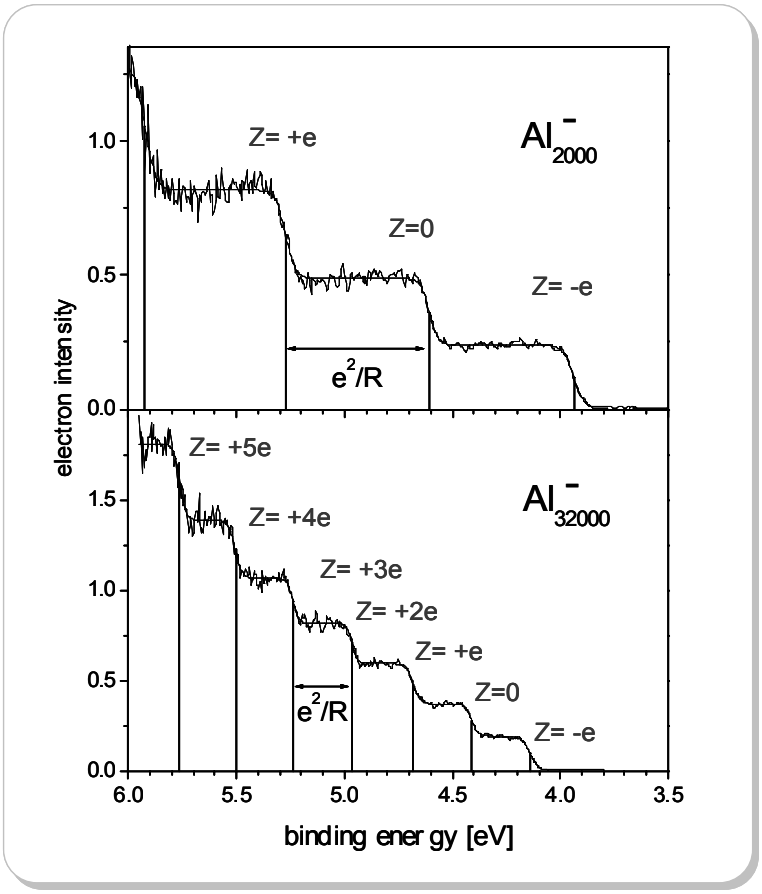

Figure 1.2 COULOMB staircase in the UV (hν = 6.42 eV) photo emission spectra of free size-selected cold aluminum cluster anions with up to 32000 atoms (taken from ref. [11]).

1.3 Overview

The aim of this work is to compare the results of free clusters in vacuum with the same clusters on surfaces. Therefore, we start in chapter 2 (pp 29) with a general introduction in metallic clusters and particles. Within this chapter, we introduce bonding types of clusters, the experimental techniques we use to investigate them, and discuss clusters grown by metal island evaporation and size-selected clusters produced in cluster sources.

After that, we present the experimental setup of the new cluster deposition machine in chapter 3 (pp 75), which we setup within the scope of this work in cooperation with C. YIN and B. V. ISSENDORFF and describe the existing Surface Science Facility.

Then, we introduce our sample systems and preparation methods in chapter 4 (pp .111) and prepare different buffer layers and functionalized surfaces on different substrates for the growth or deposition of metal clusters.

Finally, we present and discuss our experimental results in chapter 5 (pp .131). We perform photoemission studies of large grown and deposited size-selected metal clusters on rare gas layers, as well as scanning tunneling spectroscopy investigations of small size-selected silver clusters and conclude with a summary and an outlook.

Chapter 2

CLUSTERS AND PARTICLES

Several researchers intensively investigated metal clusters and small metallic particles [.12] during the past two decades [.13,.14] in the field of cluster physics. Cluster physics deals with the interesting area between atomic and solid-state physics. While on the atomic scale the single atom has quantized electronic states, an electronic band structure determines the properties of the bulk material. Cluster physics, which is our field of research, investigates the not necessarily smooth transition from atoms and molecules to large clusters and bulk-like metal islands.

One way to gategorize clusters is by size (see table 2.1). The field of cluster physics uses the common X_n notation for cluster characterization where X denotes the chemical symbol and n the number of atoms. This even holds for X_1, X_2, or X_3 clusters, that molecule physicists mostly call single atom, dimer, and trimer. In the same way, we will refer to very large clusters with, *e.g.*, 3000 atoms as X_{3000} instead of *micro crystal*. However, more important than the nomenclature of clusters are their properties, which depend on their size. While large clusters show an almost bulk-like behavior, small clusters appear more molecular-like. They are extremely sensitive to a change of their size, because every

atom counts [9]. There exist so-called *magic cluster sizes*, which we briefly introduce in section 2.4.2.2. Moreover, we present an introduction dealing with larger particles in section 2.3 and motivate our experiments in section 2.4.2 by summarizing some results of clusters investigated in a free beam, while section 2.4.3 focuses on our main field of research: clusters on surfaces.

micro clusters	3 to 13 atoms
small clusters	14 to 100 atoms
large clusters	100 to 1000 atoms
micro crystallites	more than 1000 atoms

Table 2.1 Nomenclature of clusters.

2.1 Bonding Types

The bonding type between atoms and molecules determines fundamentally the geometry of clusters. In this section, we introduce the four important bonding types for clusters. In principle, we can divide the bonding types, which hold together two or more atoms within a molecule, into the *covalent* and the *ionic* bonding. Some other bonding types, like *dipole-dipole-interaction* (VAN-DER-WAALS-Bond) or the *metallic bond* are important for solid-state bodies and liquids. However, the chemical bond – regardless of the type – has always the same cause: The lowering of the energy of the stable, bonded molecule compared to the total energy of its far away atomic components. This energy benefit, results in an attractive force between the atoms, once their distance exceeds a specific equilibrium value. The mechanism of the bonding depends on the one hand on the electrostatic interaction between atoms or ions of the system, and on the other hand on the wave properties of the electrons and the property of the PAULI *Exclusion Principle*.

In our experiments, we mainly use metallic clusters. On the atomic scale, we can describe metals by means of the metallic bond.

2.1.1 Metallic Bond

For metals, in general – clusters and solid-state samples – the metallic bond involves the delocalized sharing of free electrons among a lattice of metal atoms. In metals, one or two valence electrons of *each* atom can move freely inside the crystal and *every* atom shares these electrons. Therewith, one can imagine this kind of crystal as a lattice of fixed ordered positive ions embedded into a *Sea of Electrons* or electron gas (see figure 2.3). The attractive force between the positively charged lattice and the negatively charged electron gas leads to the metallic bond.

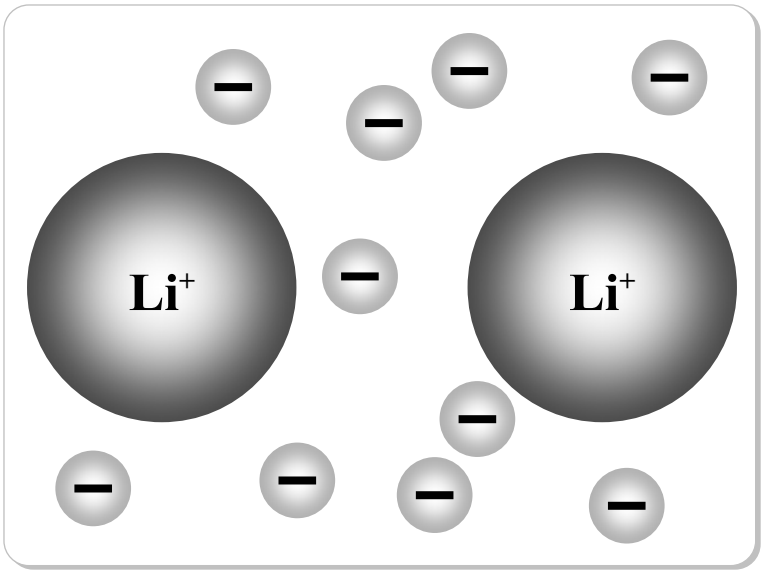

Figure 2.3 Schematic illustration of the metallic bond.

The electrons are delocalized and form a *Sea of Electrons*.

To understand the metallic bond, we discuss in the following as an example solid Lithium (Li). The electron configuration of the Li atom is $1s^2 2s$. The radial wave function of the $2s$-electron is

Equation 2.1
$$\psi_{20} = C_{20}\left(2 - \frac{r}{a_0}\right)e^{-r/2a_0}$$

C_{20} - normalization constant , a_0 – BOHR radius

Figure 2.4 (a) depicts the probability density of a wave function for a single Li atom at $r = 0$ in one dimension showing an exponential decay versus zero in case of $r \to \pm\infty$. Figure 2.4 (b) shows the probability density of an electron in the metal, which is identical in the environment of each Li nucleaus. The maxima of the probability density are located closer to the positive Li nuclei than in case of single atoms. Therefore, the potential energy of the electrons is lower. The lattice order of the atoms restricts the electrons to the area of ± 0.3 nm around the core, in contrast to a free atom, where the available volume is larger. The uncertainty principle postulates an increase of the momentum and the kinetic energy of the electron. The metallic bond is stable, because the decrease of the potential energy overcompensates the increase in the kinetic energy. This results in a minimization of the system's total energy. The effect is greatest for large size differences between the atom and the nucleus (large decrease of the potential energy) and small numbers of valence electrons (increase of the kinetic energy as small as possible). These conditions are the more fulfilled, the more one moves within the periodic table of elements to the left [.15].

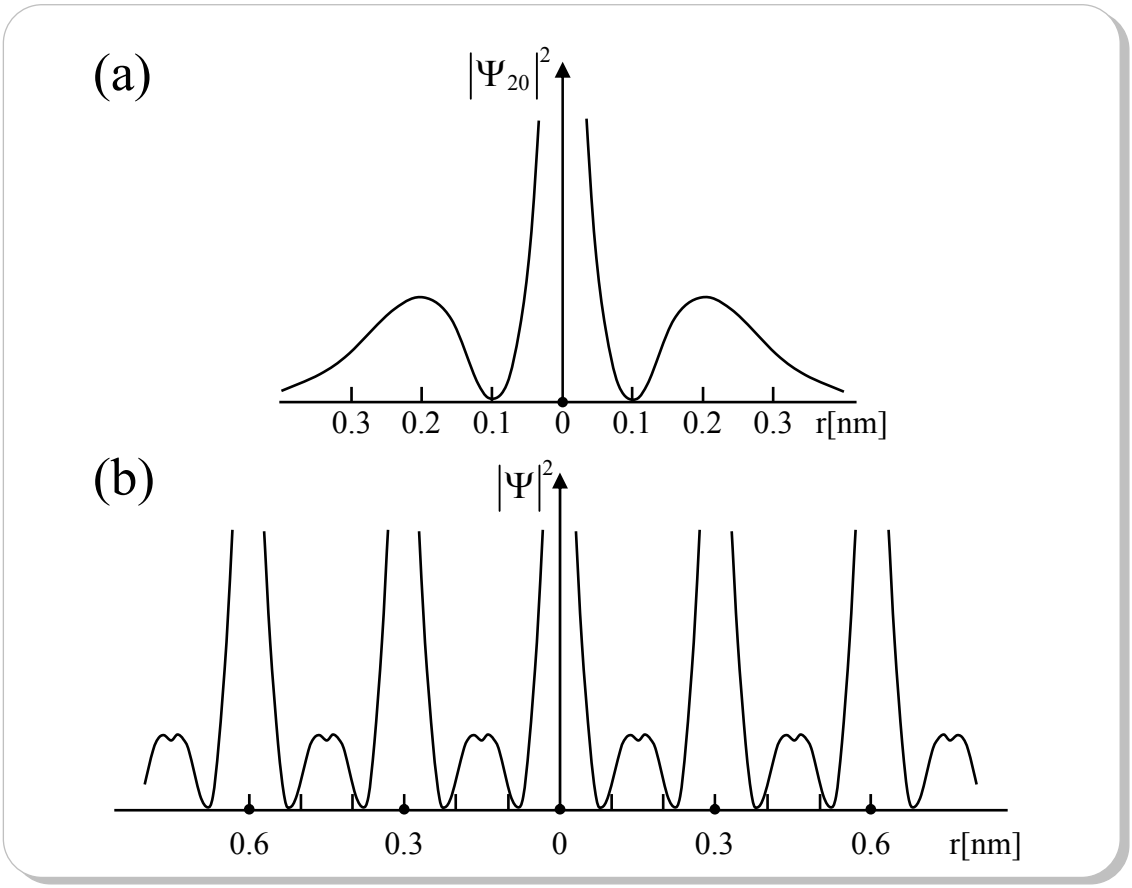

Figure 2.4 Probability density of (a) the 2*s* electron in an isolated Li-Atom, and (b) of the 2*s*-electrons in a one-dimensional Li crystal (taken from [15]).

2.1.1.1 Jellium-Model

An extended model for the description of the electronic structure of clusters is the so-called *Jellium-Model*[4] [16, 17]. While the model of metallic bonds describes discrete atomic nuclei, the *Jellium-Model* assumes the existence of a uniform background of positive charges. A good illustration of the COULOMB interaction between electrons and cores is the picture of a smeared out jelly-like background. In this model, the system properties (at zero temperature) depend only on the density of electrons. The mass spectrum of sodium clusters was the first experimental indication of the validity of the *Jellium-Model* for clusters (see 2.4.2.2, p. 66).

[4] The name of the *Jellium-Model* derives from *jelly*.

2.1.2 Covalent Bond

The *covalent bonding* is a quantum mechanical phenomenon. It results from the distribution of one or more electrons to at least two equal or similar atoms. Hereby, the symmetry of the molecular wave function (molecular orbital), which is formed by the superposition of the single atom orbitals, thus electrons, determines whether the interaction results in a bonding. The wave function of the symmetric state Ψ_S exhibits large values in the region between the nuclei, the potential energy becomes minimal, and a bonding takes place. The anti-symmetric wave function Ψ_A reaches only a small value in this region. The chemical bonding between different atoms is described frequently as mixture of a covalent and a ionic bond (see 2.1.4) [.15].

Materials using the covalent bonding do not have the tendency to build most closely packed geometries, because the atoms preferentially bind each other using specific angles. A typical example is Carbon (C), which has up to four binding partners. Commonly found preferred angles are 180°, 120° (planar), or 109.5° (tetrahedral). V. HELDEN *et al.* observed for Carbon clusters (C_n) several structures: simple ring structures for C_n clusters with $n \geq 7$, multiple ring structures ($n \geq 22$), and spherically shaped fullerenes [.18].

2.1.3 VAN DER WAALS-Bond

Rare gases are atoms with a closed outer shell. Therefore, no bonding using a metallic or covalent bond is possible. The one and only process by which noble gases attract each other is the VAN DER WAALS bonding, also known as *London Force*, *Instantaneous Dipole Effect*, or *Induced Dipole Interaction*. This bonding type is an intermolecular force or interatomic force that causes an attraction between temporarily induced dipoles in nonpolar molecules and atoms. The dipole of the atom in ground state is temporarily distinct from zero due to fluctuations and the quantum mechanical uncertainty. This dipole moment also induces a dipole moment in a neighbor atom, so that they attract each other due to the dipole-dipole interaction leading to the VAN DER WAALS bonding. For this reason,

the attractive potential is proportional to $1/r^6$ (r – distance between the atoms) and consequently the bonding is isotropic, resulting in atoms which are as closely packed as possible. They prefer structures with the maximal number of next neighbors.

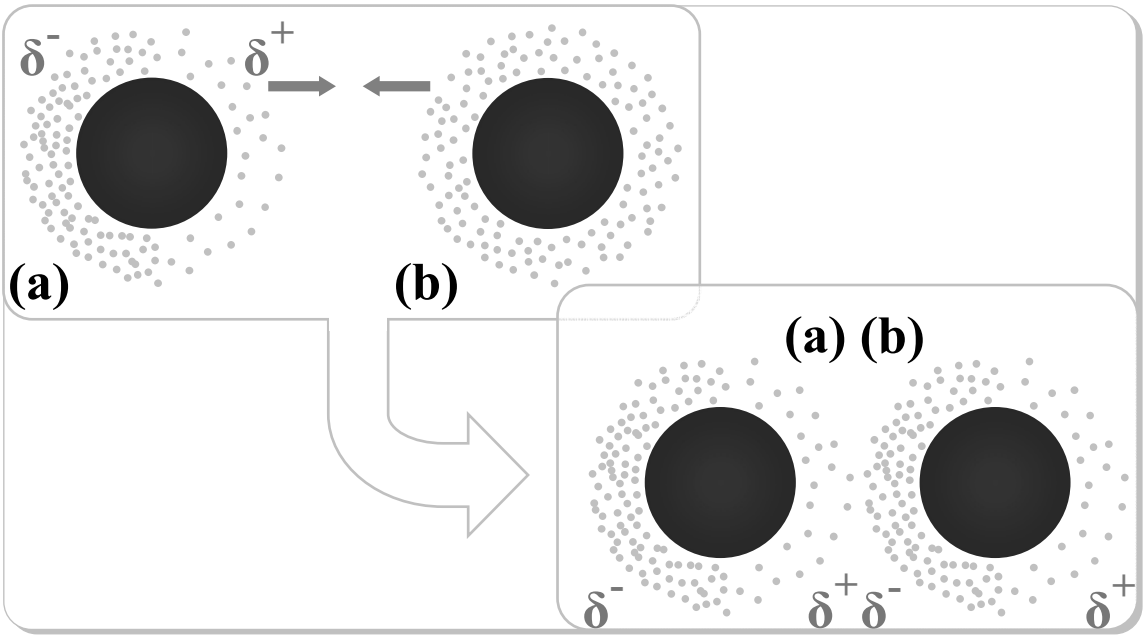

Figure 2.5 Schematic illustration of the VAN-DER-WAALS bond.

(Top) at the time atom (a) approaches atom (b) only the atom (a) has an asymmetric charge distribution. δ^+ attracts δ^-. (Bottom) Atom (a) induces a shift of the charge in that way that the positive polarized part of the atom attracts again the negative part. The larger the surface of the atom the large is the distance between the outer electrons and the nucleus and the higher the probability of polarization. For this reason, the VAN DER WAALS forces increase with increasing atomic mass.

2.1.4 Ionic-Bond

Another bonding type is the *Ionic bond*. This type of a chemical bond is based on electrostatic forces between two ions with opposing charges. Due to a low electronegativity a metal donates an electron in ionic bond formation, to form a positive ion or cation. In ordinary household salt, *e.g.*, ionic bonds exist between the sodium and chlorine ions. In

case of small distances, the PAULI *Exclusion Principle* counters the approach and a minimum in the potential curve U(r) arises [15].

2.2 Experimental Techniques

The experimental techniques we use within this work are Scanning Tunneling Microscopy (STM), Scanning Tunneling Spectroscopy (STS), and Ultraviolet Photoelectron Spectroscopy (UPS) [19]. Other authors describe the basic principles and theoretical bases of STM, STS, and UPS in more detail in many educational books [15, 20] and articles [21] of the recent past. Therefore, the following sections simply consist of a short overview and a summary of the relevant aspects.

2.2.1 Scanning Tunneling Microscopy

The STM represents a powerful method to investigate the geometric and electronic structure of solid-state surfaces. With an STM, a topographic imaging in real space of conducting and semi-conducting materials becomes possible. G. BINNIG and H. ROHRER [22, 23, and 24] invented in 1982 the first apparatus using the principle of STM and, later on in 1986, got the NOBEL prize together with E. RUSKA. Today the STM is one of the most important tools for surface analysis of metals or semiconductors down to atomic resolution.

2.2.1.1 Tunneling Effect

The quantum mechanical tunneling effect represents the basic principle of an STM. G. GAMOW [25] and independently at the same time, E. U. D. CONDON and R. W. GURNEY [26, 27] developed the idea of this effect in 1928. They explained the large fluctuation of the average lifetime of the α-decay of radioactive nuclei.

Figure 2.6 (top) schematically illustrates the tunneling effect.

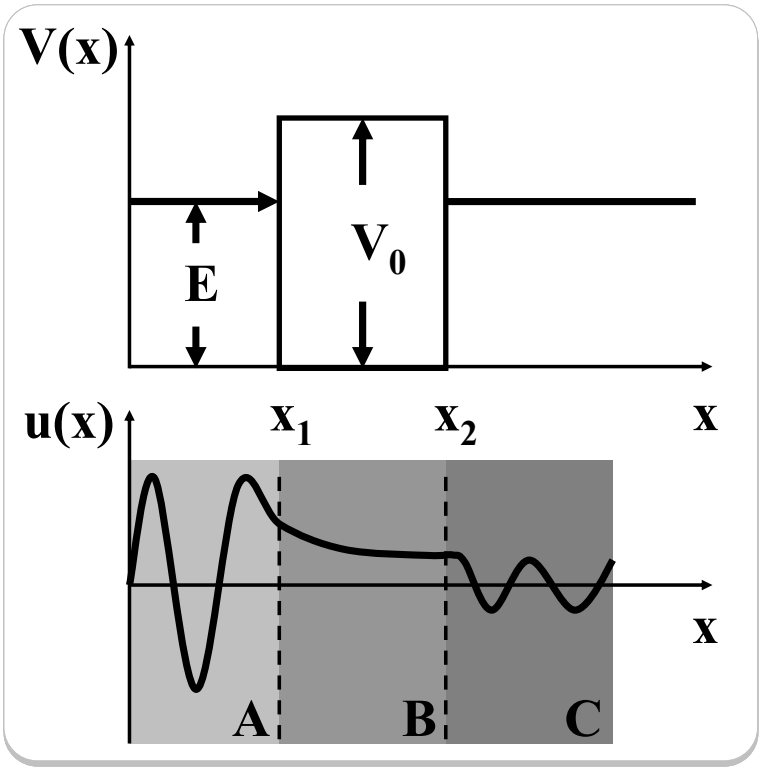

Figure 2.6 Schematic diagram of the wave function at a potential barrier.

(Top) Potential barrier with height V_0: incoming particle beam from the left has to be reflected if the kinetic energy E_{kin} is lower than the height of the barrier V_0. (Bottom) (A) The reflected and the incoming wave are superposed to the left of the potential well. (B) Inside of the potential well $(E_0 < V_0)$, the wave function decays exponentially. (C) To the right of the potential well the wave function is an outgoing planar wave with small amplitude. (based on figure 1 from ref. [28]).

Within classical physics, a potential barrier reflects particles of a particle beam after a collision, if their kinetic energy E_{kin} is lower than the height of the barrier V_0. Within the scope of quantum mechanics, particles with a kinetic energy $E_{kin} < V_0$, have a non-zero probability to penetrate into, *i.e.*, *to tunnel* through, the barrier V_0. The tunneling process originates in the uncertainty principle. For the localization of the wave function at the *classical* inflection point, the wave function contains - because of the uncertainty princi-

ple between position and momentum - components of the momentum, which correspond to energies above the potential barrier. There also exists an uncertainty between energy and time. This uncertainty of energy ΔE allows energies above the potential barrier for the particles in a time Δt. The transmission coefficient is a measure of the tunneling effect. Its definition is the ratio of the amplitudes of outgoing to incoming particle beam. Amplitude in this context means the absolute value of the squared wave functions.

In the one-dimensional case, one has to solve the SCHRÖDINGER equation of the matter wave of the particle, whereas one has to continue the wave function at the interfaces. In case of the steady state, the reflected and the incoming wave exhibits a superposition on the left side of the potential well. Inside of the potential well $(E_0 < V_0)$, the wave function decays exponentially (see figure 2.6, area B), and on the right side it is an outgoing planar wave with only small amplitude (see figure 2.6, area C). In the case of a rectangular potential well, the transmission coefficient decreases fast with increasing width and decreasing energy [29].

2.2.1.2 Principle of Scanning Tunneling Microscopy

We illustrate the basic principle of the Scanning Tunneling Microscope in figure 2.8. It is important to operate the STM commonly under UHV conditions in order to keep the surface free from impurities. We use an extremely sharp metallic tip (*tunneling tip*) to probe a conducting or semi-conducting surface. We approach the tunneling tip to the surface down to less than one nanometer distance between tip and surface. A tunneling voltage between tip and substrate results in a tunneling current due to the quantum mechanical tunneling effect (see 2.2.1.1). In this process, the finite distance between tip and substrate represents a potential barrier (see figure 2.7) for electrons, where tunneling through this barrier becomes possible. Depending on the polarity of the tip-sample bias, the tunneling electrons flow from the occupied states of the tip into the unoccupied states of the surface states and vice versa (see figure 2.10). To obtain a direct image of the sample surface, one moves the tunneling tip over the sample in a very close distance to the

surface by piezo electric crystals. While scanning a sample area of a few square nanometers up to some square micrometers, one records the tunneling current, and uses it as measurement signal for the generation of an STM image. In principle, one obtains a microscopic image directly by measuring the local variation of the tunneling current, while the distance between tip and surface remains constant (*constant height modus*). In the majority of cases, one uses a control unit in order to keep the tunneling current constant (*constant current modus*) by varying the distance between tip and sample surface. In such a case, the STM images contain the local z-position of the tunneling tip. Therefore, the STM allows the imaging of surfaces with atomic resolution.

Nevertheless, the STM image never shows the exact morphology of a sample. The STM image is always a convoluted image of the scanned object and the shape of the tip. Figure 2.8 schematically illustrates this broadening effect due to the convolution with the tip for different objects. At the bottom, we depict different tip positions during a line scan. In the top part of the picture, the bold line gives the trajectory of the tip scanning the objects. One can see that the height measurement of an object is exact, in contrast to the measurement of the width, because the tip shape broads the scanned object. Due to the last atom at the outer end of the micro-tip it is possible to resolve a single atom (a), some surface atoms (b), and a step edge (d). Larger objects (c), *e.g.*, a cluster, give a broad line profile, in which only the cluster height is real. To determine the lateral diameter of a cluster, we used transmission electron microscopy (TEM). For small silver and gold clusters, we estimated a diameter to height ratio of $d / h \approx 1.4$ [30, 31].

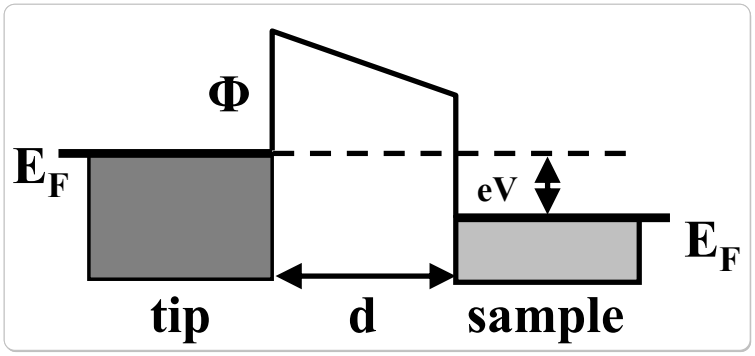

Figure 2.7 Band theory model of a one dimensional potential well (quantum well).

The work function Φ of the tip and the sample is equal (based on figure 4.2.4 from ref. [32]).

One feasible way to describe the physical background of the STM images is to apply the TRANSFER HAMILTONIAN OPERATOR to the tunneling process according to BARDEEN [33]. This model assumes the wave functions of the surface states of both electrodes (tunneling tip and sample surface) to overlap in order to carry out perturbation theory. Based on this, TERSOFF and HAMANN developed a simple theory of the STM [34, 35]. Since one does not know the real shape in general, one can approximate the tunneling tip to a spherical potential well with the radius R and could treat them like a metallic s-Orbital. We illustrate the tip geometry in figure 2.9. The position vector $\vec{r}_0$ defines the center of the tip. We name the smallest distance between tip and sample d. Assuming that the bias voltage U is low, the tunneling current is determined by

Equation 2.2
$$I \propto U \rho_{tip}\left(E_F\right) \rho_{sample}\left(\vec{r}_0, E_F\right)$$

$\rho_{tip}\left(E_F\right)$ – density of states of the tip, $\rho_{sample}\left(\vec{r}_0, E_F\right)$ – density of states of the sample surface at the center of the tip orbital, at the FERMI energy E_F.

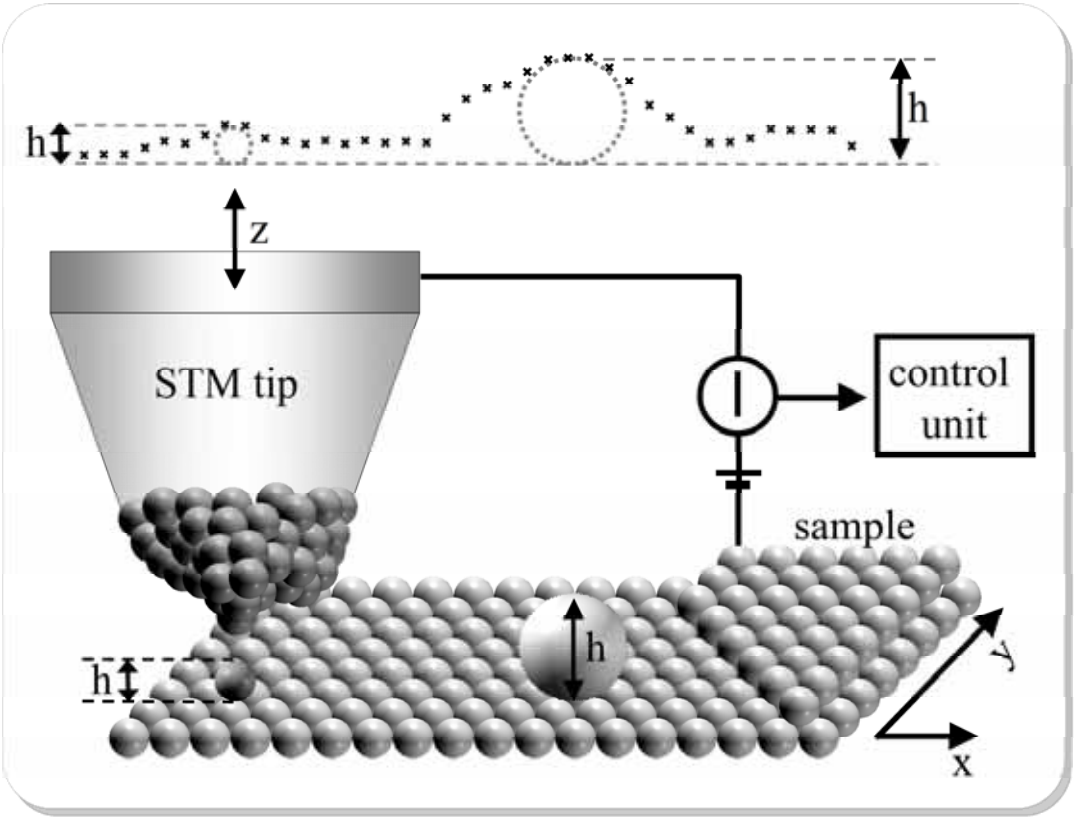

Figure 2.8 (Bottom) Schematic illustration of sample imaging with STM.

The height measurement of an object is exact, in contrast to the measurement of its width, which is broadened by the tip shape. (Top) Line profile of different objects. Line profile of (a) a single atom, (b) surface atoms, (c) a larger object, *e.g.*, a cluster, and (d) a step edge.

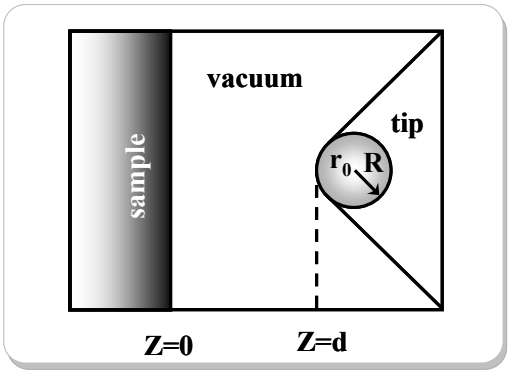

Figure 2.9 Schematic illustration of the tunneling geometry in the theory of TERSOFF and HAMANN. The tunneling tip has been approximated by a spherical potential well with the radius R [34, 35]. (Figure taken from ref. [.36]).

Therefore, at low voltages, the STM images the electronic density of states (DOS) at the surface of the sample close to the FERMI energy. This means, that the STM images do not directly show atoms of the sample surface, but their electronic states bound to the surface atoms. Accordingly, in the case of a constant tunneling current STM images show surfaces of constant DOS at the FERMI Level [34, 35]. The DOS of the tunneling tip, as well as the one of the sample surface influences the STM measurement.

In a first approximation, the DOS of the surface states decays exponentially in the vacuum with the effective inverse decay length κ_{eff}:

Equation 2.3
$$\rho_{sample}(d) = \rho_{sample}(d=0)\exp\left[-2\kappa_{eff}d\right]$$

d – distance to the surface

From equation 2.2 and equation 2.3 it follows, that the tunneling current also decays exponentially with increasing distance z between sample and tip:

Equation 2.4
$$I \propto= \exp\left[-2\kappa_{eff}z\right]$$

In which the effective inverse decay-length κ_{eff} is

Equation 2.5
$$\kappa_{eff} = \sqrt{\frac{2m_eB}{\hbar^2} + \left|\overline{k_{||}}\right|^2}$$

m_e: electron mass, $\overline{k_{||}}$: parallel wave vector of the tunneling electrons, B: barrier height

The height of the barrier B is approximately a function of the applied voltage U and the work functions ϕ_{sample} and ϕ_{tip} of the sample and the tip, respectively:

Equation 2.6
$$B = \frac{\phi_{tip} + \phi_{sample}}{2} - \frac{|eU|}{2}$$

The probability of the tunneling process reduces exponentially with decreasing geometric distance. In addition, one has to take the energy difference to the barrier into account. The

exponential current–voltage dependence determines the accuracy of the measurement because a small change of the distance results in a huge change of the tunneling current.

The description of the tunneling current according to equation 2.2 is restricted to low voltages. Since for the investigation of semi conductors in particular, one requires voltages in the order of 2 V – 3 V because of the existing band gap, one has to modify the theory. Hence, it follows:

Equation 2.7

$$I \propto \int_{E_F}^{E_F+eU} \rho_{tip}(E)\,\rho_{sample}(E+eU)\,T(E,U)\,dE$$

$T(E,U)$ – Transmission coefficient, dependent on the energy of the electrons and the applied voltage.

Thus, the tunneling current additionally consists of the product of the DOS of the tip and the sample for all different energies involved in the tunneling process. According to this, an image taken at, *e.g.*, -2 V, at the sample shows all occupied states with energies from the FERMI energy up to 2 eV below the FERMI energy. If a band gap exists, *e.g.*, for semi conductors, only the existing occupied states are imaged. Tunneling with a positive voltage leads to the imaging of unoccupied surface states in an energy interval defined by the tunneling voltage. Among the local distribution of the DOS, their energy dependence is of interest, which one can deduce from equation 2.7 by using the current-voltage curve. Therefore, the information about the transmission coefficient from equation 2.7 is necessary, which is a big obstacle for the practical processing, even with the use of approximations [37]. Therefore, one prefers an experimentally more feasible way, where one can approximate the DOS in the following way:

Equation 2.8

$$\rho_{sample}(eU) \approx \frac{dI}{dU} \Big/ \frac{I}{U}$$ (see [38, 39])

The LDOS between the sample FERMI energy E_F and the shifted FERMI level Φ_S of the tip determines the tunneling current I. For higher electron energies, the tunneling probability

through the potential barrier increases. Therewith, it is possible to determine the DOS experimentally dependent on the energy in relation to the FERMI level, with simultaneously high local resolution [29].

2.2.1.3 Scanning Tunneling Spectroscopy

We use the STM not only for the investigation of the local geometric structure as we describe above, but we also operate the STM for the investigation of the local electronic structure of the sample surface in spectroscopy mode. The lateral position of the tip remains constant, while the tunneling current $I_{tunneling}$ is measured dependent on the gap voltage $U_{tunneling}$. Figure 2.10 depicts the electronic states involved in the tunneling process. One can access the unoccupied LDOS by positive voltages (a) while one can measure the occupied states using negative sample bias (b). Assuming a constant tip DOS and low voltages the differential conductivity dI/dV is directly proportional to the local density of states (LDOS) of the sample surface [35]. The set point (I, V) determines the signal amplitude before starting the spectroscopy procedure,according to the condition

Equation 2.9

$$I = \int_0^V \left(\frac{dI}{dV} \right)\Big|_{\tilde{V}} d\tilde{V}$$

The signal-to-noise ratio increases for low voltages and high currents, which on the other hand leads to more instable tunneling conditions, particularly for clusters.

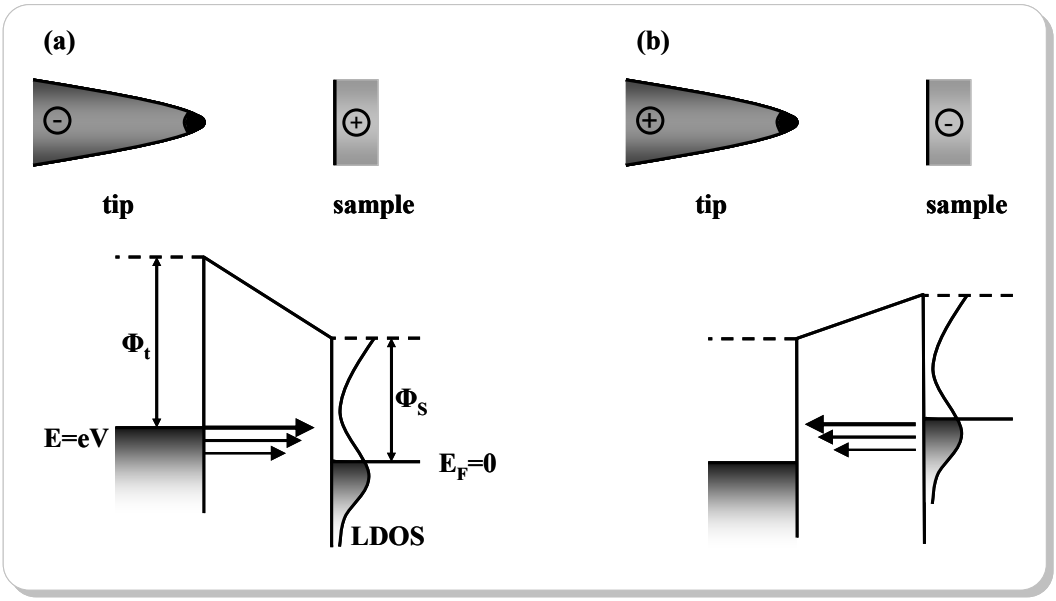

Figure 2.10 Schematic diagram of the involved states of the tunneling process of tip and sample depending on the polarity of the external bias voltage.

(a) Positive sample bias → Investigation of the unoccupied states (b) negative sample bias → Investigation of the occupied states. The shape of the potential between tip and surface depends on the respective work functions Φ_t and Φ_S.

If we repeat the spectroscopy for several lateral tip locations we can display the resulting data either as a set of voltage dependent dI / dV curves, or as so-called dI / dV maps. Usually one represents the dI / dV maps in a gray scale image, in which one depicts the dI / dV values for all locations at a particular voltage. As an improved technique for the performance of scanning tunneling spectroscopy (STS), we use a lock-in detection method. In this process, we use a lock-in detection instead of the numerical differentiation of the I(V) curves in order to improve the signal-to-noise ratio [36]. For further details about the lock-in detection and a more quantitative description of STS, see ref. [.40].

This combination of high energetic and spatial resolution turns STS into a powerful spectroscopic method.

2.2.2 Ultraviolet Photoelectron Spectroscopy

In several experiments we use UPS as a surface sensitive analysis method to investigate the occupied states of a sample based on the photoelectric effect. The photoelectric effect was first observed in 1887 by H. HERTZ [41] and in 1888 by W. HALLWACHS [42]. P. LENARD proved that the charged particles leaving a metal are electrons. He found that the kinetic energy of the released electrons was independent of the intensity and depended only of the wavelength of the light [43]. This behavior is in disagreement with the classical theory of waves of electromagnetic radiation. In 1905 A. EINSTEIN [44] succeeded in explaining the photoelectric effect based on the idea of the quantization of light (photons).

S. HÜFNER presents a good introduction into the topic of photoelectron spectroscopy in ref. [45] and describes in detail the development of photoemission spectroscopy from the early days to recent publication together with F. REINERT in ref. [46].

The basic principle of UPS shows figure 2.11 (top left): The sample is irradiated with light, which in case of sufficient photon intensity releases electrons from the sample. In our Surface Science Facility we describe in section 3.1 (pp 75), we use ultraviolet light of a differentially pumped helium gas discharge lamp with the energy $h\nu = 21.22$ eV (He I line) to excite the electrons. The photon energy is transferred to the electrons, which extracts them out of the solid-state sample, if their after-excitation energy is high enough to overcome the vacuum energy. Finally, one can detect the electrons as a function of their kinetic energy. The resulting energy distribution curve contains the number of detected electrons depending on their energy. In the following, we refer to these energy distribution curves as *spectra* or *UPS spectra*. UPS is a surface sensitive method, caused by the short mean free path of the electrons in the solid-state sample. The mean free path of the electrons for this specific energy range is about 1 nm. Hence, only electrons of regions close to the surface are able to leave the sample and are detectable. For this reason, the significantly larger mean free path of the photons is irrelevant for the surface sensitivity.

Starting point for the interpretation of the energy distribution curve is the EINSTEIN relation:

Equation 2.10 $$E_{kin} = h\nu - \phi_s - E_B$$

E_{kin} – kinetic energy of the electron, ϕ_S – work function of the sample, E_B – binding energy of the electron before emission

Within this single particle model, the electron absorbs the entire energy, which remains in the form of kinetic energy after the emission process. Further contributions of the interaction between photoelectron and the solid-state sample remain unconsidered for this approach. Moreover, one assumes that no change takes place for the solid-state sample concerning the many body character of the states involved.

BERGLUND and SPICER explain the correlation between the measured spectra and the DOS introducing the so-called *three-step model* [47]. This model treats the photoemission process as three independent steps. In the first step, the electron is optically excited into an unoccupied final state by photo-adsorption. In a second step, the electron is transported to the surface of the solid-state sample and finally the electrons are emitted into the vacuum.

The second and third step depend only slightly on the energy. Therefore, the *structures* observed in the spectra result from the energy dependency of the optical excitation of the electrons. This optical excitation probability corresponds essentially to the combination of the DOS of the initial and final state of the electron, which one can calculate using FERMI'S golden rule. The structure in the final DOS decreases with increasing energy, so that the DOS of the final state normally influences the spectra only slightly. Consequently, the intensity of the measured signal is in good agreement with the occupied states of the sample. We schematically illustrate this in figure 2.11.

The usually broad maximum of the energy distribution curve at lower energies results from inelastic scattered secondary electrons. Their contribution to the photoelectrons gradually decreases for higher energies and one observes a flat, less structured back-

ground in the spectra. In spite of the negligence of surface and many body effects, the three-step model is well suited for the prediction of the position and maxima in the UPS spectra [36].

However, for a quantitative description of the UPS spectra one has to consider many-body theory [48].

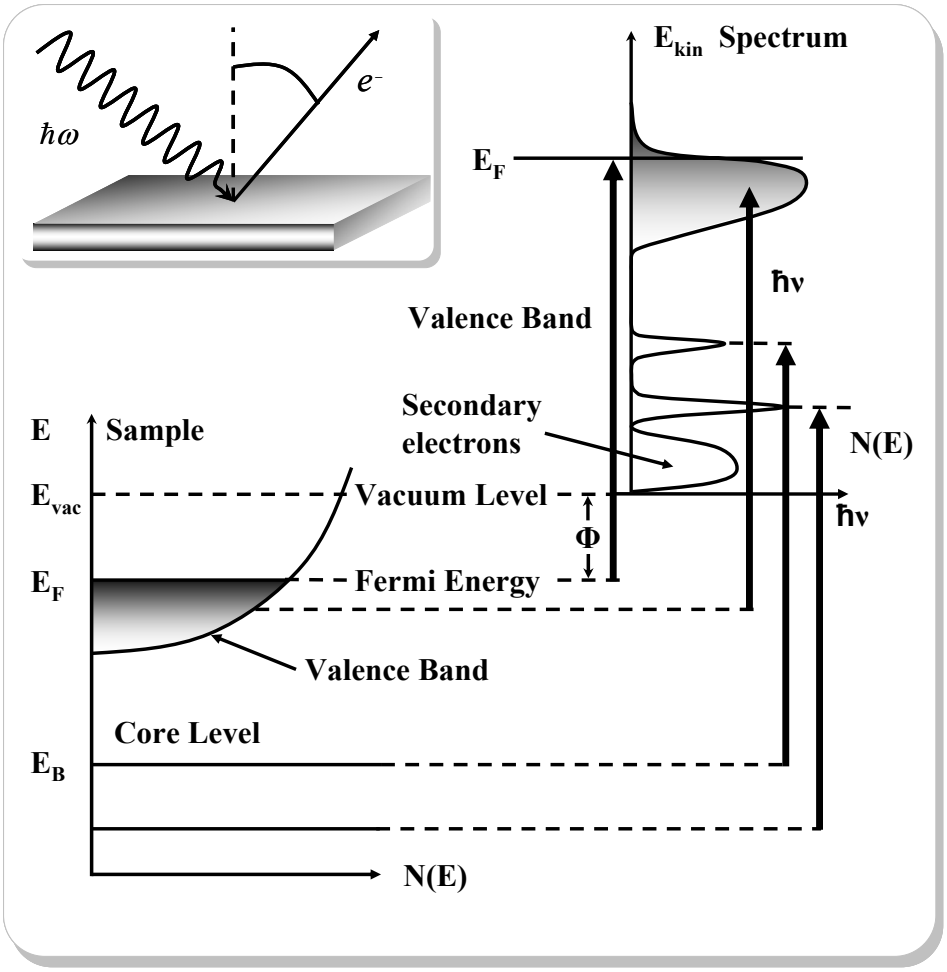

Figure 2.11 Energy scheme and geometry of the photoemission process.

(Top left) Geometry of the photoemission process: The photon excites an electron, which can be detected after leaving the sample. (Right diagram) In case of a constant final-state DOS the spectrum (top) is an image of the sample DOS (bottom) at the energy according to equation 2 from ref. [45]. The quantitative description of UPS spectra is only possible with many body theories [48].

2.2.3 Photoemission Techniques and Effects

Besides STM investigations (see sec. 2.2.1, pp 36), we perform UPS measurements (see sec. 2.2.2, pp 46) of clusters. In our studies, we use a not commonly known technique to measure the xenon film thickness during the adsorption process, which we describe in section 2.2.3.1. After that, we also shortly introduce the work function (2.2.3.2) and the charging energy (2.2.3.3) of clusters on surfaces. Finally, we discuss the *Dynamic Final State Effect* in section 2.2.3, which we have to consider for the interpretation of our results.

2.2.3.1 Photoemission of Adsorbed Xenon

One can compare the work functions of different samples by adsorbing a xenon layer onto a solid-state surface [49, 50]. Therefore, we use the strong signal of the $5_{p1/2}$ – niveau of the xenon atoms. Equation 2.11 describes the relation of the binding energy of the xenon $5_{p1/2}$ – peak (with respect to the FERMI level) to the work function of the bare surface φ_C and the binding energy E_B^V of the xenon $5_{p1/2}$ – peak (with respect to the vacuum level).

WANDELT measured E_B^V for several substrates (among other things for Pd, Pt, Ir, Ni, Cu, Ag, Au, Si, ZnO, and TiO_2) with different work functions and verified equation 2.11 [51]. UPS measurements in normal emission result in an essentially constant value for $E_B^V\left(5_{p1/2}\right) = E_B^F\left(5_{p1/2}\right) + \varphi_c = 12.3 \pm 0.1\ eV$.

Equation 2.11

$$E_B^F + \varphi_C = E_B^V = const$$

E_B^F – Binding energy of the xenon $5_{p1/2}$ – peak with respect to the FERMI level, φ_C – clean metal work function, E_B^V – Binding energy of the xenon $5_{p1/2}$ – peak with respect to the vacuum level.

WANDELT gives an interpretation of the striking invariance of the $5_{p1/2}$ ionization potential with respect to the vacuum level for different surface orientations and metals in figure

2.12. Two different metals (metal 1, metal 2) with equal FERMI energy E_F show different vacuum energies $E_{vac,1}$ and $E_{vac,2}$ due to their different work functions $\varphi_{C,1}$ and $\varphi_{C,2}$. The reference energy for the Xenon $5_{p1/2}$ – peak of an adsorbed Xenon film is not the FERMI energy, but the respective vacuum energy, which results in different positions within the UPS spectra. This is because the diameter of a Xenon atom is relatively large (approximately 4.5 Å). The center of such an atom adsorbed on a surface is located outside of the electrostatic surface potential. The curve $\Phi_1(z)$, which connects $E_{vac,1}$ outside the surface with $E_{int,1}$ inside the metal, represents the variation in electrostatic potential (including image effects) that any charge will experience when brought from infinity through the surface into the bulk due to the well known charge double layer (electron-spill over). Xenon atoms of the first monolayer decouple from the substrate, because the surface potential is too weak to affect the nucleus. This surface potential effects the second, third, and all other Xenon layers even less. Hence, all binding energies of the Xenon layer are independent of the FERMI energy. The reference energy is the vacuum energy of the substrate. For this reason, the position of the $5_{p1/2}$ – peak is constant with respect to the vacuum energy.

Therefore, we can use this so-called *Photoemission of Adsorbed Xenon* (PAX) to determine the work function difference of two samples, by measuring the position of the $5_{p1/2}$ – peaks of two xenon-covered samples in UPS. The difference of these two peak positions is equal to the difference of the work functions.

Moreover, we use PAX to carry out a controlled xenon adsorption, by measuring the $5_{p1/2}$ – peaks of the first five monolayers *in situ* with UPS, as described in section 4.1.4.1 (pp .119) [.52].

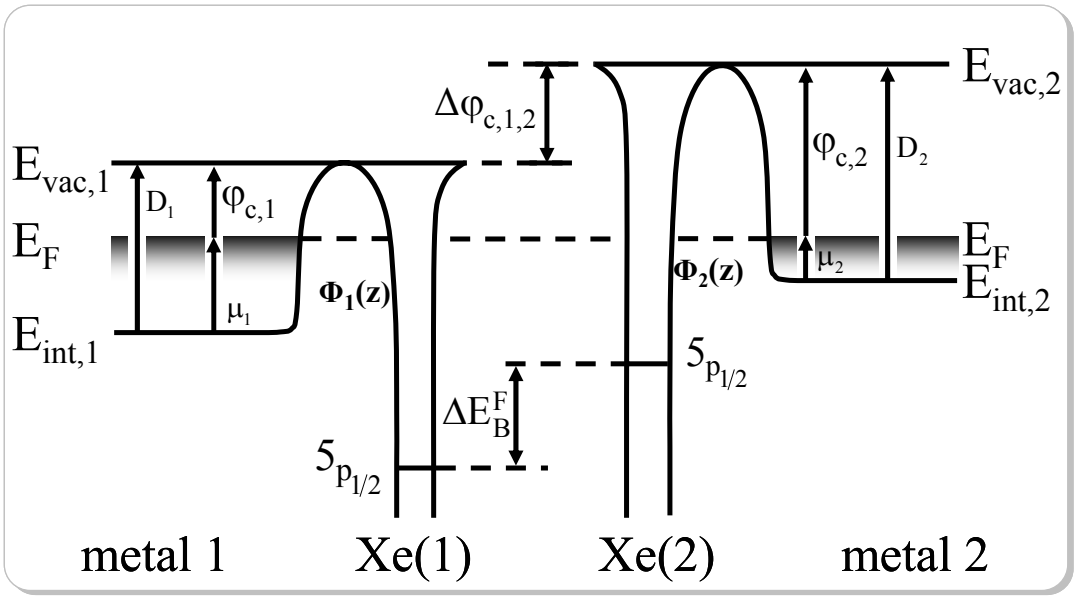

Figure 2.12 Potential energy diagram for xenon atoms Xe(1) and X(2) adsorbed on the two semi-infinite metals of different work functions $\varphi_{c,1}$ and $\varphi_{c,2}$ on one φ - heterogeneous surface.

$E_{vac,1}$ – vacuum level of metal 1, E_F FERMI level, and $\varphi_{c,1}$ – work function of the bare surface (based on figure 1 from [51]).

2.2.3.2 Work Function

The work function Φ is an important property of metals and defined as minimum energy needed to remove an electron from a solid to a point outside the solid surface, far from the surface on the atomic scale, but still close to the solid on the macroscopic scale. The magnitude of the work function is commonly about a half of the ionization energy of the corresponding free atom.

For the interpretation of the observed effects we report in section 5.2 (p..146) the work function is of particular importance. We always measure the work function of the samples at several steps in an experimental run. The work function Φ_S of our sample is

Equation 2.12 $$\Phi_S = h\nu - \Delta E_{spectra},$$

$h\nu = 21.2$ eV - photon energy, $\Delta E_{spectra}$ – total width of the photoelectron spectra

where $h\nu = 21.2$ eV is the photon energy and $\Delta E_{spectra}$ is the total width of the photoelectron spectra. To obtain $\Delta E_{spectra}$ we apply a bias voltage of $U_{bias} = 5.00$ V to the sample and determine the position of the FERMI energy and the level of the lower so called cut-off energy, which is given by the onset of the secondary electron peak [45] (see figure 2.13, and also figure 2.11).

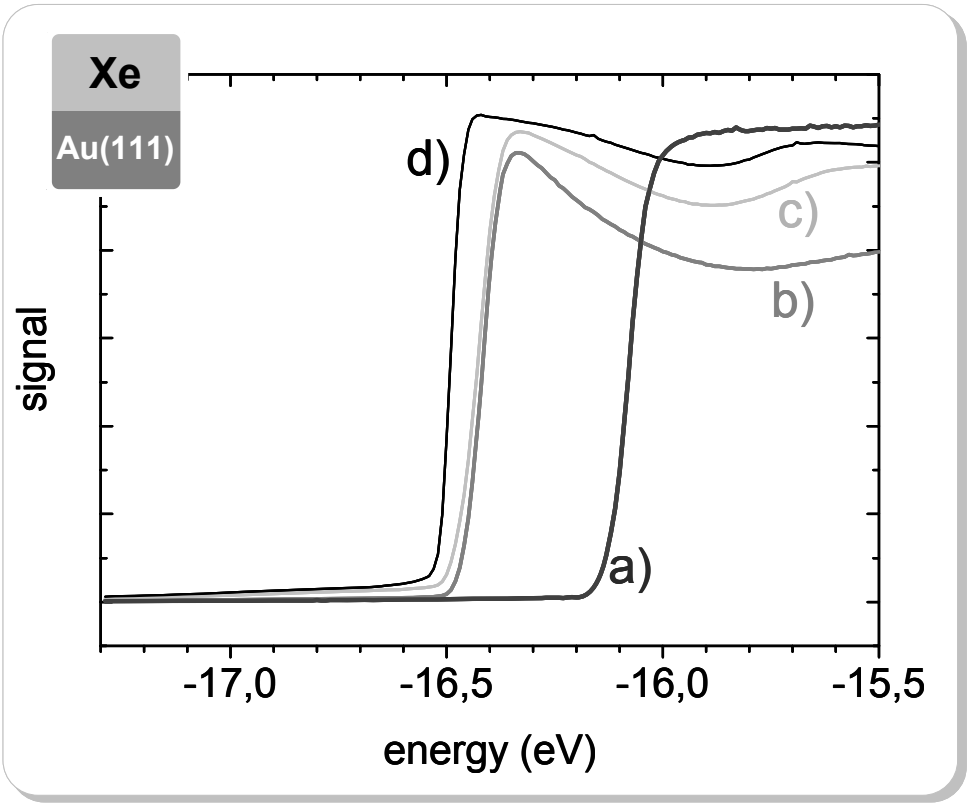

Figure 2.13 Lower cut-off energy of the UPS spectra.

a) Pristine Au(111) substrate, b) 10 ML Xe / Au(111), c) 30 ML Xe/Au(111) and d) 160 ML Xe/Au(111). The spectra are scaled to similar maximum signal for better visualization. A bias voltage of +5eV was applied to the sample. The energy scale is given by the FERMI energy $E_F = 0$ eV.

2.2.3.3 Charging Energy

The charging energy (COULOMB Energy) of metallic nanoparticles, which are (weakly) coupled to the environment is of general interest, *e.g.*, in single electron devices [.53]. R. WILKINS *et al.* were able to measure the charging energy directly for isolated supported nanoparticles using a scanning tunneling microscope [.54].

In our experiments, the charging energy of small metal islands plays an important role. In the following, we discuss the charging energy exemplarily for a spherical nanoparticle (cluster), because we can approximate the islands in our experiments in a first order as spherical.

The capacitance of a sphere is

Equation 2.13
$$C_{sphere} = 4\pi\varepsilon\varepsilon_0 R\,.$$

ε_0 – vacuum permitivity , ε - material constant (in vacuum ≈ 1), R – radius of the sphere

The electrostatic energy of an island or cluster with the capacitance C is

Equation 2.14
$$E(Q) = \frac{Q^2}{2C}\,.$$

C – total capacitance of the cluster or island, Q – charge on the cluster or island

The (excess) charge Q is a multiple of the elementary charge e:

Equation 2.15
$$Q = n \cdot e$$

e – charge of one electron, n – number of electrons.

The energy which is needed to charge a neutral cluster (n = 0) with ±1e is

Equation 2.16
$$E_C = \frac{e^2}{2C}\,.$$

Table 2.2 shows typical capacities and charging energies in the order of macroscopic, mesoscopic, and atomic objects.

CAPACITANCE AND CHARGING ENERGIES			
R= 0.1 m	$C = 10^{-12}$ F	$E_C = 7 \cdot 10^{-8}$ eV	macroscopic
$R = 10^{-6}$ m	$C = 10^{-17}$ F	$E_C = 7 \cdot 10^{-3}$ eV	mesoscopic
$R = 10^{-9}$ m	$C = 10^{-20}$ F	$E_C = 7 \cdot$eV	atomic (estimation)

Table 2.2 Order of magnitude of capacitance and charging energies for spherical particles.

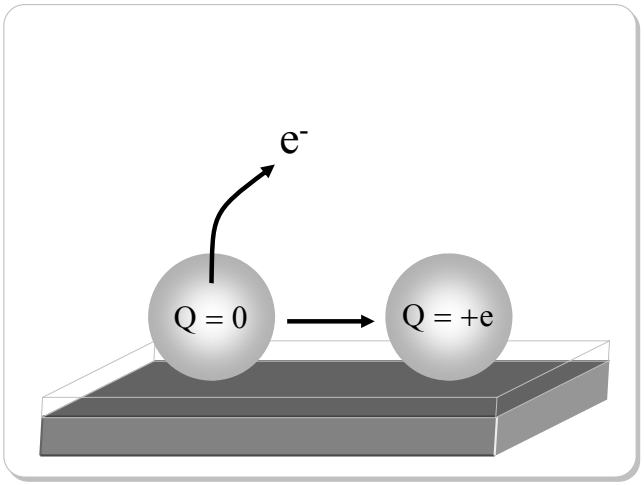

Figure 2.14 Schematic illustration of the charge process of a spherical particle.

2.2.3.4 Dynamic Final State Effect

For the investigation and interpretation of UPS measurements of clusters on substrates we have to consider the final state effects. Figure 2.15 schematically illustrates the UPS process.

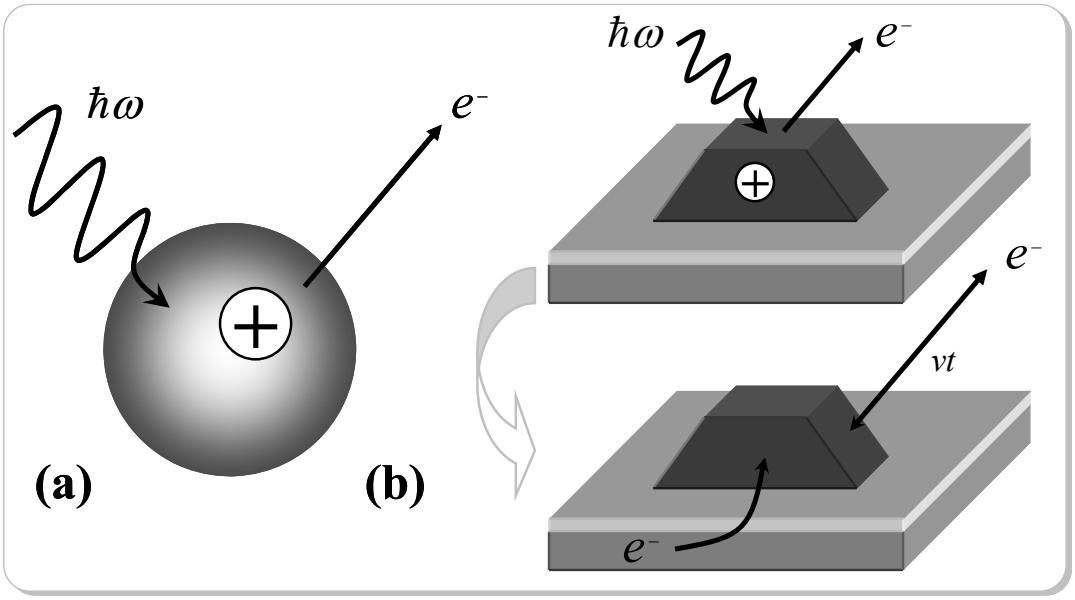

Figure 2.15 Schematic illustration of the photoemission process for metal clusters.

(a) Free cluster: The photo hole persists within the relevant electron-hole interaction time. The kinetic energy of the photoelectron is lowered. (b) Cluster on a surface: The photo hole is neutralized by an electron from the substrate in a time t.

Figure 2.15 (a) shows a free cluster. An incoming photon produces a photoelectron, and a positive charge remains on the cluster. The lifetime of the positive charge on the isolated cluster is large compared to other timescales of the experiment. This allows a description from the static point of view. In case of supported clusters, an electron of the sample neutralizes the positive charge in a time t, that remains on the cluster after the photoemission process. The remaining positive charge attracts the emitted electron. This results in an energy shift of the detected electron, which thereby looses kinetic energy. The time for the neutralization depends on the coupling of the cluster to the substrate. For metal clusters on a metal surface, the neutralization takes place very fast due to the good electrical coupling to the surface. In this case, one can interpret the UPS spectra according to a solid-state sample as usual. Nevertheless, for clusters, *e.g.*, on semi conducting surfaces or rare gas layers, one observes a so-called *dynamic final state effect*. For the interpretation of the UPS spectra one should not neglect the time scale on which the neutralization takes

place. For further details and calculations of the energy shift see ref. [55], [56], [57] and [58].

2.3 Metal Island Growth

The investigation of metal islands and clusters grown on surfaces was a topic of many previous publications. HEYRAUD and METOIS [59], *e.g.*, studied the equilibrium shape of gold crystallites on a graphite cleavage surface. Former studies in our group treat the electronic and geometric properties of a broad range of cluster sizes grown in nanometer-sized pits (*nanopits*) on graphite [31, 55, 60, and 61].

In this section, we will start with an introduction in the general growth and nucleation process of clusters grown on surfaces, exemplarily within an excursion to cluster growth in nanopits.

After this, we describe the technique, we use within this work to produce large metal clusters, namely ***B**uffer **L**ayer **A**ssisted **G**rowth* (BLAG) [62] (see 2.3.2).

2.3.1 Growth and Nucleation of Clusters on Surfaces

Figure 2.16 schematically illustrates the cluster growth process for clusters grown by metal evaporation. The atoms produced by an evaporator, *e.g.*, an *Evaporator with Integrated Flux Monitor* (see sec. 4.1.1, p. 112) or an *Evaporator with Resistive Heating* (see sec. 4.1.2, p.114) arrive at the surface and hit an existing cluster (direct impingement) or adsorb on the substrate between the clusters. In the first case - the direct impingement - they adsorb with the probability 1, and in the second one, they diffuse between the clusters performing a random walk. After they have moved a mean length before desorption λ_{diff} they desorb again, except they are captured by an existing cluster, another atom, a step, or a nanopit edge. ANTON and KREUTZER, *e.g.*, report a mean diffusion length before adsorption for gold on graphite of $\lambda_{diff} = (5.8 \pm 2.4)\,\mathrm{nm}$ [63] at T = 350 °C.

For two metal atoms, there is a high probability for them to stick together and become a dimer, which adheres at defects or step edges of the substrate. VENABLES *et al.* [64] refer to a molecule or a small cluster of a specific size as *critical nucleus*, which preferentially adheres at pit or step edges (see [31, 65, and 66]).

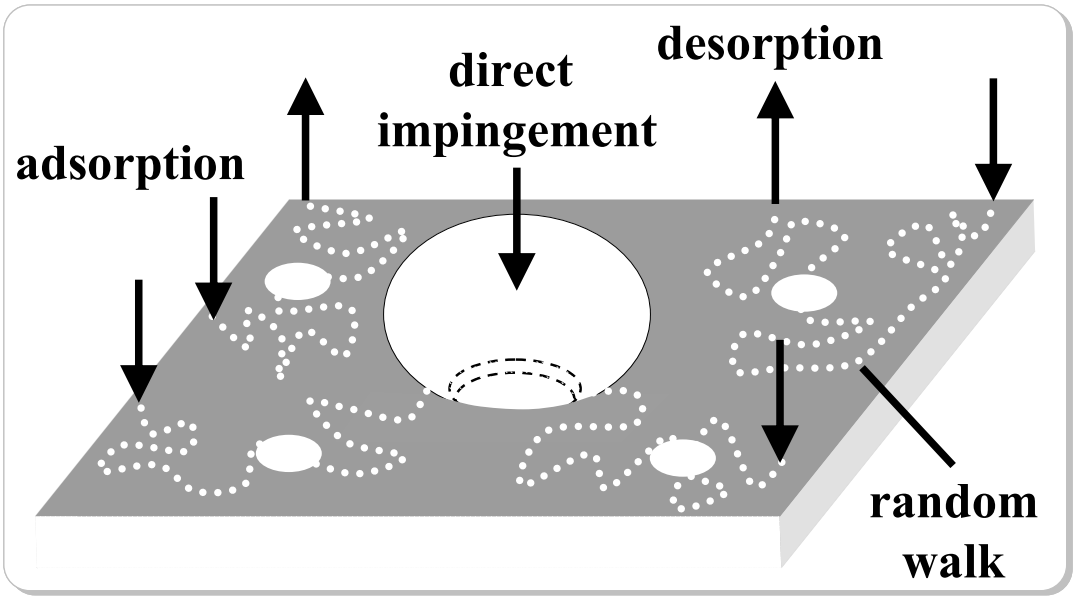

Figure 2.16 Schematic diagram of the nucleation and growth of clusters on surfaces.

Nevertheless, for clusters at such defects, one has to distinguish between different locations of the clusters. The authors in the references [66, 67, 68, 69, 70 and 71] deposit metal particles electrochemically and observe in many cases decorations on top of the steps. In contrast, some other groups in the references [59, 72, 73, and 74] observe the nucleation below a step edge and at the bottom of a nanometer sized defect (see figure 2.17), which we call *nanopit*.

We studied 15 clusters on nanostructured graphite, before and after a tip induced displacement by the STM tip (*e.g.*, during STS measurements), to determine the exact position of the clusters (for details see [30], published within [55], p. 70). For such displaced clusters, we compared images, in which a cluster was at least partly visible before the

displacement, with images afterwards, when the underlying pit edge became visible. We could confirm that the clusters grow neither only below nor only above the step edge for all 15 different clusters. The pit edge crossed the (previous) cluster diameter, even if we corrected the lateral cluster size for the broadening by the tip shape (see figure 2.8, p. 41). We consider a cluster diameter of 1.4 times the cluster height as discussed in ref. [.75]. We concluded that the clusters start to grow at the pit edge and finally take an equilibrium shape overlapping the edge.

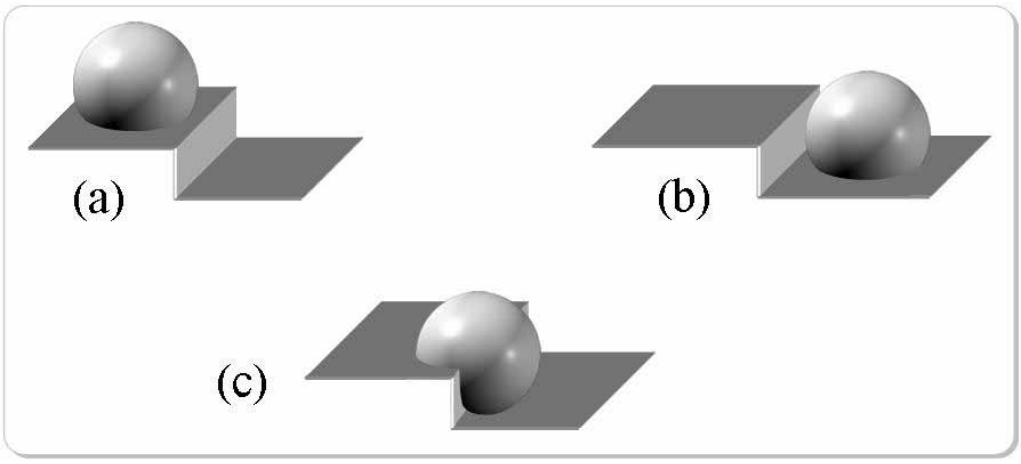

Figure 2.17 Location of clusters grown by metal island evaporation on surfaces.

(a) The cluster is located on top, (b) at the bottom, and (c) overlapping at a step or pit edge.

2.3.2 Mechanism of Buffer-Layer-Assisted Growth

Several other groups use rare gas layers in their experiments to reduce the interaction between metal islands or clusters grown or deposited on surfaces. We mention only two typical examples. FAUTH *et al.* deposit Platinum (Pt) atoms and small Pt clusters into a thin rare gas layer on a graphite surface to study the influence of the cluster-surface interaction [.76]. The rare gas strongly reduced the surface diffusion and they observe specific shifts induced by an interaction of the clusters with defects such as step edges. In ref. [.77] OHNO *et al.* evaporated Ag atoms on a Xe layer on GaAs. They study the formation of Ag

clusters and the subsequent immersion of the clusters into the Xe film with x-ray photoelectron spectroscopy. WADDIL *et al.* developed this process first to produce abrupt interfaces [78] and later refined the method and called it *Buffer Layer Assisted Growth*. [79]. We use this method to produce large clusters with several thousands of atoms as we describe in section 4.1.5.1 (p. 125) and deposit them onto a rare gas layer (see 4.1.4.1, p. 119). Finally, we present the results in section 5.1 (pp 132).

The main idea of the BLAG process is to adsorb inert buffer layers at low temperatures in order to prevent deposited atoms to directly interact with the substrate. The adatoms diffuse on the buffer layer [62] and form three-dimensional clusters or islands. Cluster formation on a Xenon buffer layer, *e.g.*, is understandable considering extremely low surface free energy (see sec. 2.4.3, pp 71) ($\gamma_{Xe} \cong 0.063\,J/m^2$) for Xe(100) and a very weak interaction with an adatom, giving a low interface energy γ_i. Therewith the condition for a three dimensional growth is always fulfilled, $\gamma_{Xe} < \gamma_d + \gamma_i$ where γ_d is the surface free energy of deposited material ($\sim 0.62\,J/m^2$ for Ag(111)). The nucleation and growth takes place independent of the underlying substrate.

2.4 Size-Selected Clusters

The second type of clusters we use in the present work are size-selected clusters. In contrast to the clusters we produce by metal island growth, size-selected clusters consist of an exactly defined number of atoms. We built our cluster deposition machine, we describe in 3.2 (pp 78), for the deposition of size-selected clusters. We use a new high-transmission time of flight mass selector (see sec. 3.2.3, p. 92) to generate clusters of a broad range of cluster sizes. In this section we introduce the geometry of size-selected (2.4.1) and, in particular, magic clusters (2.4.2.2) as well as the two main topics within the DFG priority project, namely clusters in a free beam (2.4.2) and clusters on surfaces (2.4.3).

2.4.1 Geometry

Beside the cluster density per area, the only reliable information in our STM investigations is the cluster height. In a first analysis, we always compare the cluster heights we measure with STM to the estimated calculated height.

We describe the morphology of hard landed clusters, which pin to the surface, as well as grown clusters at defects, as a first approximation as truncated spheres [75].

Figure 2.18 (b) schematically illustrates the model of a truncated sphere. In previous experiments [23, 61, and 60], we used a combination of STM for measuring the cluster height and TEM for measuring the lateral cluster size. With this, as already mentioned in section 2.2.1.2 (pp 38), we measure a diameter to height ratio of $d/h \approx 1.4$ for several samples. The mean cluster heights are in the range of $h = 1.8\ \text{nm} - 6.7\ \text{nm}$. The truncated sphere model then leads to the cluster volume

Equation 2.17
$$V_{ts} = \left(\pi \cdot h^2/3\right)\left(3 \cdot d/2 - h\right) = 1.152 \cdot h^3 .$$

h – cluster height, d – cluster diameter

We describe the volume of soft-landed clusters not pinned to a surface analogously, but in this case using the volume of a simple sphere

Equation 2.18
$$V_S = \frac{4}{3} \cdot \pi \cdot \left(\frac{1}{2} \cdot h\right)^3 = 0.524 \cdot h^3 .$$

h – cluster height

In solid-state samples silver atoms are arranged in the fcc structure with a lattice constant of a = 0.409 nm [80] and four atoms per unit cell. The volume of the unit cell is a^3, and the resulting volume of a Ag_n-cluster is:

Equation 2.19
$$V_{Ag_n} = \frac{a^3}{4} \cdot n .$$

For a Ag_{55} cluster, *e.g.*, the volume is $V_{Ag_{55}} = 0.94\ \text{nm}^3$.

Using equation 2.17 and equation 2.18 the estimated silver cluster height is consequently

Equation 2.20 $$h_{Ag_n}^{ts} = \sqrt[3]{V_{Ag_n} / 1.152}\,.$$

$h_{Ag_n}^{ts}$ – Cluster height of an Ag_n cluster, calculated by using the model of a truncated sphere.

and

Equation 2.21 $$h_{Ag_n}^{s} = \sqrt[3]{V_{Ag_n} / 0.524}$$

$h_{Ag_n}^{s}$ – Cluster height of an Ag_n cluster, calculated by using the model of a simple sphere.

respectively.

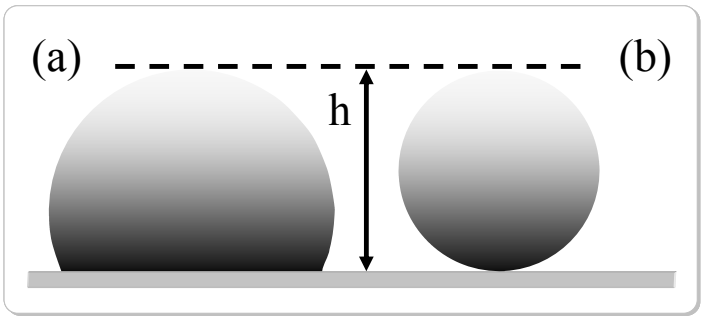

Figure 2.18 Schematic depiction of two possible geometric models for clusters on surfaces with given height h. (a) Truncated sphere, (b) simple sphere.

According to this, we plot the estimated cluster height for Ag_n (n = 1 – 1000) clusters versus the respective number of atoms in Figure 2.19. Table 2.3 summarizes the calculated cluster heights for the clusters generated within our experiments.

However, the heights we measure in STM can be slightly different because the STM tip measures lines of constant density of states (see 2.2.1.3, pp 44). Variations of the tunneling voltages between -0.5 V and +1 V usually leads to height difference in the order of a few 0.1 nm.

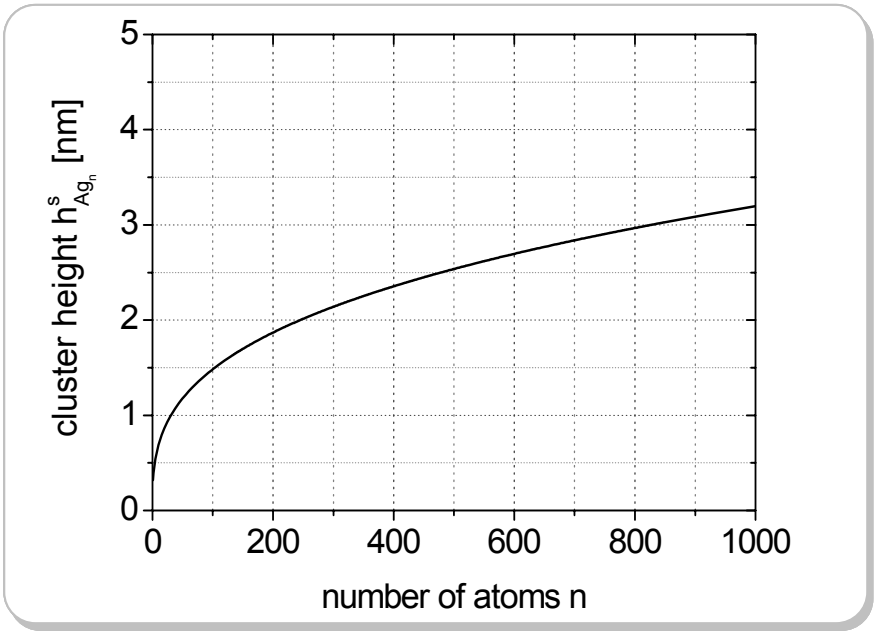

Figure 2.19 Calculated cluster height of Ag_n clusters (n = 1 – 1000) plotted versus the number of atoms.

For this calculation, we apply a model of a simple sphere (see equation 2.21).

CLUSTER HEIGHTS OF SELECTED AG CLUSTERS

$h^{ts}_{Ag40} = 0.8$ nm	$h^{s}_{Ag_{309}} = 2.16$ nm
$h^{ts}_{Ag_{80}} = 1.05$ nm	$h^{s}_{Ag_{561}} = 2.64$ nm
$h^{ts}_{Ag_{55}} = 0.93$, $h^{s}_{Ag_{55}} = 1.22$ nm	$h^{s}_{Ag_{923}} = 3.11$ nm
$h^{s}_{Ag_{147}} = 1.69$ nm	$h^{s}_{Ag_{2130}} = 4.11$ nm

Table 2.3 Calculated cluster heights of clusters deposited within this thesis (see sec. 5.2, pp.146).

2.4.2 Clusters in a Free Beam

Our collaborators B. V. ISSENDORFF *et al.* study clusters in a free beam using photoelectron spectroscopy (PES). The motivation of these studies are the characterization of the

electronic and geometric structure of small to large clusters as well as the measurement of the charging energies of big clusters.

Within SPP 1153, we compare the results of free clusters with the results of clusters on surfaces.

2.4.2.1 Shell Model for Clusters

For the structure of free clusters, one can apply in a first approximation FRIEDEL'S rule

The cluster structure that has the largest number of next neighbor bonds has the highest bonding energy and hence, is the most stable of all structures.

Following this rule, the most structures conform to a pattern of platonic bodies. Here, the most important structure is the icosahedron. This structure can be formed for clusters with a number of atoms n = 13, 55, 147, 309, 561, 923, and 1415. One atom is located in every corner and inside the icosahedron. Due to the 12 corners, a cluster with 13 atoms has 12 surface atoms and one volume atom. Larger atom numbers fill a new shell according to an icosahedral structure. Because of the larger bonding lengths, in the k^{th} shell is space for $10 \cdot k^2 + 2$ atoms. Therefore, in the first shell is space for 12 atoms (*e.g.*, Ag_{13}), in the second for another 42 atoms (*e.g.*, Ag_{55}), in the third for 92 atoms (*e.g.*, Ag_{147}), *etc.* For all these shells, there exist 12 atoms at the corners and additionally $10 \cdot k^2 - 10$ atoms at the surfaces of the icosahedron. In this configuration a geometric structure is formed. In analogy to atomic physics with its stable noble gases, there exist also very stable clusters due to the closed electronic shells. We introduce these so-called geometrically or electronically magic clusters in the next section (2.4.2.2).

Figure 2.20 exemplarily depicts the kinetic energy of the electrons depending on the cluster radius according to the spherical Jellium-background-model for the Na_{20} cluster [81]. The energy levels represent the cluster shells. Rightmost one can see the maximum numbers of atoms per energetic level, while the numbers in brackets are the numbers of degeneracies per level. The labeling *s, p, d, f* of the energetic levels represents the angular

quantum number according to atomic physics. The first number represents the zero of the wave function of the quantum mechanical harmonic oscillator. At the 2s-level one can see the two electrons with spin up and spin down, which are in the outer shell of the Na_{20} cluster. This potential of the electrons in which a uniform background of positive charge exists is comparable to the WOOD-SAXON potential in nuclear physics.

Figure 2.21 depicts the WOOD-SAXON potential of nucleons. The picture combines a rectangular potential and the potential of the harmonic oscillator. In the left part of this picture, one can find the WOOD-SAXON potential of neutrons; and to the right, the one for protons, where in addition the COULOMB energy has been included. Both describe nucleons as FERMI gas. One can see the energetic levels, which represent the shell structure of the atomic nucleus. A specific number of nucleons can fill the shells.

A further analogy is the similarity to the periodic table of elements. The successively filling of cluster shells with electrons illustrates figure 2.22. In this picture, the arrangement of energetic levels within a cluster occurs in shells, in accordance to nuclear physics. Leftmost one can see the list of the shells *1s, 1p, 1d* and *2s* and to the right the corresponding Na cluster, each with their respective number of electrons per energetic level. The more atoms per cluster exist, the more electrons occupy free positions within the shells, until electrons completely occupy and close the shell. Commonly one names clusters with closed shells electronically *magic clusters*, which we discuss in the section below.

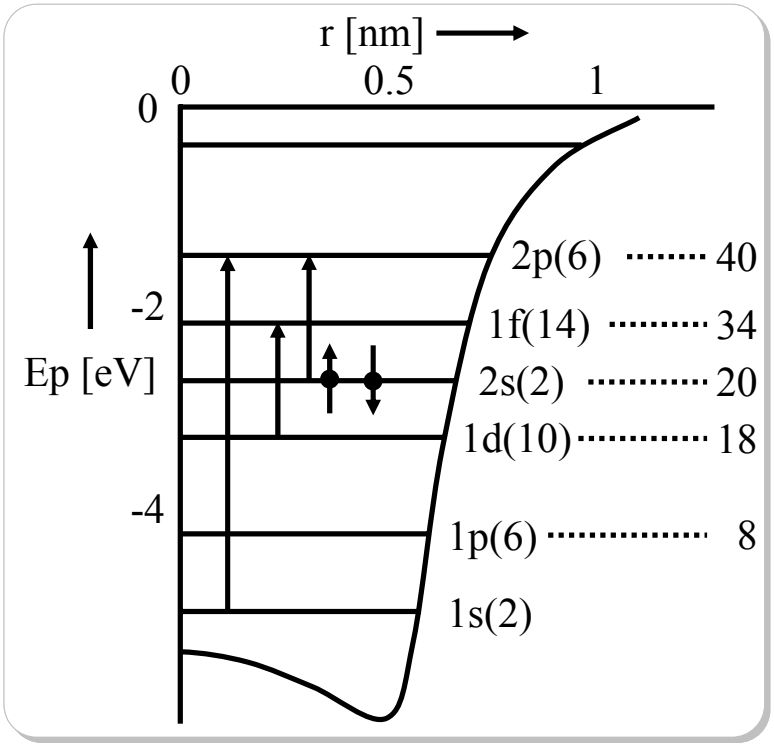

Figure 2.20 Kinetic energy of the electrons depending on the cluster radius according to the spherical Jellium-background-model exemplarily for the Na_{20} cluster.

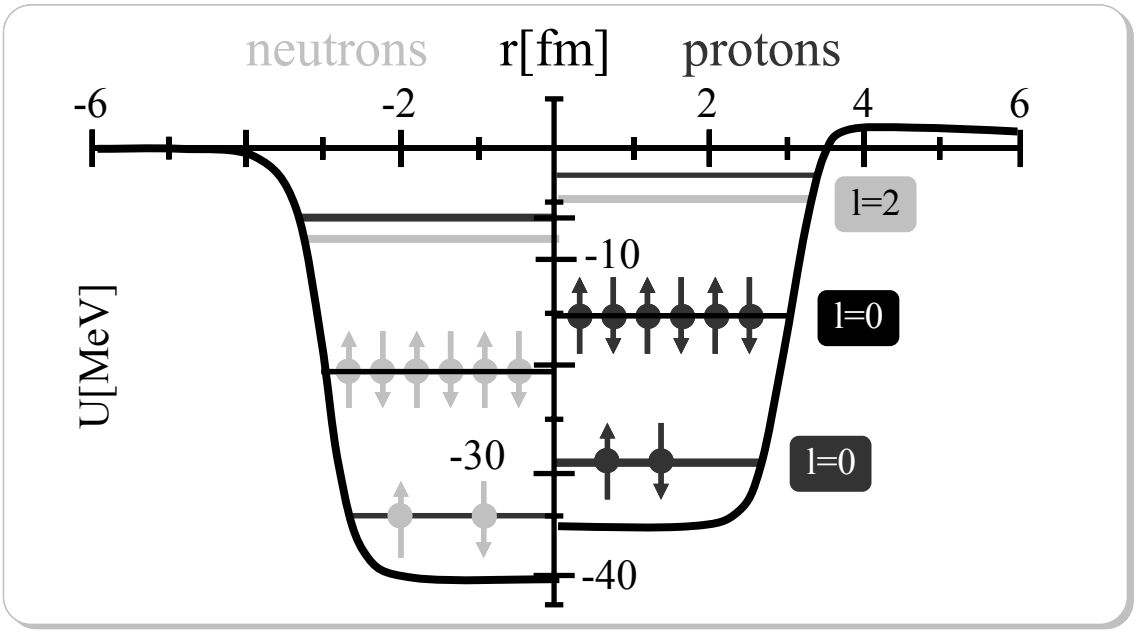

Figure 2.21 WOOD-SAXON potential of nucleons.

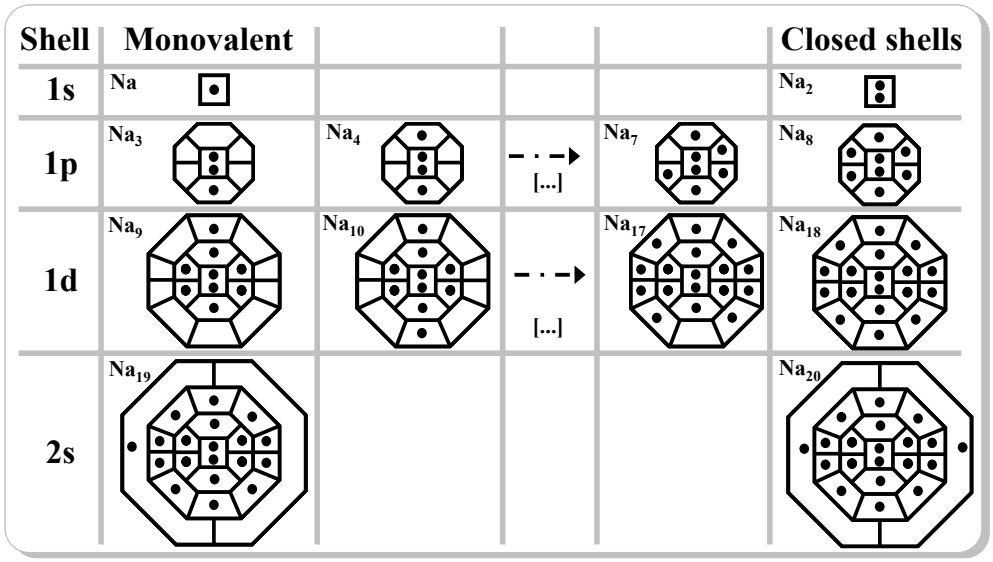

Figure 2.22 Electronic periodic table for small sodium clusters.

The periods (1s, 2p, 2s, …) are defined by the electronic shells obtained within the Jellium-model. The first group in this table is formed by the monovalent clusters with an expected high chemical reactivity. The closed shell clusters Na_2, Na_8, and Na_{40} are also found in the mass spectrum in figure 2.23 (from ref. [82]).

2.4.2.2 Magic Cluster Sizes

Clusters with such an electron configuration as described above are extremely stable due to the high binding energy. In case of sodium clusters, one observes the magic numbers in the mass spectrum (see figure 2.23). This plot shows the intensity of the cluster signal plotted versus the cluster mass. Clearly visible are the pronounced peaks for Na_2, Na_8, Na_{40}, and Na_{58}. Theses clusters exhibit 2, 8, 20, 40, and 58 electrons per cluster. Due to the higher binding energies of electrons in magic clusters it takes higher energies to remove an electron from the cluster, or add an electron to the cluster. Clusters with one more atom, thus clusters where an additional electron starts filling the next shell, are less stable and show significantly lower intensities in the mass spectra. BRÉCHIGNAC *et al.* also observed the shell structure of clusters in ionization potential measurements of Na clusters, even though they observe some irregularities according to theoretical calcula-

tions [.83], which can be explained by the CLEMENGER-NILSSON-Model, we introduce in the next section.

In contrast, for rare gas clusters geometrically magic clusters define exceptionally stable cluster sizes, *e.g.*, the icosahedral shapes for n = 13, n = 55, n = 309, n = 561, n = 923, and n = 1415. Figure 2.24 schematically depict the so-called MACKAY icosahedrons [.84] for clusters up to 561 atoms.

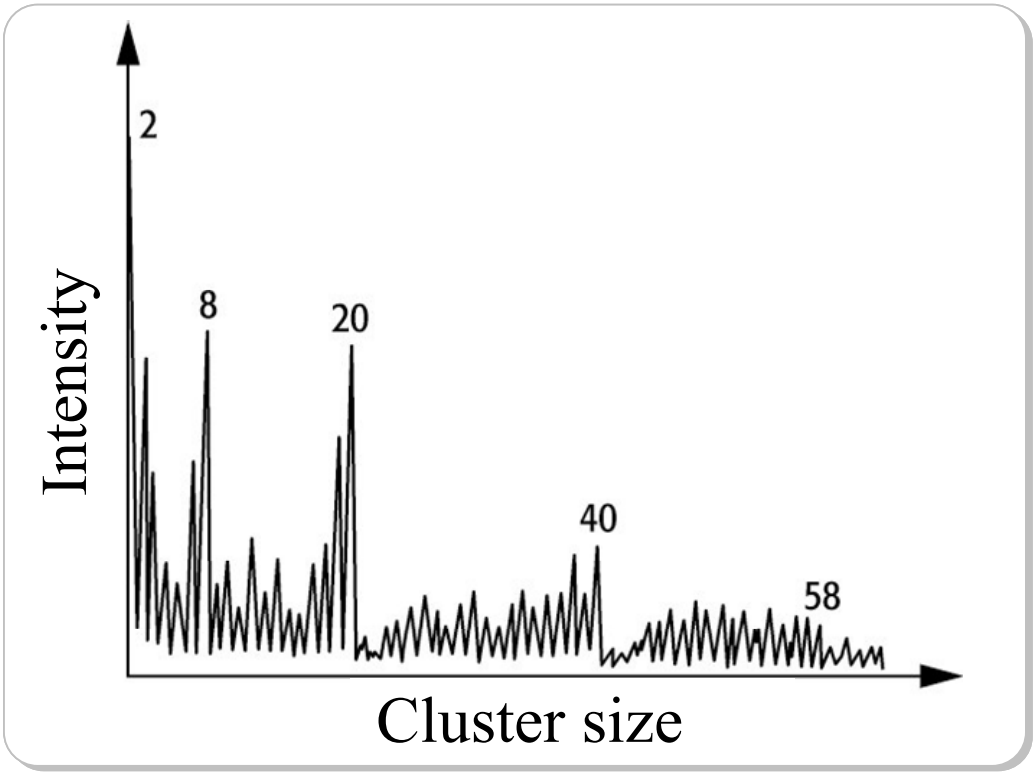

Figure 2.23 Mass spectrum of hot sodium clusters.

Some cluster masses, e.g., Na_n (n = 2, 8, 20, and 40 atoms) show higher intensities, and are referred to as electronically *magic clusters*. There exists a correlation for hot clusters between higher intensity in the mass spectrum and higher binding energies, which means higher stability of the cluster. One can explain these results in case of sodium using the Jellium-Model (from [.85], see also [.86]).

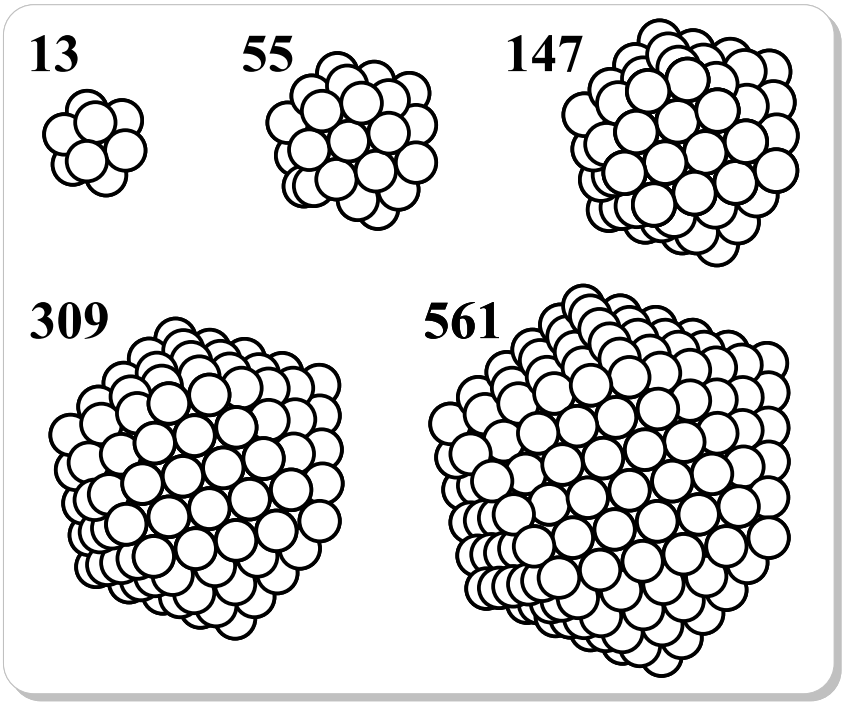

Figure 2.24 Structures of rare gas clusters.

For n = 13 one obtains the well-known icosahedral structure, where one atom in the center is surrounded by two 5-fold caps consisting of six atoms. For larger clusters atoms are attached to this icosahedron until for n = 55, 147, 309, and 561 the next shells are filled [.87, .88].

2.4.2.3 CLEMENGER-NILSSON-Model

The simple Jellium-Model presumes that all clusters are spherical. It neglects the electron configuration regarding the filling of the shells. In reality, only magic Jellium clusters, thus the clusters with closed shells and full-occupied energetic levels are spherical. Other cluster sizes exhibit a non-spherical shape due to the asymmetric distribution of the electrons within the cluster. This phenomenon is the JAHN-TELLER-effect (or JAHN-TELLER distortion) [.89, .90]. One can explain the deviations between ionization potential measurements and calculations of Na clusters by the CLEMENGER-NILSSON-model [.91], which, in contrast to the Jellium-Model, considers the non-spherical clusters. Figure 2.25 schematically illustrates the energy of the cluster depending on the distortion parameter δ. In case of $\delta = 0$ the clusters are spherical. Clusters with closed electron configuration sit on

the vertical axis crossing the x-axis at zero, which means high degeneracy for magic clusters. For distortion parameters, $\delta < 0$ or $\delta > 0$ the clusters are compressed and stretched, which changes the cluster shape to an oblate or a prolate. Therewith, the degeneracy has been shifted and the energetic levels split up into sub levels or shells. The more the distortion parameter converges towards zero, the more the sub levels overlap. Now, one can explain the minima of the ionization potential for magic cluster sizes, by means of the CLEMENGER-NILSSON-model: Electrons of non-spherical clusters are located in sub shells and have consequently a lower energetic level than electrons of spherical clusters with closed shells. This model can also explain the deviation in the ionization potential between theory and experiment, because the calculations do not consider the non-spherical cluster shapes.

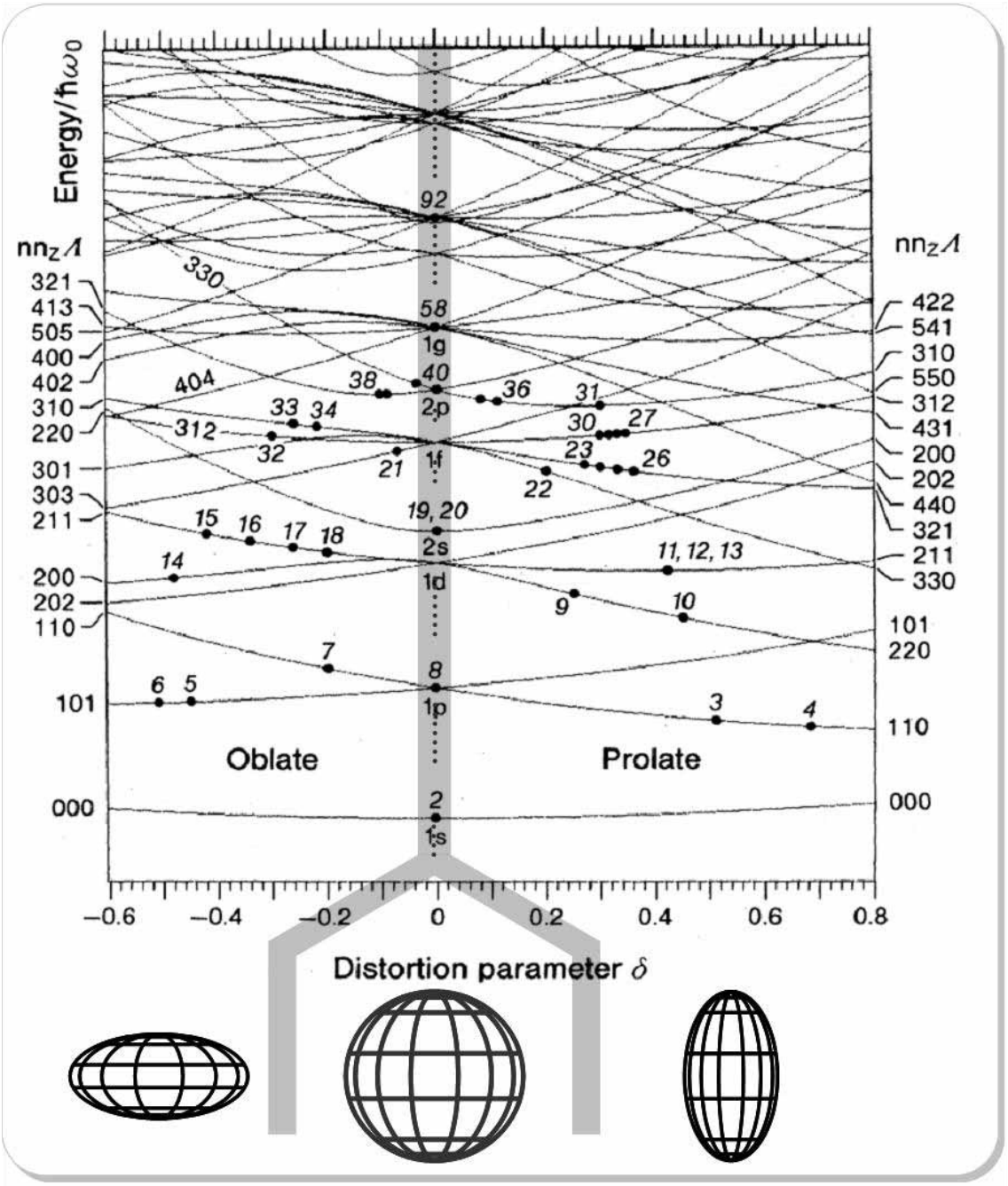

Figure 2.25 The CLEMENGER-NILSSON-model of cluster energy levels as a function of the distortion parameter δ [91].

The energy scale is dimensionless in order to accommodate all cluster sizes, and the zero is suppressed; the 1s-1p energy difference at δ = 0 is exactly $\hbar\omega_0$. The points on the figure indicate the position of the highest occupied level for each cluster, at the value of δ corresponding to the assigned ground state.

2.4.3 Clusters on Surfaces

As already mentioned in the introduction, for technological applications it is mandatory to bring the clusters in contact with a surface. We therefore discuss now some basic effects of the cluster-on-surface system.

Considering clusters on a substrate, the interaction with the substrate strongly influences the crystalline structure of the clusters leading to effects like preferential orientation or epitaxial growth of the clusters on the substrate. One can compare this to the dependence on the deposition parameters like, *e.g.*, temperature, and the dependency on the cluster size for the cluster substrate interaction [61].

For gold clusters grown in nanopits on graphite at T = 623 K, we observe a transition from a three-dimensional growth for smaller cluster sizes (< 10^3 atoms) to a mainly lateral growth after the formation of hexagonal (111) facets on top of larger clusters (> 10^4 atoms) [75]. Electron diffraction patterns lead to the result of facets with their (111) plane oriented parallel to the HOPG (0001) surface [55]. The occurrence of diffraction rings in theses measurements instead of discrete spots indicates a random lateral orientation, which we later confirmed by the investigation of the lateral orientation of faceted Au clusters with STM.

Using macroscopic concepts, the orientation dependent surface energy γ governs the three-dimensional equilibrium crystal shape (ECS) of a solid.

GIBBS first introduced the concept of the surface free energy γ (see ref. 1, 2 in [8]), and defined it for a one-component material as *the work dW required to create a new surface area dA at a constant temperature and chemical potential*:

$$\gamma = \frac{dW}{dA}$$

The minima in γ for closed-packed surfaces correspond to a small number of different facets defining the ECS [8]. Thus, the ECS at T = 0 K is formed by well-defined polygonal facets with sharp edges between them. Surface energies are mostly calculated for a temperature T = 0 K (see, *e.g.*, [92, 93]), experiments for the shape of µm-sized particles

[8, 94, 95, 96, and 97] use temperatures which are high enough to achieve the ECS is archived in a suitable time [98]. I. BARKE estimates for spherical particles at T = 350° C relaxation times τ in the order of $\tau \approx 10^{-4}$ s for a particle with a radius of 1 nm, and $\tau = 10^{-2}$ s for a radius of r = 4 nm [55]. Because the orientation-dependent surface energy changes with temperature, we estimate the relaxation time again for clusters at room temperature in section 5.4.2 (p. 179).

The anisotropy reduces with T approaching the melting temperature T_m [96], which is equivalent to more and more spherical particles with small facets [94, 95]. In addition, the step energy gets more and more isotropic at higher temperatures, which results in nearly circular facet shapes close to T_m [97]. A quantitative comparison with calculations requires an exact study of the ECS in a broad range of different temperatures [96].

Generally, the shape of clusters differs from the macroscopic ECS. For clusters in contact with a surface, the cluster-surface interaction modifies the cluster morphology. In general, this is a complicated problem for small clusters [99, 100] but, using macroscopic concepts in the limit of large particles, the resulting shape can be predicted using the substrate surface and interface energy [101, 102]. We did not observe faceted cluster shapes for silver clusters. In contrast, as mentioned above for gold clusters grown at elevated temperatures (623 K – 873 K) we observed a preferential orientation with the (111) surface of the facets parallel to the substrate, measured with electron diffraction. The hexagonal facets on top of larger gold clusters are well known from investigations with STM [103] and TEM [63].

We present a full study of the morphology of Au clusters on HOPG with its three dimensional growth for smaller gold clusters and the transition to mainly lateral growth for larger clusters, which is connected with the formation of (111) facets on top of the clusters in detail in ref. [75].

According to the CLEMENGER-NILSSON-model (2.4.2.3, pp 68), one expects a reduced degeneracy due to a symmetry break for clusters in contact with a surface. The symmetry is already broken due to the presence of the surface, even if the cluster shape is as sym-

metric as in the free beam. Therefore, the use of rare gas layers is promising due to the reduction of the coupling to the surface (see also sec. 5.1, pp .132 and sec. 5.3, pp .156).

To investigate these fundamental effects of clusters on surfaces, also for size-selected clusters, one has to study the change of the geometric and / or electronic properties through the contact with the surface. To start these investigations it is of advantage to keep the shape of the clusters as far as possible similar to that of free clusters. However, one would expect a distortion, fragmentation, or coalescence of clusters during or after the deposition process. This experimental challenge leads to the topic of *soft-landing*.

On the other hand, for the deposition of size-selected clusters, we have to consider the effects, that occur for different kinetic energies during the deposition process [.104].

2.4.3.1 Hard-Landing and Soft-Landing

To preserve the geometric, electronic, and magnetic properties of clusters measured in the free cluster beam [9] after the deposition onto a surface, one needs a method for the non-destructive cluster deposition. BROMANN et al. perform a so-called *soft-landing* of clusters, using two different methods [.105]. First, they used impact energies lower than 1 eV per atom and were able to soft-land silver nano-clusters nondestructively on a bare Pt(111) surface. For higher kinetic energies, they observe fragmentation and substrate damage. To prevent these effects, they use as a second method an Argon (Ar) buffer layer on the platinum substrate, which efficiently dissipates the kinetic energy. A rare gas buffer layer seems to be well suited due to its high chemical inertness. Moreover, the rare gas partially desorbs, while the clusters hit the buffer layer and hence absorbs its kinetic energy. After the deposition, a slow heating of the sample desorbs the rare gas buffer layer [.106].

CHENG and LANDMANN determine the energy transfer between absorbed energy ΔE_{int} and kinetic energy of the cluster E_{kin} [.107] in a simulation of soft-landing with molecular dynamics:

Equation 2.22

$$\frac{\Delta E_{kin}}{E_{kin}} \propto \left(\frac{\rho_{rg} c_{rg}}{\rho_C c_C} \right)^2$$

ρ_{rg} – Density of the rare gas layer, ρ_C – density of the cluster, c_{rg} – speed of sound of the rare gas layer, and c_C – speed of sound of the cluster.

In addition, ZANG *et al.* present in a recent publication molecular dynamic simulations for the soft-landing process [.108].

Due to the high mobility of atoms and clusters on a rare gas layers (see 2.3.2, p. 58) coalescence can not be excluded. To prevent coalescence, in particular during the buffer layer desorption, ANTONOV *et al.* [62] use an additional capping layer (see also ref. [.109]).

Chapter 3

EXPERIMENTAL SETUP

3.1 Low-Temperature Surface Science Facility

We carry out all sample preparations and the analysis of the samples using a low-temperature (LT) ultra high vacuum (UHV) Surface Science Facility (SSF) [.110] (manufactured by the Omicron Nanotechnology GmbH [.111]) (see figure 3.26). The SSF is based on a two chamber UHV system connected with a sample manipulator cooled by liquid helium (LHe) allowing cold transfer of samples (and tips) between the two chambers. The first chamber, the preparation chamber (PCH), carries the high-resolution photoelectron analyzer together with the sample preparation methods (evaporation, sputter cleaning, and heating). The second one, the analysis chamber (ACH), contains the LT STM. The base pressure in SSF is $p_{prep} = 2 \cdot 10^{-11}$ mbar. Gaisch et al. realized first a full in situ flexible tip and sample exchange in UHV at the IBM Zurich Research Laboratory [.112] within a successful setup of an LT UHV STM. I. BARKE extended this setup to a home-built low-temperature sample holder (SH_{LT}) [.113]. We use the SH_{LT} to

cool down our samples to a temperature of approximately T = 10 K, allowing us to prepare and analyze samples in the preparation chamber at low temperatures. Since we use this SH_{LT} we are able to transfer the sample into the LT-STM, keeping the sample temperature constantly below T = 30 K. At these low temperatures, we were also able to keep a tip shape, which is capable of imaging, *e.g.*, clusters for days. We produce such well defined tungsten tips with a tip radius of a few nm, which prevent a strong broadening of the lateral cluster shape [60] (see also sec. 2.2.1.2, pp 38) and allow to image the clusters, using *ex situ* electrochemically etching and an *in situ* preparation with heating and field-emission sputtering [.114].

In the SSF, we transfer samples and tips by means of an x-y-z sample translator with fast-load lock for sample insertion that connects both chambers [.19, .115].

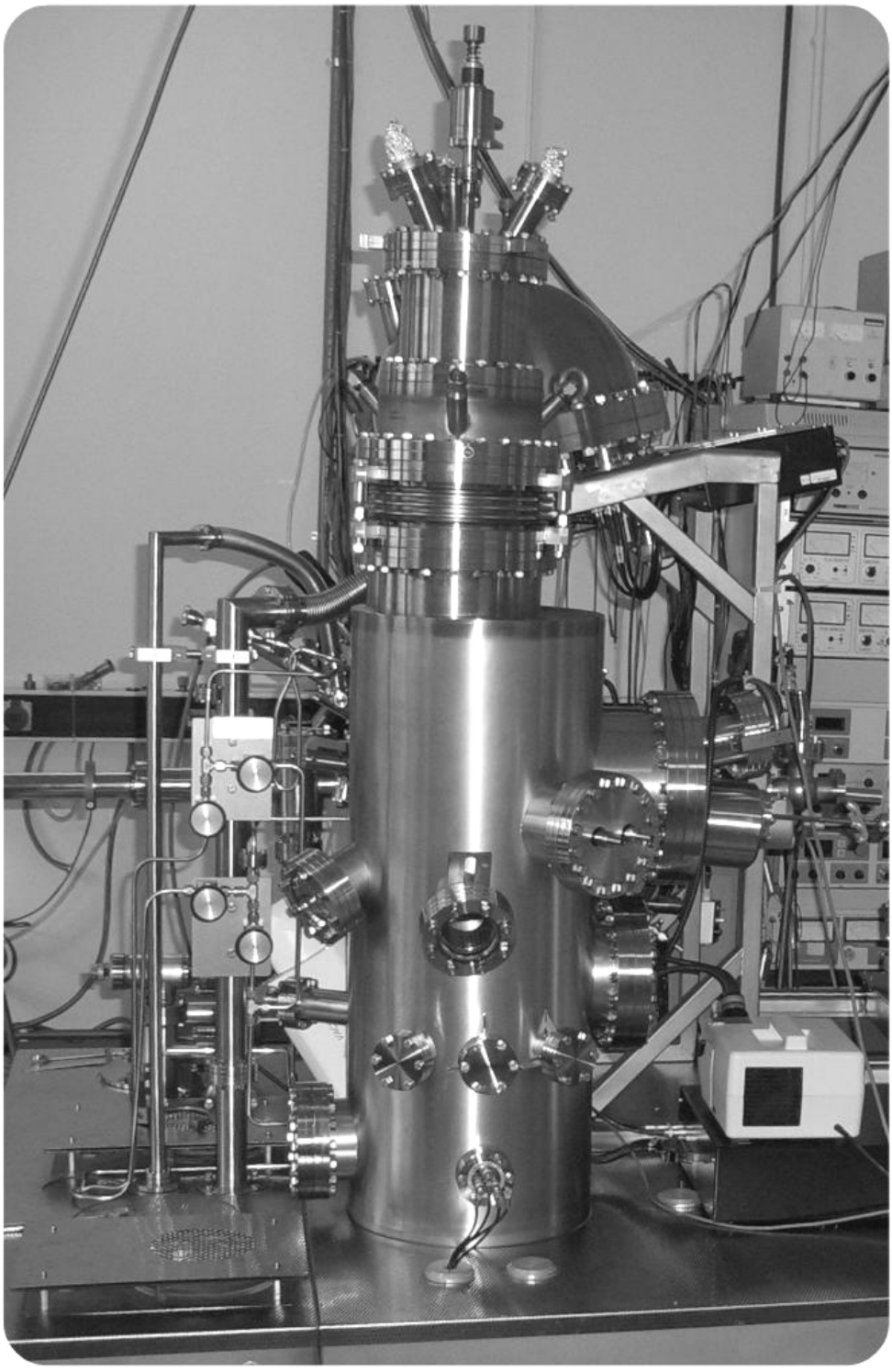

Figure 3.26 Picture of the Surface Science Facility in the laboratory of the University of Dortmund.

3.2 Cluster Deposition Machine

We develop and build the new High Transmission Cluster Deposition Machine for the production and deposition of mass-selected clusters onto surfaces within the DFG priority program SPP 1153 (see 1.1, p. 23).

In previous chapters, we pointed out that clusters, and in particular size-selected clusters, are interesting to investigate. Furthermore, our unique combination of a cluster machine together with a low temperature surface science facility that includes the combination of *in situ* LT STM / STS and UPS holds a large research potential. Mainly, we are interested in the geometric and electronic properties of clusters on surfaces, which we will compare with the results of the same clusters in a free cluster beam (see 2.4.2, pp 62) investigated by the group of V. ISSENDORFF of the University of Freiburg.

The apparatus consists of a magnetron-sputter-gas-aggregation cluster-source [116], a differential pumping stage with a cryo-pump, and a new high-transmission-infinite-range mass-selector [117]. The mass-selector chamber connects the cluster machine with the surface science facility.

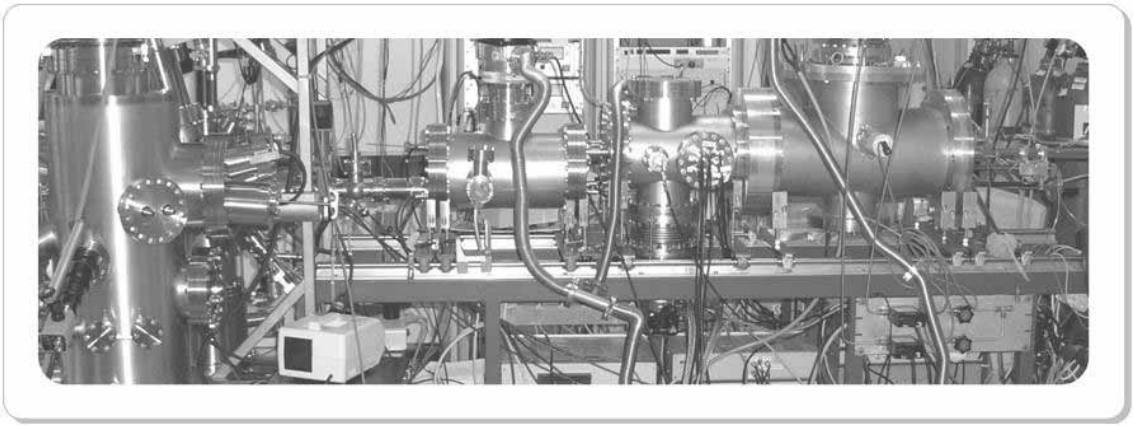

Figure 3.27 Picture of the new cluster machine in the laboratory of the University of Dortmund.

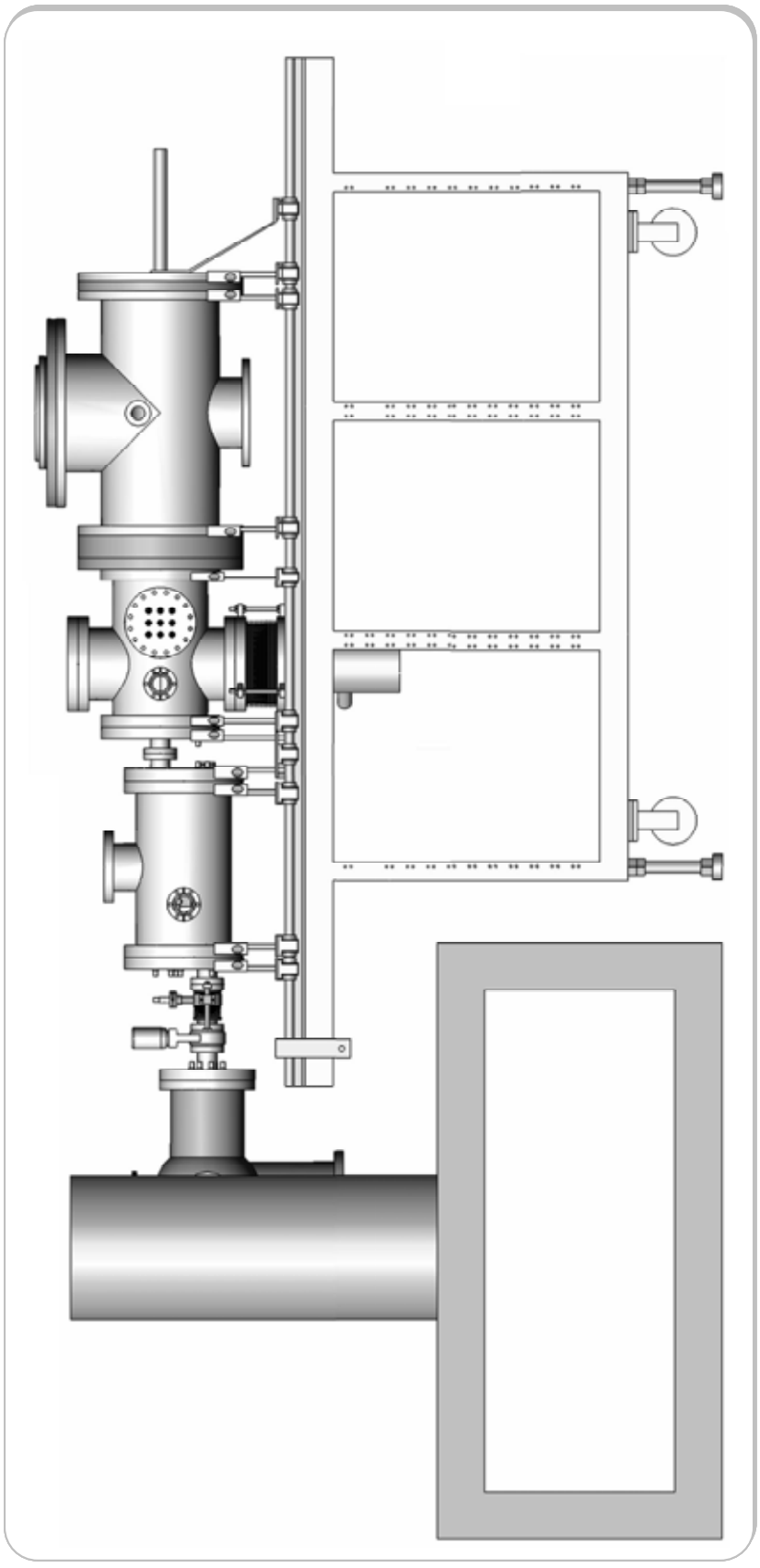

Figure 3.28 Full-sized schema of the cluster-deposition machine.

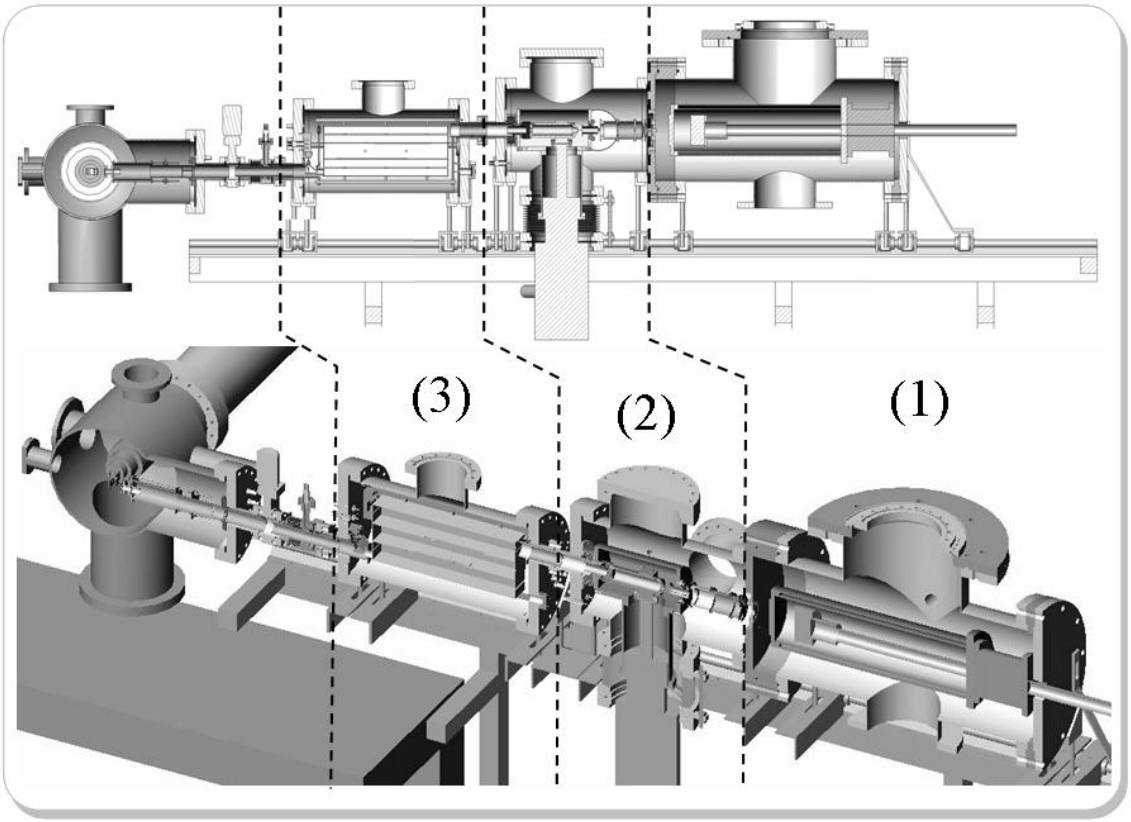

Figure 3.29 Cross-sectional view of the cluster-deposition machine.

Two-dimensional side view (top) and three-dimensional trimetric view (bottom). (1) 1st stage - cluster source, (2) 2nd stage – cryo-pump, and (3) 3rd stage – mass-selector.

3.2.1 First Stage – Magnetron Sputter Source

The first stage of the cluster machine we use in this new setup for cluster generation is the well-known Magnetron-Sputter-Gas-Aggregation Cluster Source, first introduced by the group of H. HABERLAND [116]. The drawing in figure 3.29 shows a sectional-view of the cluster source chamber. A turbo molecular pump (TPS) (TURBOVAC TW 701, LEYBOLD vacuum [118]) evacuates the source chamber (SCH) (see figure 3.29 (1) and figure 3.30). The final pressure in the source chamber is $4.8 \cdot 10^{-8}$ mbar without gas load and between $8.8 \cdot 10^{-3}$ mbar and $2.7 \cdot 10^{-2}$ mbar with gas load (depending on the Argon (Ar) / Helium (He) flux ratio). The pumping speed for Nitrogen (N_2) and Ar is

680 $l \times s^{-1}$ and for He 530 $l \cdot s^{-1}$. The chamber contains a liquid nitrogen (LN_2) cooled aggregation-tube with a movable magnetron-sputter-discharge head (m).

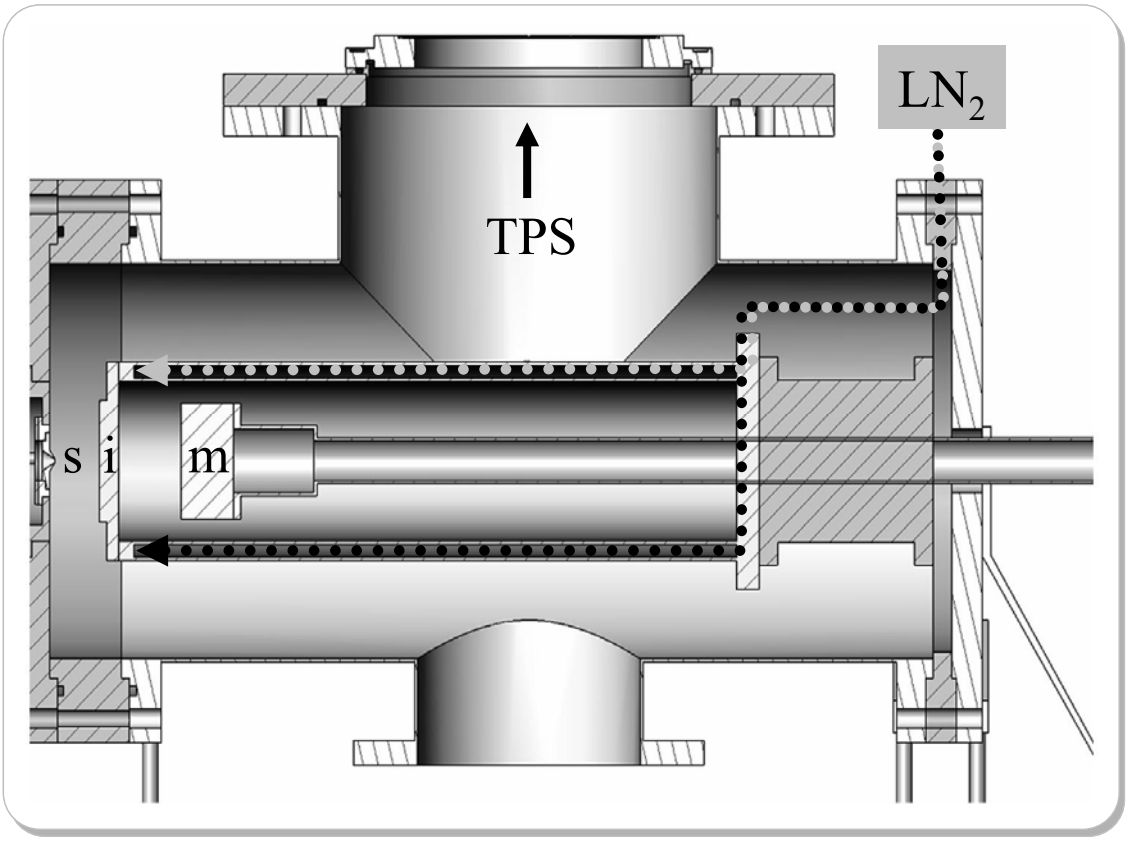

Figure 3.30 Cross-section of the first stage of the cluster machine – the cluster source chamber.

We automatically stabilize the temperature of the source by an LN_2 flux control system that we build within this work. Figure 3.31 shows a schematic diagram of the control system.

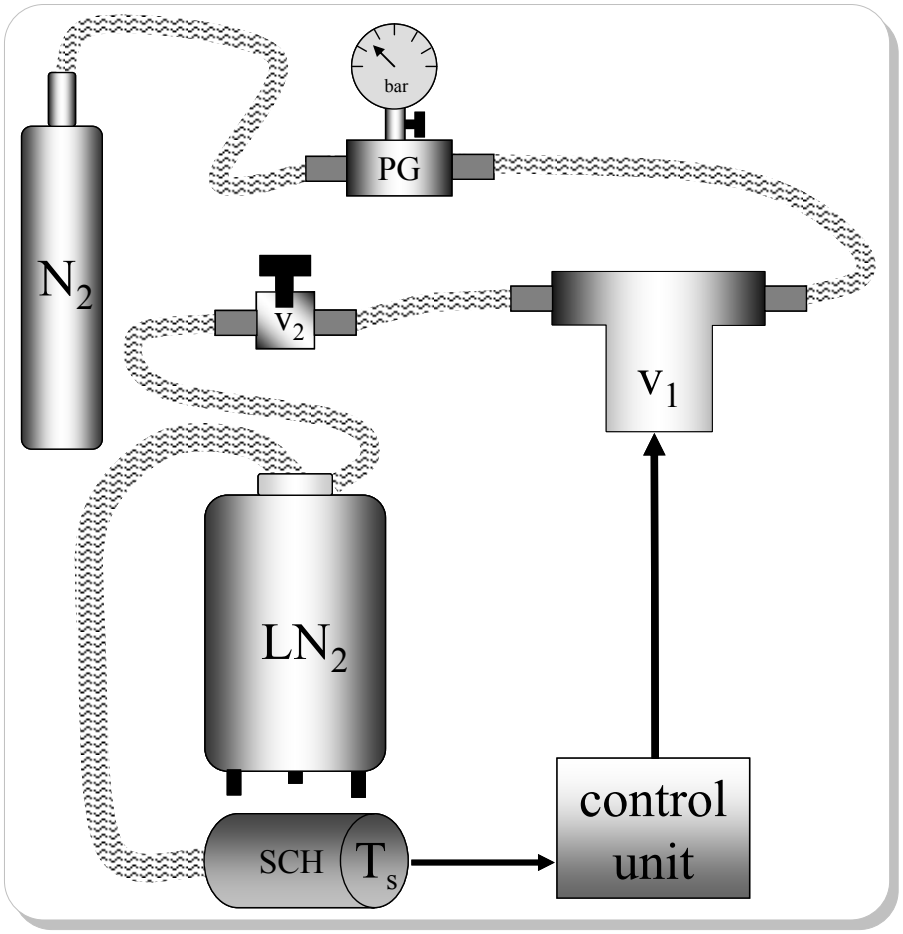

Figure 3.31 Schematic diagram of the automatic LN_2 cooling system setup.

N_2 – Nitrogen bottle, PG – pressure gauge, V_2 – stop valve, V_1 – electrical valve, LN_2 – liquid Nitrogen tank, SCH – cluster-source chamber, and T_S – cluster source temperature.

A pressure gauge connects the N_2 bottle to an electrical valve V_1. A simple stop valve V_2 connects the valve V_1 to the LN_2 tank. We then connect the LN_2 tank directly to the SCH. The control unit monitors the cluster source temperature T_S. We usually set the trigger temperature to -169 °C, though this can slightly vary for different cluster-source parameters during operation. Whenever the temperature rises and exceeds the trigger level, the control unit opens the electrical valve V_1 and applies a pressure to the LN_2 tank, to increase the LN_2 flux, and cool the cluster source. The LN_2 flows through a flow cryostat surrounding the cluster source. Cooling the cluster source is important because magnet temperatures above 80 °C destroy the magnetron. Cooling with LN_2 prevents overheating

of the magnetron cathode for high powers from 5 to 20 W. Furthermore, the LN_2 cools the Ar / He mixture and leads to a better cluster condensation.

For a more detailed description of the cluster condensation process, we enlarge the region between magnetron m and skimmer S in figure 3.30 to that in figure 3.33. We operate a 5 cm diameter magnetron-sputter-discharge cathode k at a pressure in the order of 10^{-2} mbar in a mixture of Ar and He. The Ar floats directly over the sputter target t, while we inject the helium from the back. Increasing the He to Ar flux ratio increases the number of smaller clusters. Decreasing the ratio increases the cluster size. Typical fluxes are Φ_{He}=200 sccm (sccm[5] – Standard cubic centimeters per minute) and $\Phi_{Ar} = 80$ sccm for small clusters (n = 1-70), and $\Phi_{He} = 100\ sccm$ and $\Phi_{Ar} = 100\ sccm$ for larger clusters ($n \approx 10^3$).

The magnetron cathode k is located behind the Target t, which we can bias up to 1.2 kV. The magnetron cathodes strong electric field ionizes the injected Ar. A high voltage accelerates the Ar ions towards the target and produces silver atoms as well as secondary electrons. The magnetic field forces the secondary electrons to cyclotron orbits and ionizes more Ar. The Ar ions produce more silver atoms plus secondary electrons, which remain again in the discharge area and so forth. The silver atoms leave the discharge area and enter the condensation region c. In this region, the silver atoms collide with the Ar and helium atoms, resulting in a cluster condensation. The cluster size depends on the distance between target t and iris i, as well as on the diameter of the iris. The cluster size increases both with closing the iris or increasing the target-iris-distance and vice versa.

The clusters then pass the iris i and are focused by the ring r towards the skimmer S into the next chamber. The iris as well as the skimmer potential can be set to ± 50 V. In the experiments within this thesis, we produce only positively charged clusters. Hence, we set all electrodes to negative voltages.

[5] Standard Cubic Centimeters per Minute is the flux measured at standard conditions, such as a pressure of 100 kPa (1 bar) and a temperature of 273,15 K

The silver target we use in all experiments is an AMERICAN SILVER EAGLE coin [.119]. This coin consists of 99.9 % pure silver. .

Figure 3.32 shows a picture of a brand-new (before sputtering) and a used coin (after sputtering the target for about 20 h at 5 Watt). The structure on the used coin indicates the position of the torus shaped ring of the sputter discharge (plasma) during the operation of the sputter source. For further details of the sputtering yield see ref. [.120].

Figure 3.32 Picture of the AMERICAN SILVER EAGLE used as silver sputter target.
(Left) before and (right) after 20 h sputtering at 5 W. The AMERICAN SILVER EAGLE consists of one troy ounce of 99.9 % pure silver.

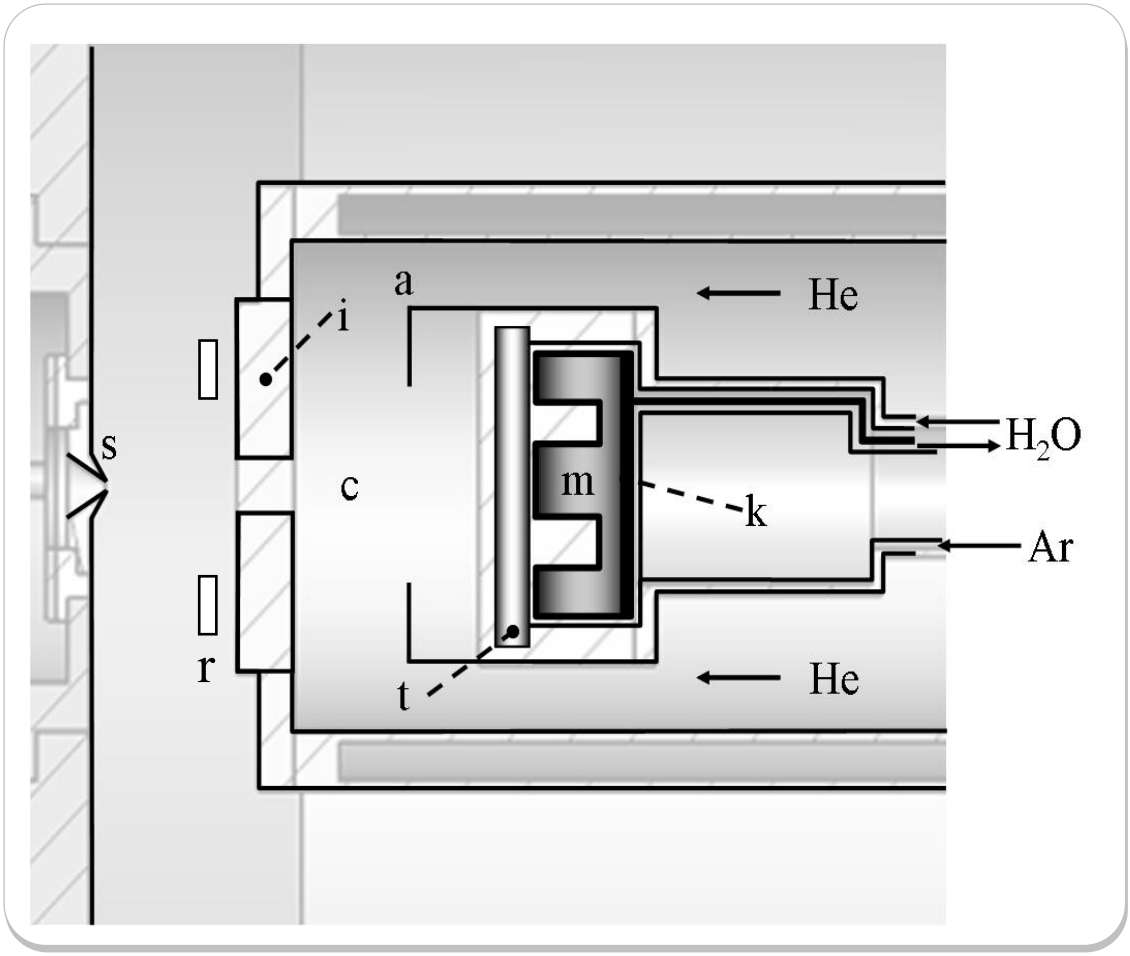

Figure 3.33 Enlarged view of the magnetron region.

k: magnetron sputter cathode, m: magnetron-sputter-discharge head, c: condensation region, t: target, a: aggregation tube, i: iris, s: skimmer, r: ring.

3.2.2 Second Stage – Cryo-Pump

After the cluster generation inside the cluster source chamber the clusters with a broad cluster size distribution enter the second stage of the cluster machine - the cryo-pump chamber (CCH) (see figure 3.29 (2)) - through the skimmer, which can get a bias voltage of ±50 V . The skimmer is a conical shaped aperture, separating the core of the expanding cluster beam from the diffuse border. We then accelerate and focus the clusters by several electrodes E, deflect the cluster beam in x-y-direction by four deflector plates D_{xy}, and guide them through the field free region inside the cryo tube t_K before they leave the

chamber again towards the mass selector chamber (see figure 3.29 (3) and enlarged in and figure 3.37).

The turbo molecular pump of the cryo-pump chamber (TPC) (VARIAN TV301 Navigator [121]) provides a final pressure of $p_{CC}=4.6\times10^{-7}$mbar without gas load and operating cryo-pump. The pumping speed for N_2 is 280 $l\cdot s^{-1}$ and for He 230 $l\cdot s^{-1}$. In this machine we use the dual stage cold head H *Coolpower 5 / 100 T* of the manufacturer LEYBOLD [118] to freeze out Ar and other impurities (especially water (H_2O)) coming out of the cluster source (for a detailed drawing see figure 7.92, appendix 7.2). We measure temperatures for the first stage St_I and the second stage St_{II} of about $T_{ST_{II}} \approx 10K$ and $T_{ST_I} \approx 30K$ while operating the cluster machine. Theses temperatures can vary slightly depending on the gas load and / or the thermal coupling of St_{II} to H (see discussion of the Boron Nitride foil below). A performance test shows that the temperatures T_{ST_I} and $T_{ST_{II}}$ reach their respective values in approximately 2.5 h (see figure 3.34). Furthermore, we perform a gas analysis with a quadrupole mass-spectrometer, mounted inside the preparation chamber. It turns out that almost all of the Ar adsorbs at the cryo tube t_c (temperature $T_{ST_{II}}$) and even at the outer shielding S_o (temperature T_{ST_I}). Consequently, it freezes out H_2O and other impurities. Hence, with an operating cryo-pump the final pressure in the CCH is $p_{CC}=4.5\cdot10^{-8}$mbar without, and in the order of 10^{-6}mbar with, gas load, depending on the He / Ar flux ratio. We can screw the cool head up and down by using the three adjusting screws $AS_{1\text{-}3}$. One of them is visible in figure 3.35. It is important to align exactly the cryo tube with respect to the cluster beam axis. Otherwise, the clusters would not be able to pass the cryo tube region after leaving the last acceleration electrode and could not enter the mass selector chamber. We discuss the electrodes E we mention above as well as the x-y-deflector plates D_{xy} in the following chapter in more detail.

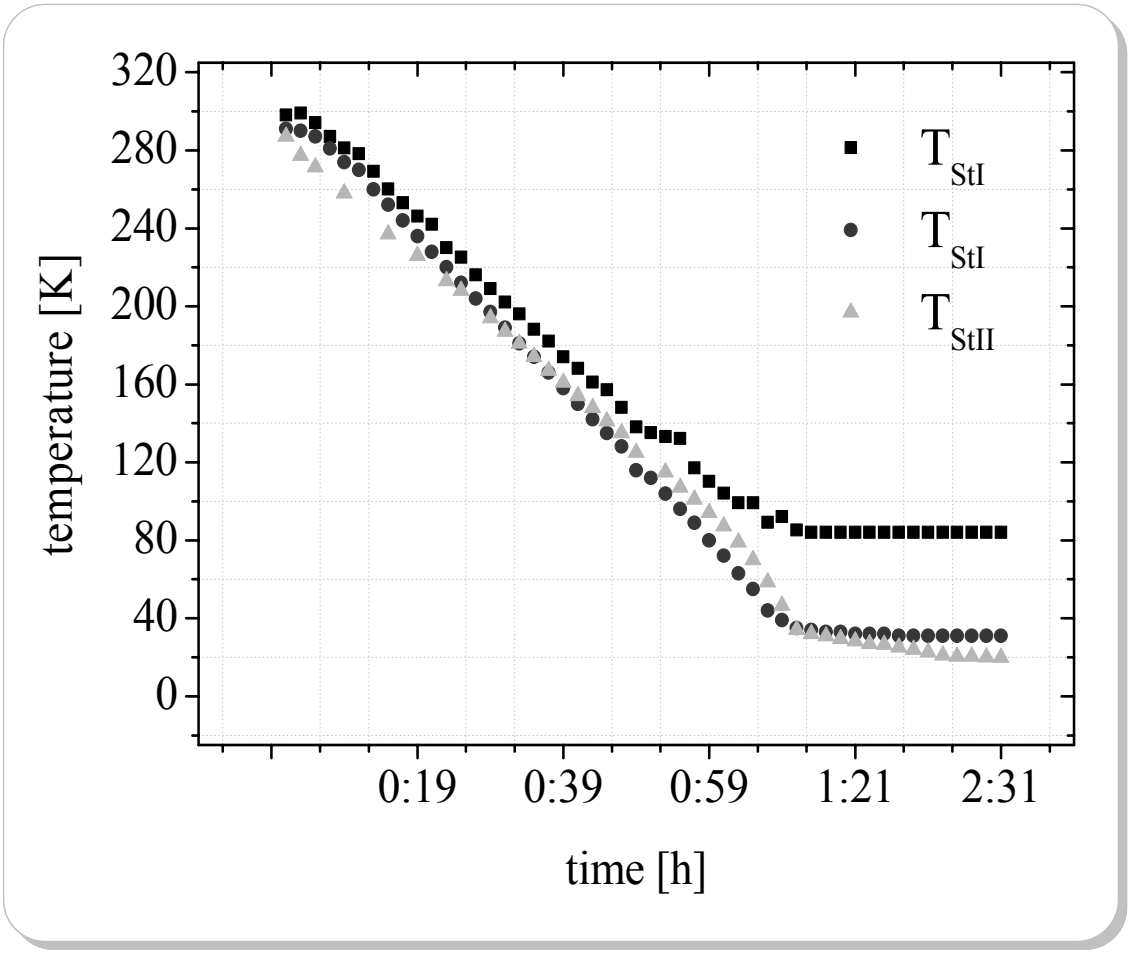

Figure 3.34 Temperature of the 1st and 2nd cold stage of the cool head.

(■) T_{StI} – Temperature of the 1st (outer) cooling stage ST_I measured by a thermocouple, (●) T_{StI} – measured by a Si-diode, and (▲) T_{StII} – Temperature of the 2nd cooling stage measured by a Si-diode.

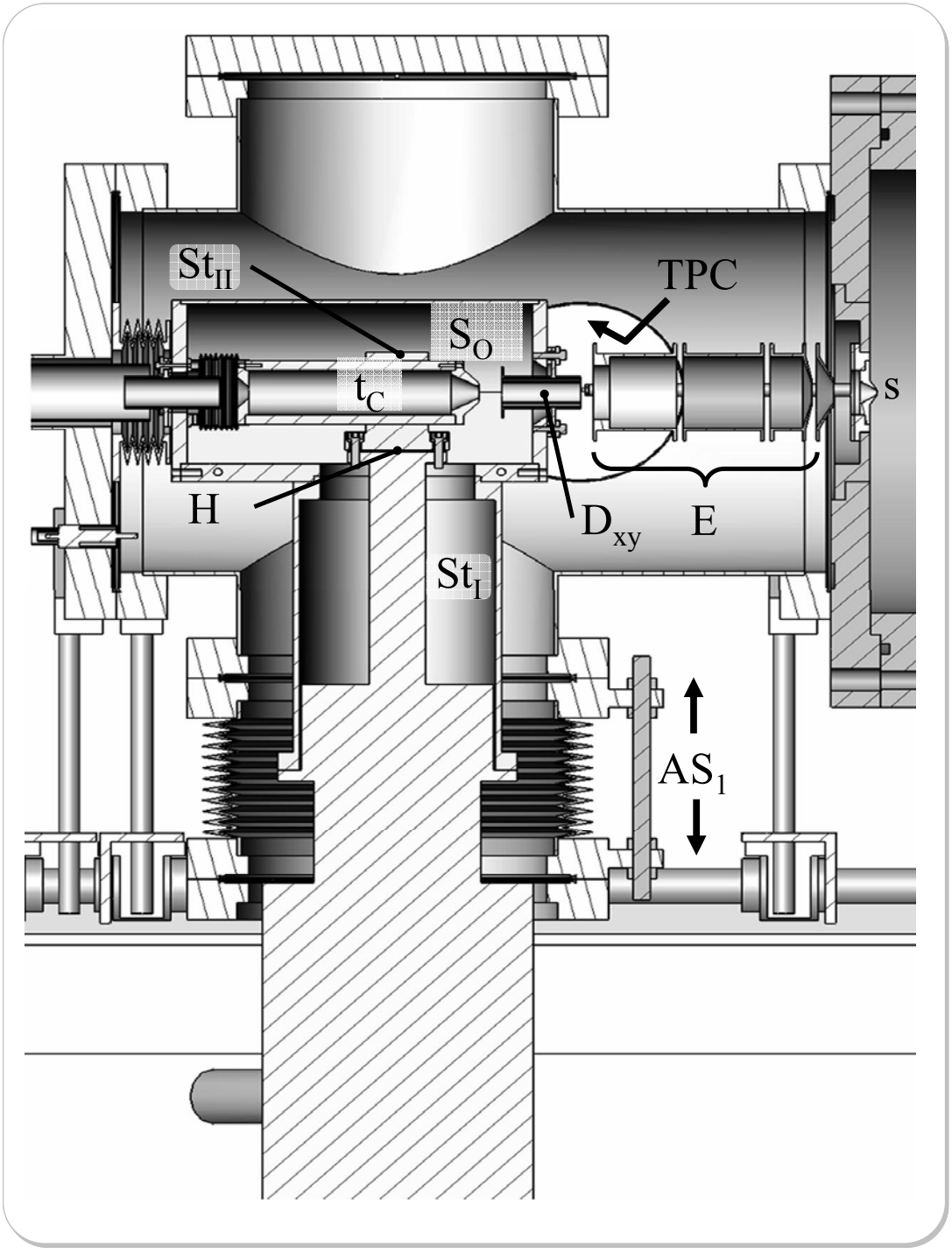

Figure 3.35 Cross-section of the second – the cryo-pumping-stage.

S: skimmer, E: set of electrostatic lenses, D_{xy}: x-y-deflector plates, TPC: Turbo Pump, H: cool head, S_O: outer shielding, S_{TI}: first stage of the cool head H, t_C: cryo tube, ST_{II}: second stage of the cool head H, AS_1: one of the three adjusting screws.

3.2.2.1 Ion Optics

The combination of four electrodes A_1, A_2, A_3, and V_f represent three electrostatic lenses. By changing the voltages of A_1 to A_3, one can focus or defocus the beam, respectively, while the floating Voltage V_f = -500 V remains constant.

Our collaborators in Freiburg use the ion optics simulation program SIMION [.122] for the simulation of the trajectories of the clusters. Figure 3.38 exemplarily depicts the focusing of an EINZEL LENS. The simplest EINZEL LENS usually consists of three electrodes. The electric field, established by two different potentials in-between, affects a particle passing a configuration depicted in figure 3.38. The potential energy surface view in (c) and (d) visualizes the focusing effect of this lens for two different voltages.

Because the electrodes A_1 to A_3 can only change the focal point of the cluster beam, the x-y-deflector plates D_{xy} are extremely important for beam alignment. Figure 3.36 shows a front view picture of this part. Through slight changes of the four electrode voltages to values different from the floating voltage ($U_{float.\ volt.}$ = -500 V) we can bend the cluster beam in x-y-direction.

With a well-adjusted cool head of the cryo-pump and hence perfectly aligned cryo tube t_c with respect to the beam axis direction, we can guide the cluster beam directly through the cryo tube that is on floating voltage potential. The floating voltage potential at the cryo tube is important to provide a field-free region. Within this field, the clusters can pass unaffected and straight until they reach the next chamber.

The second cooling stage directly connects the cryo tube holder to the cool head H that is on ground potential. In order to bias the cryo tube holder to floating voltage potential, we have to electrically decouple the cryo tube setup from the cool head, simultaneously getting a good thermal coupling. Therefore, between cool head H and the cryo tube holder we use a 0.5 mm Boron Nitride (BN) filled polymer foil F_{BN} (manufacturer KERAFOL® [.123]) to guarantee a good thermal conduction as well as electrical isolation as well (see F_{BN} in figure 3.37). The isolation foil is the main reason for the temperature

difference between the theoretical minimum temperatures of the second cooling stage compared to the experimentally measured.

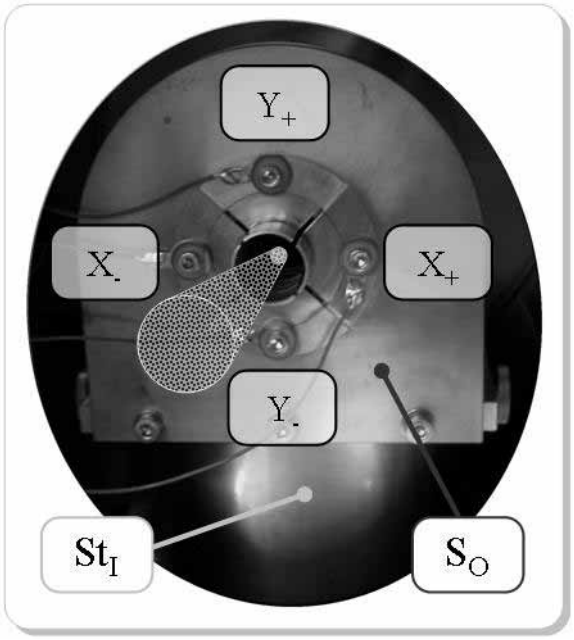

Figure 3.36 Frontal view of the X-Y-deflector plates (D_{xy} of figure 3.35)

The cluster beam (grey filled cone) enters the deflector plates perpendicular to the front panel of the outer cryo shielding (S_O), which is mounted to the first stage (St_I) of the cool head.

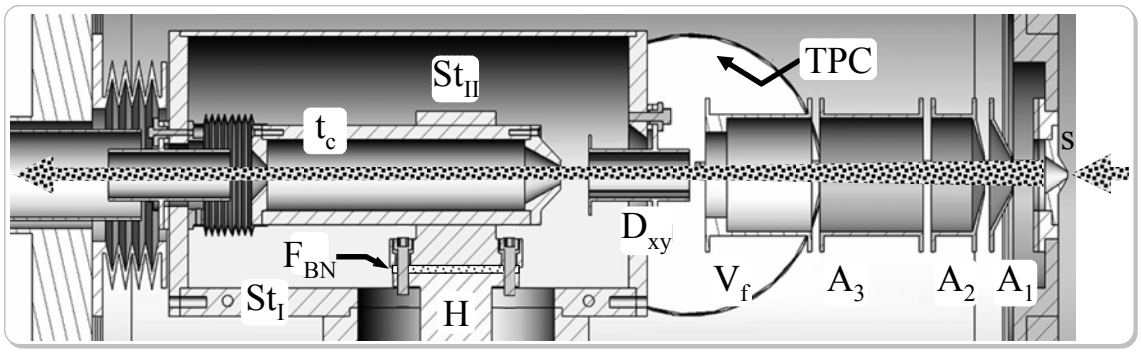

Figure 3.37 Enlarged cross sectional view of the cryo chamber (CCH).

The skimmer S is depicted rightmost, followed by a set of electrostatic lenses. The principle of an EINZEL LENS example is depicted in figure 3.38. In cluster beam direction (grey doted arrow) from rightmost to the left: skimmer s, acceleration electrodes A_1 to A_3, floating voltage electrode V_f, x-y-deflector D_{xy}, cryo tube t_c mounted to the 2nd cooling stage St_{II} of the cool head H, electrically decoupled but thermally coupled by an

Boron Nitride (BN) foil F_{BN}, outer shielding (1st cooling stage) ST_I and turbo molecular pump in the cryo-pump chamber TPC.

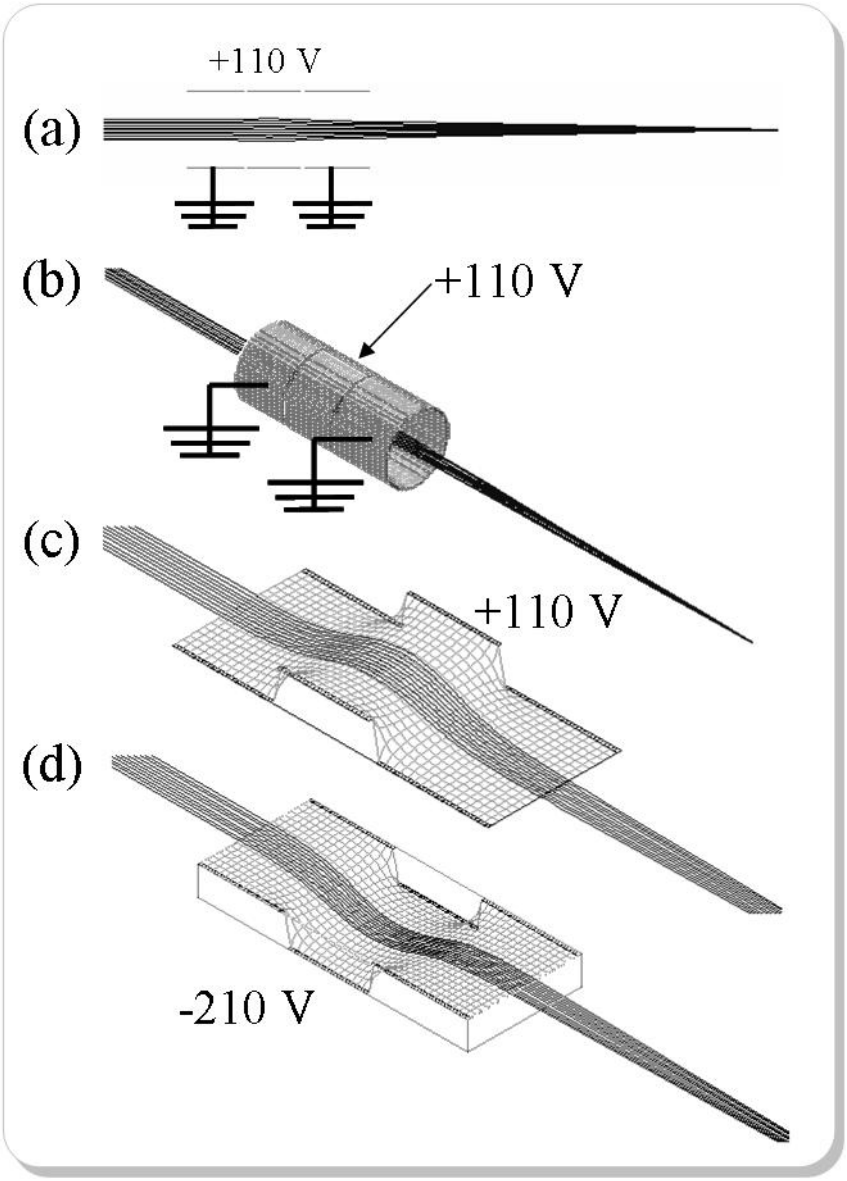

Figure 3.38 SIMION® [122] simulation of an EINZEL LENS example

(a) Cross sectional view of an EINZEL LENS example. Two electrodes are set to ground potential, the middle electrode to +110 V. (b) Three-dimensional view of the three electrodes and the particle beam. (c) Focusing effect demonstrated in a potential energy surface view. The potential causes ions to *roll* inward. (d) Changing the middle electrode to +210 V also results in focusing the particle beam.

3.2.3 Third Stage – High-Transmission Mass-Selector

The core of our cluster machine is definitely the high transmission infinite range semi continuous time-of-flight mass-selector, in the following simply called *mass selector* (MS). Our collaborators OF the University of Freiburg V ISSENDORFF *et al.* [117] first introduced and constructed the mass selector. For our experiments, we use a slightly optimized version, reconstructed by C. YIN and B. V. ISSENDORFF within the DFG priority program SPP 1153. The basic idea of this new mass selection technique is to displace an ion beam laterally by accelerating a portion of it perpendicular to its original direction by a pulsed electric field letting it drift for some time, and then stopping the perpendicular movement by a pulsed electric field in the opposite direction. Finally, the selected cluster masses leave the chamber through an exit aperture and are focused again towards the sample.

Figure 3.39 shows a cross sectional view of the third stage – the mass selector chamber (MCH). We evacuate this chamber by a turbo molecular pump (TPM) (VARIAN turbo-V 300 HT [121]). The final pressure with gas load, without baking out, is $p_{MS}=5.8\cdot10^{-8}$ mbar . After a moderate bake out of the MCH and utilizing copper rings in the CF flanges the minimum pressure is $p_{MS}=1.1\cdot10^{-8}$ mbar . The pumping speed for N_2 is $280\ l\cdot s^{-1}$ and for He $230\ l\cdot s^{-1}$.

The cluster beam enters the MCH from the right upper flange through the first electrode E_f. This electrode focuses the cluster beam to the so-called FARADAY cup electrode FC_I, which is a simple, squared stainless steel plate. We discuss the optimization and the measurement of the cluster current at this point in detail in section 3.2.5. Focusing the cluster beam to and optimizing the cluster current at this point is the most important manipulation of the cluster beam before the mass selection process due to the mass selection principle explained as follows:

The incoming clusters fill the acceleration region of the MS, well focused to FC_I. We apply a first electric high voltage pulse of -800 V to the upper acceleration plate. The starting pulse accelerates the positively charged Ag clusters downwards through an

l = 80 mm long and w = 10 mm wide slit aperture. All cluster ions gain the same momentum and in this way a cut out l = 80 mm long cluster beam portion drifts downwards conserving their lateral velocity. The cluster beam passes a field-free region, because the body of the mass-selector is set to floating voltage. Before they pass an identical slit aperture, they reach the deceleration region (DR). A second high voltage pulse identical to the first one but in the opposite direction is applied to the deceleration plate (DP). The stopping pulse decelerates the clusters in the beam, which continue their lateral movement. Because of the identical start and stop pulse, the whole cluster beam is displaced vertically to its original direction, while conserving the focal point at the point of the exit aperture of the MS. Because all cluster ions gain the same momentum, clusters with smaller masses accelerate more, and gain a higher velocity perpendicular to their original direction. The cluster beam splits into parallel beams of different masses. By changing the timing of the high voltage pulses, one can select masses from Ag_1 to almost unlimited size.

Figure 3.40 schematically illustrates the timing of the high voltage pulses. The high voltage start pulse is applied when the acceleration region AR is filled with ions. The stop pulse is started when the ions have reached the second pulse region, the deceleration pulse region DR. The delay time between the two pulses is τ_d. The waiting time τ_w between two consecutive start pulses is given by the time necessary to fill the pulse region. The time both of the starting and stopping pulse trains is $\tau_w + \tau_p$. One can use this to determine the transmission through the mass selector. Every $\tau_w + \tau_p$, an ion package of the length l is transmitted through the mass selector. During this time an ion package of the total length $l_p = (\tau_w + \tau_p)\, v_0$ has entered the selector (v_0 – velocity of the ions). Therefore, the theoretical transmission efficiency for the selected mass is $T = l / l_p$. With ideal parameters, this can be close to 100 %. This means, despite the use of a pulsed technique, it is possible to obtain an almost continuous mass-selected beam. The times τ_w, τ_p, and τ_d are integer multiples of the period of the frequency generator. The real times are there-

fore $\tau_w \cdot f^{-1}$, $\tau_p \cdot f^{-1}$, and $\tau_d \cdot f^{-1}$, where f is the frequency. For a detailed calculation of the parameters, see ref. [117].

We can calculate the selected mass m with equation 3.23

Equation 3.23

$$m = \frac{e \cdot U_p}{x \cdot d_1}\left(\tau_p^2 + \tau_p \cdot \tau_d\right) \cdot \frac{1}{f^2}$$

e – elementary charge, U_p = 863 V – pulse voltage, x = 0.1 m – total displacement (see **X** in figure 3.39), d_1 = 0.04 m – plate separations.

To obtain the cluster mass in amu, one has to divide the result of equation 3.23 by the mass of a proton ($1.67 \cdot 10^{-27}$ kg). For a detailed derivation, see ref. [120].

After the mass selection process, the mass-selected clusters leave the MCH through the exit aperture. Several electrostatic lenses focus the clusters towards the sample inside the preparation chamber. We measure the cluster current behind the exit aperture of the mass selector with a channeltron, which we describe in section 3.2.5.

The main advantage of this mass selection principle is the high transmission of 80 % and the almost infinite range of selectable cluster masses together with a compact setup.

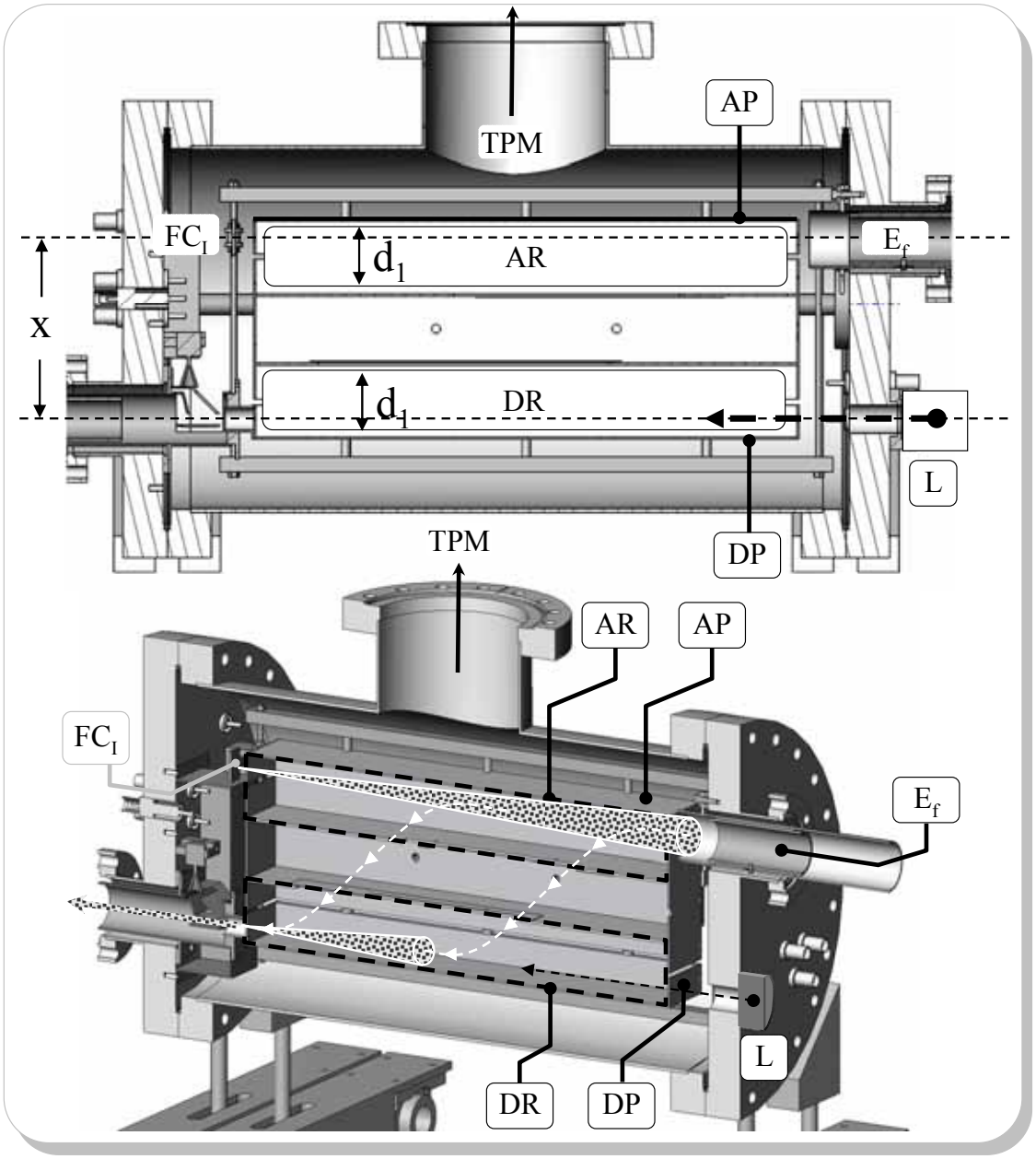

Figure 3.39 Cross sectional view of the mass selector.

E_f: focus electrode, AP: acceleration plate, AR: acceleration region, TPM: Turbo Pump in the Mass-selector chamber, L: Laser, DP: decceleration plate, DR: deceleration region, FC_I: FARADAY Cup I, x: total displacement, d_1: plate separations.

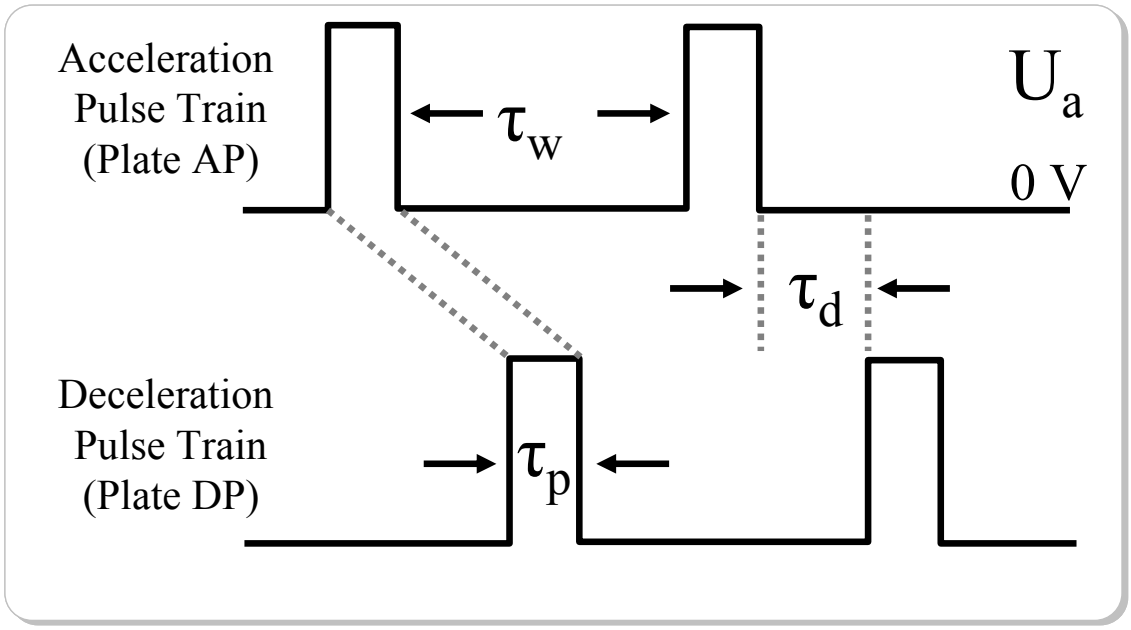

Figure 3.40 Schematic illustration of the timing of the high voltage pulses.

Trains of identical pulses, displaced in time, are applied to the plates AP and DP (see figure 3.39). τ_p: pulse length, τ_d: drift time between acceleration and deceleration pulse, τ_w: time between consecutive acceleration pulses.

3.2.4 Deposition Optics

One of the biggest challenges for us in this project is to connect the new cluster machine to the preexisting surface science facility. We connect the lower flange of the mass selector chamber via a below-tube-below-construction to a UHV valve V_{CP} (see figure 3.41) that we attach directly to the flange of the preparation chamber. Hence, V_{CP} separates the preparation chamber of the surface science facility from the cluster machine. To ensure an unhindered guiding of the cluster beam inside this tube, we construct a movable tube t_m and insert it in the below-tube-below construction. We use a TEFLON isolation ring to guide the movable tube and use the connector U_{tm} to bias it up to 1.5 kV. We choose the length of the movable tube in such a way that it reaches into the exit tube e_t of the mass selector flange as well as into the tube of the deposition electrode D_4. The potential of D_4 is identical to the one of the movable tube that is close to the floating voltage

$U_{float.}$ = -500 V . By changing the potential of t_m or D_4, we can strongly focus the cluster beam, because the gap between D_3 and D_4 represents a strong electrostatic lens (see figure 3.38).

We present an enlarged view of D_3 in figure 3.42. We use this lens of the deposition optic to focus the cluster beam to the sample and in combination with the deflector plates $D_{y\pm}$ also for bending the beam up- or downwards and left or right. Finally, the following deposition electrodes D_2 and D_1 focus the cluster beam through the small aperture at the end of D_1 directly towards the sample.

The LT and the heatable (SH_H) sample holder themselves can be biased up to ± 800 V. This is important for the cluster deposition with varying kinetic energies (see 2.4.3.1, p. 73).

We summarize working sets of parameters for all applied voltages starting with U_{ring}, U_{Iris}, and $U_{skimmer}$ proceeding with the voltages of A_3 to A_1 and the deflectors in the cryo chamber, and ending with all voltages of the deposition optics exemplary for different cluster sizes detailed in section 7.3.

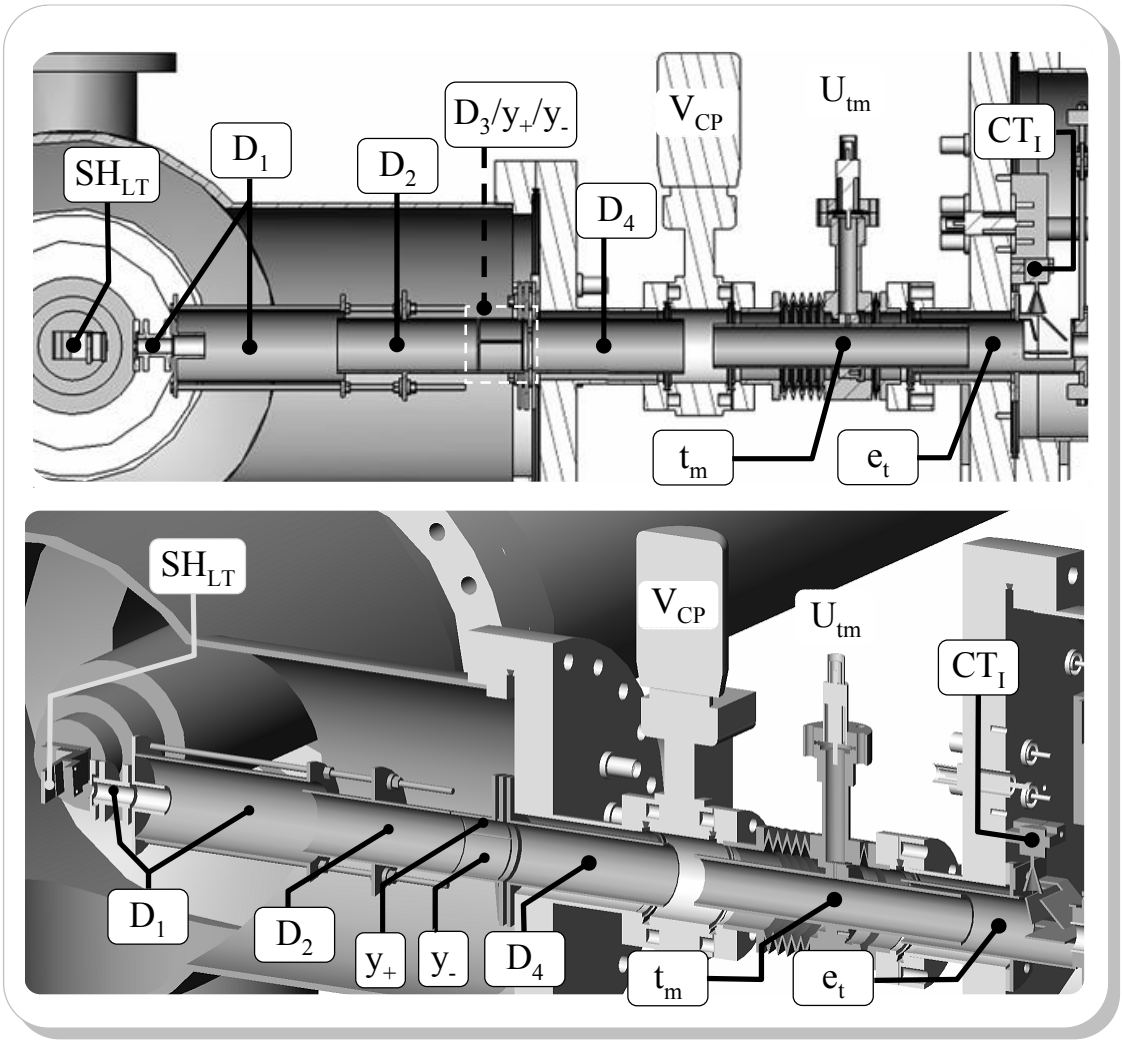

Figure 3.41 Cross sectional view of the deposition optics.

C_{T1}: Channeltron I, e_t: exit tube, U_{tm}: high voltage connector for the movable tube, t_m: movable tube, V_{CP}: valve between cluster machine and preparation chamber of the SSF, D_4 to D_1: deposition optics, y_+/y_-, y-deflector plates, SH_{LT}: LT-sample holder.

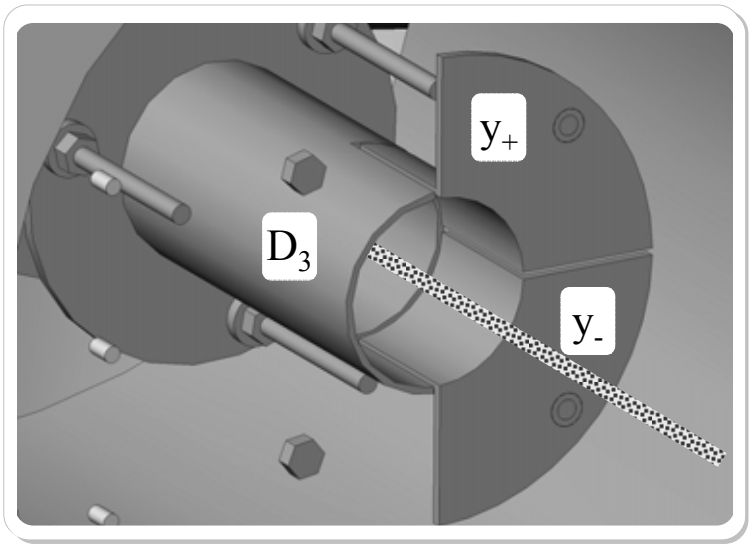

Figure 3.42 Enlarged view of the electrode D_3 with deflectors y_- and y_+.

Changing the potentials D_3, y_+, and y_-, bents the cluster beam (grey filled line) in all directions as necessary.

3.2.5 Cluster Current Measurements

As mentioned in the chapters above the measurement of the cluster current is extremely important for several different reasons. At first, the cluster current is directly proportional to the number of clusters per second. The more clusters of a specific size we measure, the better the resolution of the mass selector and the adjustment of the cluster beam are. A maximum cluster current directly measured at the sample position indicates the following: well adjusted cluster source parameters (He to Ar flux ratio, Iris position, target distance and ring-, iris and skimmer potential), optimized voltages at all lenses and deflectors, and suitable mass selector settings. This is in principle only characteristic for our mass selector, due to the dependence of the resolution of the specific geometric dimensions [117].

When we started operating the cluster machine for the first time, the very first guiding of the cluster beam through all parts of the machine to the sample turned out to be a big challenge. Therefore, an exact measurement of the cluster current is necessary. We distinguish between the multiplied and the direct current measurement, as we explain in the following section.

3.2.5.1 Direct Current Measurement

All metallic parts inside the machine that are not on ground potential provide direct access to measure the cluster ion current. We either use the internal voltage source of a KEITHLEY picoamperemeter or up to three high voltage batteries (± 300 V each) to measure a floated electrode.

The final aim during the adjustment process is always to guide the ions through all parts of the machine until the clusters reach one of the FARADAY cups. Because of the already mentioned specific geometry of our mass selector, a larger cluster ion current indicates a better mass resolution. Therefore, we always try to measure the maximum cluster current at the sample position.

In the following, we give an exemplary detailed explanation of the cluster current adjustment process:

(1) We measure the cluster current at the skimmer (see figure 3.37 or full-sized view in appendix 7.1, p. 193).

(2) We optimize the He to Ar flux ratio together with a suitable source power to the desired cluster size (see 3.2.1, pp 80).

(3) We adjust the target-iris distance and the potentials of the iris, the ring and the skimmer for maximum skimmer current. A typical skimmer current is $I_{skimmer}$ = 100 - 200 nA.

(4) We measure the cluster current at A_1 - first electrode inside the cryo chamber (see figure 3.37) - while tuning the skimmer potential.

(5) We optimize the cluster current at A_2, A_3 and the floating voltage electrode, while we adjust A_1, A_2, and A_3.

(6) We adjust the x-y-deflectors to maximum current at the cryo tube t_c (see figure 3.37). A typical cluster current at t_c is in the order of several tens of nA.

(7) We use the so-called FARADAY Cup I (FC_I) for the final optimization of the focus within the mass selection process.

(8) We adjust the focus electrode E_f that allows us to focus almost the whole cluster beam through the small hole at the end of the mass selector to FC_I (see figure 3.39). A typical current at the FC_I is $I_{FCI} = 20$ nA.

(9) We make use of one of the Y-deflection plates (see figure 3.43) mounted directly behind the exit aperture of the mass selector inside the exit tube e_t (see figure 3.39 or figure 3.43) as measurement electrode after the mass selection took place. We take a mass spectrum by scanning the masses by changing the mass selector frequency and plotting the measured cluster current versus the mass. Figure 3.48 shows a mass spectrum taken at the upper deflector plate.

(10) We detect the cluster current at the movable tube t_m and change the voltage until the current is almost zero. This shows that no clusters hit the wall indicating a perfectly aligned and focused beam. We set the next electrode D_4 usually to the same voltage as the movable tube to guide the whole cluster beam through this long tube. For extremely large / small cluster sizes, the potential of t_m could differ from that of D_4.

(11) We adjust the electrodes D_3, y_+, and y_-. Figure 3.42 shows a cross sectional view of the electrode D_3 with the form of a semi circle to the right side of the two y-deflector electrodes in the shape of a quarter circle. Using voltages close to the floating voltage at all three electrodes leaves the cluster beam almost unaffected. Changing the three parameters properly leads to a bending of the cluster beam in x-y-direction.

(12) We optimize the following two last deposition electrodes D_2 and D_1 according to the same procedure as, for example, the electrodes A_1 to A_3.

(13) We measure the cluster current directly at the sample position with a second FARADAY Cup (FC_{II}). The FC_{II} consists mainly of two hollow stainless steel cyl-

inders electrically isolated from each other (see figure 3.47). The outer box OB represents a FARADAY cage and we connect the inner box IB to the picoamperemeter. The charged ions enter FC_{II} through one of the two holes and accumulate inside the inner box. We are able to measure cluster currents in the order of 0.01 pA without significant noise. We mount the whole setup on a manipulator we use for accurate positioning of the entrance hole with respect to the sample position and the cluster beam. S. KRAUSE built this new setup of a FARADAY Cup within her diploma thesis [120] that provides a detailed description. Figure 3.44 depicts a mass spectrum measured directly at the sample position.

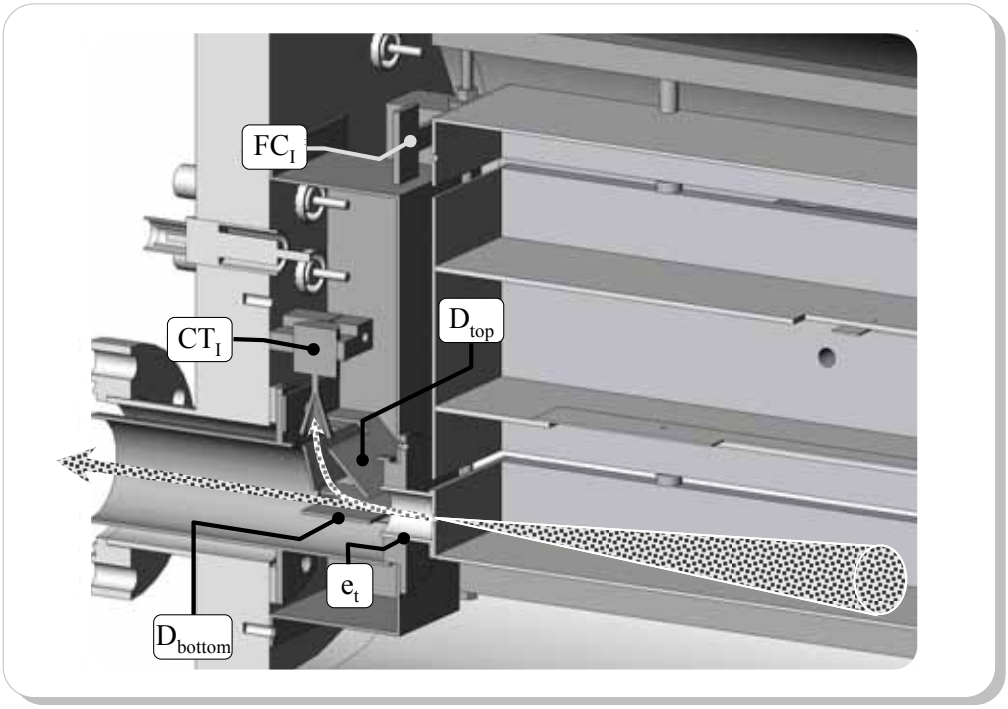

Figure 3.43 Enlarged view of the area behind the mass selector.

Changing the deflector plates potentials D_{top} and D_{bottom} bents the cluster beam (grey filled line) upwards into the first channeltron CT_1.

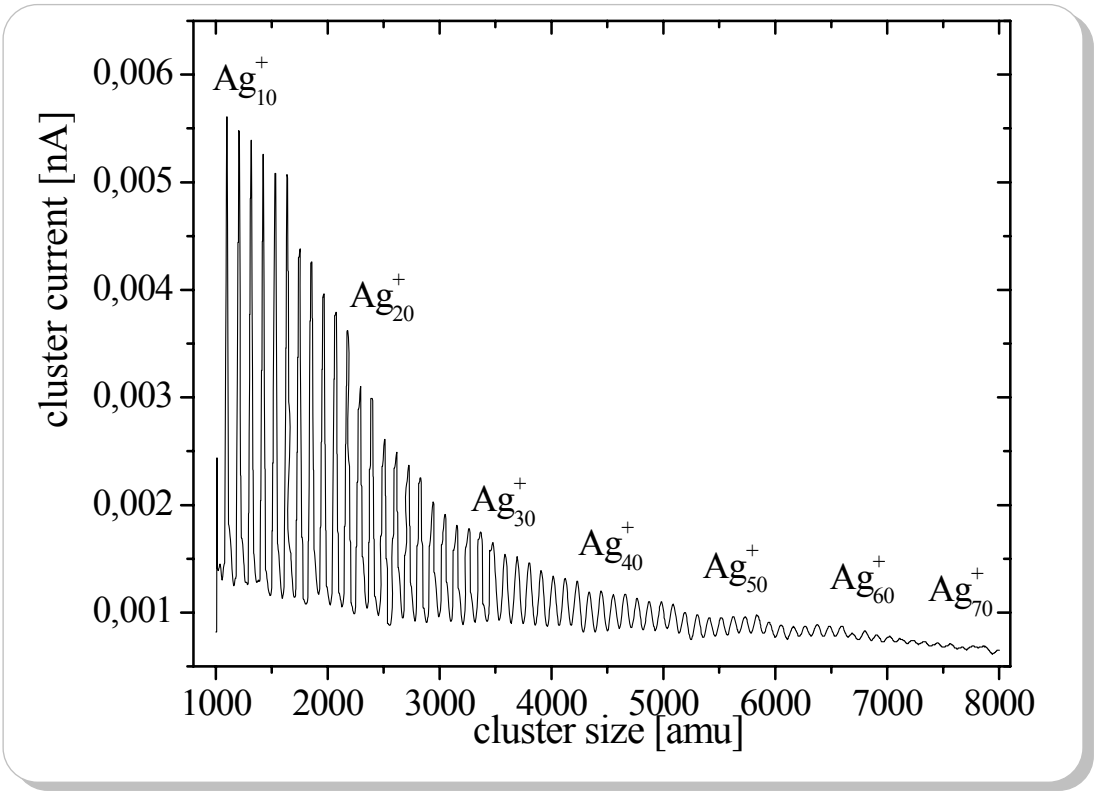

Figure 3.44 Directly measured mass spectrum of Ag_{10} to Ag_{70}.

We use the small hole of FC_{II} to determine the diameter of a cluster beam. If we do so, we first focus the cluster beam to the small hole. In a second step, we move FC_{II} horizontally to one side until the cluster current vanishes. This is a position where the small hole is just beside the cluster beam. We move FC_{II} to the other side and determine the location where the cluster current vanishes again. The distance between these two points is in a first approximation equal to the diameter of the cluster beam.

One advantage of the new mass selector is the almost infinite range of selectable cluster masses. We can change the frequency f of the frequency generator to very low values, to select extremely large cluster sizes. A frequency of f = 23476.6 Hz, for example, leads to silver $Ag_{3333\pm24}$ clusters. Decreasing the waiting time τ_W leads in general to a higher transmission and consequently to a higher cluster ion current. Nevertheless, one should not set τ_W too short, because the slow vertical movement of large clusters should be

finished before the next pulse starts to displace the next cluster beam portion. Otherwise, one observes a double peak in the mass spectra (see figure 3.45).

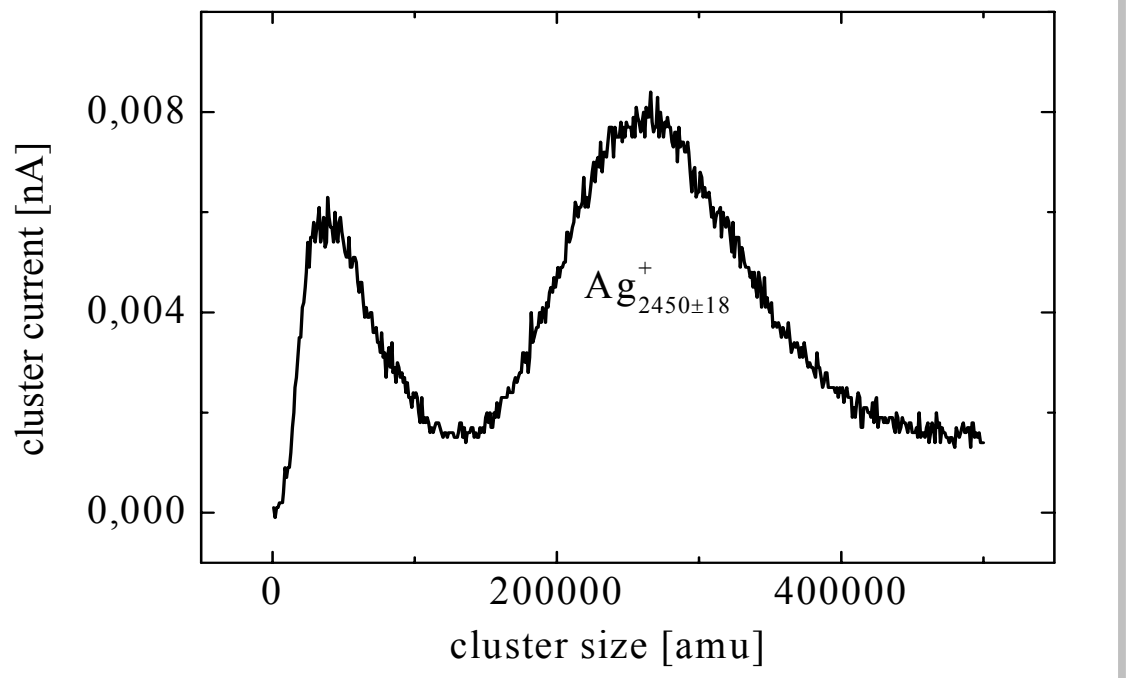

Figure 3.45 Directly measured mass spectrum of large cluster sizes using a too short waiting time τ_w. The second peak on the left belongs to clusters that are already pulsed downwards, although not all clusters of the previous cluster beam displacement have left the mass selector.

Figure 3.46 shows an example of a mass spectrum of large clusters, which we measured with the FC_{II}. We would like to emphasize, that the broad peak only represents the broad cluster size distribution, which is provided by the cluster source. Within a deposition experiment, we cut out a very narrow region out of this size distribution, for example, $Ag_{2130\pm21}$, as we display in figure 3.46.

Usually we measure the large cluster sizes with a complete different set of cluster machine parameters. We tabulate a detailed set of parameters for $Ag_{2130\pm21}$ in table 7.23.

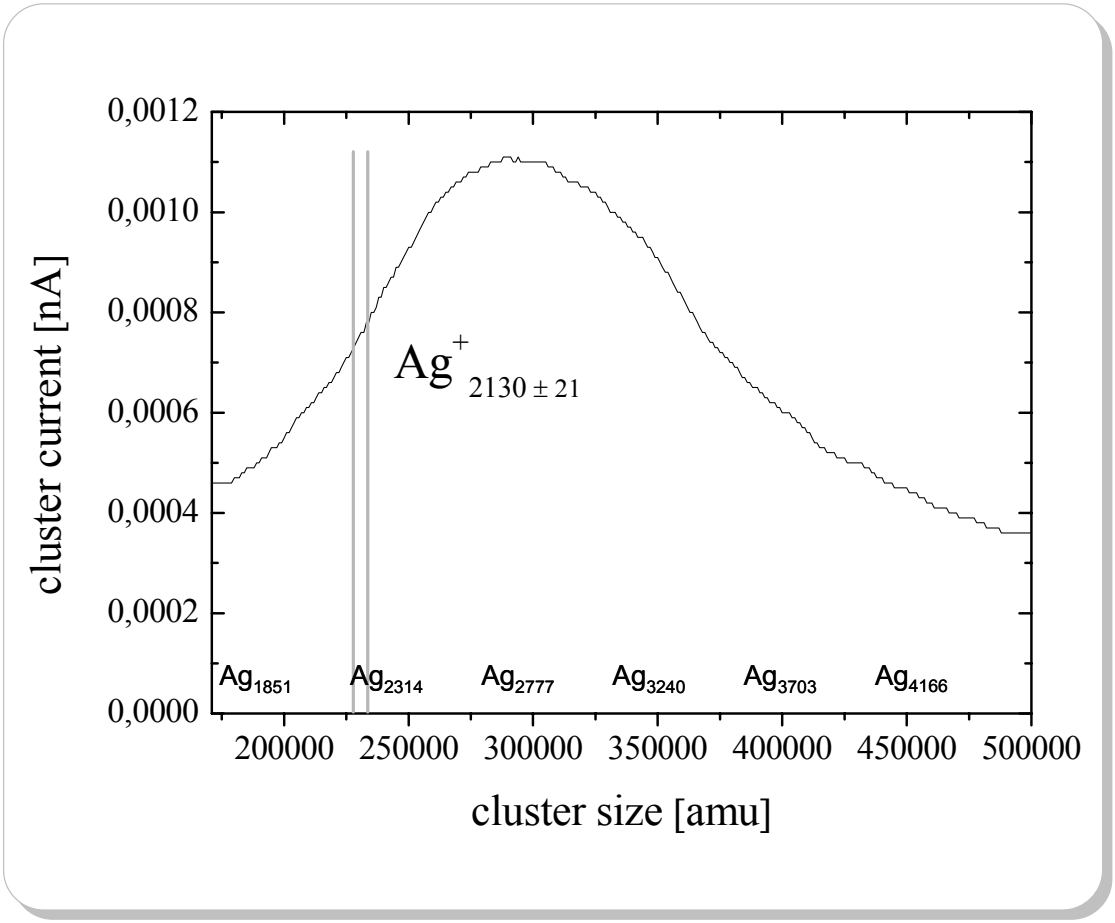

Figure 3.46 Directly measured mass spectrum of large cluster sizes.

The broad peak represents the cluster size distribution of the cluster source. The mass selector cuts out a very narrow region (grey vertical lines).

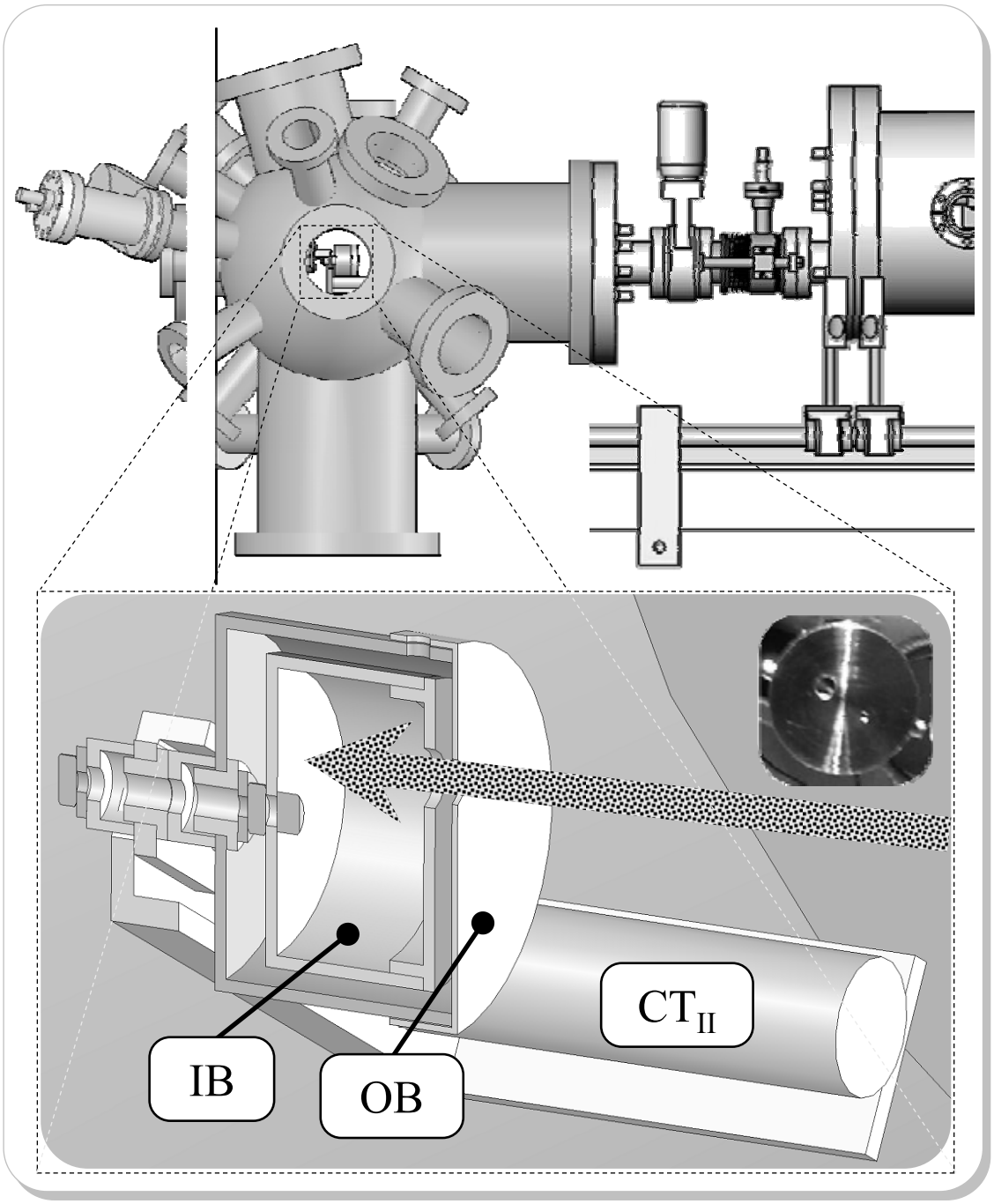

Figure 3.47 Schematic illustration of the second FARADAY Cup FC_{II}.

CT_{II}: Channeltron II, OB: Outer box of FC_{II}, IB: Inner box FC_{II}.

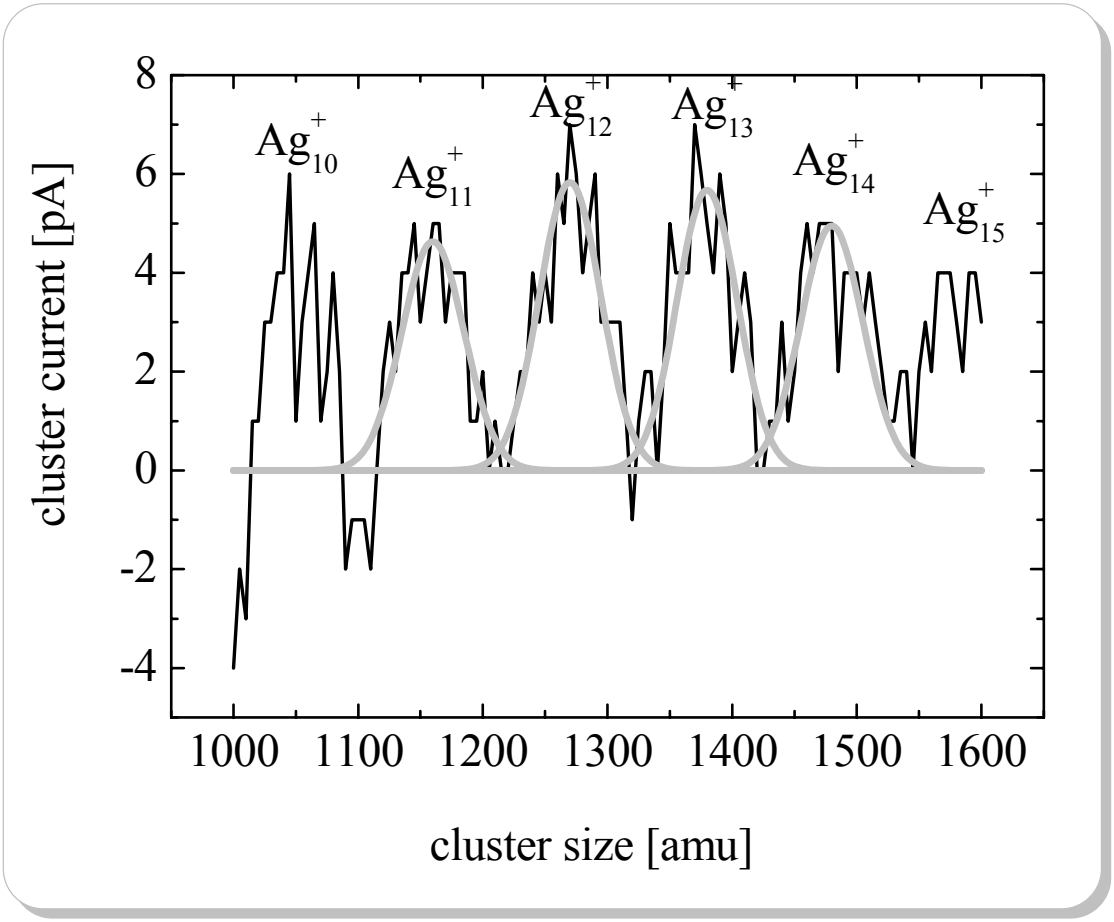

Figure 3.48 Directly measured mass spectra of Ag_{10} to Ag_{15}.

Mass resolution m / Δm = 32.

3.2.5.2 Multiplied Current Measurement

In the case of a bad signal-to-noise ratio, we use a channeltron in addition to the FARADAY Cup to detect a multiplied signal. We use two channeltrons of the type *5900 Magnum Electron Multiplier*™ of the manufacturer BURLE [.124]. Operating the channeltrons at a voltage of –3000 V increase the current by a factor of the order of $6 \cdot 10^7$.

We mount the first channeltron CT_I directly behind the mass selector (see figure 3.43) and the second one together with the FARADAY cup FC_{II} at the extension rod of the manipulator (see figure 3.47).

We use CT_I to measure the cluster current right after the mass selection process. In order to bend the cluster beam upwards into the channeltron, we modify the voltages of the upper (D_{top}) and the lower (D_{bottom}) deflector plate.

The channeltron multiplies typical cluster currents of a few pA to several tens of μA. Figure 3.49 shows a typical multiplied mass spectrum taken right behind the mass selector (see figure 3.43). The grey line represents a GAUSSIAN multi peak fit for the calculation of the mass resolution. For details, see ref. [120].

We operate the second channeltron in the same way. Figure 3.50 displays a typical mass spectrum, measured using CT_{II} inside the preparation chamber close to the sample position.

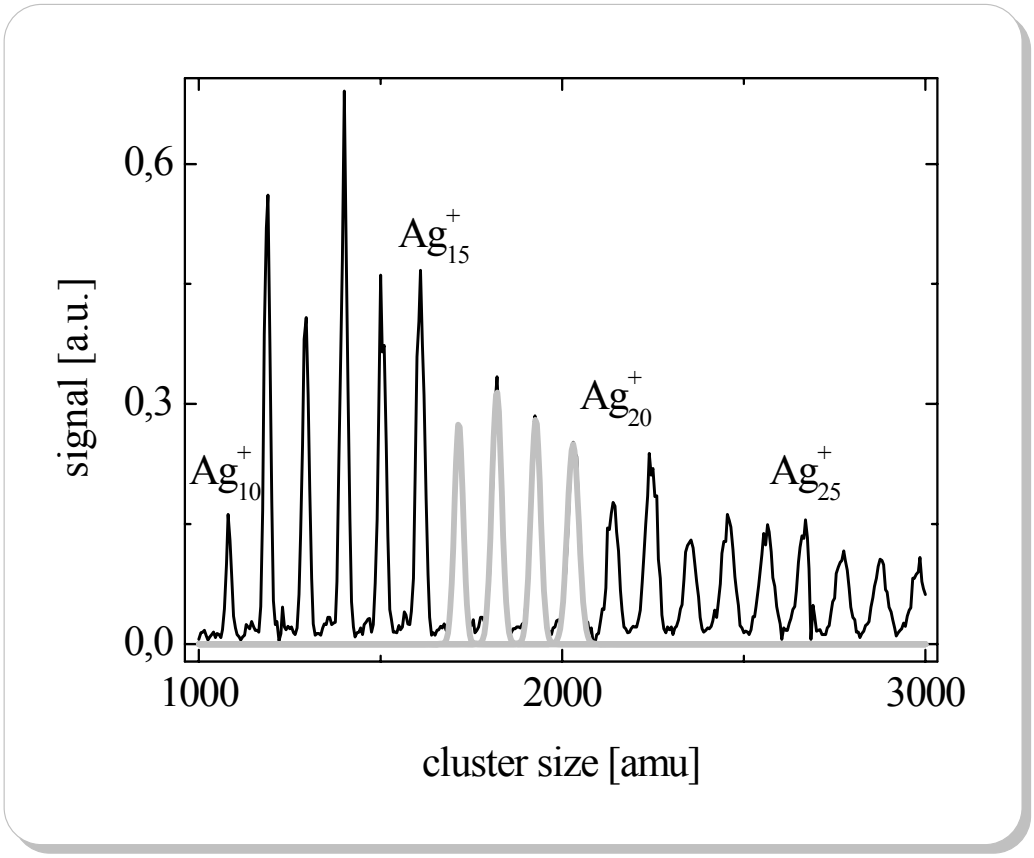

Figure 3.49 Multiplied mass spectrum taken with the first channeltron CT_1.

Mass resolution m / Δm = 68.

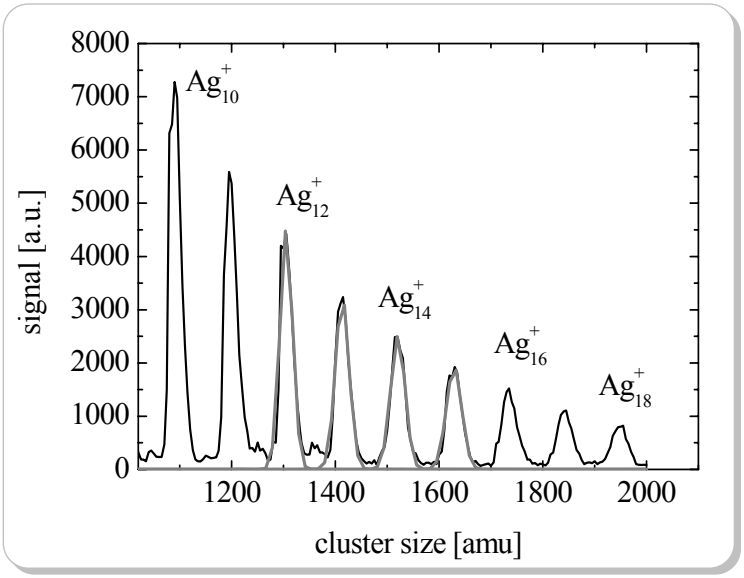

Figure 3.50 Multiplied mass spectra measured with the second channeltron CT_2.

Mass resolution m / Δm ≈ 55.

CLUSTER ION CURRENTS

Ag_{13}	90 pA	Ag_{561}	58 pA
Ag_{40}	20 pA	Ag_{923}	30 pA
Ag_{55}	93 pA	Ag_{1415}	12 pA
Ag_{80}	67 pA	Ag_{1851}	21 pA
Ag_{147}	92 pA	Ag_{2129}	1 pA
Ag_{309}	85 pA	Ag_{3333}	12 pA

Table 3.4 Typical maximum cluster currents obtained for different masses as detected directly at the sample position with FC_{II}.

Chapter 4

SAMPLE PREPARATION

In the following chapter we describe the preparation methods for the cluster sample systems. For our experiments, we used a number of different sample substrates: a Au(111) and a Pb(111) single crystal, a 100 nm Au(111) film on mica, and a graphite substrate.

We used buffer monolayers of different rare gases like Ar and Xenon for decoupling the clusters electronically and geometrically from the substrate. Especially for size-selected clusters, rare gas buffer layers are interesting to realize soft-landing conditions. In addition, the evaporation of one monolayer of C_{60} onto a substrate proved to result in a functionalized surface for the deposition of size-selected clusters - even at room temperature.

In the final preparation step, we produced clusters on the sample system in one of two ways: by growing metal islands after evaporating atoms or by using the cluster deposition machine.

Future experiments may see other cluster, sample, or buffer layer materials. We plan to deposit, *e.g.*, gold, silver, and lead clusters on rare gas layers on a silver single crystal and to use different cluster materials (*e.g.*, gold, platinum, iron, or aluminum) for size-selected clusters deposited on different surfaces (*e.g.*, 1 ML C_{60} on a silver single crystal).

4.1 Evaporators

Our experiments used two different types of evaporators. For atomic evaporation of gold, lead, or silver (the latter we will be using in the future) we use an Evaporator with integrated Flux Monitor (EFM). Instead of using one of the EFM's we installed a simple thermal evaporator with a direct current heater to produce the C_{60} functionalized surface.

4.1.1 Evaporator with Integrated Flux Monitor

To investigate cluster rare gas substrate systems it is important to calibrate exactly the amount of the evaporated cluster material. The Surface Science Facility (see chapter 3, p. 75) contains two EFM's to evaporate gold, silver, or lead. What follows is an exemplary description of the EFM's functionality and its calibration based on a gold EFM, which equally holds for the silver and lead EFM.

The evaporator [125] allows an *in situ* flux measurement utilizing the flux of ionized atoms produced by the electron-beam heating of the tungsten crucible filled with gold (current I_{em} at a voltage of 800 V). A part of this flux is collected in the orifice of the evaporator (I_{flux}), and similar to the function of an ion-flux pressure gauge [126] the evaporation rate is then given by $\kappa \cdot I_{flux}/I_{em}$ with κ a constant determined by the geometric shape of the setup for a fixed material and electron acceleration voltage. We use a quartz-micro-balance in a separate vacuum chamber to determine useful parameters for the electron-beam heating and measure κ for a new evaporant. Nevertheless, in this way the accuracy in calibrating κ is limited for two reasons: differences in the geometric

placement of evaporator and substrate and the non-negligible influence of thermal drifts of the microbalance when we use small evaporation rates similar to those in the cluster growth experiments.

Significantly higher rates are not recommended, since there is no guarantee of the proportionality of the evaporation rate to I_{flux}/I_{em}, *e.g.*, due to space charge effects for high electron or ion currents. For the exact calibration of κ we therefore use homoepitaxial growth of gold on Au(111) in the same setup and with similar evaporation rates as for the gold cluster growth. For this purpose, we prepared a Au(111) surface with atomically flat terraces (several $(100\times100)\,\mathrm{nm}^2$ large) by sputtering and heating ($T=623\,K$ for 1h) a gold film on mica. To obtain monoatomic islands with a diameter of a few 10 nm, we used a substrate temperature of $T=273\,K$ during the gold deposition. At this temperature, we can safely assume a condensation coefficient of 1 for the gold atoms on the Au(111) surface. In figure 4.51 we show an STM image[6] after gold was evaporated for 20 s with $I_{em}=29\,mA$ and $I_{flux}=10\,\mu A$. With the microbalance data, this should result in roughly 1/3 of a gold monolayer (ML). We determined the gold coverage to be (0.23 ± 0.01) ML from height histograms of the STM images taken on large flat terraces, and a resulting κ of about $\kappa=33$ ML/s. We use this value for calculating the gold coverage in the cluster growth experiments.

[6] All STM figures within this thesis were processed with the program WSxM 4.0 Develop 8.5 © (2005) by Nanotec Electronica S.L. see http://www.nanotec.es/. Some functions of this program are explained in [30].

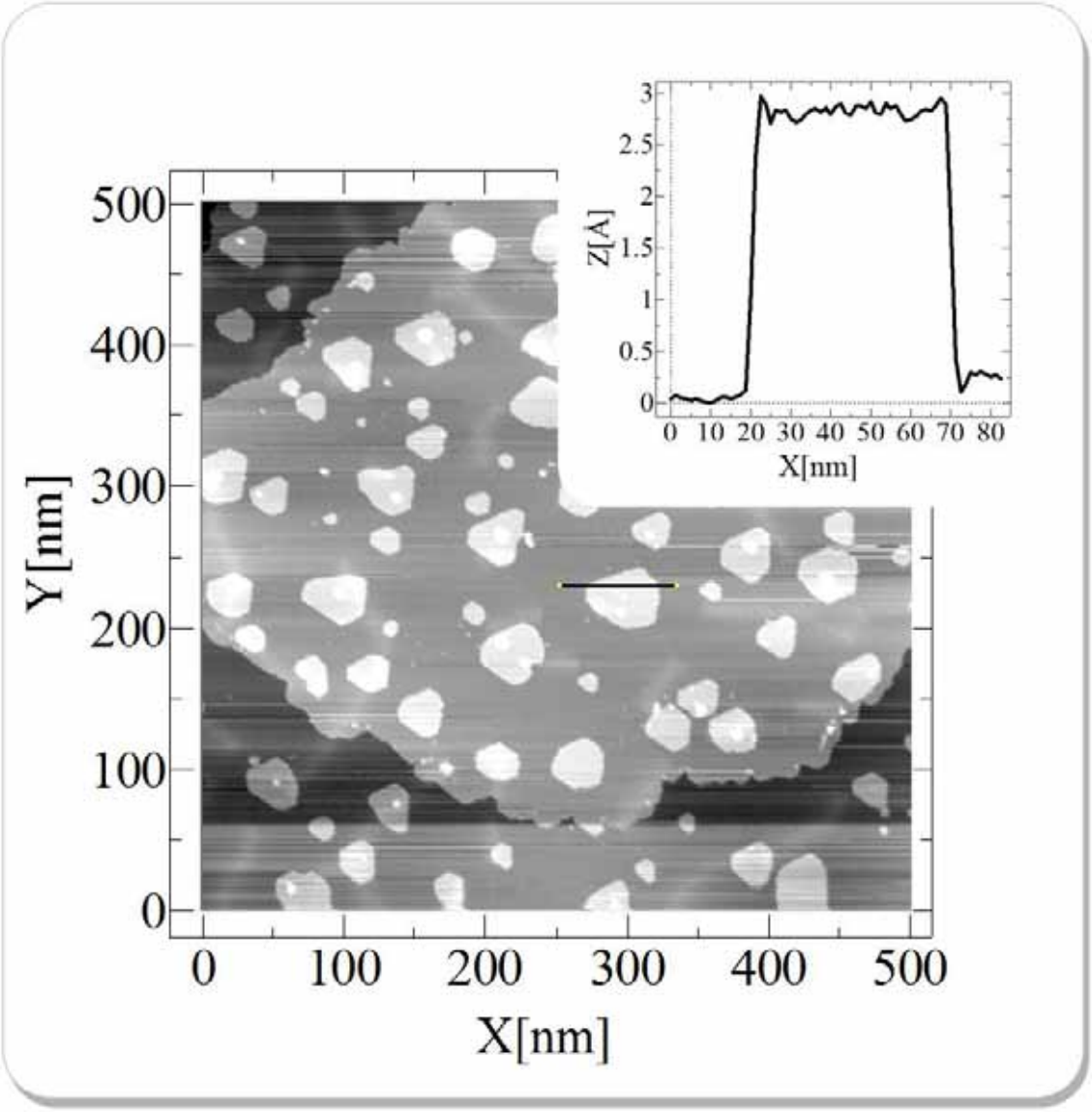

Figure 4.51 STM image of gold deposited at $T = 273\ \mathrm{K}$ on Au(111). The STM image shows a coverage of (0.23 ± 0.01) ML gold.

($U_{tunelling}$ = 1.12 V/ $I_{tunneling}$ = 0.098 nA).

4.1.2 Evaporator with Resistive Heating

To evaporate the C_{60} we used in the following experiments an Evaporator with Resistive Heating (ERH).

The core of this evaporator is a crucible with resistive heating. After heating the crucible for 20 min., it reaches its equilibrium temperature. We measure the temperature with a

type-k thermocouple. To evaporate C_{60} we heated a poly-crystalline C_{60} powder manufactured by the MER Corporation [.127] until the evaporation took place. We used a shutter with an aperture to determine the position and the spot on the sample as well as the evaporation length of time. To evaporate 1 ML C_{60} typical parameters are $I = 2$ A and $U = 4$ V for approximately 5 minm which corresponds to a crucible temperature of 470° C [.109].

Reference [.109] describes further details of the ERH construction as well as a detailed description of the calibration process using a quartz-microbalance.

4.1.3 Sample Substrate Preparation

To investigate clusters on surfaces, extremely clean sample surfaces are necessary. Adsorbates on sample surfaces would hinder controlled experiments. In case of grown clusters, adsorbates would act as nucleation centers and prevent a controlled cluster growth. In case of deposited clusters, STM investigations can only be successful, if one can certainly distinguish between clusters and adsorbates. Moreover, buffer layers like one monolayer C_{60}, or a few monolayers of rare gases, would neither grow nor adsorb properly, in the case of a contaminated surface with adsorbates or even a thick water film.

The preparation of the sample substrates we have used within this work is well know from several other thesises of our group (see [30, 36, 40, and .128]). We will summarize the essential preparations steps in the following sections.

4.1.3.1 Gold Substrate

The sample substrate mostly used in the experiments we present here is an in (111)-direction oriented gold single crystal; we refer to as Au(111). Each deposition experiment uses a freshly prepared Au(111) sample which rests at most for 12 h under the same UHV conditions $\left(p_{Ana} = 2 \cdot 10^{-12}\,\text{mbar}\right)$ established in our analysis chamber before we start the actual deposition.

We sputter the Au(111) surface with high energetic Ar ions to clean the surface from adsorbates and formerly deposited clusters. In a first heating cycle, we desorb water and molecules with a low desorption temperature from the sample surface and impurity atoms diffuse from inside of the sample to the surface. Sputtering the sample removes several monolayers from the respective sample surface. Furthermore, heating the sample heals and atomically flats the distorted surface again. In doing so, the diffusion of surface atoms leads to a recreation of the pristine surface. We have to repeat the sputtering-heating-cycle in case of hard contamination, *e.g.*, by exposure to air. To prevent impurities emerging from deep out of the crystal at the final heating cycle, the last sample heating should take place at lower temperatures compared to the ones before.

To check the degree of cleanness we use the Au(111) surface state [.129], which is clearly visible in the UPS spectra in case of a clean surface. Moreover, we can use the $23x\sqrt{3}$ Au(111) surface reconstruction as indication for a bare and clean substrate [.130].

In case of the experiments for lead clusters on Au(111) or gold clusters on Pb(111), respectively (see sec. 4.1.5.1, pp .125), we sputtered the samples after the experiment at low temperatures (150 K) to prevent a diffusion of the cluster material into the single crystal. CHLADEK und BETZ observed this effect already for copper atoms on a lead surface [.131]. Nevertheless, later experiments indicate that this routine is not necessary, because the sputtering removes enough surface material to remove the impurities.

.Table 4.5 summarizes the typical parameters. In general, one can apply the rule of thumb: the longer the time of sputtering and heating, the better the quality of the sample surface.

	Energy [eV]	Temperature [°C]	TIME [min.]
1st sputtering	1000 eV	RT	60
1st annealing	-	500	60
2nd sputtering	1000 eV	RT or (150 K)	60
2nd annealing	-	400	60

Table 4.5 Parameters for the preparation of the Au(111) surface.

The Ar pressure during the sputtering process is always $p_{Ar} = 2.0 \cdot 10^{-6} mbar$, which results commonly in a corresponding sample current of $I_{sample} \approx 2\mu A$. (for further details of sputtering see [32])

4.1.3.2 Lead Substrate

Beside the Au(111), we use as complementary sample substrate an (111)-oriented lead single crystal, in the following called Pb(111). The Pb(111) sample is prepared in the same way as described above for Au(111) with only slightly different parameters. Because of the lower melting point of lead $T_{melt,Pb} = 327.46\ °C$, one has to be very careful while heating the sample close to this temperature. Table 4.6 summarizes the typical parameters.

	Energy [eV]	Temperature [°C]	TIME [min.]
1st sputtering	1000 eV	RT	40
1st annealing	-	220	60
2nd sputtering	1000 eV	RT or (150 K)	40
2nd annealing	-	200	60

Table 4.6 Parameters for the preparation of the Pb(111) surface.

The Ar pressure during the sputtering process is always $p_{Ar} = 2.0 \cdot 10^{-6} \text{mbar}$, which results commonly in a corresponding sample current of $I_{sample} \approx 4\,\mu\text{A}$ (for further details of sputtering see [32]).

4.1.3.3 Graphite Substrate

The last substrate used in these experiments is a Highly Oriented Pyrolytic Graphite (HOPG) of the best grade (*e.g.*, ZYA). HOPG is a form of high purity carbon providing surface microscopists with a renewable and smooth surface. HOPG is non-polar and provides a background with only carbon in the elemental signature. This is useful for samples that also undergo elemental analysis. The extreme smoothness of HOPG results in a featureless background, except of course, at atomic levels of resolution. Graphite in general and HOPG in particular consist of a lamellar structure, like mica, molybdenum disulfide and other layered materials that are composed of stacked planes. All of these examples of lamellar structures have much stronger forces within the lateral planes than in-between, thus explaining the characteristic cleaving properties.

The usual approach to cleave HOPG is to take a piece of tape (*e.g.*, 3M® *Scotch Brand* tape [.132]), press it onto the flat HOPG surface then pull it off, and the tape invariably takes with it a thin layer of HOPG. This freshly cleaved surface is what we use as sample substrate-material.

The HOPG has a polycrystalline structure with crystals of varying sizes, typically several μm in size and exhibits high chemical inertness. The freshly cleaved surface consists of atomic steps, 0.2 - 0.3 nm, and steps of several or dozens of atomic layers. The height of a single step is 0.34 nm [.133].

In the following experiments a freshly tape cleaved HOPG sample is prepared under UHV conditions by heating the sample at a temperature of T = 600 °C for one hour to remove the water from the surface. For further properties of HOPG see ref. [.134].

4.1.4 Preparation of Buffer Layers and Functionalized Surfaces

Except for clusters deposited directly onto an HOPG substrate with high kinetic energy (see sec. 5.1, p..132) we used buffer layers for different reasons. In cases of large grown (see sec. 5.2) and large size-selected (see sec. 5.3) clusters, we used rare gas layers to decouple the clusters geometrically and electronically from the substrate to produce so-called *free clusters on surfaces* (see sec. 5.1, pp .132). In case of deposited size-selected magic silver clusters, we produced one monolayer C_{60} onto the Au(111) substrate. The C_{60} layer is well suited for the cluster deposition at room temperatures due to two reasons. On the one hand, a C_{60} functionalized surface turns out to be very inert, preventing the surface from contamination, even for long deposition times. On the other hand, one can easily image soft-landed clusters with the STM due to their strong bonding to the surface in contrast to, *e.g.*, soft-landed clusters on HOPG (see 5.1).

4.1.4.1 Controlled Rare Gas Layer Adsorption

To investigate cluster / rare gas / substrate systems, as discussed in section 5.2, an exact measurement of the rare gas layer thickness is essential. We used an *in situ* control of the film thickness during monolayer-by-monolayer adsorption of the rare gas films by observing the $5p_{1/2}$ and $5p_{3/2}$-signal *in situ* with UPS, while introducing xenon into the

preparation chamber. One can observe the polarization induced shift between the first and second ML [135] and the quantum well states for larger film thicknesses [52]. Figure 4.52 shows the controlled rare gas adsorption process, where one can see the UPS spectra displayed in a color-coded plot versus the adsorption time. We established a xenon pressure $p_{Xe} = 1.5 \cdot 10^{-7}$ mbar for a time t = 2450 s. The sample temperature during the adsorption was $T_{sample} \approx 30$ K. At this temperature, the diffusion of xenon on the sample surface is fast enough to allow a layer-by-layer growth, but the temperature is low enough for the adsorption of multilayers of xenon. In case of too low sample temperatures during xenon adsorption, we were not able to observe the characteristic UPS spectra for each monolayer, because a rough film was grown.

At t = 0 the Au d-bands are visible. When xenon is introduced into the preparation chamber after t = 90 s the Au d-bands vanish and the characteristic xenon $5p_{1/2}$ - peak of the first monolayer increases and finally decreases again. In equidistant time intervals $5p_{1/2}$-peaks of the second, third, fourth, and fifth monolayer increase and decrease in the same way. One can extrapolate the adsorption time for film thicknesses larger than about five monolayers. In this way, we are able to produce well-defined xenon layers with known thicknesses by simply counting the monolayers of xenon.

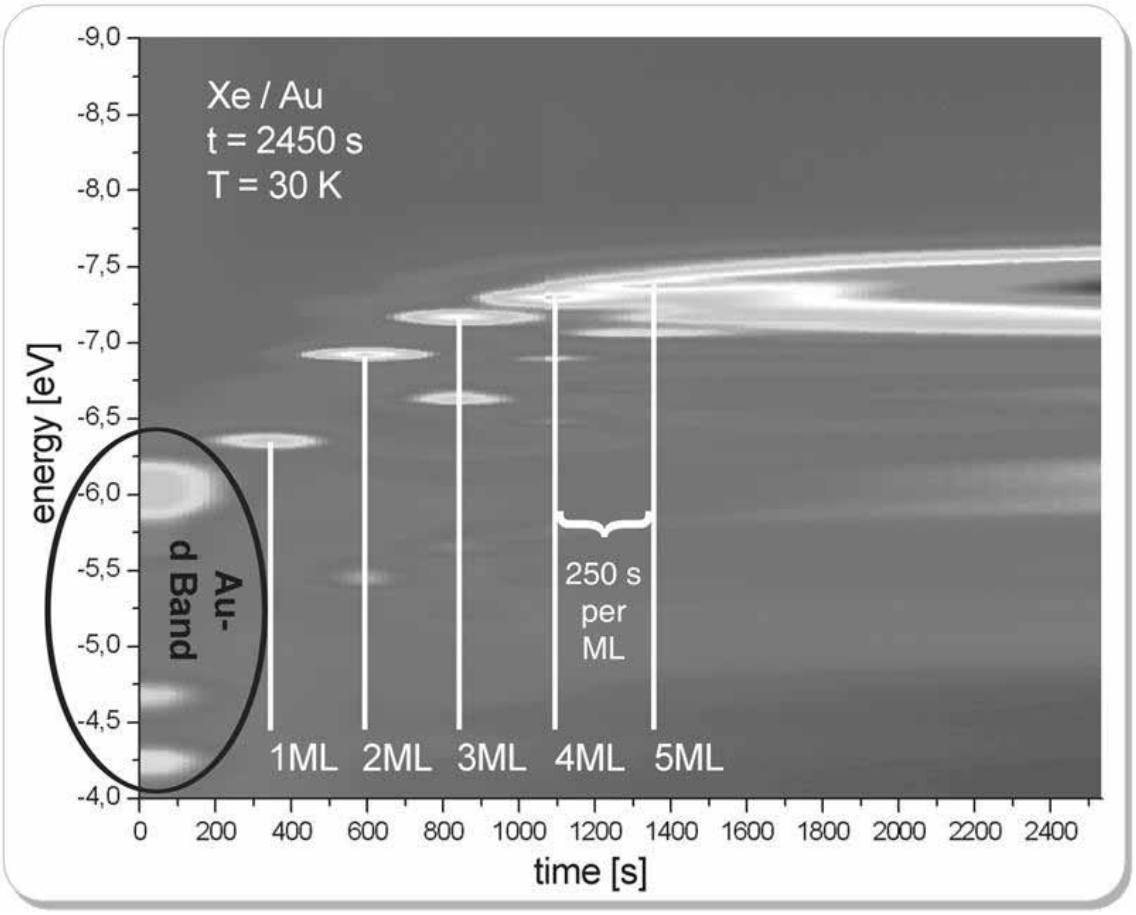

Figure 4.52 Controlled xenon adsorption on Au(111) by using a color coded display of the UPS data. The Au-d band signal disappeared, while Xe was introduced into the preparation chamber with a pressure $p_{Xe} = 1.5 \cdot 10^{-7}$ mbar at a temperature T = 30 K. We obtained the exact xenon layer thickness from the characteristic UPS spectra for the $5_{p1/2}$ signal of Xe for one to five ML xenon coverage and an extrapolation of the adsorption time for larger film thicknesses. In addition, the $5_{p3/2}$ signal is visible, *e.g.*, at about -5.5 eV for 2 ML and 3 ML.

4.1.4.2 Functionalized Surfaces for Cluster Deposition

For the deposition of size-selected clusters (see sec. 5.4, pp .159), we choose an alternatively prepared substrate. As mentioned above it turns out, that 1 ML C_{60} is well suited for the deposition of size-selected clusters at room temperature.

We evaporated 1 ML of C_{60} onto the freshly prepared sample substrate by opening the shutter of the ERH for 5 minutes after heating up the ERH for 20 minutes. After that, we had to anneal the system C_{60} / sample substrate for about 25 minutes at approximately

500 K. Otherwise we would not observe large flat and perfectly ordered 1 ML high C_{60} islands [.136]. Figure 4.53 shows an STM image of 1 ML C_{60} on a Au(111) substrate prepared as described above. We imaged the sample at a temperature of T_{STM} = 77 K and found perfectly ordered C_{60} molecules in this (300 x 300) nm² large STM image. We also observe several (100 x 100) nm² up to (200 x 200) nm² islands with an identical height of approximately 1 nm. The pattern visible in the enlarged view of the C_{60} functionalized Au(111) surface in figure 4.53 is due to two different orientations of C_{60} molecules with respect to the gold surface [.137, .138].

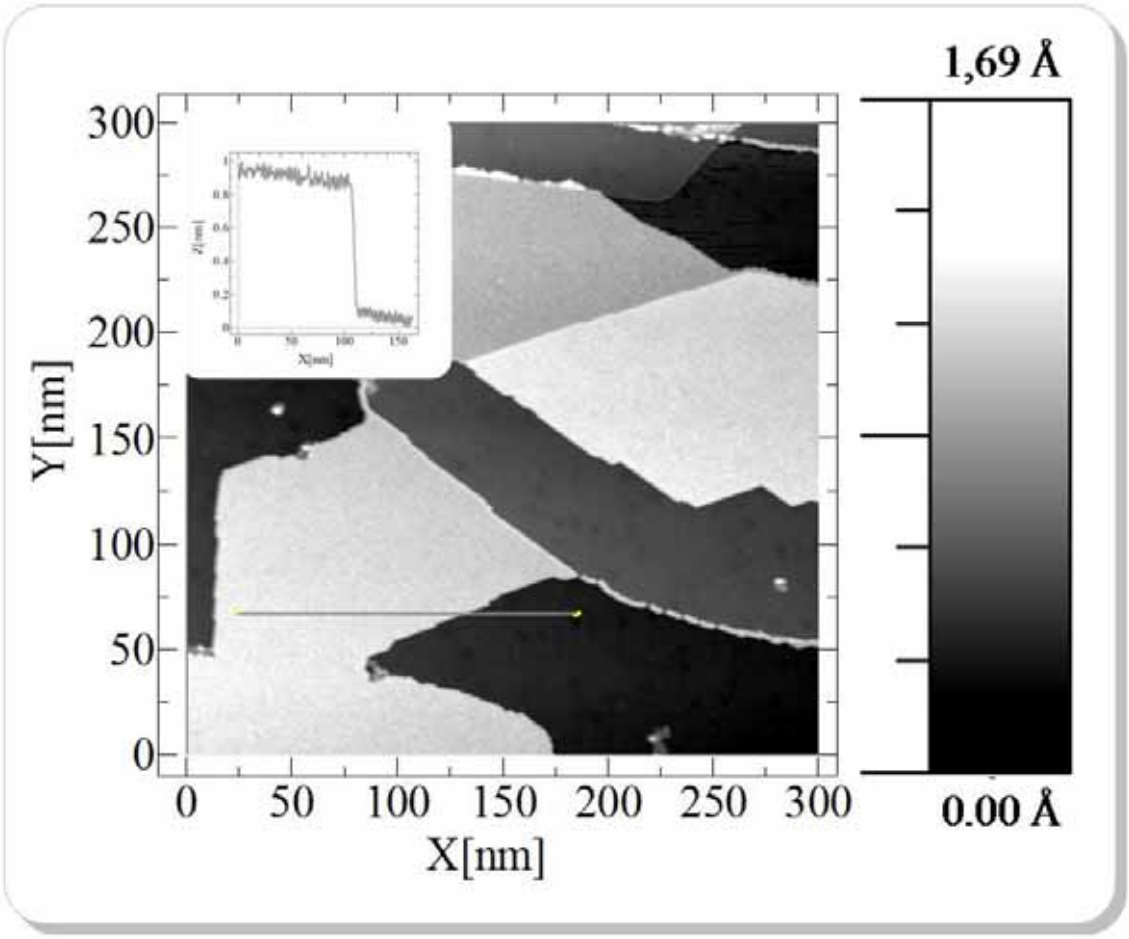

Figure 4.53 STM image of 1 ML C_{60} on a Au(111) substrate.

The inset shows a line profile of a C_{60} step edge. ($U_{tunelling}$ = 2 V / $I_{tunneling}$ = 0.03 nA).

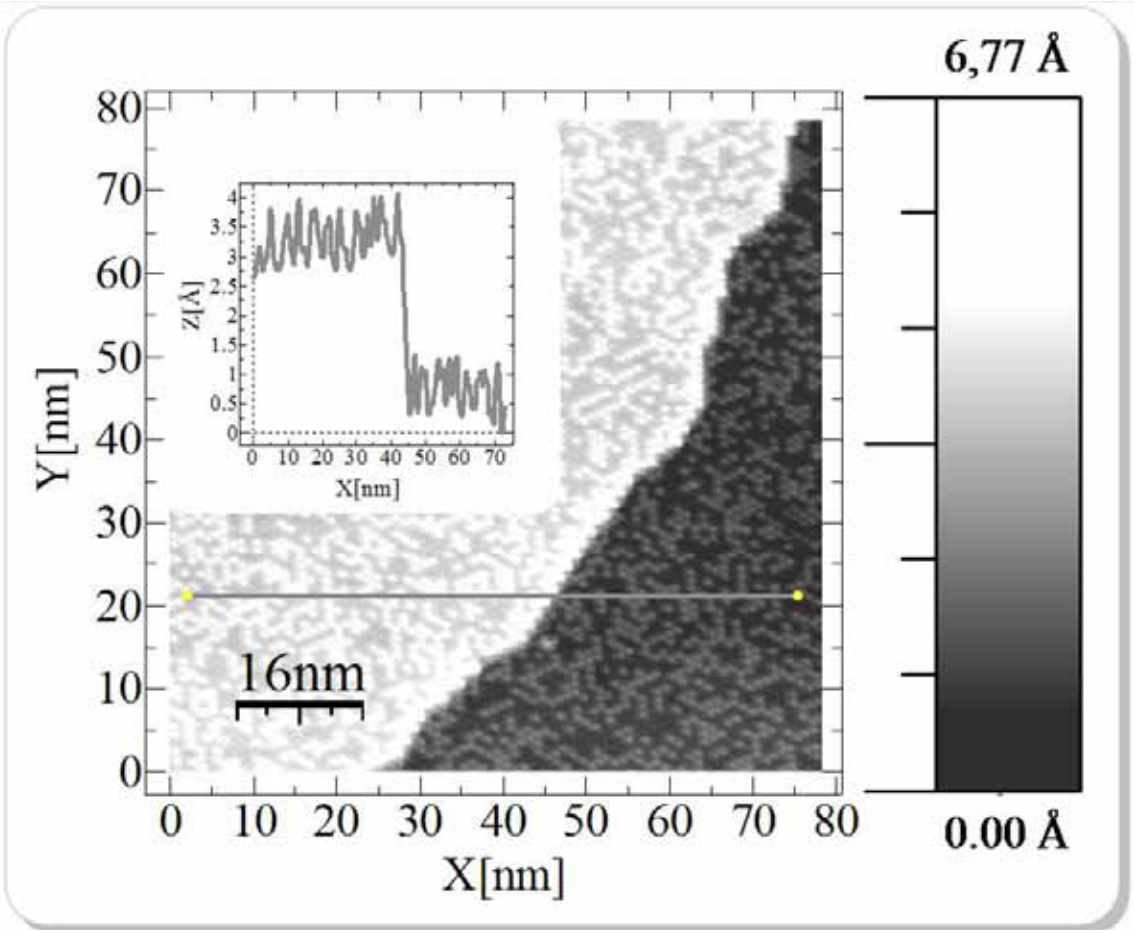

Figure 4.54 Enlarged view of a C_{60} covered gold surface.

The inset shows a line profile of an underlying gold step edge. ($U_{tunelling}$ = 2 V / $I_{tunneling}$ = 0.139 nA).

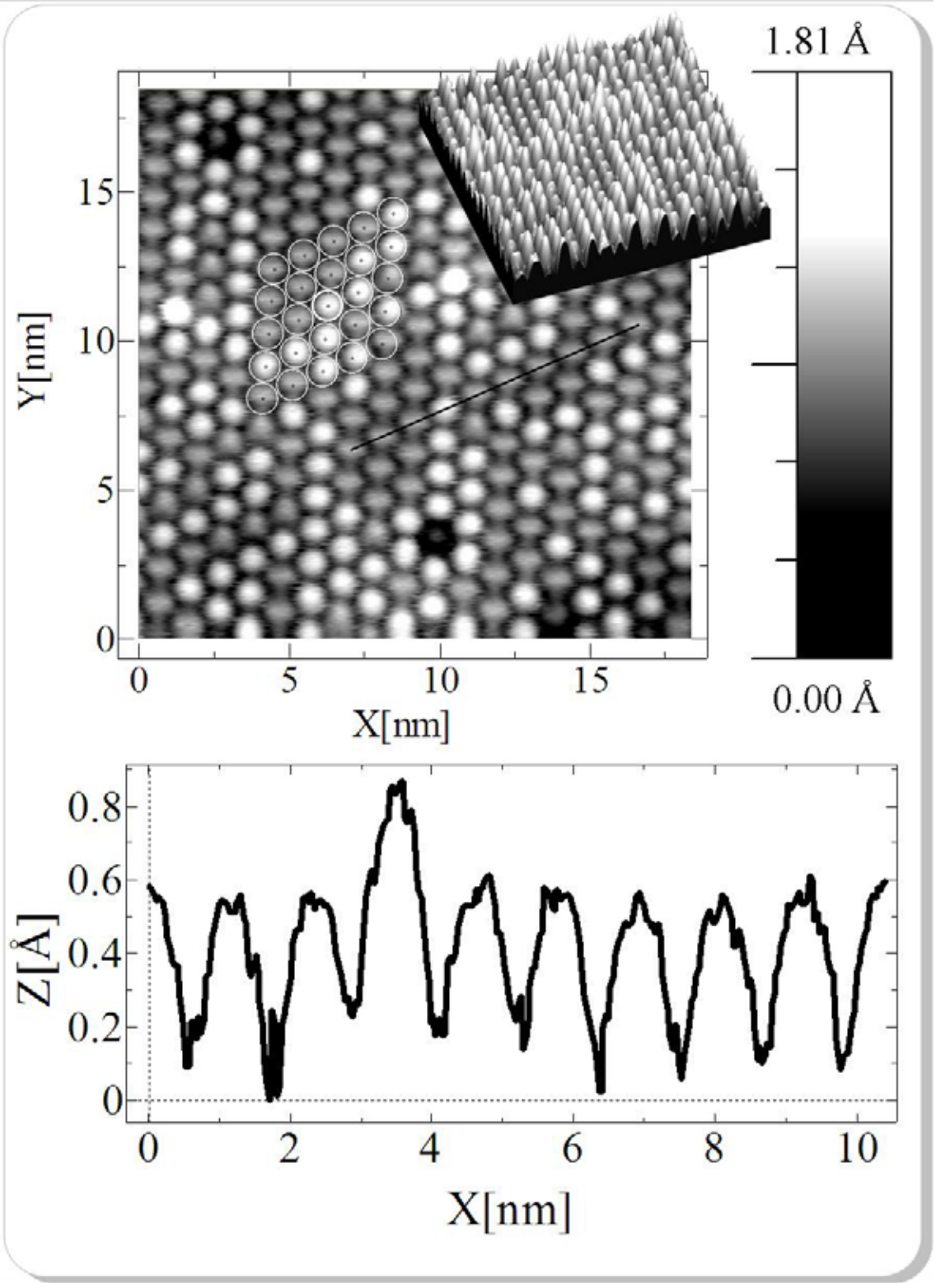

Figure 4.55 Enlarged view of a C_{60} covered gold surface.

(Bottom) line profile of C_{60} molecules. ($U_{tunelling}$ = 0.1 V / $I_{tunneling}$ = 0.254 nA).

4.1.5 Clusters on Surfaces

The final step in the preparation process is the cluster preparation. We distinguish between to different cluster types: grown clusters and size-selected clusters.

4.1.5.1 Grown Clusters on Surfaces

For the preparation of grown clusters on surfaces, we deposited lead or gold onto the sample. We controlled the evaporated amount of metal by an integrated flux monitor and a calibration measurement (see sec. 4.1.1 p. 112, also published in [75]).

For the samples, we present in the following we used a surface temperature of $T = 30$ K when we deposited the gold or lead coverage with a rate in the order of 0.01 ML/s. For a detailed description of the lead evaporator calibration measurement see ref. [139]. Afterwards we performed UPS measurements at 10 K. Then we investigated the cluster morphology with STM at $T = 5$ K. This is possible in case of clusters grown on a thin film up to 10 ML Xenon or after the desorption of thick rare gas layers up to 60 ML. The cluster size distribution of grown clusters is rather broad.

4.1.5.2 Deposited Mass-Selected Clusters on Surfaces

Beside grown clusters on surfaces, we are interested in mass-selected clusters on surfaces studied within this thesis. We constructed and optimized the new cluster deposition machine introduced in section 3.2 (p. 78) for the deposition of size-selected clusters. In contrast to clusters produced by metal island growth, deposited mass-selected clusters show extremely narrow size distributions.

First, we optimize the cluster machine parameters to the desired cluster size. We achieve this by maximizing the cluster current measured with the FARADAY cup at the sample position (see sec. 3.2.5.1, p. 100). Afterwards, we remove the FARADAY cup and place the sample holder in front of the last deposition optic D_1 (see figure 3.41).

In order to estimate the deposition location on the sample we mount a laser to the mass selector chamber (see L in figure 3.39). If we have aligned the setup accurately, the Laser spot is clearly visible on the sample (see figure 4.57).

We biased the sample holder, usually the LT-sample-holder, either to -800 V for the deposition with high kinetic energy (see 5.1, p. 132) or only to a few Volts for the so-called soft-landing deposition. We switched on the cluster source, turned the sample into the cluster beam for the desired deposition time, and finally transfered the sample into the STM.

Figure 4.56 shows a plot of the cluster ion current versus the sample bias voltage to exemplify the dependency between deposition energy and sample bias for two different samples. The Ag^{+}_{309} cluster current decreases at approximately +17 V (see symbol ● in figure 4.56). For this sample bias, about 50 % of the cluster ions do not have enough energy to reach the FARADAY cup or the sample, respectively. For the cluster deposition we choose a deceleration voltage at the onset of the cluster ion current decay, in this case, *e.g.*, + 10 V. Hence, a large part of the clusters gets the sample with low kinetic energy. Because the individual cluster machine parameters, differ usually from cluster mass to cluster mass and particularly from deposition to deposition, the optimal deceleration voltage changes in each experiment. This illustrates the second curve (symbol ▲ in figure 4.56).

In addition to the macroscopic potential given by the bias voltage the image potential of clusters with a single positive charging attracts them to the surface while approaching the sample substrate on a microscopic scale. This kinetic energy amounts to a few eV per cluster.

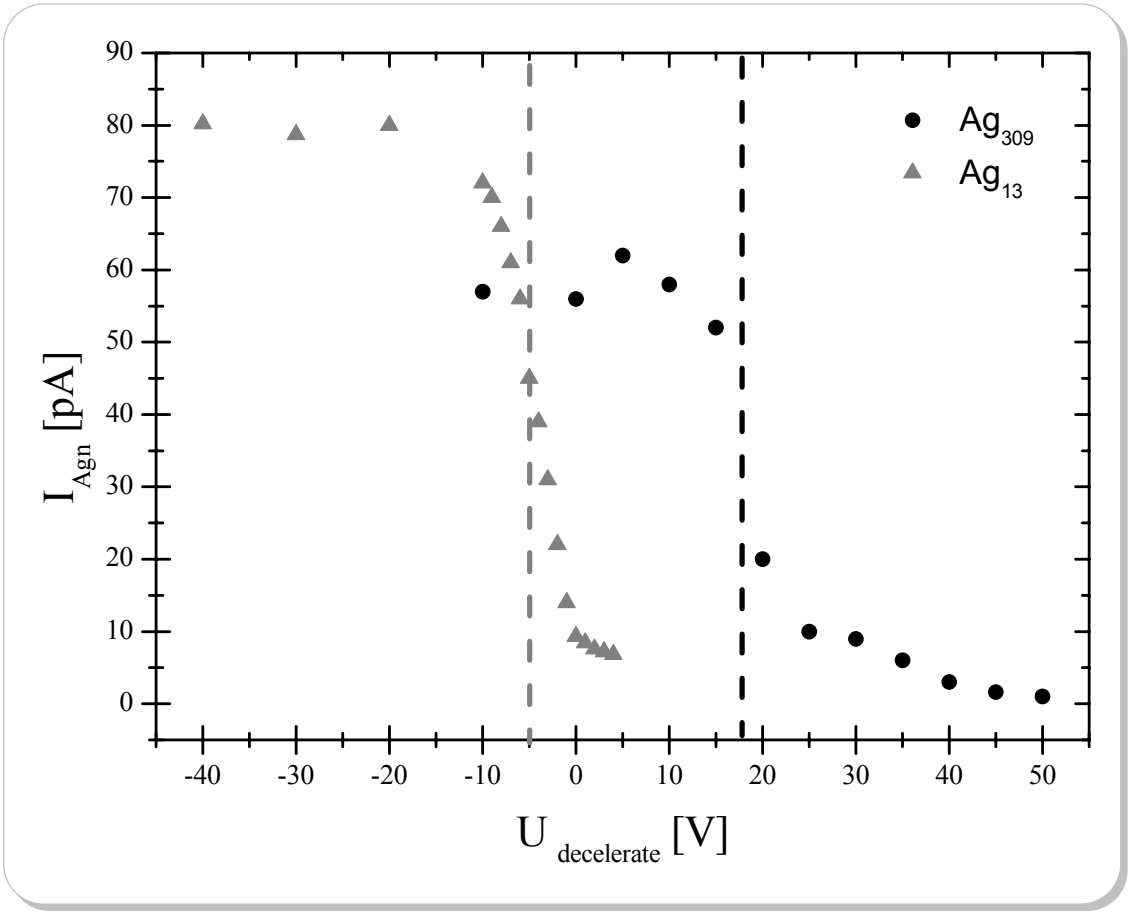

Figure 4.56 Cluster ion current for Ag^{+}_{n} clusters (n=13 and 309) depending on the bias voltage of the sample.

The cluster ion current decreases if the kinetic energy of the clusters is too low to reach the FARADAY cup.

4.1.5.3 Estimation of the Deposition Time

Within this section, we present an estimation of the deposition time exemplary for Ag_{40} clusters. We measure approximately 5 pA cluster ion current at the sample position. This results in:

Equation 4.24

$$1\mathrm{A} = \frac{1C}{s} \Rightarrow 5\mathrm{pA} = 5 \cdot 10^{-12} \frac{C}{s}$$

The clusters are single charged and carry the elementary charge $e = 1.6 \cdot 10^{-19} C$, which results in

Equation 4.25

$$5\text{pA} \triangleq \frac{5\cdot10^{-12}C}{1.6\cdot10^{-19}C} = 3.1\cdot10^{7}\ \text{ions/s}.$$

We estimated the deposition spot area by using the second small hole of the FC_{II} (see inset picture in figure 3.47) as follows: We start outside the beam where we do not measure any cluster current. Than we move the FC_{II} with its small hole until a very low cluster current is measurable. We mark the position of the FC_{II}, continue the movement wiping the cluster beam until the signal completely vanished, and note again the final position. From this two coordinates we calculated the diameter of the cluster beam and estimated a deposition spot of approximately $\left(2\cdot10^{-3}\text{m}\right)^2$. A suitable image size for STM measurements is an area of $\left(100\cdot100\right)\text{nm}^2 = 10^{-14}\text{m}^2$ herein after referred to as *standard picture size* (SPS). We then calculate the number of deposited clusters on an SPS.

From this, we get:

Equation 4.26

$$3.1\cdot10^{7}\ \text{ions/s}\cdot\frac{10^{-14}\text{m}^2}{\left(2\cdot10^{-3}\text{m}\right)^2} = 7.5\cdot10^{-2}\text{ions/s} \Leftrightarrow 13\text{s/ ion}$$

In order to reach 100 ions or clusters per SPS, we have to chose a deposition time of about 1300 s = 20 min.

In some other experiments, we reach cluster ion currents up to 90 pA, even for large masses, *e.g.*, Ag_{309}, which consequently leads to shorter deposition intervals. (see also typical maximum cluster currents in table 3.4)

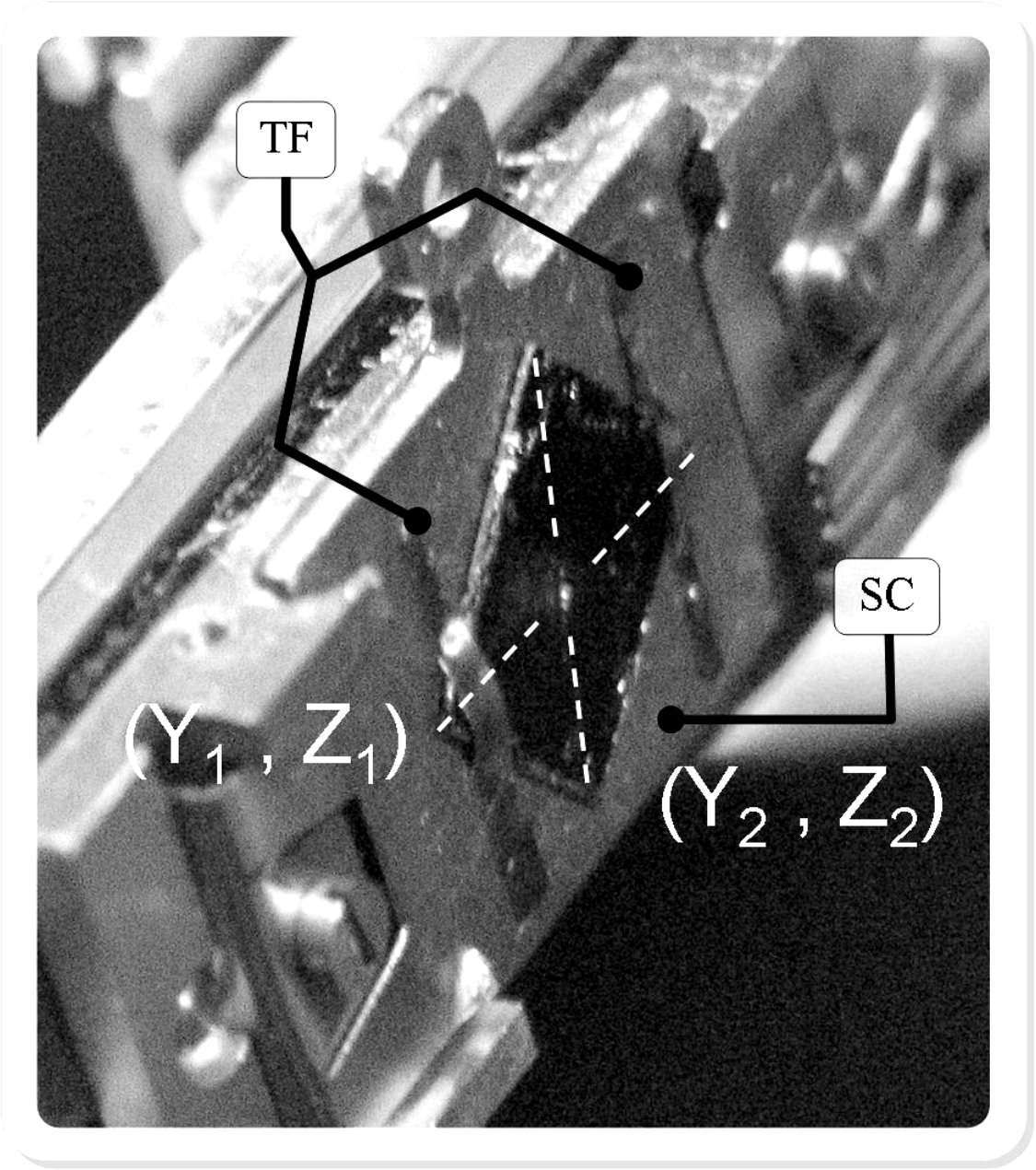

Figure 4.57 Picture of the heatable sample holder SH_H with an HOPG sample and laser spot. Tantalum foils (TF) and sample carrier (SC) can be identified in this picture. The laser indicates the approximate deposition area, which is set to the center of the HOPG substrate by using the coordinates of two edges (Y1, Z1) = (20.4 mm, 132.15 mm) and (Y2, Z2) = (14.8 mm, 137.2 mm). Hence the deposition position results in (x, y, z) = (22.9 mm, 20.4 mm, 137.2 mm). The angle φ of the sample is about 84° that is almost perpendicular to the cluster beam axis.

Chapter 5

RESULTS AND DISCUSSION

In the previous chapter, we described in detail the preparation of our sample systems. We introduced three different sample substrates (gold, lead, and graphite), explained two different methods to produce buffer layers (rare gases and C_{60}), and presented two procedures to place clusters onto these surfaces (metal island growth and deposition with the cluster machine). Hence, in this following chapter, we present the experimental results of our investigation of the different sample systems, and divide this chapter into four parts: In section 5.1, we will present and discuss first our photoemission studies of the so-called *free clusters on surfaces*. After that, we will proceed in section 5.2 to the results of our first experiments using the cluster deposition machine, namely the results of the deposition of small size-selected silver clusters. Finally, in section 5.3, we present our results of large size-selected silver clusters on rare gas layers and in section 5.4 the deposition of silver clusters on a C_{60} functionalized gold substrate.

5.1 Photoemission Studies of *Free Clusters on Surfaces*

During the construction and the setup of the cluster deposition machine, we used the existing SSF for some first studies for clusters on rare gas layers. To preserve the electronic and geometric properties of size-selected clusters after the collision with a surface, we plan to use buffer layers. In the case of rare gas buffer layers, one can use them for soft-landing (see 2.4.3.1, pp .73) as well as for the decoupling of the clusters from the substrate.

Therefore, we investigated several combinations of Au and Pb clusters, Ar and Xe films, and Au(111) and Pb(111) substrates. We differentiate between *symmetric systems* such as Pb clusters on rare gas on a Pb(111) substrate and *asymmetric systems* such as Au clusters on rare gas on a Pb(111) substrate. The nomenclature is as follows: cluster / rare gas / substrate; *e.g.*, Pb/Xe/Pb or Au/Xe/Pb.

5.1.1 Asymmetric Sample Systems

In this section, we start presenting the asymmetric cluster / rare gas / substrate systems:

- Au / 10 ML Xe / Pb,
- Au / 60 ML Xe / Pb, and
- Pb / 60 ML Xe / Au.

5.1.1.1 Au Clusters / 10 ML Xe / Pb(111)

To decouple the clusters from the surface we prepared different thicknesses of the rare gas layer. We started with Au clusters on 10 ML Xe on Pb(111). The FERMI-level onset of the gold clusters in the UPS spectra had the same energetic position as the pristine Pb(111) substrate as we measured before adsorption. We then transferred the cold sample into the analysis chamber and imaged the clusters with the STM at a temperature of 5 K.

Figure 5.58 and figure 5.59 show STM images of the gold clusters before and after desorption of the xenon. We describe the amount of gold as an effective film thickness, in this case 3.6 ML Au. We desorbed the Xenon by increasing the sample temperature to 100 K for a few minutes.

We averaged four different (50 x 50) nm^2 sized STM images to determine the cluster density before desorbing the Xe film and obtained (206 ± 14) clusters per SPS.

Stable imaging of larger sample areas was not possible. After the xenon desorption we were able to image four SPS areas with a cluster density of (204 ± 7) clusters per SPS. After the Xe desorption the clusters form larger aggregates, but we could still identify the individual clusters. In addition to the statistical errors given above, we have considered systematic errors for STM imaging, *e.g.,* the changing of the tip shape and the resulting distortion of the cluster shape by tip-cluster convolution [60]. Due to this effect, we may observe separated clusters as aggregates. We estimate that this will lead to systematic errors of at least of 10% for the cluster density. ANTONOV *et al*. [62] did not observe significant coalescence during desorption for a rare gas film thickness below 10 ML. Imaging clusters with a 10 ML xenon layer before desorption indicates that the clusters were not completely decoupled, but had some contact to the substrate. This is consistent with the position of the cluster FERMI edge in the corresponding UPS spectra. The thickness of a 10 ML xenon film is 2.48 nm and consequently in the same order of magnitude as the average height of the gold clusters, which is approx. 2 nm as we measured after the Xe film desorption. We assume that the clusters partly or totally immersed in the xenon film and established in this way the tunneling contact for imaging the clusters with STM.

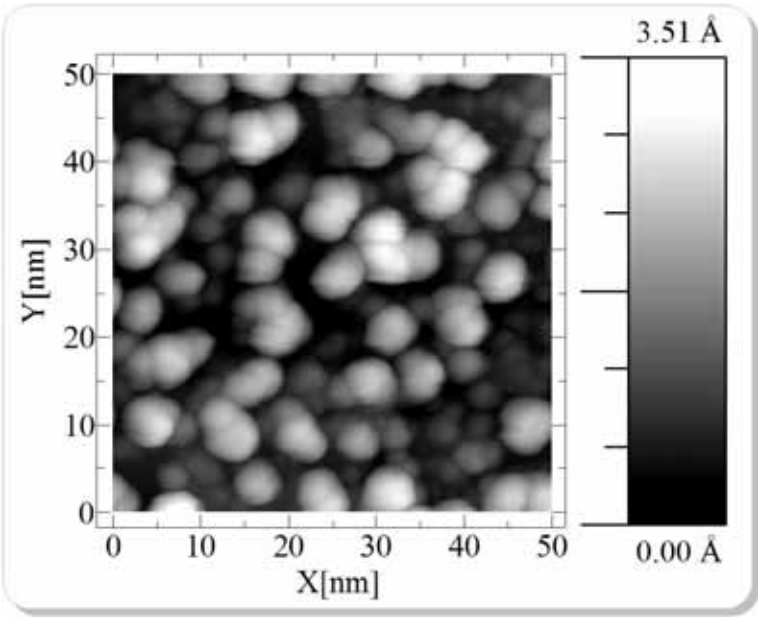

Figure 5.58 STM images (T = 5 K) for 3.6 ML Au on 10 ML Xe on a Pb(111) substrate before Xe desorption. Approx. 206 clusters per SPS. ($U_{tunelling}$ = 1.3 V / $I_{tunneling}$ = 10 pA).

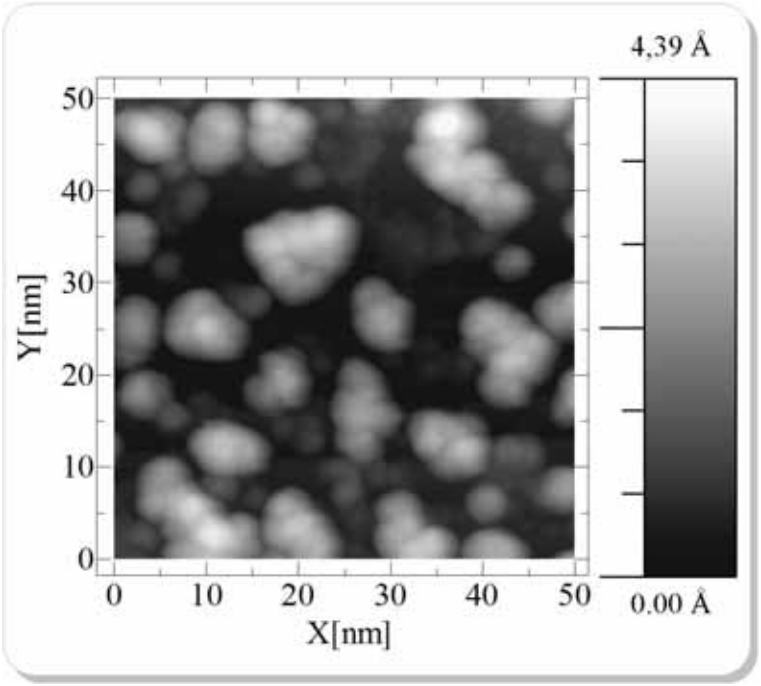

Figure 5.59 STM images (T = 5 K) for 3.6 ML Au on 10 ML Xe on a Pb(111) substrate after Xe desorption. Approx. 204 clusters per SPS ($U_{tunelling}$ = 1.5 V / $I_{tunneling}$ = 20 pA)

($U_{tunneling}$ = 1.5 V, $I_{tunneling}$ = 20 pA).

5.1.1.2 Au Clusters / 60 ML Xe / Pb(111)

In order to completely decouple the clusters geometrically and electronically from the substrate we use in all of the following experiments 60 ML of xenon to ensure that even immersed clusters continue to have no contact to the substrate. In order to check that no simple static charging of the xenon film was present, we investigated a sample with a xenon layer up to 160 ML thickness and did not see any change in the xenon spectra. For static charging, one expects a clearly visible shift of the Xenon $5p_{1/2}$-peak to lower energies. Figure 5.60 summarizes the results for the asymmetric system Au clusters on 60 ML Xe on Pb(111). We display - from bottom to top - UPS spectra at important steps in the preparation of the sample system. In the spectra of the pristine Pb(111) surface, the sharp FERMI edge of the lead substrate is located at the reference FERMI edge, which we set to 0 eV. After we adsorbed 60 ML xenon, the signal of the FERMI edge vanished. Then we evaporated gold onto the Xenon-covered surface in four steps and took UPS spectra after each evaporation step (we show two in figure 5.60 top). We observed a stronger growing FERMI edge with increasing amounts of evaporated gold, which shifts about -1.7 eV with respect to the reference FERMI energy. The same shift occurs for the onset of the d-band (-2.4 eV → -4.1 eV). The bottom of figure 5.60 shows the FERMI edge region of the spectra after each evaporation step. We used the spectra with different coverages mainly to confirm that the signal of the cluster features increases with coverage. We do not discuss the differences for the different coverages, but always measure the shift for the largest coverage of about 3 ML. We plan more quantitative studies for the cluster-size dependent shifts with mass-selected clusters. We found a pronounced FERMI edge in the spectra for 3 ML Au and a clearly visible shift of -1.7 eV. This was a surprisingly large shift. For cluster sizes of a few nanometers, the deviations to the bulk material should be small. However, we can explain it as we demonstrate in figure 5.61, which contains a schematic diagram for the FERMI edge shifts in the UPS spectra, which is in analogy to Photoemission of Adsorbed Xenon (PAX) (see sec. 2.2.3.1, pp 49) [49, 51].

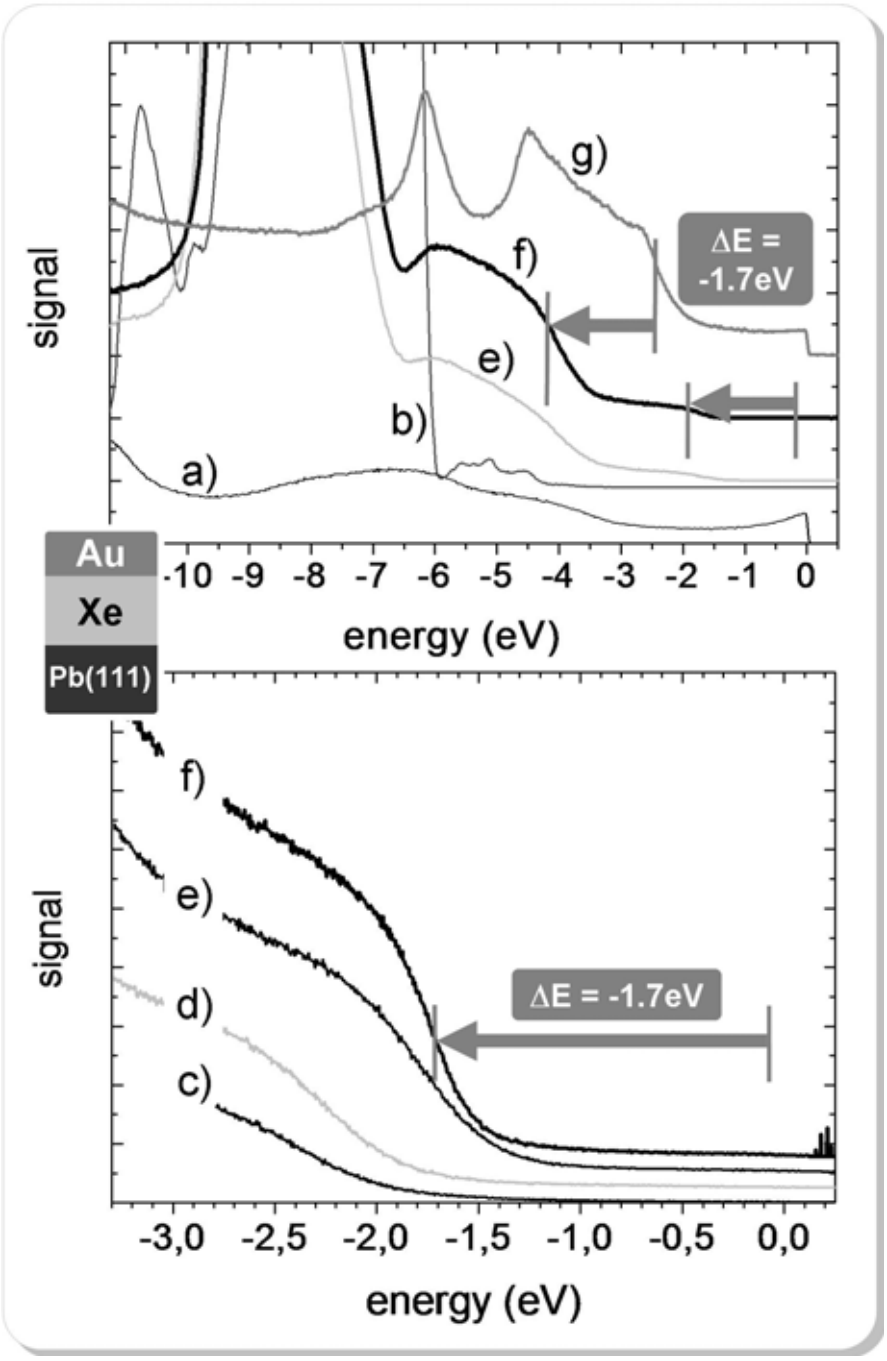

Figure 5.60 UPS spectra of Au/Xe/Pb(111).

(Top) UPS spectra: a) pristine Pb(111) surface, b) after xenon adsorption (60 ML), e) after evaporation of 1.8 ML Au on 60 ML xenon / Pb(111), f) with a total amount of 3 ML Au on 60 ML xenon / Pb(111) and g) after xenon desorption. (Bottom) FERMI edge spectra for different amounts of gold: c) 0.6 ML, d) 1.2 ML, e) 1.8 ML, and f) 3.0 ML Au on 60 ML xenon on Pb(111). Because of $\Phi_{Pb} < \Phi_{Au}$ the FERMI edge of the Au clusters shifted to *lower* energies, compared to the FERMI energy (0 eV) of the substrate.

In principle, the work function Φ is highly sensitive to changes concerning the surface. Therefore, it may be size dependent for small clusters. For the large cluster sizes we consider here, we assume that Φ for the cluster material is approximately the same as for the corresponding bulk material. The left side shows sample system Au/Xe/Pb we mentioned above together with the Pb(111) substrate. We measure FERMI energies E_F of Pb(111) and Au(111) that are equal to the reference FERMI energy of the apparatus. This is because the sample holder connects all metal substrates electrically to the apparatus body and therefore on earth potential, as we symbolize with the ground icon. The reference energy for the decoupled gold clusters on the Au/Xe/Pb sample is no longer the FERMI energy but the vacuum energy $E_{vac(Pb)}$ of the Pb(111) substrate. This is similar to the behavior of the Xenon $5p_{1/2}$ and $5p_{3/2}$ signals, which is the basis of PAX. In this way the existing work function difference $\Delta\Phi$ between Φ_{Au} and Φ_{Pb}, leads to a shift ΔE of the cluster FERMI edge. The work function of lead is smaller than the work function of gold resulting in a shift of the gold-cluster FERMI edge to lower energies $< 0\,\mathrm{eV}$. We mention here that other groups discussed this change of the reference energy for decoupled clusters in their studies [.77, .140]. But in those experiments they measured core level signals of the cluster material that might be affected by additional shift mechanisms, as, *e.g.,* core level shifts due to the large number of surface atoms in clusters [.141] or due to lattice strain [.142]. In our experiments, we observe further evidence for the decoupling of the clusters from the surface by measuring UPS during controlled sample heating. We continuously took UPS spectra while heating the sample from 50 K to 60 K at a rate of 0.2 K / min. (see figure 5.62). The shifted FERMI edge of Au clusters on xenon decreased constantly until it vanished completely. At the same time the FERMI edge of the Pb substrate and of clusters coupled to the substrate arise at the reference FERMI energy of 0 eV.

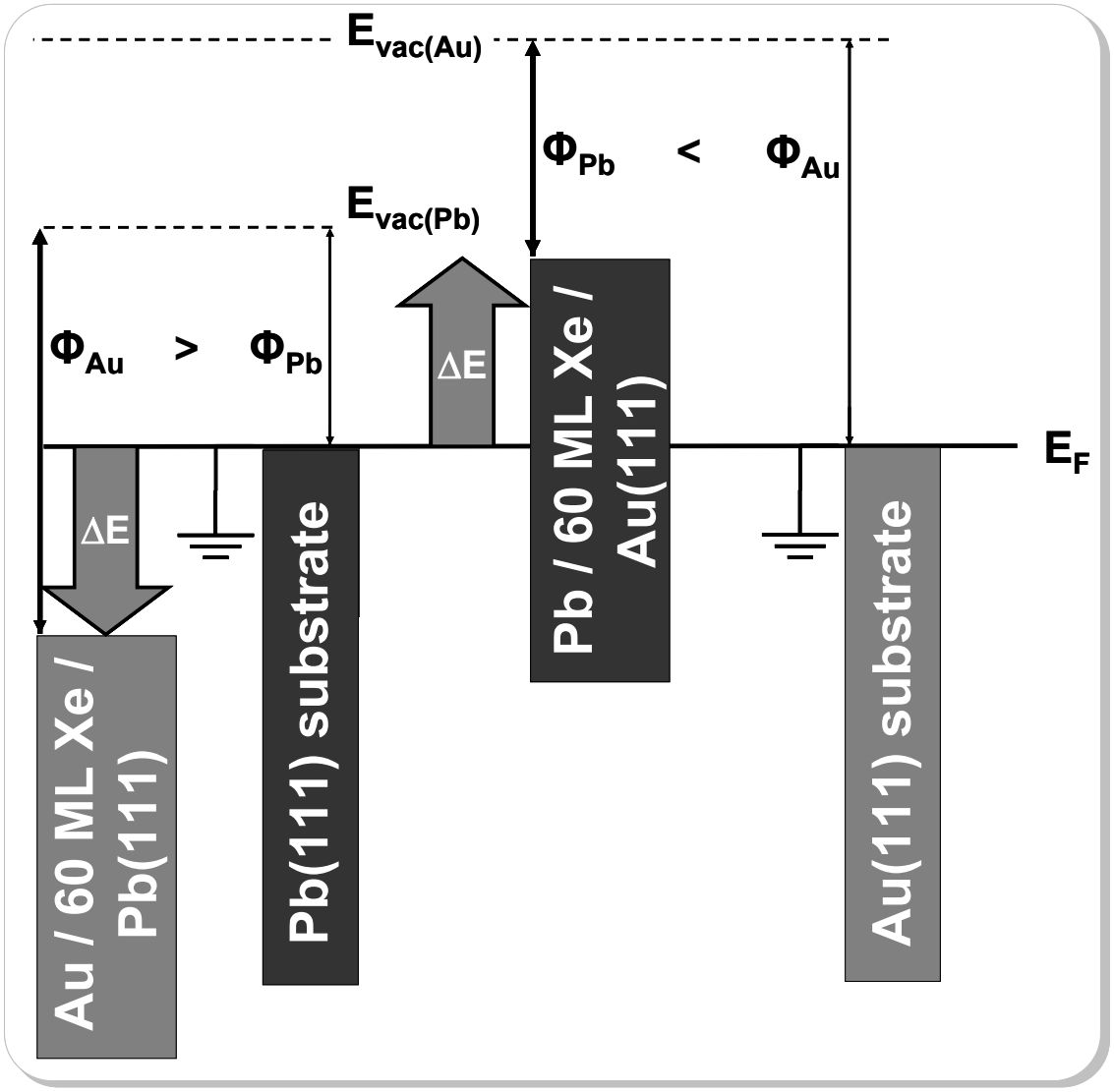

Figure 5.61 Schematic diagram for the FERMI edge shifts ΔE in our UPS spectra in analogy to Photoemission of Adsorbed Xenon (PAX) (see sec. 2.2.3.1, p. 49 and ref. [52]).

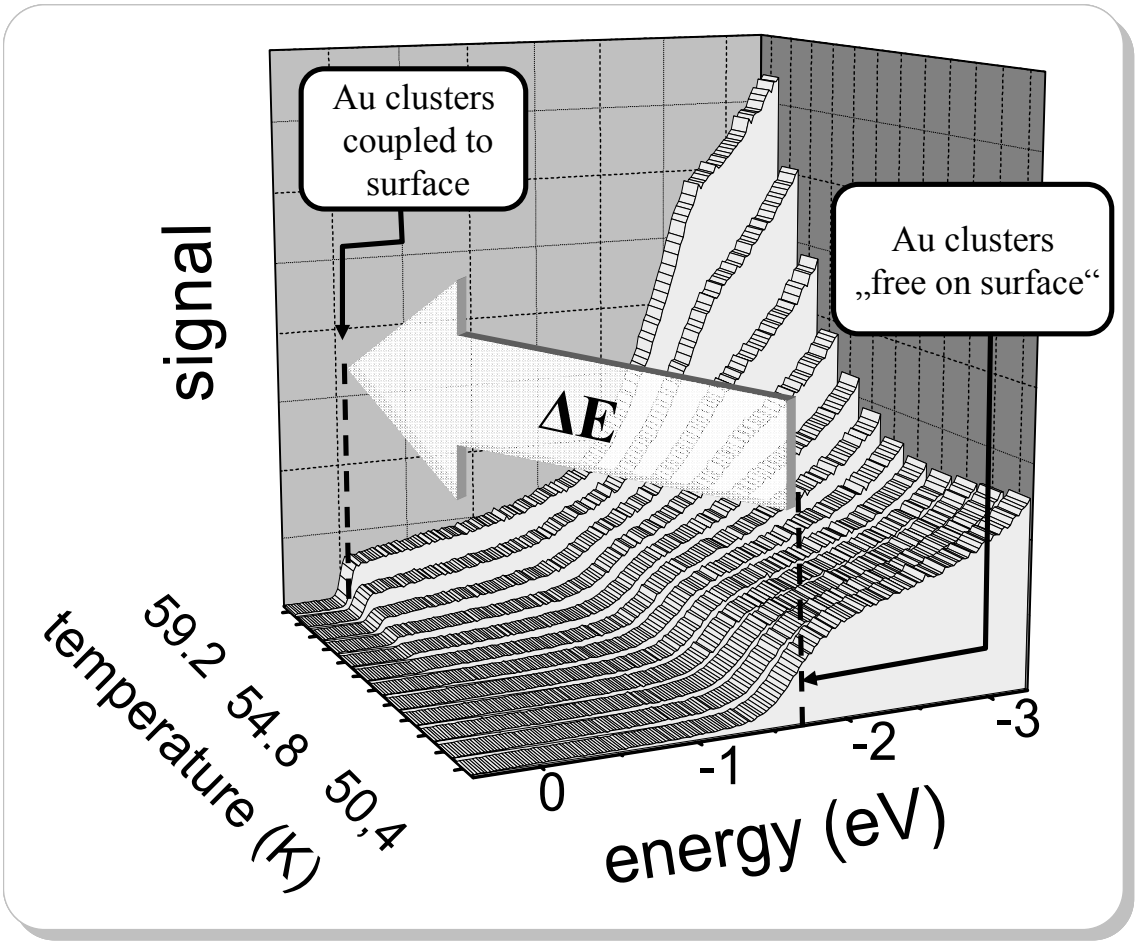

Figure 5.62 Change of the UPS spectra for Au Clusters on 60 ML Xe on Pb(111) during controlled sample heating.

We heat the sample from 50 K to 60 K at a rate of 0.2 K / min.. We observe a constant decrease of the shifted FERMI edge of Au clusters on xenon until it vanishes completely; while the FERMI edge of the Au substrate and of the clusters coupled to the substrate arise at the reference FERMI energy of 0 eV.

5.1.1.3 Pb Clusters / 60 ML Xe / Au(111)

Next, we try to confirm the explanation of the shifts due to the work function differences by investigating the inverse asymmetric system Pb on 60 ML Xe on Au(111). Here, we expect a large positive shift ΔE because of $\Phi_{Pb} < \Phi_{Au}$. Indeed, figure 5.63 shows the positive shift to higher energies we expected of about +1 eV. This is rather unusual for solid-state samples, because no one would expect a signal above the common FERMI

energy. Charging effects do not give an explanation, because positive charging due to electron emission would lead to a shift in the negative direction. However, we can give an interpretation in terms of decoupled clusters as figure 5.61 schematically depicts. The right hand side shows the Au(111) substrate referenced to the FERMI energy E_F together with the sample system Pb/Xe/Au. The xenon layer decouples the Pb clusters from the substrate. Hence, the new reference energy is the no longer the FERMI energy but the vacuum energy $E_{vac(Au)}$ of the Au(111) substrate. The work function difference $\Delta\Phi = \Phi_{Pb} - \Phi_{Au}$ leads to a shift of the lead-cluster FERMI edge to higher energies, because of $\Phi_{Pb} < \Phi_{Au}$. To compare both asymmetric sample systems, figure 5.64 illustrates the observed shifts in one diagram.

As we discuss above, the work function difference predicts the same absolute value for both of the asymmetric systems. We can explain the different absolute sizes of the FERMI edge shifts for Au/Xe/Pb and Pb/Xe/Au by an additional effect: the cluster charging energy in the final state of the photoemission process (light grey arrows) [11, 56, 57, and 143]. In both cases, the contribution of this charging energy is negative. However, in the case of Pb/Xe/Au the observed absolute shift is $\Delta\Phi - E_C$ compared to $\Delta\Phi + E_C$ for Au/Xe/Pb.

Because of the broad cluster size distribution, one could not define the charging energy quantitatively, but has to consider a corresponding distribution for E_C.

This can also explain the significantly larger width of the FERMI edge for the cluster signal as compared to the sharp FERMI edge for the substrates.

Due to the nanometer size of the clusters, one expects a charging energy of the order of 0.1 eV. The measured work functions of the clean Au(111) substrate and the clean Pb(111) substrate we use in figure 2.13 are 5.44 eV and 4.05 eV, respectively. This would correspond to the work function difference of $\Delta\Phi \approx 1.4\,\text{eV}$.

After we adsorbed the Xe film, the work function decreased for both substrates. The shift of -0,32 eV for 1 ML Xe/Au(111) [144] is only slightly smaller than the work function

change for the larger film thicknesses up to 160 ML as considered here (see figure 2.13). This agrees with the observation that the work function change saturates after a few monolayers [145]. The work function difference changed only slightly after the Xe adsorption.

$$\Delta\phi = \phi_{Xe/Au} - \phi_{Xe/Pb} \approx 5.0\,eV - 3.9\,eV \approx 1.1\,eV\,.$$

This is smaller than the size of the $\Delta\Phi$ - arrows in figure 5.64. With $\Delta\Phi$ = 1.1 eV one would only need a small charging energy for the lead clusters, but an unrealistic large $E_C \approx 0.6$ eV for the gold clusters. However, for the gold clusters we cannot exclude some static charging, as we will discuss below.

5.1.2 Symmetric Sample Systems

In case of the symmetric sample systems Pb/Xe/Pb and Au/Xe/Au, we expect no large work function difference

$$\Delta\Phi = \Phi_{clusters} - \Phi_{substrate} \approx 0\,.$$

It is not *a priori* clear whether we have to take Φ for the substrate and / or the clusters, with or without the Xe induced decrease, into account. In addition, we may identify the cluster work function with bulk surfaces of different crystalline orientations. This leads to some uncertainty or distribution of $\Delta\Phi$ in the order of 0.3 eV. Similar variations have also occurred for $\Phi_{substrate}$ in different experimental runs, *e.g.,* with different preparation procedures. However, this does not change significantly the cluster-induced shifts as figure 5.65 shows (top). We did not detect a large shift of the FERMI edge of the Pb clusters on xenon on lead (system Pb/Xe/Pb). An explanation of the small negative shift of about -0.2 eV could be the charging energy E_C. Nevertheless, there is also some signal also above $E_F = 0$ eV which one cannot explain by E_C but may be due to contributions with $\Delta\Phi < 0$.

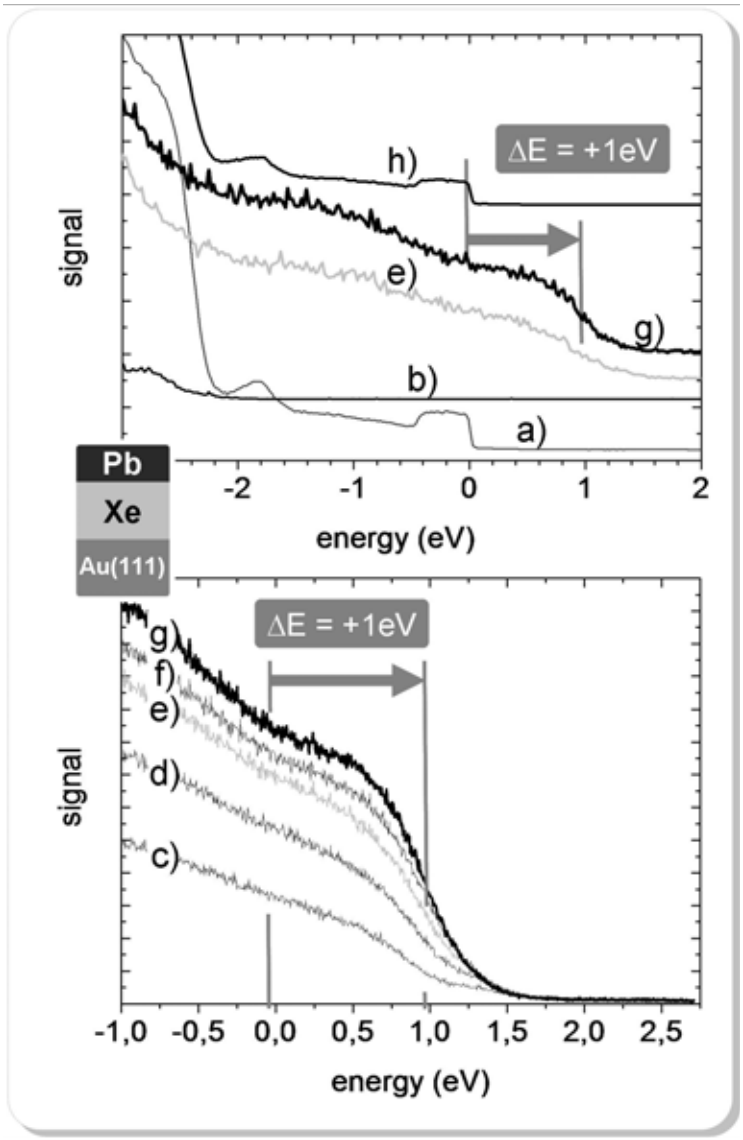

Figure 5.63 UPS spectra for Pb/Xe/Au(111).

(Top) UPS spectra: a) pristine Au(111) surface, b) after xenon adsorption (60 ML), e) after evaporation of 1.5 ML Pb on 60 ML xenon / Au(111), g) with a total amount of 2.5 ML Pb on 60 ML xenon / Au(111), and h) after xenon desorption. The box-shaped structure from about -0.5 eV to 0 eV for samples a) and h) is due to the angle-integrated signal of the Shockley surface state on Au(111). The fact that it is still visible for sample h) after the Xe desorption shows that the sample stayed rather clean during all the preparation steps.(Bottom) FERMI edge spectra for different amounts of lead: c) 0.5 ML, d) 1.0 ML, e) 1.5 ML, f) 2.0 ML, and g) 2.5 ML Pb on 60 ML xenon on Au(111). Because of $\Phi_{Au} > \Phi_{Pb}$ the FERMI edge of Pb clusters shifts to *higher* energies compared to the FERMI energy (0 eV) of the substrate.

The behavior of the other symmetric sample system Au/Xe/Au is different. The UPS results (see figure 5.65 bottom) show a large FERMI edge shift of 1.4 eV though there should be no significant work function difference between cluster material and the substrate. In order to check for potentially static charging of the sample in this experimental run, we investigated first 160 ML Xe/Au(111). In the UPS spectra, we observe no shift of the Xe $5p_{1/2}$-peak and take this as an indication that no static charging of the clean Xe film occurs up to this thickness as we mentioned above.

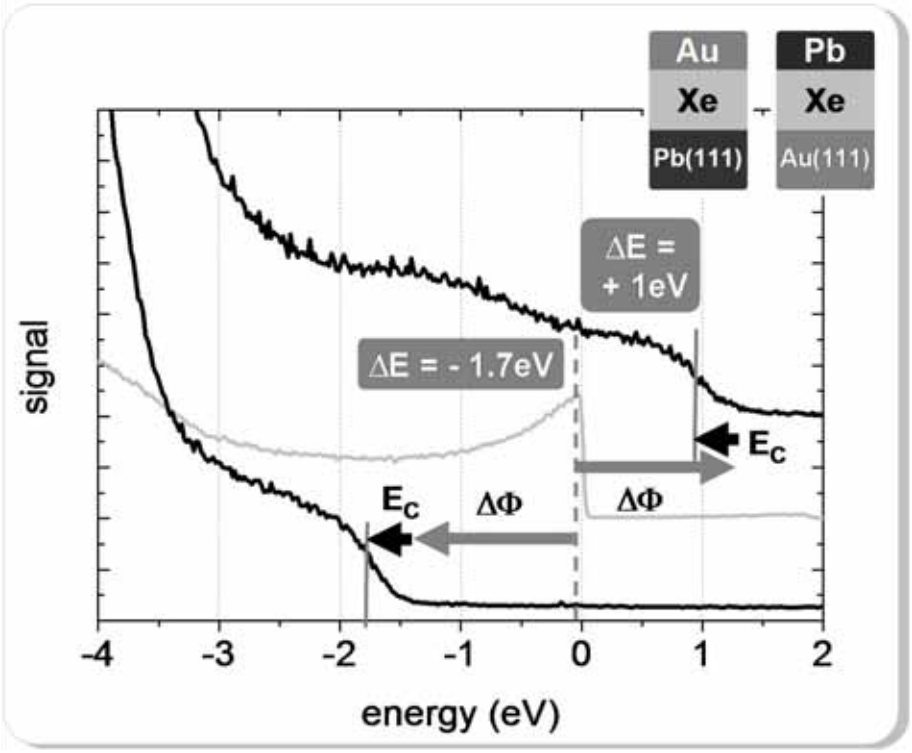

Figure 5.64 Shift of the FERMI edge due to the work function difference ΔΦ (dark grey arrows) between Au and Pb.

The cluster charging energy (light grey arrows) explain the difference between the shifts for Au/Xe/Pb and Pb/Xe/Au. A broad cluster size distribution prohibits an exactly defined E_C. We discuss the modified interpretation with ΔΦ = 1.1 eV, as given by the measured work function difference for the two substrates, the smaller charging energy in the case of Pb/Xe/Au and some static charging for the Au/Xe/Pb sample in the text above.

However, we do see a significant shift of the $5p_{1/2}$-peak when we evaporated Au onto this surface. The shift becomes already visible at a gold coverage of 0.3 ML – with about 0.5 eV - and increases with the gold coverage. We then covered the sample with additional layers of Xe after the Au deposition, resulting in even larger shifts that can amount to several eV. We observe in this case some variation with time and the intensity of the UV light, a behavior typical for static sample charging.

We can explain these results by assuming the Xe film to have some residual conductivity preventing the growth of static charges, even for large film thicknesses. At least partially, it may be due to photoconductivity induced by the He-discharge lamp [.146]. In contrast, we observe strong static charging in case of a bare Ar film with a thickness of 60 ML starting at film thicknesses above 10 ML. This is possibly connected to the larger gap for Ar (14.15 eV) as compared to Xe (9.3 eV) [.146]. Differences for the charge transport in films of the different rare gases were studied in the past, *e.g.*, with photoelectron spectroscopy [.147]. However, a gold coverage seems to reduce the conductivity of the Xe film, so that we cannot exclude some static charging in this case. We mention here that, in contrast to the samples with Pb clusters, we also observe the aforementioned shift of the Xe $5p_{1/2}$-peak for the Au/Xe/Au and Au/Xe/Pb samples with a 60 ML xenon film. So far, we have to assume that the large shift with respect to Au/Xe/Pb may partly be due to static charging as well, prohibiting a quantitative interpretation of results in view of work function changes, and charging energies.

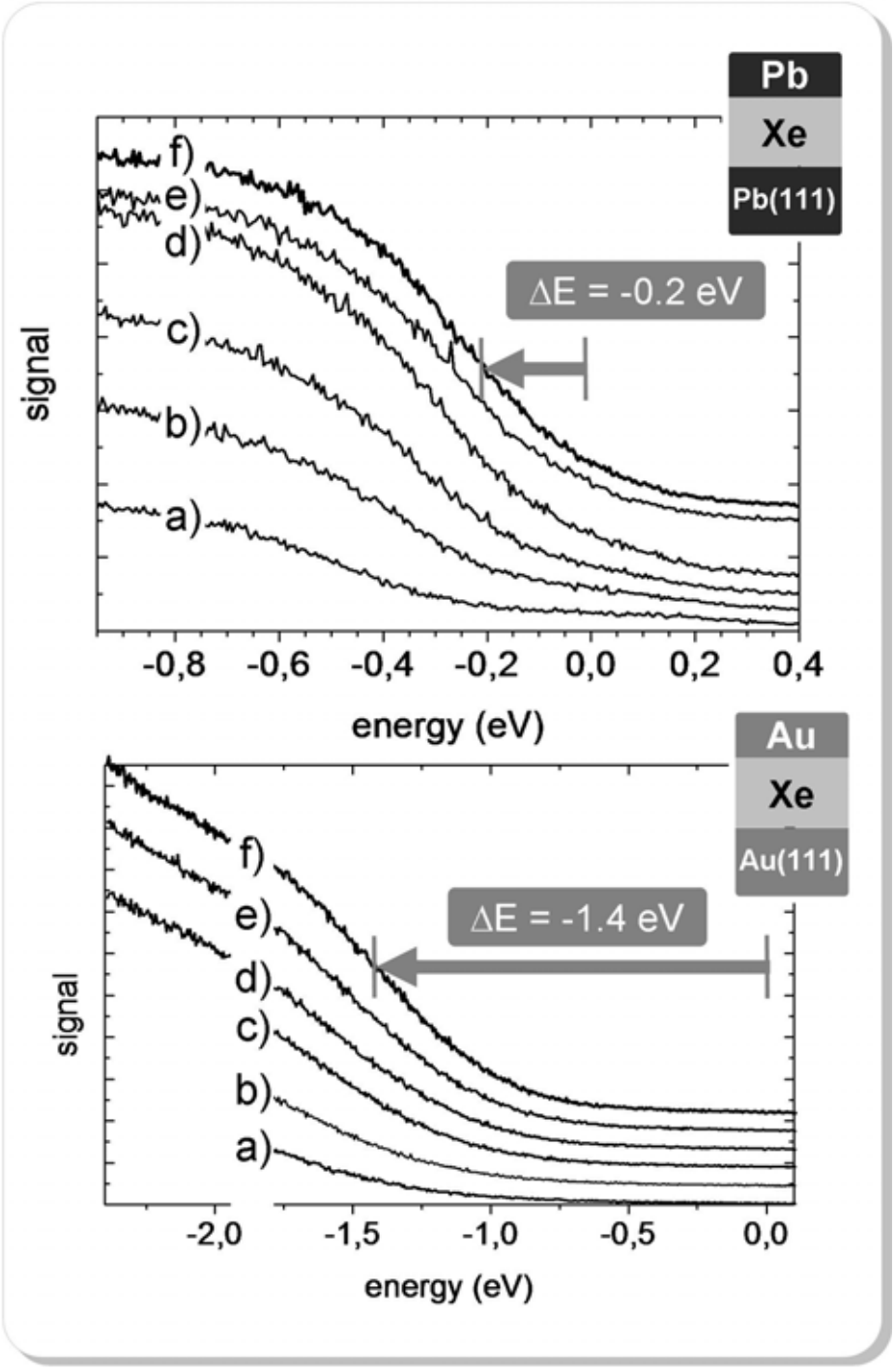

Figure 5.65 Symmetric samples systems Pb/Xe/Pb(111) and Au/Xe/Au(111).

(Top): FERMI edges for different amounts of lead on 60 ML xenon on Pb(111). The cluster charging energy E_C explains the small shift because of $\Delta\Phi \approx 0$. (Bottom) FERMI edges for different amounts of gold on 60 ML xenon / Au(111): a) 0.7 ML, b) 1.0 ML, c) 1.4 ML, d) 1.7 ML e) 2.1 ML, and f) 2.4 ML. Static charging explains, at least partially the large shift (see text for details).

Nevertheless, this does not alter our qualitative interpretation that static charges cannot cause, *e.g.*, the positive shift in case of the Pb/Xe/Au sample. We expect to conduct a quantitative analysis in future experiments with mass-selected clusters with better-defined charging energies.

5.2 STM Studies of Small Size-selected Clusters on HOPG

For several, mostly experimental, reasons we chose Ag clusters on an HOPG substrate to become the starting point for our deposition experiments of mass-selected clusters. At first, the properties of HOPG we describe in section 4.1.3.3 (p. 118) promised to be a well suitable and particularly easy to handle sample substrate. Furthermore, the deposition of mass-selected Ag clusters with varying kinetic energy onto HOPG is well known from literature, which gives us the opportunity to test the performance of our cluster machine and compare the new results with former results of CARROLL *et al*. [104].

5.2.1 Experimental Results

We deposited the cluster sizes Ag_{40}, Ag_{55}, and Ag_{80} at room temperature (RT) onto the freshly prepared HOPG sample (see sec. 4.1.3.3, p. 118) with a rather high kinetic energy of about 800 eV and investigated them at 77 K with the STM.

5.2.1.1 Ag_{40} / HOPG

First, we optimized the cluster machine, in order to deposit the mass of Ag_{40} (4126 amu). We measured a cluster ion current of about 6.3 pA. Therefore, a deposition time of t_D = 20 min is suitable to produce approximately 100 clusters per SPS (see calculation of clusters per area in section 4.1.5.3, pp 127). A sample bias of – 800 V resulted in 20 eV kinetic energy per atom. After the deposition interval, we investigated the sample at 77 K with the STM and measured the cluster ion current again with the FARADAY Cup. The

slightly lower current of about 2.8 pA could be due to some instability of the voltage sources and consequently small changes of the cluster beam focus.

Table 5.7 summarizes the relevant deposition parameters. The whole parameter set appears in the appendix (see table 7.16, appendix 7.3.1, p. 199).

3RD DEPOSITION – Ag_{40} CLUSTERS / HOPG			
Deposition time t_D [min.]	20	Power P_{source} [watt]	5
Sample bias U_{sample} [V]	- 800	Temperature T_{sample} [°C]	RT
Frequency f [Hz]	223569.70	Waiting time t_w [µs]	2
Mass m [amu]	4126	Cluster current I_{bd} (before deposition) [pA]	6.3
Flux Φ Ar / He [sccm/sccm]	80 / 200	Cluster current I_{ad} (after deposition) [nA]	2.8

Table 5.7 Deposition parameters for the sample system Ag_{40} on HOPG.

Figure 5.66 shows an STM image of the Ag_{40} on HOPG sample. We observe several objects with heights between 0.9 nm and 2.0 nm and an average height of 1.33 nm. Compared to the heights we calculated using the truncated sphere model [30], we estimate cluster heights in the order of 0.8 nm (for a detailed calculation see section 2.4.1, pp 60). With the STM, we observed cluster heights significantly higher than calculated. Due to the broad height distribution and the unexpected low cluster density, we can explain this with a coalescence of the clusters during or after the deposition.

Because of the stable imaging of the clusters on HOPG, we assume a pinning of the clusters to the surface, due to the high kinetic energy. In fact, defects became visible after the displacements of clusters by the STM tip (see figure 5.67).

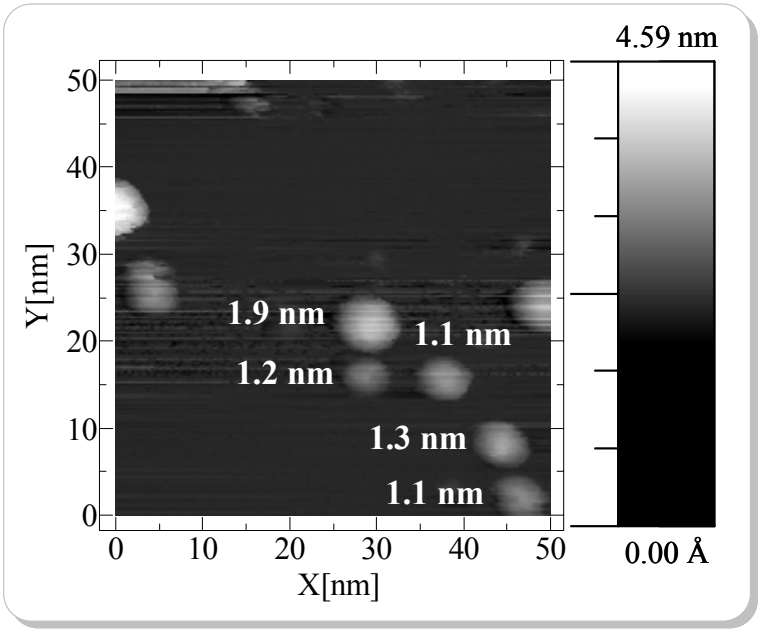

Figure 5.66 STM image of Ag_{40} clusters deposited onto an HOPG substrate.

($U_{tunelling}$ = 1.5 V / $I_{tunneling}$ = 0.01 nA).

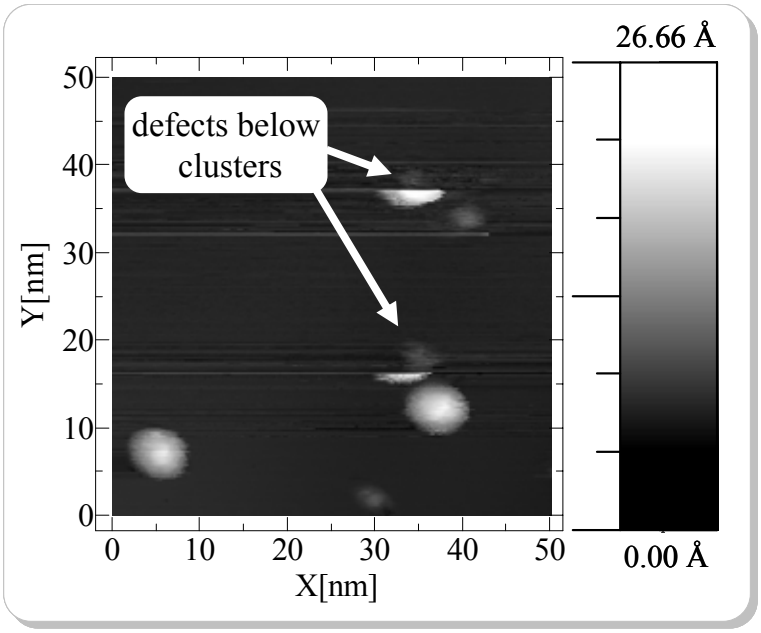

Figure 5.67 Defects became visible after the displacement of the Ag_{40} clusters by the STM tip.

($U_{tunelling}$ = 1.5 V / $I_{tunneling}$ = 0.01 nA).

Because we never found clusters beyond a radius of 0.5 mm around the center of the deposition spot, we estimate the diameter of the cluster beam spot to approximately 1 mm. This fits the estimated cluster-beam-spot size we measured using the small hole of the FARADAY Cup (see sec. 3.2.5.1, p. 100).

5.2.1.2 Ag_{55} / HOPG

Analogous to the experiment mentioned in the previous section, we deposited the Ag_{55} clusters onto the HOPG substrate. The most relevant deposition parameters summarizes table 5.8. In this experiment, we measured a cluster ion current of about 5.48 pA before and 2.6 pA after the deposition. We deposited a similar amount of Ag_{55} clusters, therefore we chose again a deposition time of 20 min.

Figure 5.68 represents a typical STM image of the Ag_{55} / HOPG sample. We see no single clusters on step edge free areas, because the clusters aggregate either to larger islands of partially coalesced Ag_{55} clusters (see figure 5.68), or adhere partially coalesced at step edges. We estimate cluster heights for Ag_{55} clusters in the order of 0.9 nm according to equation 2.20:

$$h_{Ag_{55}}^{ts} = \sqrt[3]{V_{Ag_{55}} / 1.152} = 0.93\,nm\,.$$

The cluster heights we determined experimentally are approximately in the same order of magnitude, *i.e.* between 0.6 nm and 1.0 nm high. Some clusters seem to be coalesced to larger objects. We could identify clusters, which we measure even smaller than the calculated cluster height for a single Ag_{55} cluster, with cluster fragments.

The height of the aggregated clusters we observed on step edge free areas (see figure 5.69) showed heights between 1.7 and 3.4 nm. This is a significantly larger height than the heights of clusters at step edges (see figure 5.68) and must be due to a stronger coalescence.

The kinetic energy of 14.5 eV per atom is probably not high enough to pin the clusters to the surface. These results are qualitatively consistent with the findings of PALMER'S

group in ref. [104], where they find out a pinning threshold at a kinetic energy of 10 eV per atom.

4TH DEPOSITION – Ag_{55} CLUSTERS / HOPG			
Deposition time t_D [min.]	20	Power P_{source} [watt]	5
Sample bias U_{sample} [V]	- 800	Temperature T_{sample} [°C]	RT
Frequency f [Hz]	186267	Waiting time t_w [µs]	3
Mass m [amu]	5948	Cluster current I_{bd} (before deposition) [pA]	5.48
Flux Φ Ar / He [sccm/sccm]	80 / 200	Cluster current I_{ad} (after deposition) [nA]	2.6

Table 5.8 Deposition parameters for the sample system Ag_{55} on HOPG.

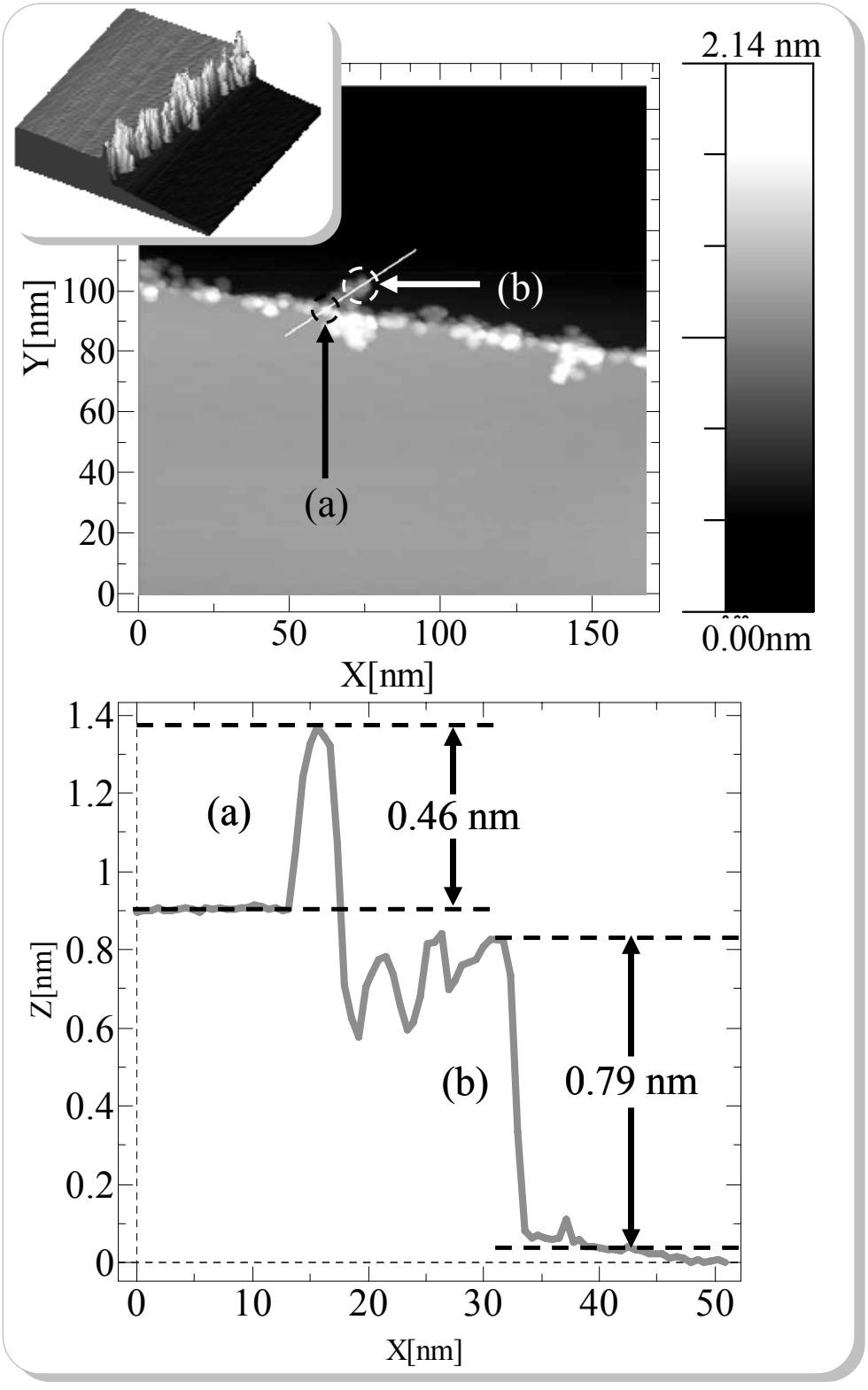

Figure 5.68 STM image of Ag_{55} clusters deposited onto an HOPG substrate.

($U_{tunelling}$ = 1.8 V / $I_{tunneling}$ = 0.01 nA).

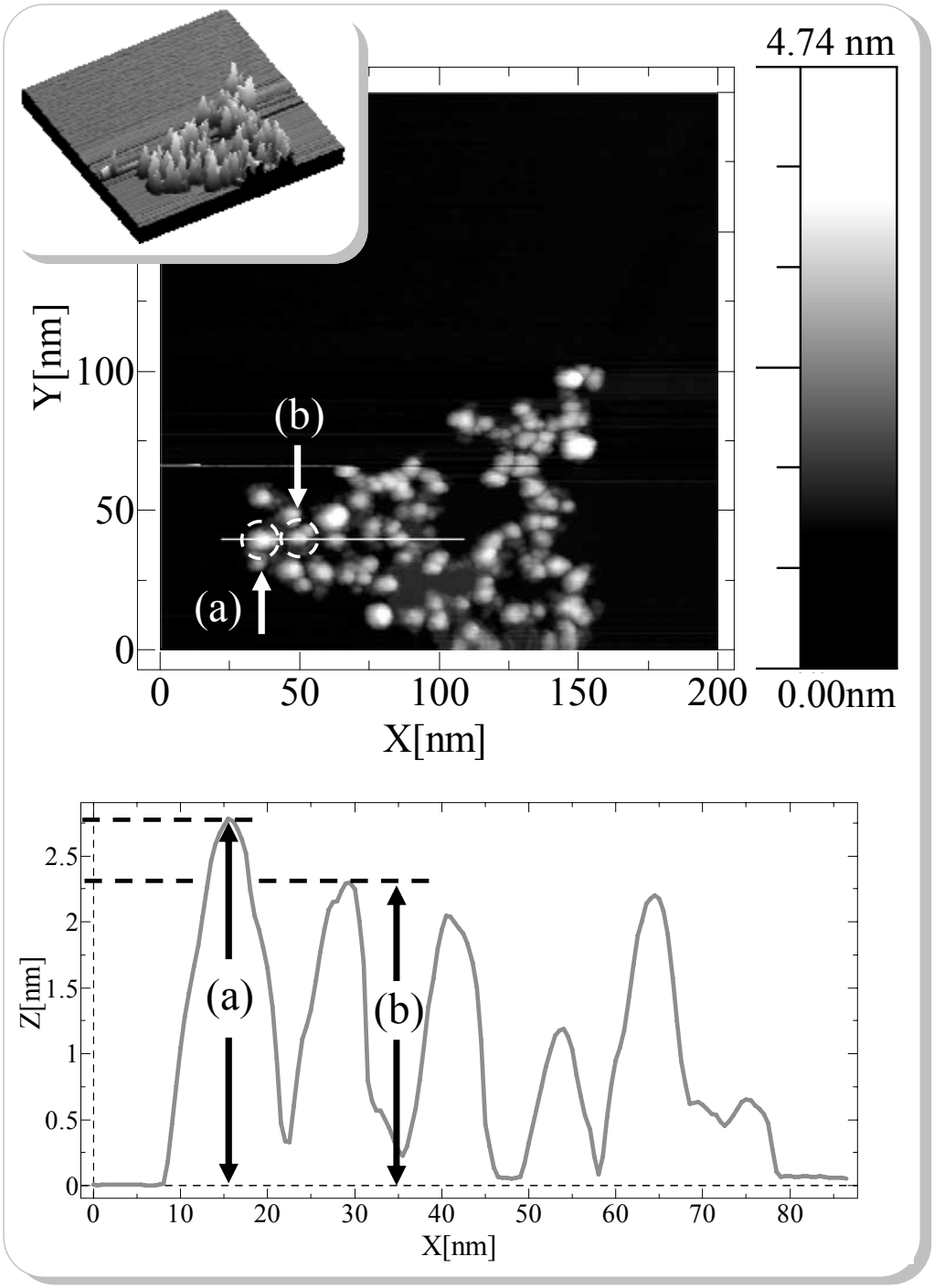

Figure 5.69 STM image of Ag_{55} clusters deposited onto an HOPG substrate. (Bottom) Line profile of some clusters (a) = 2.77 nm, (b) = 2.29 nm. ($U_{tunelling}$ = 1.8 V / $I_{tunneling}$ = 0.01 nA).

5.2.1.3 Ag_{80} / HOPG

For the last experiment within this deposition series we chose Ag_{80} clusters. An overview of the deposition parameters displays table 5.9. In this case, we found almost all clusters coalesced at the step edges of the HOPG substrate. We imaged several sample areas similar to the one we depict exemplarily in figure 5.70. The geometrically calculated height for Ag_{80} clusters is

$$h_{Ag_{80}} = \sqrt[3]{V_{Ag_{80}} / 1.152} = 1.06\,nm\,.$$

The measured cluster height, lies between 2 nm and 3.5 nm, which are significantly higher than the calculated.

5TH DEPOSITION – AG_{80} CLUSTERS / HOPG			
Deposition time t_D [min.]	20	Power P_{source} [watt]	5
Sample bias U_{sample} [V]	- 800	Temperature T_{sample} [°C]	RT
Frequency f [Hz]	154585.10	Waiting time t_w [µs]	3
Mass m [amu]	8649	Cluster current I_{bd} (before deposition) [pA]	3.4
Flux Φ Ar / He [sccm/sccm]	80 / 200	Cluster current I_{ad} (after deposition) [nA]	2.9

Table 5.9 Deposition parameters for the sample system Ag_{80} on HOPG.

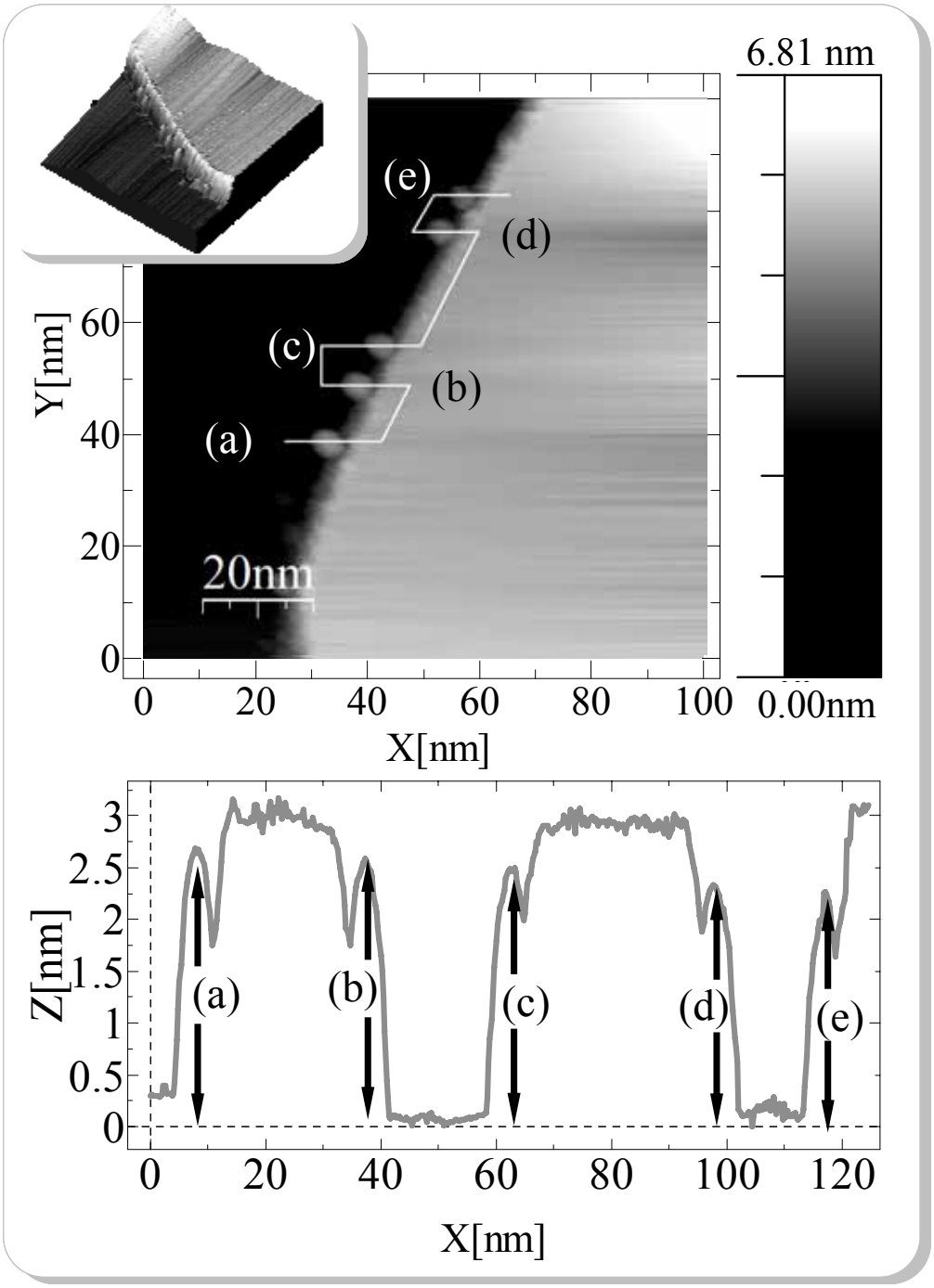

Figure 5.70 STM image of Ag_{80} clusters deposited onto an HOPG substrate.

(Bottom) Line profiles. (a) = 2.4 nm, (b) = 2.5 nm, (c) = 2.4 nm, (d) 2.2 nm, and e =2.1 nm. ($U_{tunelling}$ = 1.4 V / $I_{tunneling}$ = 0.01).

5.2.2 Discussion

These first deposition experiments represent a successful performance test of the setup of the cluster deposition machine. We imaged Ag_{40} clusters on HOPG, which we observed pinned to the surface. In this case, the clusters produced defects due to the high kinetic energy of about 20 eV per atom and stick to their defects. We were able to visualize these defects by displacing the Ag_{40} clusters by the STM tip. The second (Ag_{55}) and the third (Ag_{80}) sample show neither pinned clusters nor defects. We gather from this observation, that already the kinetic energy of Ag_{55} with 14.5 eV is not high enough for the cluster pinning. With this, we can verify the threshold behavior for pinning from ref. [104].

The coalesced Ag_{55} and Ag_{80} clusters we observed mainly at step edges speak for a high diffusion rate of the clusters on the surface. The experimentally determined cluster heights presented a curious role of the Ag_{55} clusters:

$$h_{Ag_{55}} < h_{Ag_{40}} < h_{Ag_{80}}$$

Furthermore, only for Ag_{55} clusters we observed some areas where their height remains almost constant (see figure 5.69). This may indicate the formation of islands of aggregated clusters due to the closed shell geometric structure of Ag_{55}, which exhibit, like other magic cluster sizes (see sec. 2.4.2.2, pp 66) a very high stability (see also, *e.g.*, [148]). Of course, with these results we can only give one possible interpretation, which we have to confirm in future with additional experiments.

Moreover, the position of the Ag_{80} clusters with respect to the step edge is interesting. As we discussed in section 2.3.1 (pp 56) grown clusters prefer a position overlapping the step edge (see figure 2.17 (c) and ref. [30] published within [55]). Nevertheless, the Ag_{80} clusters lay exclusively below the step edge, which is clearly visible in figure 5.70, especially in the three dimensional view in the top left corner. This is a further evidence for the high mobility of the clusters on the HOPG surface and the deposition of size selected clusters, because only multiple step edges with a height in the order of the cluster height

act as nucleation center. In contrast to single atoms evaporated onto a substrate to produce clusters by metal island growth, the EHRLICH-SCHWÖBEL barrier [.149, .150, .151, .152, and .153] does not stop the movement of Ag_{80} clusters, in contrast to, e.g., Ag_{55} clusters (see figure 5.68) or grown clusters in nanopits (see sec. 2.3.1, pp 56) which nucleate on both sides of the step edge. According to this observation, we imaged four areas with SPS with single and double step edges without any clusters.

5.3 Spectroscopy of Large Size-Selected Clusters on Xe on HOPG

After the deposition of mass-selected clusters became possible (see sec. above), we extended our studies of clusters produced by metal island growth to the study of size-selected clusters. In the following sections, we present first results of UPS measurements, which we will use in future to determine the charging energy quantitatively.

5.3.1 Experimental Results

In contrast to the cluster / rare gas / substrate systems, we presented in section 4.1.5.1 (pp 125) we now focus on size-selected cluster experiments. As a sample, we used an HOPG substrate freshly prepared under UHV conditions as we described in section 4.1.3.3 (pp 118). We use HOPG instead of a metal substrate, due to the formerly planed UPS measurements after the rare gas desorption. In this case, we would have preferred HOPG, due to its structure-less UPS spectrum.

We cooled the sample holder down to a temperature of $T_{sample} = 30$ K. To determine the reference FERMI energy of the apparatus, we measured the sharp FERMI edge of the tantalum foil as we depict in figure 5.71 (a), which we used to attach the HOPG sample to the sample carrier (see figure 4.57, p. 129). Afterwards, we adsorbed approximately 10 ML Xe onto this sample using the controlled rare gas adsorption we explain in section 4.1.4.1

(pp .119). We could not adsorb more than 10 ML Xe due to the weak thermal coupling of the HOPG to the sample holder, and consequently $T_{sample} > 30$ K. As we display in figure 5.71 (b) the bare xenon film shows as usual no structures at the FERMI edge. Finally, we deposited silver clusters of the size $Ag_{2130\pm21}$ onto the xenon covered HOPG substrate with the parameters collected in table 5.10. After that, we observed a slightly shifted, rounded silver cluster FERMI edge, which shows figure 5.71(c). We discuss this result in the next section.

9^{TH} DEPOSITION – $AG_{2130 \pm 21}$ CLUSTERS / 10 ML XE / HOPG			
Deposition time t_D [min.]	30	Power P_{source} [watt]	5
Sample bias U_{sample} [V]	-50	Temperature T_{sample} [K]	30
Frequency f [Hz]	30092.9	Waiting time t_w [µs]	16.62
Mass m [amu]	230000	Cluster current I_{bd} (before deposition) [pA]	0.98
Flux Φ Ar / He [sccm/sccm]	85.8 / 136	Cluster current I_{ad} (after deposition) [nA]	0.88

Table 5.10 Deposition parameters for the sample system $Ag_{2130\pm21}$ on 10 ML Xe on Au (111).

The entire parameter set is displayed in table 7.23 (sec. 7.3.8, p. 206)´.

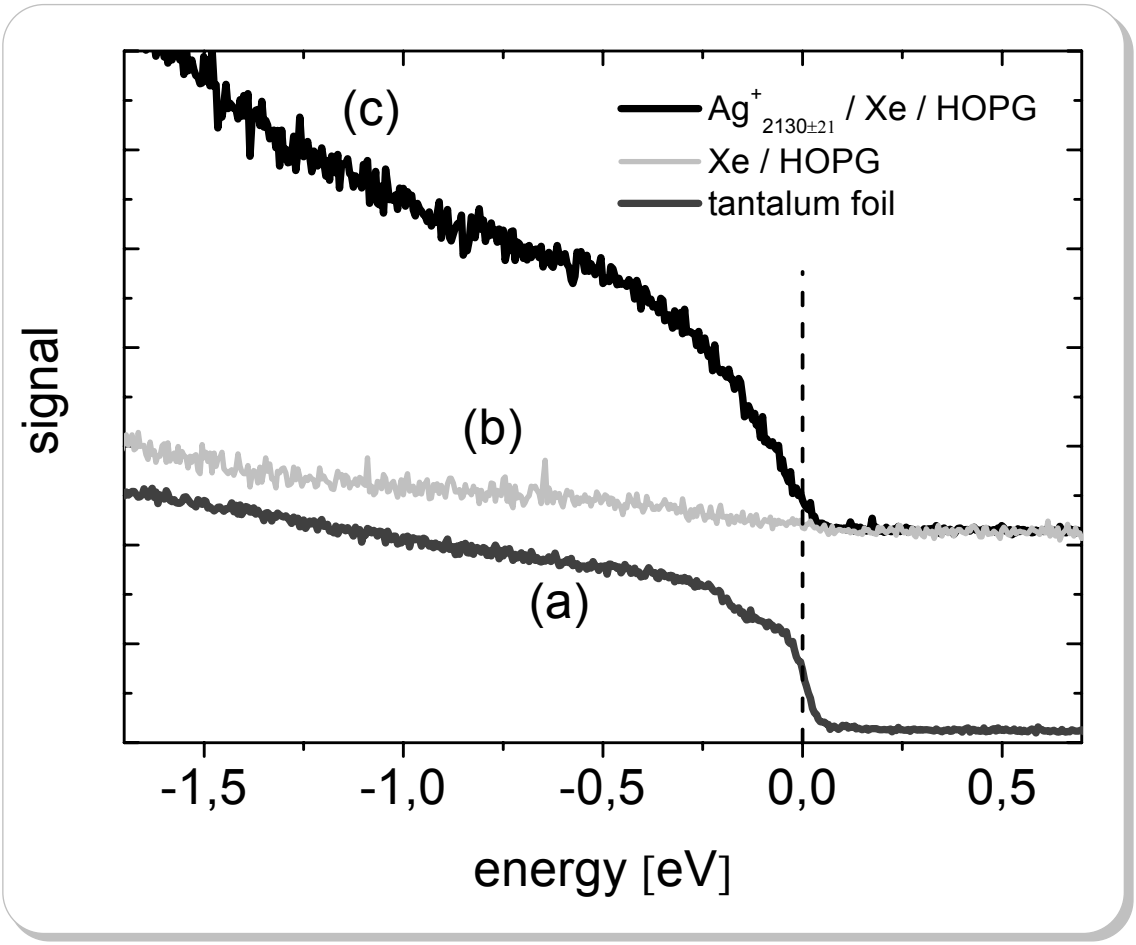

Figure 5.71 UPS spectra of $Ag_{2130\pm21}$ clusters on 10 ML Xe on HOPG.

(a) UPS spectra of the tantalum foil, where the sharp FERMI edge is the reference FERMI energy and set to 0 eV. (b) UPS spectra of 10 ML Xe on HOPG. (c) Cluster FERMI edge signal of the $Ag_{2130\pm21}$ on 10 ML Xe on HOPG.

5.3.2 Discussion

The slightly shifted and rounded cluster FERMI edge we observe in the UPS spectra of $Ag_{2130\pm21}$ clusters on 10 ML Xe on HOPG are already well known from former experiments with clusters produced by metal island growth (see sec. 5.1.1.1, pp .132). We also observed rounded FERMI edges for clusters, which are not completely decoupled, but still have some contact to the surface. Therefore, we also assume here that the clusters immersed completely or partially in the xenon film. One can calculate the cluster height out

of the volume V_S of a simple sphere, by assuming an fcc-closed-packing of the silver atoms within this sphere with equation 2.21. The cluster height is approximately $h_{Ag_{2130}} = 4.1\,\mathrm{nm}$ and consequently in the same order of magnitude compared to the thickness of a 10 ML xenon film, which is 2.48 nm. Although we deposited the clusters rather softly, with a kinetic energy of 0.02 eV per atom, most of the clusters immersed in the Xenon film instead of staying on top of it.

Because of the rather long deposition time of 30 min., chances for the contamination of the Xenon film during the deposition are likely. The degree of contamination also prohibits a reasonable measurement after desorption. We were able to decrease the deposition time for large clusters in more recent experiments up to a factor of 60 (see sec. 3.2.5, table 3.4, p. 109). Therefore, in future we will be able to deposit large size-selected clusters on rare gases at optimized conditions.

5.4 Geometric Magic Silver Clusters on C_{60} on Gold

In this section, we present results of deposited size-selected clusters. We restrict ourselves to investigate exclusively geometric *magic* silver clusters (see 2.4.2.2, p. 66).

We learned from the results in the previous sections, that depositing on HOPG would not work for cluster sizes larger than Ag_{55} due to the maximum bias voltage of the sample holder of ± 800 V. Furthermore, the deposition of large clusters onto a cold substrate requires an extremely short deposition time and / or very clean UHV conditions. WERTHEIM and BUCHANAN found, that Ag deposited on a C_{60} monolayer causes the C_{60} to be retained on the surface at temperatures where the C_{60} alone would desorb. This provides the first indication of a chemical interaction between theses two materials [154]. They conclude that metallic Ag donates electrons into the LUMO of adsorbed C_{60} molecules, resulting in a metallic conduction band. This reaction is restricted to those C_{60} molecules in direct contact with the metal substrate. Last, we supposed that the corrugation with a lateral periodicity of about 1 nm of the C_{60} molecules (see figure 4.55) is

geometrically more suited for at least small clusters than HOPG. Therefore, we use in the following a C_{60} functionalized Au(111) surface.

5.4.1 Experimental Results

The sample substrate we use within these experiments is a freshly prepared Au (111) crystal as we describe in section 4.1.3.1. After the evaporation and annealing of 1 ML C_{60}, we deposit the geometric magic cluster sizes Ag_n (n = 55, 147, 309, 561 and 923) and investigate the samples with STM. We present these results in the following sections and discuss our observations afterwards in section 5.4.2.

5.4.1.1 Ag_{55} / 1 ML C_{60} / Au(111)

We deposit the Ag_{55} clusters at approximately RT for a time $t_d = 10\ \text{min}$, with a cluster ion current of $I_{bd} = 67\ \text{nA}$ (see table 5.11).

Afterwards in the STM images, we observed clusters with an extremely narrow height distribution (see figure 5.72 and figure 5.73) of $(1.7 \pm 0.2)\ \text{nm}$. This average height slightly differs from the estimated cluster height for Ag_{55} clusters of $h_{Ag_{55}} \approx 1.2\,nm$.

For this sample, we imaged several SPS areas at different macroscopic positions within the deposition spot. Figure 5.74 illustrates four STM images taken at different positions. We schematically depict the sample carrier SC with the mounted Au(111) crystal. The deposition Spot (Dep. Spot) was in this experimental run not centric with respect to the single crystal. We depict the estimated deposition spot area (see sec. 4.1.5.3, pp 127) as light grey filled circle in the upper left corner. We took at each black point several STM images and marked the location with coordinates in arbitrary units. We could roughly translate the resulting dimensions into millimeters due to the well-known crystal diameter of 10 mm. We distinguish between different STM images by naming the measurement numbers m. Measurement m59 represents the outer diffuse border of the deposition area

and exhibits only a small number of clusters. The same holds for measurement m41, where the cluster density is marginally higher. A significantly higher cluster density we observed always in the center of the deposition spot, which we exemplarily depict with the measurements m39 and m63. We estimated for this area a cluster density of approximately (15 ± 2) clusters per SPS. In figure 5.75 we present line profiles of some randomly chosen clusters of the measurements m59 (low cluster density), m41 (higher cluster density), and m39 (highest cluster density).

As we already mentioned in section in 2.4.1 (pp 60) the measured cluster height slightly depends on the used tunneling voltage. For this reason we used different tunneling voltages between -0.5 V and + 1 V and observed a tunneling voltage dependent variation of the cluster heights of 0.1 nm. Moreover, we plotted two height histograms for clusters taken at $U_{tunelling}$ = 0.74 V and for clusters taken at $U_{tunelling}$ = 0.5 V and did not observe a significant change in the height histograms [109].

Before we discuss and interpret these results in section 5.4.2, we present further magic clusters sizes in the next sections.

13TH DEPOSITION – Ag_{55} CLUSTERS / 1 ML C_{60} / AU(111)			
Deposition time t_D [min.]	10	Power P_{source} [watt]	14
Sample bias U_{sample} [V]	- 5	Temperature T_{sample} [°C]	45
Frequency f [Hz]	185924.4	Waiting time t_w [µs]	27
Mass m [amu]	5980	Cluster current I_{bd} (before deposition) [pA]	67
Flux Φ Ar / He [sccm/sccm]	383 / 100	Cluster current I_{ad} (after deposition) [nA]	N / A

Table 5.11 Deposition parameters for the sample system Ag_{55} on 1 ML C_{60} on Au (111).

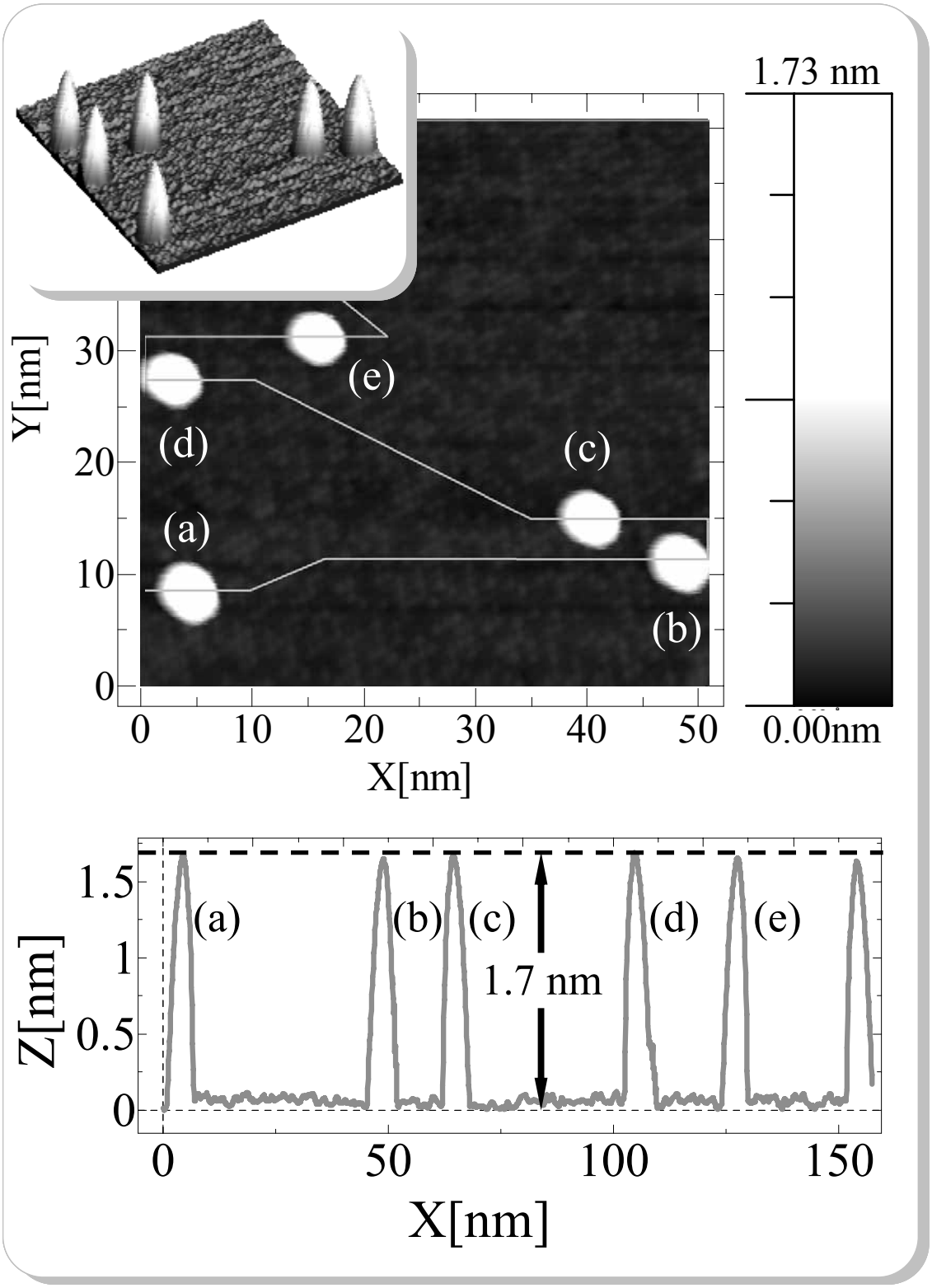

Figure 5.72 Ag_{55} deposited onto 1 ML C_{60} on Au(111) substrate.

($U_{tunelling}$ = 0.49 V / $I_{tunneling}$ = 0.42 nA).

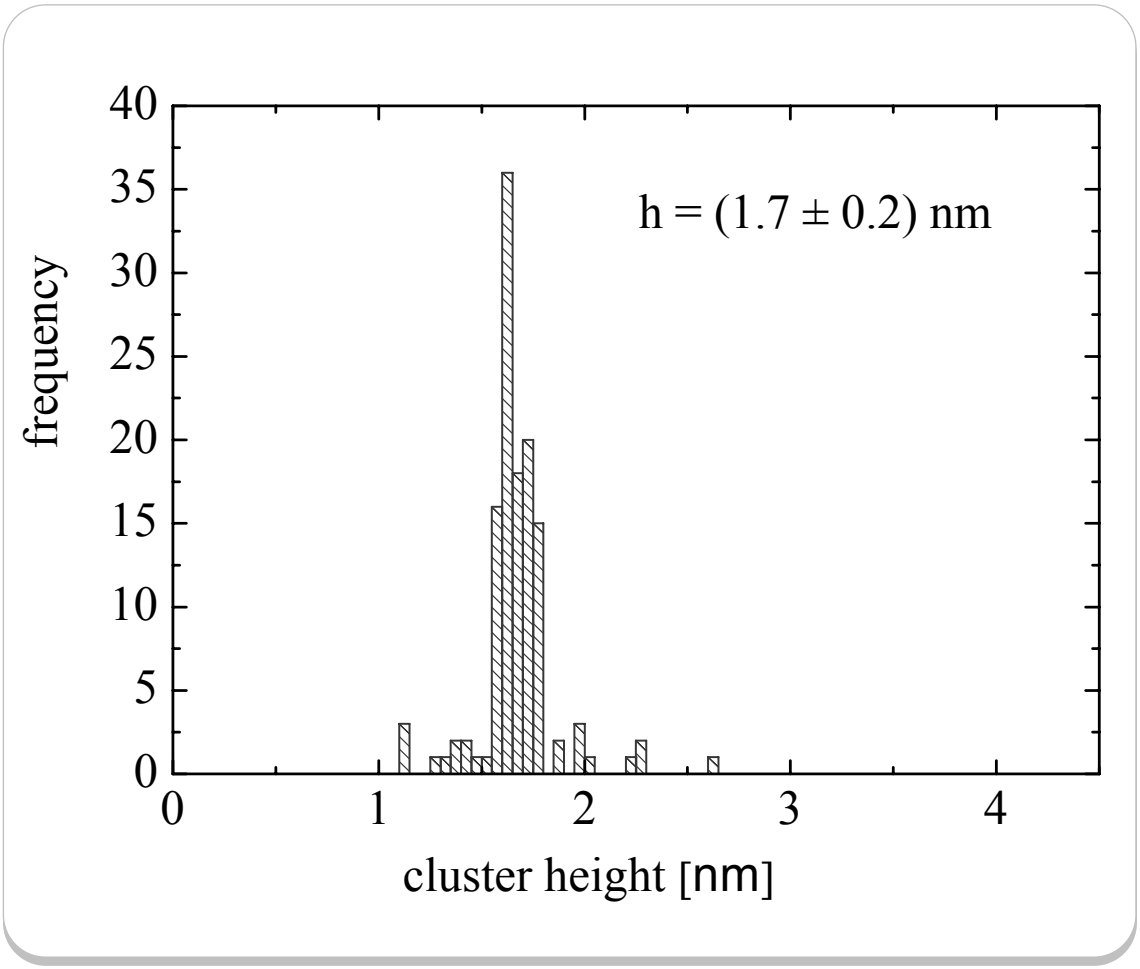

Figure 5.73 Height distribution of Ag_{55} deposited onto 1 ML C_{60} on Au (111) substrate.

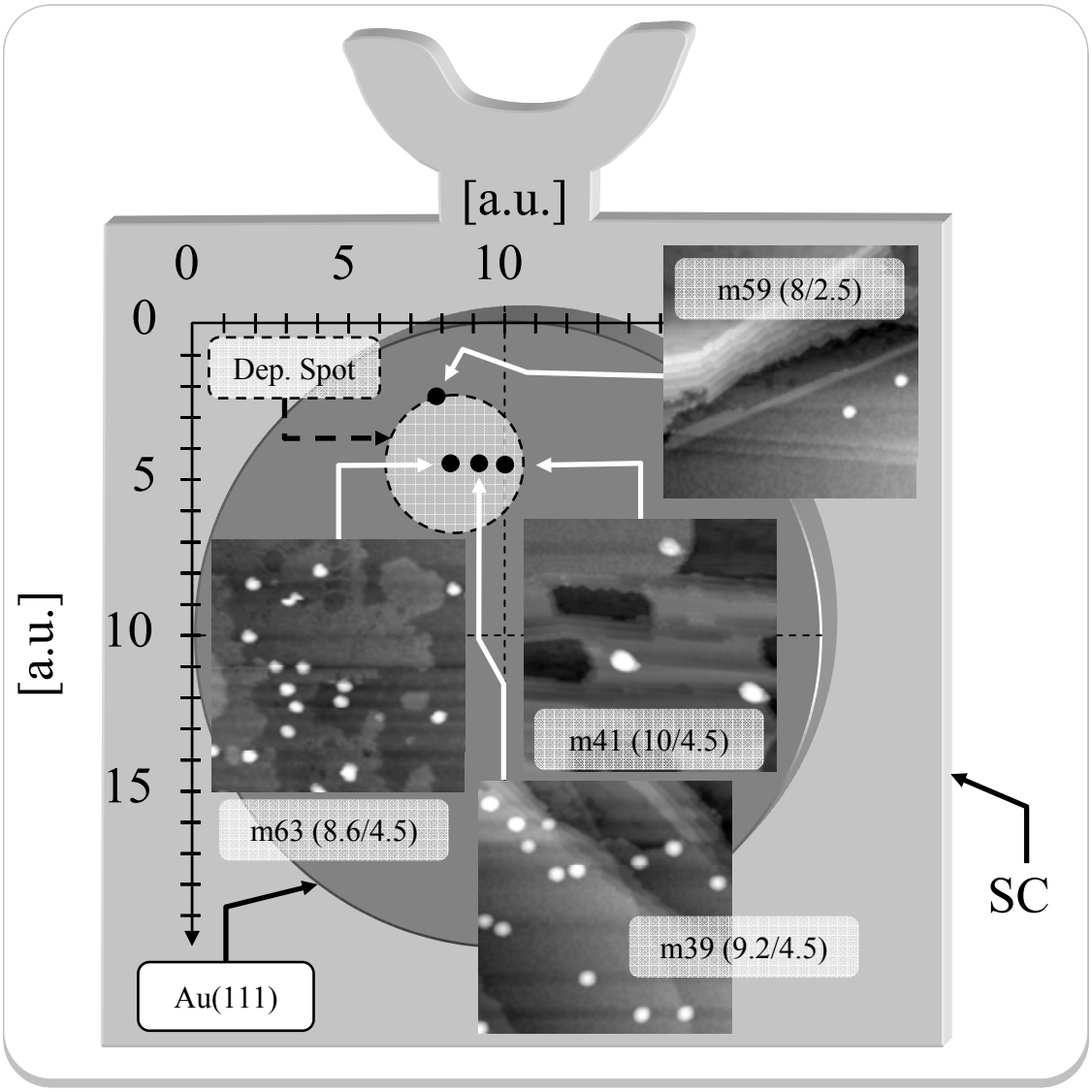

Figure 5.74 Four different macroscopic locations within the deposition spot of Ag_{55} clusters on 1 ML C_{60} on Au(111) imaged with STM.

SC: sample carrier, Dep. Spot: deposition spot, Au(111): schematic depiction of the gold single crystal, m63, m39, m41, and m59: Denotation of different measurements. The coordinates in brackets are given in arbitrary units. Typical line profiles of some clusters are shown in figure 5.75.

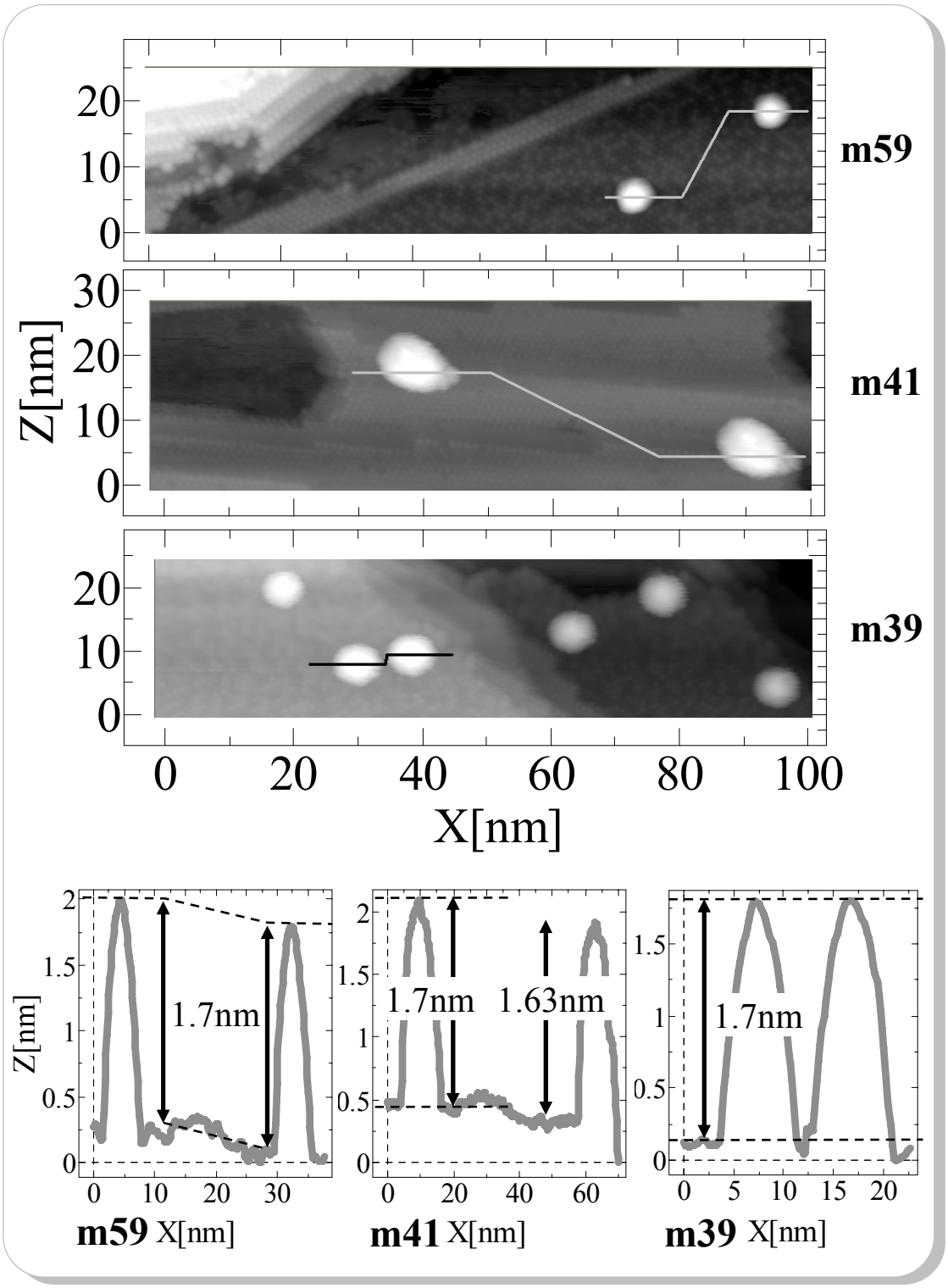

Figure 5.75 Three randomly chosen areas (top) and line profiles (bottom) of clusters of three different STM images of Ag_{55} clusters on 1 ML C_{60} on Au(111).

5.4.1.2 Ag_{147} / 1 ML C_{60} / Au(111)

Ag_{147} represents the next magic cluster size, exhibiting three closed shells (see figure 2.24, pp 68). We deposit the Ag_{147} clusters again at RT for a time $t_D = 5$ min, with a cluster ion current of $I_{bd} = 92$ nA before and $I_{ad} = 74$ nA after the deposition. We summarize the main deposition parameters in table 5.12.

With the STM we again imaged clusters with a similar narrow height distribution compared to the ones for Ag_{55} clusters (see figure 5.76). Figure 5.77 shows the height distribution of the Ag_{147} clusters with an average cluster height of (1.7 ± 0.3) nm. This height distribution is broader compared to the one of the Ag_{55} clusters due to less quality of the C_{60} film in this experimental run, which results in a broadening of the height distribution. Moreover, a tip change during the STM investigations became necessary.

Nevertheless, the average height of 1.7 nm is quite remarkable, because one would expect at least a moderate increase of the cluster height due to one further closed shell.

18TH DEPOSITION – Ag_{147} CLUSTERS / 1 ML C_{60} / Au(111)			
Deposition time t_D [min.]	5	Power P_{source} [Watt]	9
Sample bias U_{sample} [V]	- 26	Temperature T_{sample} [°C]	RT
Frequency f [Hz]	113962.3	Waiting time t_w [µs]	24
Mass m [amu]	15915	Cluster current (before deposition) [pA]	92
Flux Φ Ar / He [sccm/sccm]	509 / 100	Cluster current (after deposition) [nA]	74

Table 5.12 Deposition parameters for the sample system Ag_{147} on 1 ML C_{60} on Au (111).

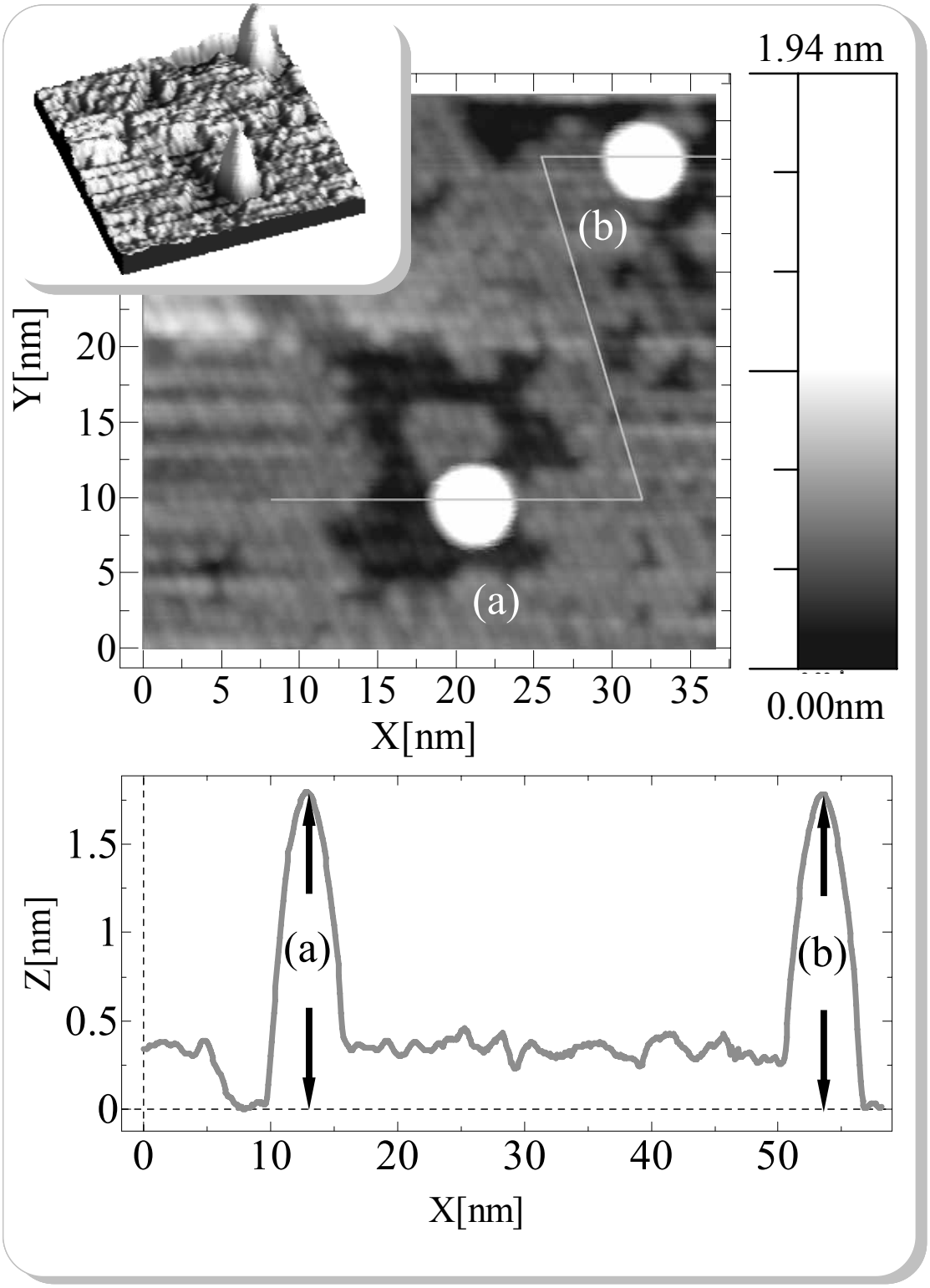

Figure 5.76 Ag_{147} clusters on 1 ML C_{60} on Au (111).

(Top) typical STM image of two Ag_{147} clusters. (Bottom) Line profile of the clusters (a) and (b) with measured heights $h_{(a)}$ = 1.79 nm, and $h_{(b)}$ = 1.76 nm. ($U_{tunelling}$ = 0.71 V / $I_{tunneling}$ = 0.079 nA).

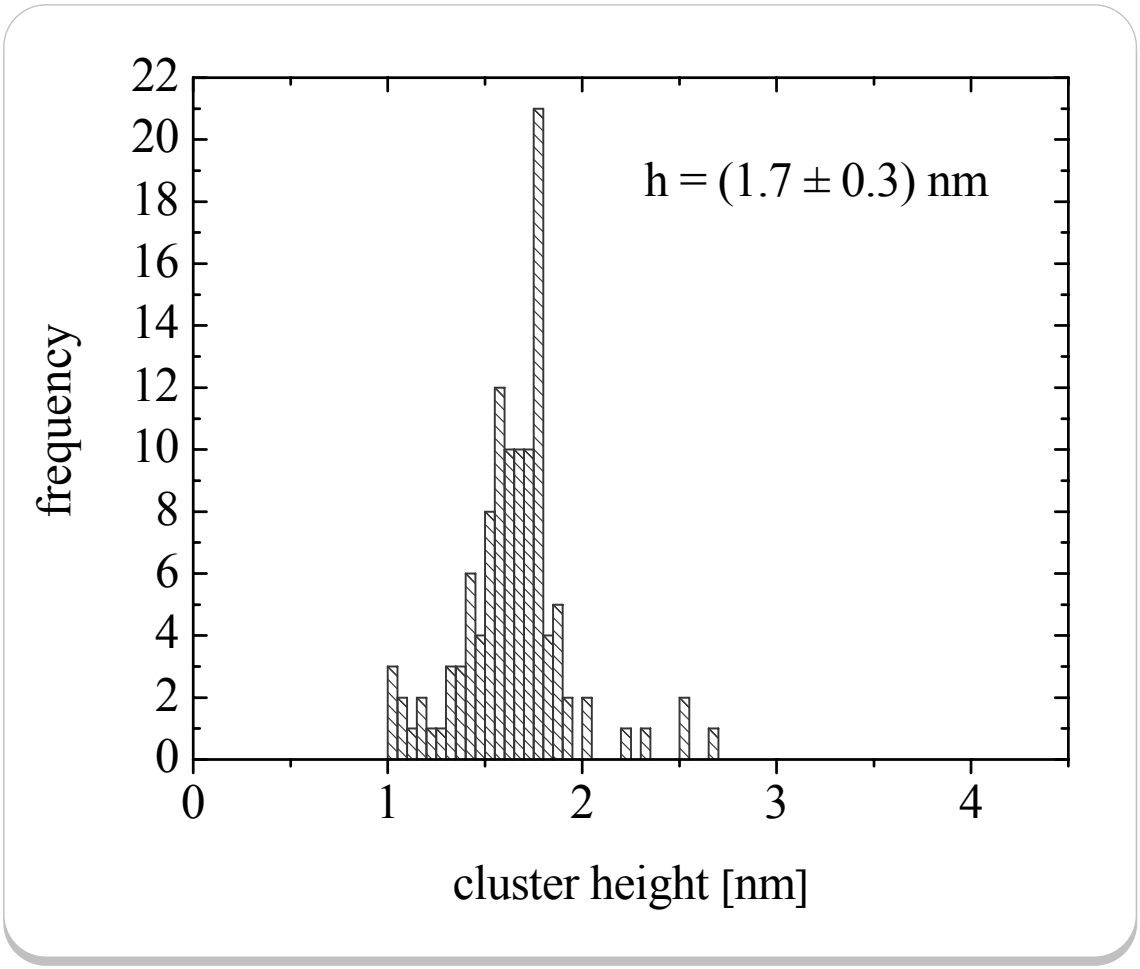

Figure 5.77 Height distribution of Ag_{147} clusters on 1 ML C_{60} on Au (111).

5.4.1.3 Ag_{309} / 1 ML C_{60} / Au(111)

The third magic cluster size we wanted to study is the Ag_{309} cluster. The appropriate MACKAY icosahedron exhibits four closed shells (see figure 2.24, pp 68). In this experiment, we used a deposition time of $t_D = 5$ min., and measured a cluster ion current of $I_{bd} = 60$ nA before and $I_{ad} = 60$ nA after the deposition. Once more, we sum up the essential deposition parameters in table 5.13.

We imaged clusters, which show again an extremely narrow size distribution (see figure 5.78). The height distribution in figure 5.79 shows an average height of (1.7 ± 0.3) nm, still without growing in height.

Later on, we repeated this experiment using a different sample bias voltage for the cluster deposition of about U_{bias} = +10 V and observe the same average cluster height (see figure 5.86 in sec. 5.4.2). We will discuss this sample in the next section.

19TH DEPOSITION – Ag_{309} CLUSTERS / 1 ML C_{60} / Au(111)			
Deposition time t_D [min.]	7	Power P_{source} [watt]	9
Sample bias U_{sample} [V]	- 50	Temperature T_{sample} [°C]	53
Frequency f [Hz]	78650.13	Waiting time t_w [µs]	51
Mass m [amu]	33412	Cluster current (before deposition) [pA]	70
Flux Φ Ar / He [sccm/sccm]	435 / 100	Cluster current (after deposition) [nA]	70

Table 5.13 Deposition parameters for the sample system Ag_{309} on 1 ML C_{60} on Au (111).

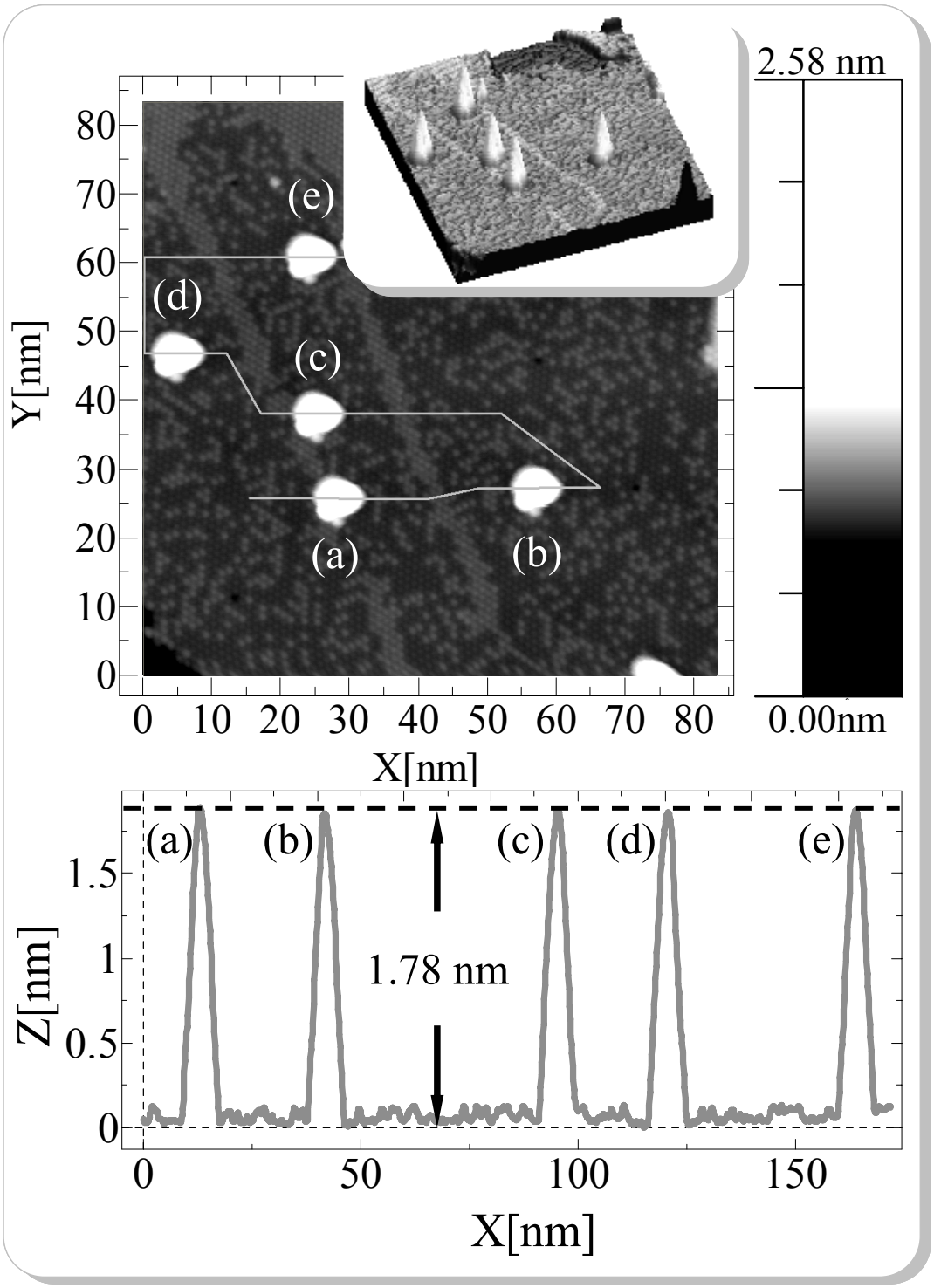

Figure 5.78 Ag_{309} clusters on 1 ML C_{60} on Au (111).

(Top) typical STM image of five Ag_{309} clusters on a C_{60} island ($U_{tunelling}$ = 2.0 V / $I_{tunneling}$ = 0.035 nA).

(Bottom) Line profiles of the clusters (a) – (e) with equal heights of about 1.7 nm.

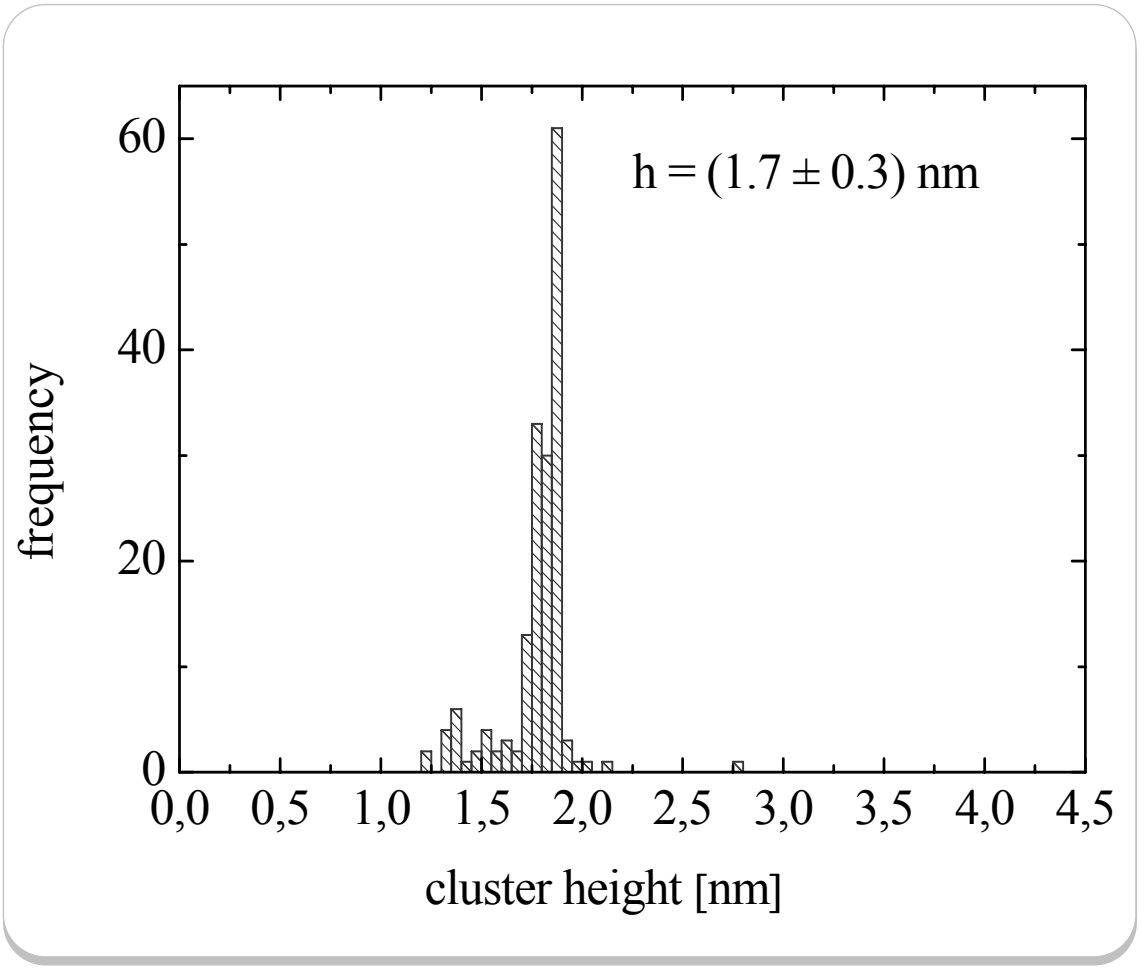

Figure 5.79 Extremely narrow height distribution of Ag_{309} clusters on 1 ML C_{60} on Au (111).

5.4.1.4 Ag_{561} / 1 ML C_{60} / Au(111)

Since the cluster height seemed to be independent of the number of atoms or shells, respectively, we continued our studies, and proceeded to the next larger magic silver cluster, which is Ag_{561}. We expect, because of the calculated cluster height for Ag_{561}, cluster heights of about $h_{Ag_{561}} \approx 2.6\,\text{nm}$. We deposited the clusters using the deposition parameters arranged in Table 5.14. In the line profile in figure 5.80, we observe a slightly broader height distribution of some larger clusters. After we analyzed 406 individual clusters, the height histogram exhibits two maxima (see figure 5.81) – one maximum again for clusters with 1.76 nm height.

23TH DEPOSITION – Ag_{561} CLUSTERS / 1 ML C_{60} / AU(111)			
Deposition time t_D [min.]	15	Power P_{source} [Watt]	9
Sample bias U_{sample} [V]	+ 10 V	Temperature T_{sample} [°C]	RT
Frequency f [Hz]	58387.2	Waiting time t_w [µs]	9 µs
Mass m [amu]	60628	Cluster current (before deposition) [pA]	60 pA
Flux Φ Ar / He [sccm/sccm]	413 / 80.8	Cluster current (after deposition) [nA]	N / A

Table 5.14 Deposition parameters for the sample system Ag_{561} on 1 ML C_{60} on Au (111).

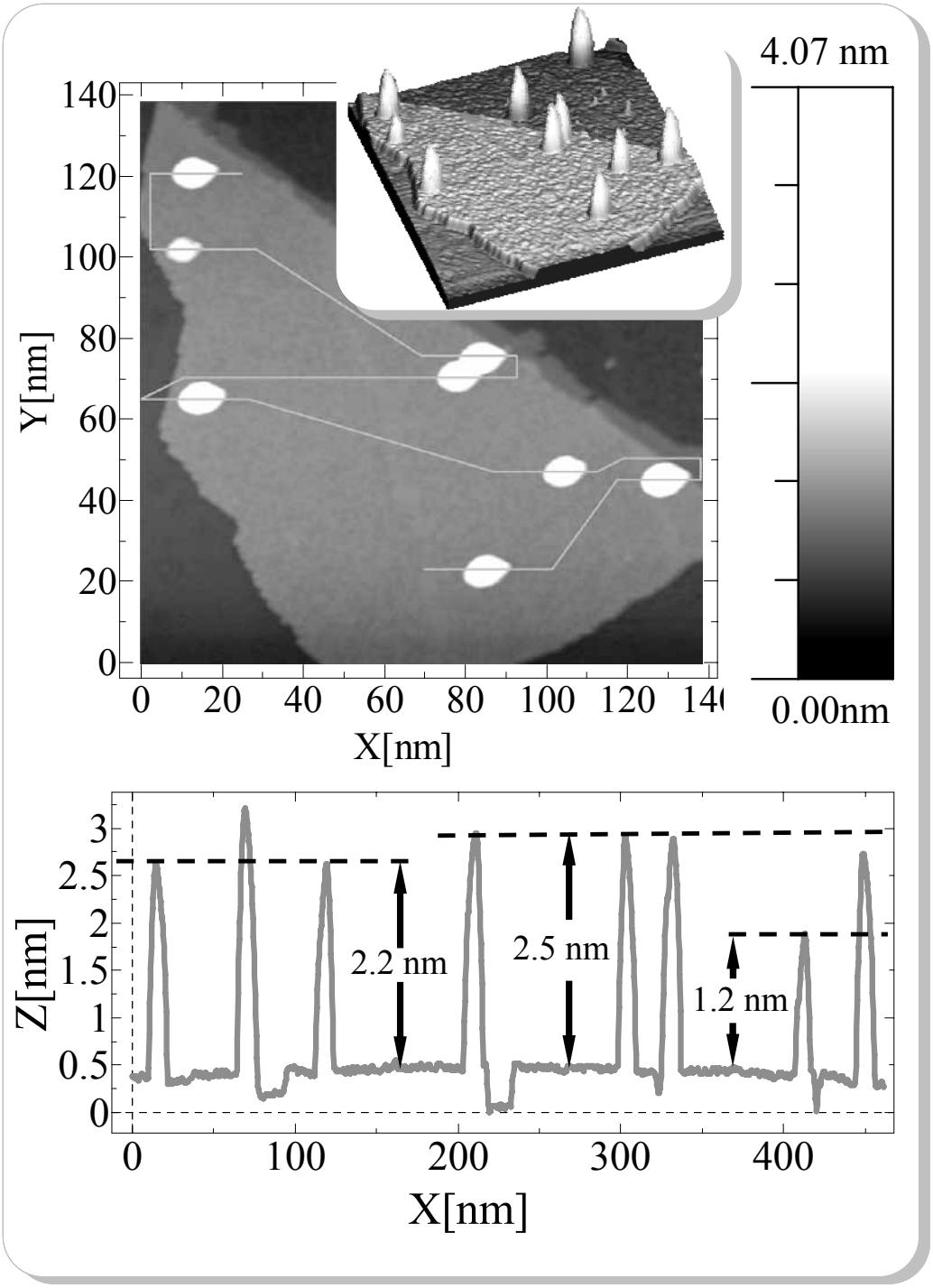

Figure 5.80 Ag_{561} clusters deposited onto 1 ML C_{60} on a Au (111) substrate.

(Top) typical STM image of several clusters on large C_{60} islands. (Bottom) Line profiles of these clusters showing slightly different heights ($U_{tunelling}$ = 2.0 V / $I_{tunneling}$ = 0.02 nA).

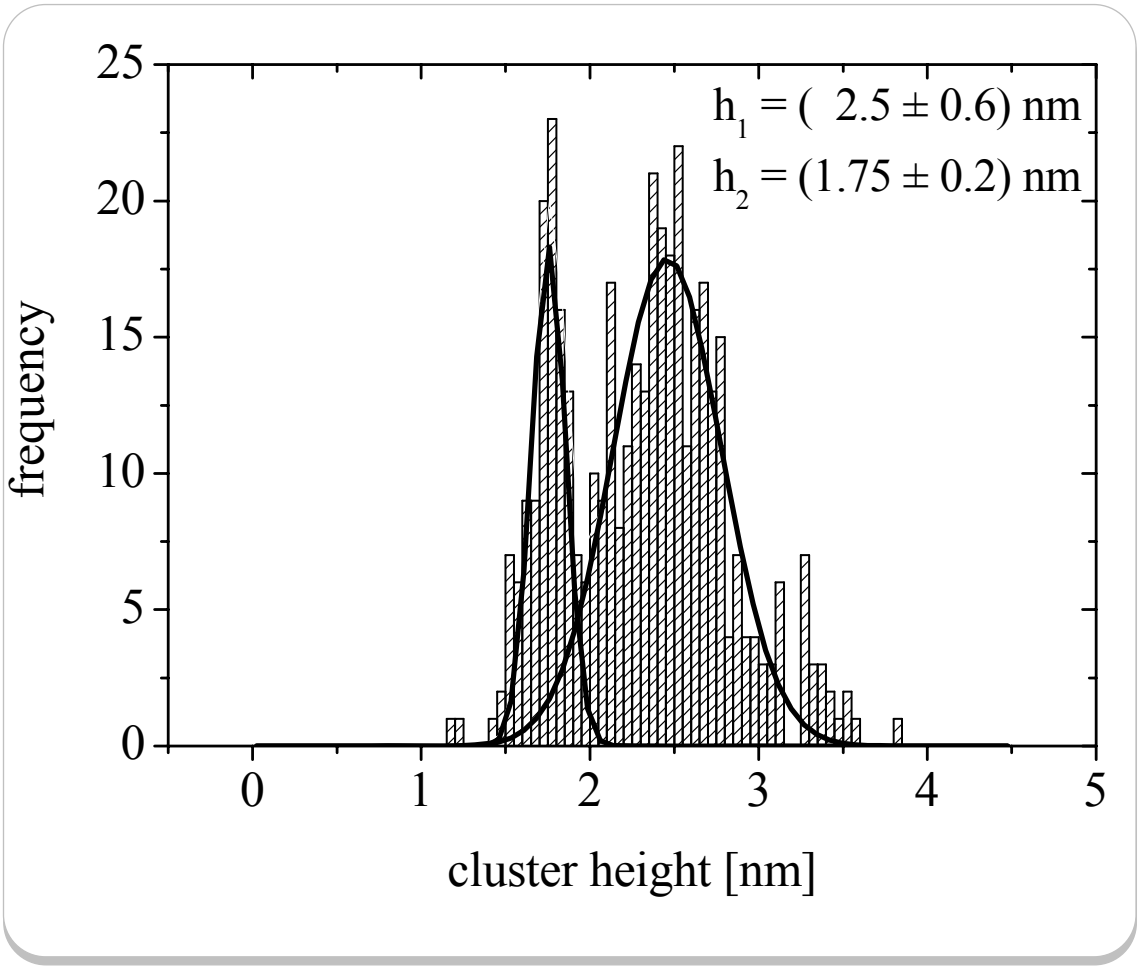

Figure 5.81 Height distribution of Ag_{561} clusters on 1 ML C_{60} on Au (111).
One observes two maxima for the cluster heights (1.75 nm and 2.5 nm).

5.4.1.5 Ag_{923} / 1 ML C_{60} / Au(111)

As final cluster size in this deposition series, we deposited Ag_{923} clusters onto the C_{60} functionalized surface. Table 5.15 contains the deposition parameters and figure 5.82 represents a typical STM image of the deposited clusters. The line profile of different clusters shows cluster heights between 2.7 nm and 3.2 nm. The estimated cluster height from equation 2.21 is $h_{Ag_{923}} = 3.11$ nm (see table 2.3, p. 62). The height distribution we depict in figure 5.83 only shows one height distribution of larger cluster sizes. This probably comes from bad tip conditions in this experimental run. We also observed several small clusters, which we could not measure accurately due to a multiple tip. We illustrate this exemplarily for one STM image, which we show in figure 5.84. The upper

most line profile represents cluster heights of real clusters, which we take into account for the height distribution (see figure 5.83). Due to a double tip, the formation of the four clusters (a) to (d) identically appears again, vertically displaced downwards of about 20 nm. The middle line profile shows the *virtual* cluster heights of these non-existing clusters (a)* to (d)*, which comes from an additional tunneling channel established by a second micro tip with around 20 nm distance with respect to the main tunneling tip. Because usually the double tip changes during an experimental run and the heights of the ghost clusters are in the same order of magnitude compared to the smaller clusters we observe in several STM images, we did not include the heights of the small clusters in the height histogram. We assume that the smaller clusters could again exhibit an average height of approximately 1.75 nm, as one can estimate from some measurable small clusters which can not be ghost images because there are no corresponding *real* clusters (see clusters (e), (f), and (g) in figure 5.84). This would also lead to a double peak in the height histogram as well as we observed for the Ag_{561} clusters (see figure 5.81).

20TH DEPOSITION – Ag_{923} CLUSTERS / 1 ML C_{60} / Au(111)			
Deposition time t_D [min.]	30	Power P_{source} [Watt]	9
Sample bias U_{sample} [V]	- 1	Temperature T_{sample} [°C]	RT
Frequency f [Hz]	45525.32	Waiting time t_w [µs]	88
Mass m [amu]	99729	Cluster current I_{bd} (before deposition) [pA]	30
Flux Φ Ar / He [sccm/sccm]	100.1 / 319	Cluster current I_{ad} (after deposition) [nA]	30

Table 5.15 Deposition parameters for the sample system Ag_{923} on 1 ML C_{60} on Au (111).

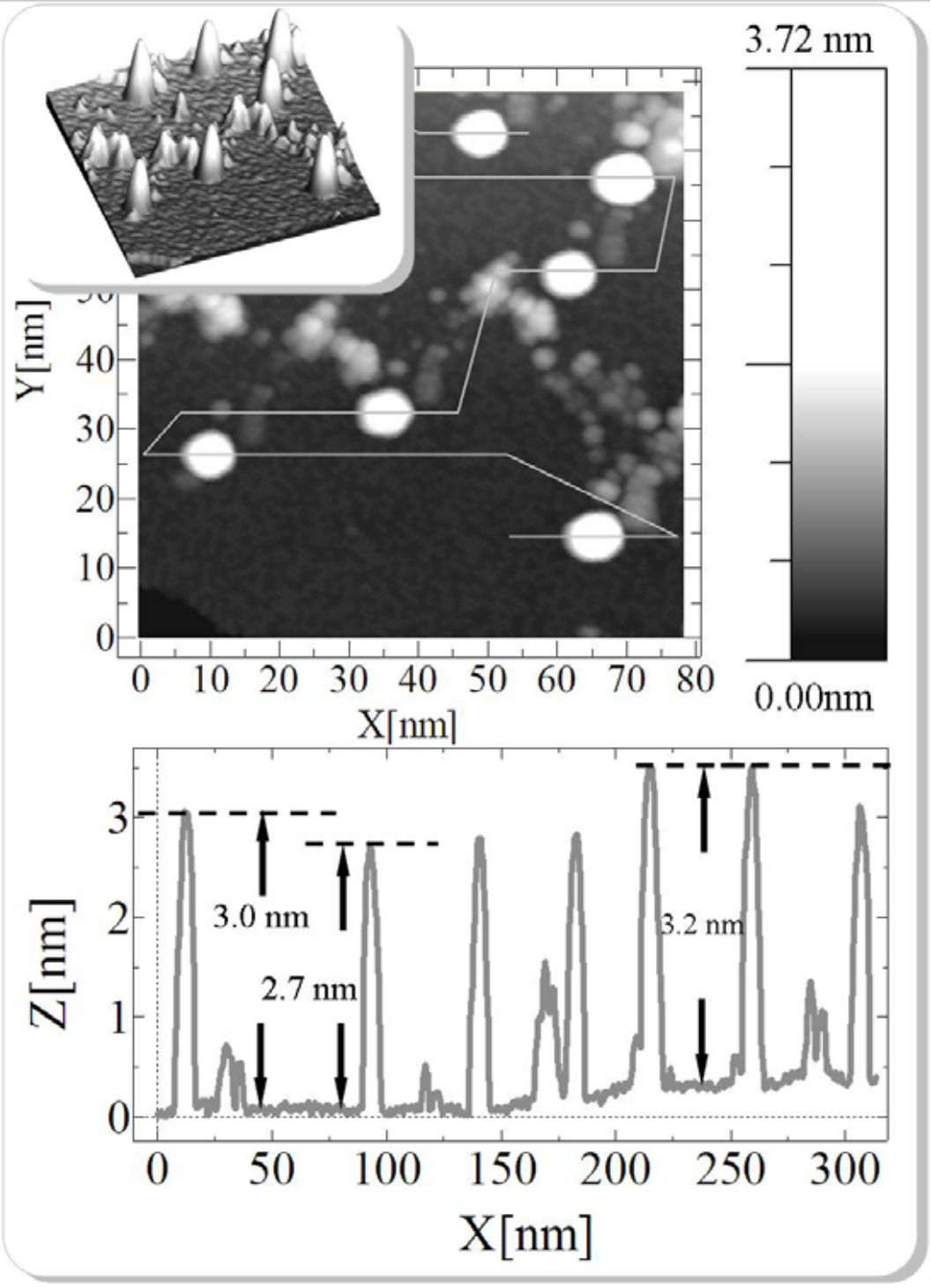

Figure 5.82 Ag_{923} clusters deposited on 1 Ml C_{60} on a Au (111) substrate.

(Top) STM image shows a typical area of this sample ($U_{tunelling}$ = 2.0 V / $I_{tunneling}$ = 0.02 nA). (Bottom) Line profile of some large and small clusters. Due to bad tip and sample conditions, the exact analysis of some smaller clusters was impossible.

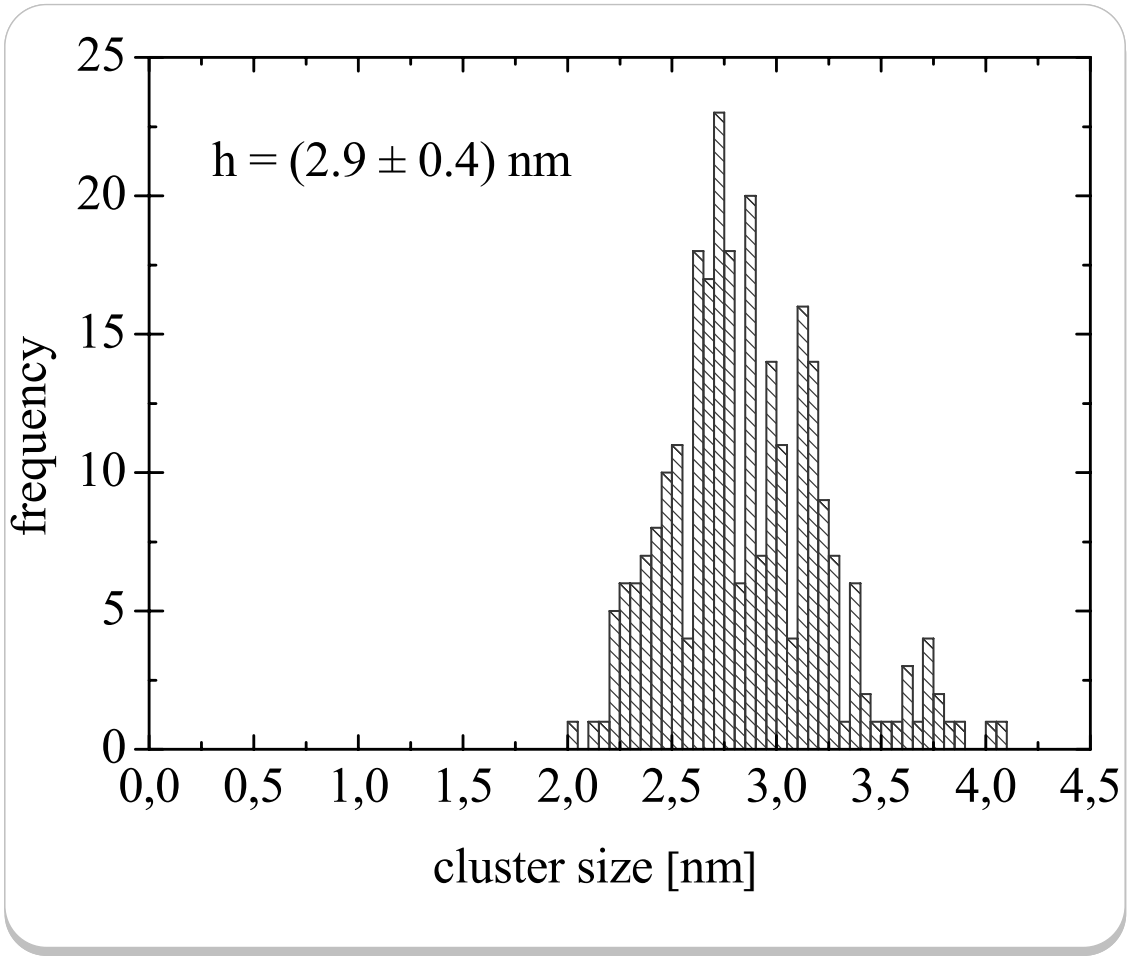

Figure 5.83 Height distribution for Ag_{923} clusters on 1 ML C_{60} on Au (111).

As discussed in the text, only large cluster have to be taken into account, due to bad tip conditions.

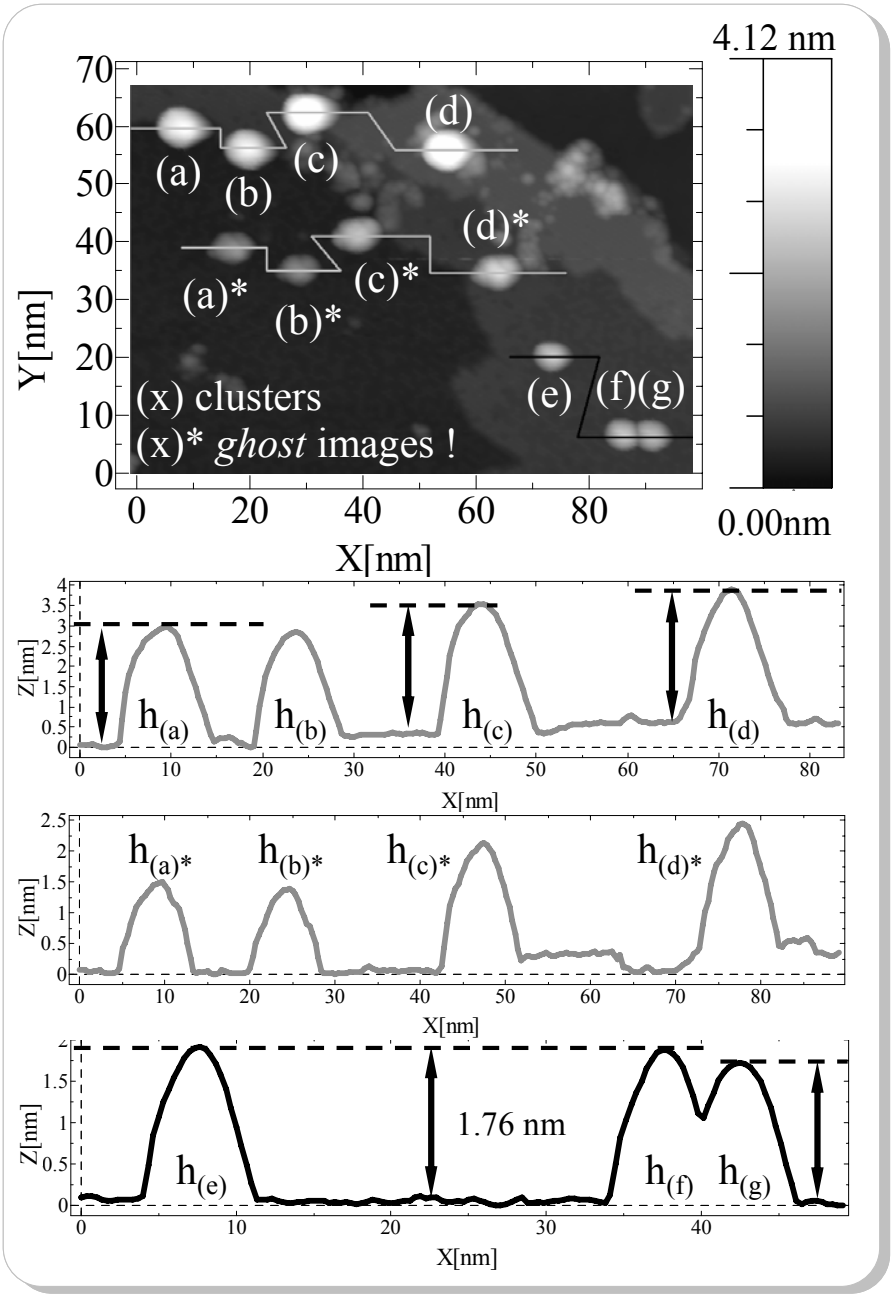

Figure 5.84 *Double tip effects* observed for Ag_{923} clusters on 1 ML C_{60} on Au(111).

The heights of measured real cluster heights: $h_{(a)}$ = 2.95 nm, $h_{(b)}$ = 2.84 nm, $h_{(c)}$ = 3.22 nm, and $h_{(d)}$ = 3.29 nm. Due to a *double tip effect*s one observes also ghost images of non-existing clusters with *virtual* cluster heights $h_{(a)*}$ = 1.48 nm, $h_{(b)*}$ = 1.36 nm, $h_{(c)*}$ = 2.06 nm, and $h_{(d)*}$ = 1.92 nm. These heights are in the same order of magnitude as some smaller clusters which again show heights of approximately 1.7 nm, *e.g.*, $h_{(e)}$ = 1.76 nm, $h_{(f)}$ = 1.76 nm, or $h_{(g)}$ = 1.70 nm. ($U_{tunelling}$ = 2.0 V / $I_{tunneling}$ = 0.02 nA).

5.4.2 Discussion

The curious results of the deposition experiments with geometrical magic size-selected silver clusters we present in the previous chapter raises several questions. We summarize the average cluster heights of all clusters in figure 5.85. Moreover, we add to this diagram the calculated cluster heights h^{s}_{Agn} using the model of a simple sphere (see equation 2.21). Therewith, the difference between theory and experiment is clearly visible. While the calculated cluster height increases with increasing number of shells, the measured cluster heights remains constant at approximately 1.7 nm, except for Ag_{561} and Ag_{923}. In theses particular cases, we observed, beside clusters with a height of 1.7 nm, larger clusters. The large cluster heights are almost equal to the estimated values. In case of Ag_{561} the calculated height of $h^{s}_{Ag561} = 2.64\,\text{nm}$ agrees with the measured one of $h^{exp.}_{Ag561} \approx 2.5$ nm for the larger clusters. In the same way, the estimated cluster height of Ag_{923} of $h^{s}_{Ag923} = 3.11$ nm is approximately equal to the measured one of $h^{exp.}_{Ag923} \approx 2.9\,\text{nm}$. Nevertheless, for these two sample systems we also observed several clusters with 1.7 nm in height. The square data point in brackets in figure 5.85 indicates that we were not able to provide a height distribution for the small clusters for Ag_{923}, although we observe several clusters with a height of 1.7 nm (see sec. 5.4.1.5 and figure 5.83, clusters (e), (f), and (g)).

As we showed exemplarily for Ag_{55} clusters, areas with different cluster densities (see figure 5.74) exhibit clusters with the same cluster height of about 1.7 nm (see figure 5.75). Therefore, we can conclude that no cluster island growth takes place, because for island growth both, the number of clusters per area and the cluster size increase with coverage. This affirms the deposition of identical objects, in contrast to the deposition of atomic material, which leads to metal island growth as we explained in section 2.3.1 (pp 56).

To exclude also deposition-induced effects due to, *e.g.*, too high deposition energies, we repeated the deposition of Ag_{309} clusters. We summarize all deposition parameters in the appendix in table 5.13. In contrast to the first Ag_{309} deposition, we used in the second one a bias voltage U_{bias} at the onset of the cluster ion current decay (see figure 4.56) of about U_{bias} = +10 V (0.03 eV per atom). We observed again clusters with heights of around

1.7 nm (see figure 5.86). Hence, we can verify the result of the first experiment with a kinetic energy of 0.16 eV per atom with the second experiment with a kinetic energy of 0.03 eV per atom. The observed cluster heights are obviously independent from the deposition energy, or at least for energies below 0.16 eV per atom.

Because all these observations point to some curious changes in the cluster topography after deposition, we perform an additional experiment, to check the long-term stability of the samples at room temperature.

In all experiments, we deposited the clusters with different cluster ion currents (see sec. 7.3, pp 199). Hence, we had to vary the deposition time between 5 minutes (*e.g.*, for Ag_{147}) and 30 minutes (*e.g.*, for Ag_{923}) to obtain equal coverages. For this reason, the samples stayed at room temperature for different time intervals until we stored them in the STM at T_{STM} = 77 K. To check the temperature dependency we used another Ag_{309} sample. We deposited the Ag_{309} clusters for 15 minutes onto the C_{60} functionalized surface at room temperature and transferred the sample after the deposition interval into the STM. The transfer time approximately amounts to another 15 minutes. Figure 5.86 shows the resulting STM image. We again observed clusters with an extremely narrow size distribution and an average cluster height of about 1.7 nm. After the STM investigation, we transfered the sample into the storage carousel inside the analysis chamber. In this way, we stored the sample at room temperature under UHV conditions for another 12 hours. After that, we investigated again the Ag_{309} clusters with the STM. Figure 5.87 shows a typical STM image and a line profile of the observed clusters. We found out that the coverage has decreased significantly, while the cluster height remains constant. We conclude that the clusters still have a high mobility on the C_{60} layers at room temperature. Because the clusters neither grow, nor shrink significantly during 12 hours at room temperature, we can exclude coalescence.

WANG *et al.* observed also a high mobility of Ag atoms and small silver clusters on a well ordered C_{60} layer on Si(111) [155]. In our case, the question arises, where do the silver clusters go?

Figure 5.88 shows an STM image of the Ag_{147} sample imaged at specific tunneling conditions. In this case, we observed beside the Ag_{147} clusters on the C_{60} islands (area (a) in figure 5.88) two more areas. Area (b) exhibits a very low C_{60} coverage. One can see decorated step edges of the Au (111) substrate. The height of a gold step edge amounts to $h_{SE_{Au}} = a/\sqrt{3} = 0.236$ nm, with a = 0.408 nm (lattice constant of gold). The third area (c) shows a 0.25 nm-high layered structure, which has lateral pattern similar to the gold reconstruction. We found these structures only on C_{60} free areas, where we deposited the Ag_{147} cluster. Because we never observed such structures on a freshly prepared C_{60} on Au (111) sample, we assume these structures to be due to the silver clusters. Depositing silver clusters directly onto the bare gold substrate could have formed these islands due to the strong metallic bonding (see sec. 2.1.1, pp 31).

CHAMBLISS and WILSON investigated the diffusion of Ag atoms on Au (111) and found a morphological instability in the formation of the first monolayer of Ag on room temperature on Au (111) [.156]. In their STM investigations, they found out that a rapid surface diffusion without rapid edge diffusion leads to a fingerlike growth of Ag on Au(111).

In our case, the silver material can only come from the deposited silver clusters. We assume that the clusters either break apart when they get in contact with the bare Au(111) surface, or diffuse from the C_{60} islands to the C_{60} free areas due to their high mobility.

Nevertheless, this does not provide an explanation for the favored cluster height of 1.7 nm. COUILLARD *et al.* investigated large size-selected Ag_n clusters (n = 1100 – 5000) on graphite at room temperature. They could clearly demonstrate, that even large clusters (n = 5000) are highly mobile on the surface [.157] but do not coalesce with one another on the time scale of one day [.158]. The time scale in COUILLARD'S experiments is comparable to our time scales. However, the properties of the graphite surface are different to our ordered C_{60} islands. We can suggest from these experiments, that the atoms of the clusters are highly mobile at room temperature, and are able to relocate their self within the cluster or at the cluster surface.

To check the order of magnitude of the relaxation time τ for the equilibrium shape, we use a formula which is derived in ref. [98] and used in ref. [95] for Au crystals with micrometer dimensions.

Equation 5.27

$$\tau = \frac{r^4 kT\sigma}{24\gamma_{Au} D_{S(Au)} \nu_{Au}^2}$$

r: cluster radius, k: BOLTZMAN'S constant, γ_{Au}: surface energy for Au [.159], ν_{Au}: atomic volume of Au, σ: area per surface atom [.160], and $D_{S(Au)}$: surface diffusivity of Au at 350 ° C [.161] (further values for D_S of different materials can be found in ref. [.162], T = 350 °C.

The formula bases on the assumption that the shape is in first order described by a sphere and that surface diffusion is the dominating mechanism for morphology changes. For gold clusters with a radius of 1 nm at T = 350 °C this results in $\tau \sim 10^{-4}$ s (from ref. [55]). Theoretical calculations of FERRANDO and TRÉGLIA shows that the diffusivity constant D_S for Ag at T = RT is almost equal to D_S of Au at T = 350 °C [.163]. All other parameters (γ and σ) are similar for Ag and Au.

Equation 5.28

$$\tau = \frac{r^4 kT\sigma_{Ag}}{24\gamma_{Au} D_{S(Ag)} \nu_{Ag}^2} = 1.12 \cdot 10^{-20} \cdot D_{S(Ag)}\ m^{-2}s^2$$

$r_{Ag55} = 0.61 \cdot 10^{-9}$ m: cluster radius, k: BOLTZMAN'S constant, $\gamma_{Ag} \approx 0.49$ J / m²: surface energy for Ag [.164], $\nu_{Ag} = 1.71 \cdot 10^{-29}\ m^3$: atomic volume of Ag, $\sigma_{Ag} = 6.7 \cdot 10^{-20}$ m²: area per surface atom [.160], , T = 300 K.

For a diffusivity constant of Ag from theoretical calculations ($D_{S(Ag)} = 2 \cdot 10^{-9}\ m^2 s^{-1}$ [.163]) this leads to the unrealistic short time τ in the order of 10^{-12} s and does not hold for geometrically magic clusters, because the assumptions are unrealistic in this case. Therefore the quantitative results are not reliable.

However, the relaxation time strongly depends on the radius of the cluster with $\tau \propto r^4$, which results in higher stability for larger clusters. This is reasonable, considering as upper limit the long-term stability of a macroscopic silver crystal at room temperature. Furthermore, we get from this calculation that the relaxation time for Ag_{923} clusters is around 4 times longer than for Ag_{309} clusters under the same conditions. We have to assume, that the clusters exhibit metastable shapes rather than equilibrium geometries and that the Ag_{923} remain their original shape until they are stored in the STM chamber at 77 K in contrast to, *e.g.*, Ag_{309} clusters, which already completely broke apart, so that we could not observe the original cluster shape afterwards in the STM. We give an outlook to future experiments, in which we will explain these results in more detail, in the next chapter.

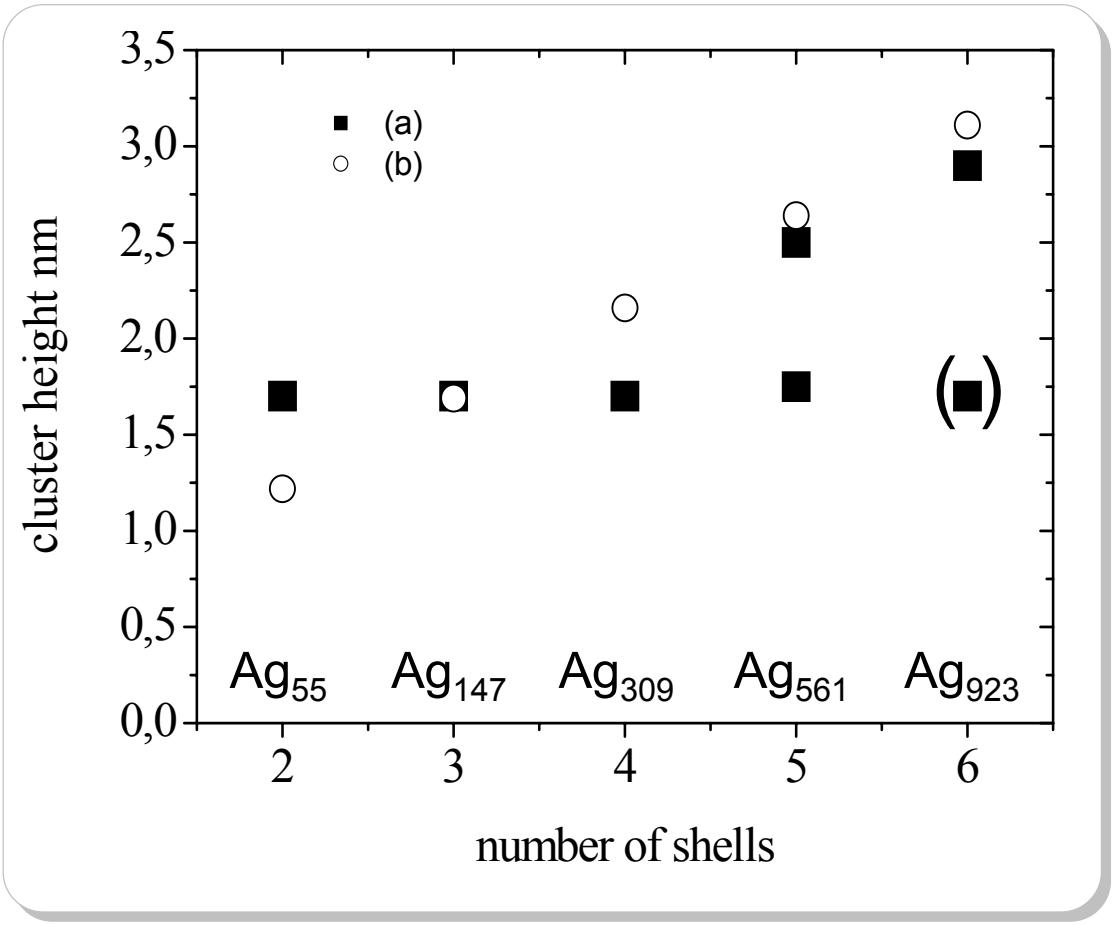

Figure 5.85 Diagram of cluster heights versus number of shells.

(a) Experimental data (b) calculated cluster heights.

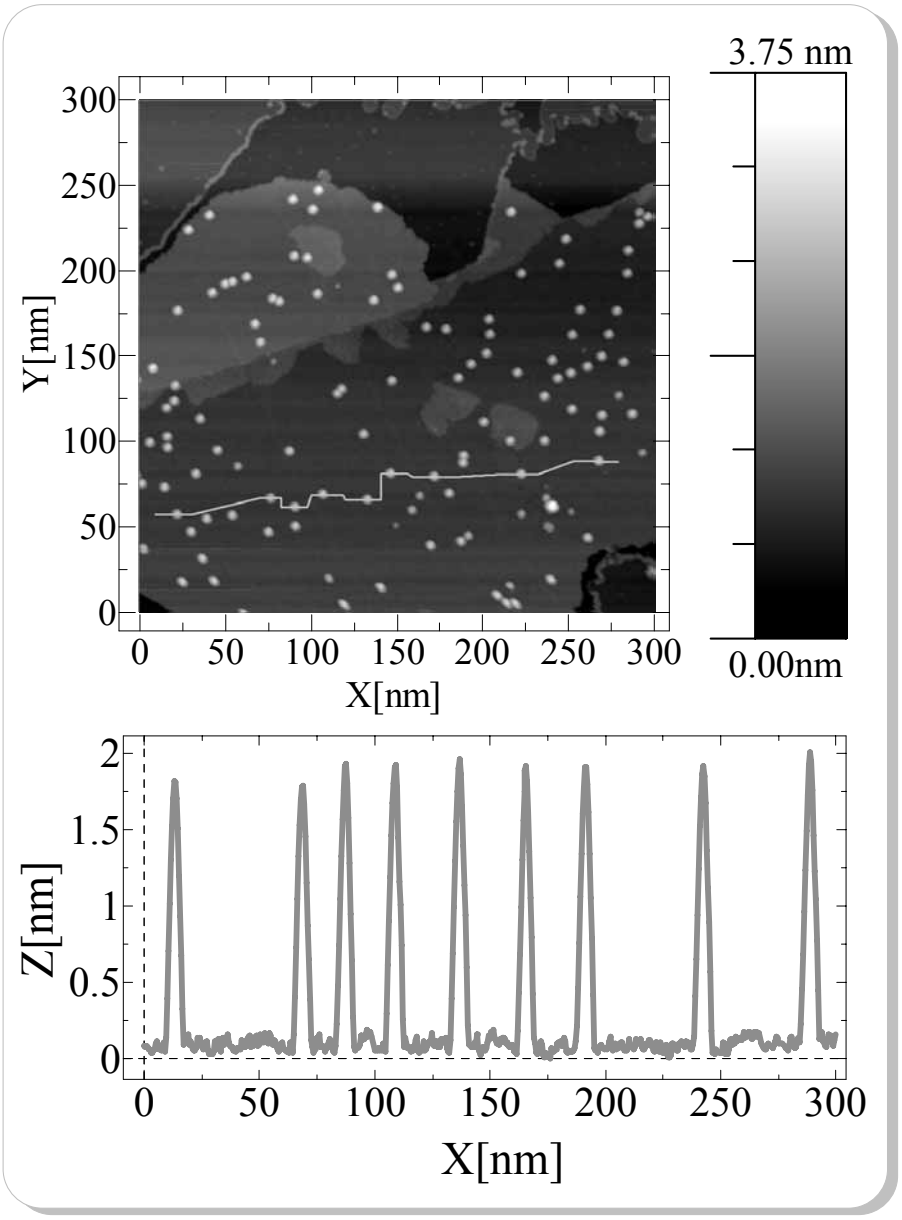

Figure 5.86 Second sample of Ag_{309} clusters (Deposition No. 21, see .7.3.5, p. 203) deposited at T_{sample} = RT, transferred after 30 min into the STM, and investigated at T_{STM} = 77 K.

(Top) typical STM image Ag_{309} clusters on large C_{60} islands ($U_{tunelling}$ = 3.1 V / $I_{tunneling}$ = 0.059 nA). (Bottom) Line profiles of some randomly chosen clusters. Sample bias of U_{bias} = +10 V used in this experiment, in contrast to the first Ag_{309} sample (deposition No. 19, see appendix .7.3.4, p. 202 and sec. 5.4.1.3, pp .168).

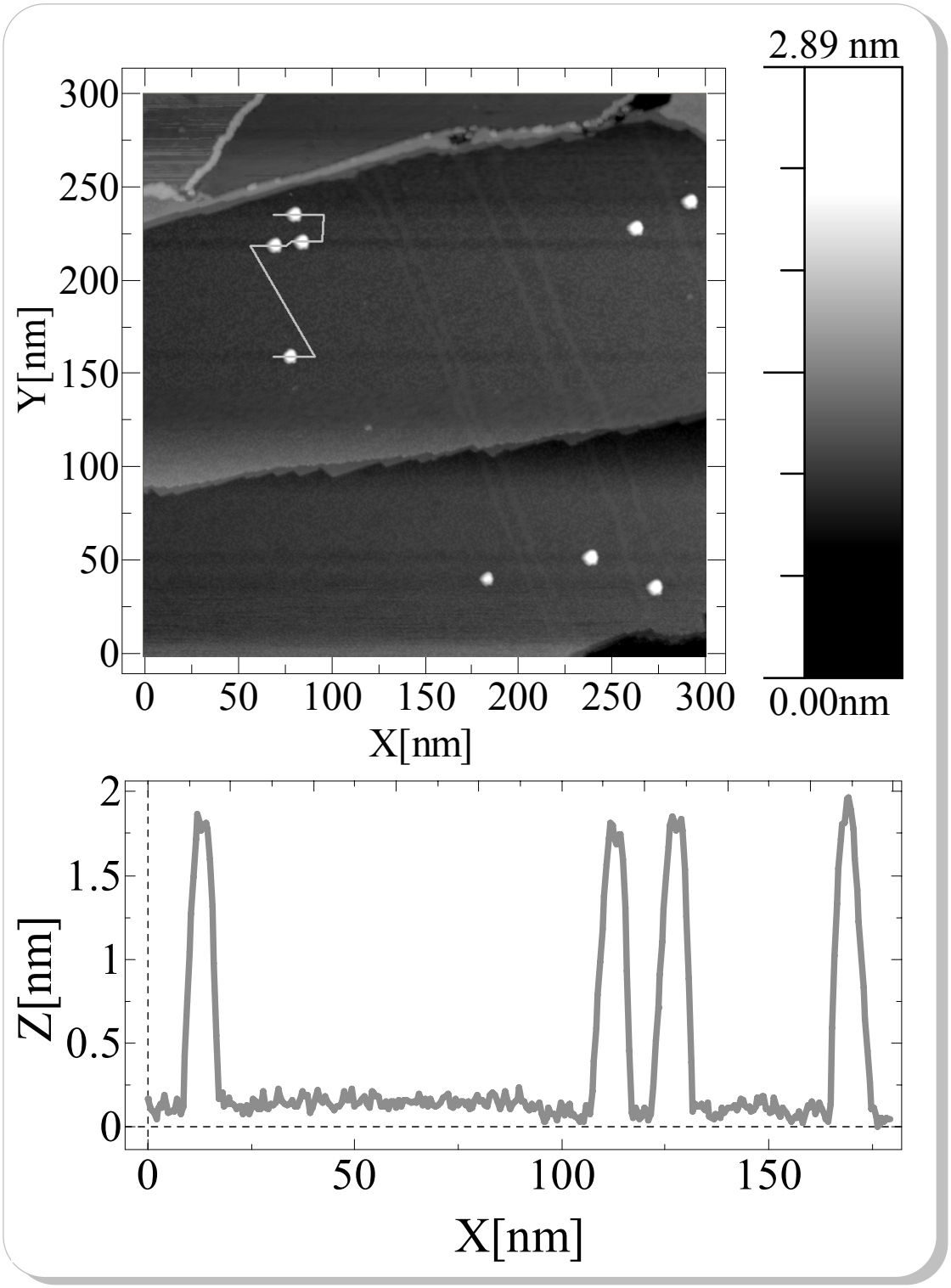

Figure 5.87 The same Ag_{309} cluster sample after storing 12 h at T_{sample} = RT. (Top) typical STM image taken at T_{STM} = 77 K ($U_{tunelling}$ = 2 V / $I_{tunneling}$ = 0.03 nA). (Bottom) Line profile of four randomly chosen clusters.

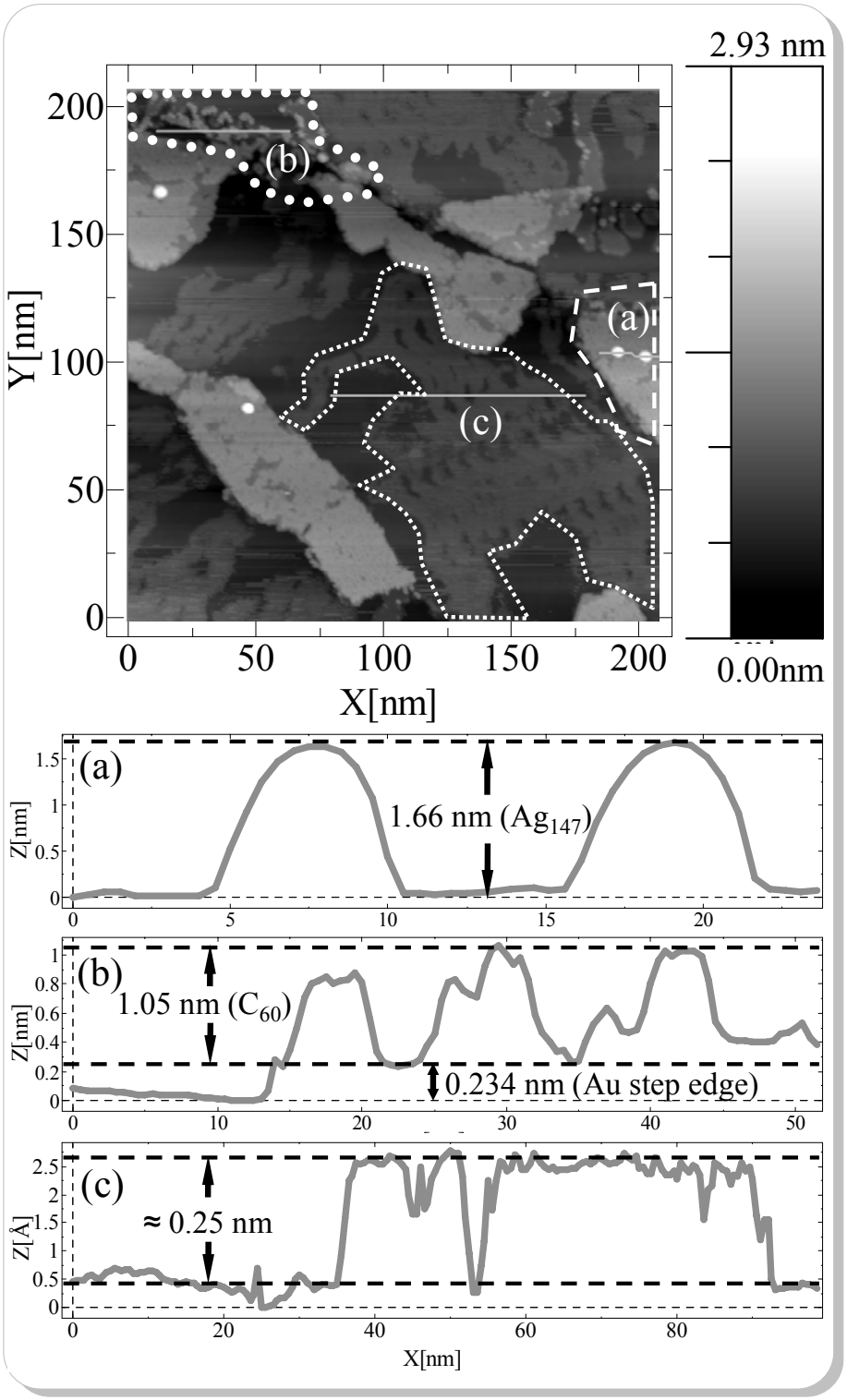

Figure 5.88 Ag_{147} clusters on 1 ML C_{60} on Au(111).

($U_{tunelling}$ = 1.1 V/ $I_{tunneling}$ = 0.057 nA).

Chapter 6

SUMMARY AND OUTLOOK

In the present work, we reported our research project about metallic clusters (chapter 2) on surfaces. We prepared sample systems of different cluster types and materials (sec. 4.1.5) grown or deposited on various buffer layers (sec. 4.1.4) on miscellaneous substrate systems (sec. 4.1.3). We used the experimental techniques STM (sec. 2.2.1) and UPS (sec. 2.2.2) to investigate the interesting effects of clusters with varying coupling to a surface.

We were able to decouple Au and Pb clusters electronically from the metallic substrate by a Xe film of 60 ML thickness (see sec. 5.1.1.2, pp .135). This resulted in a change of the reference energy and lead in particular for Pb clusters on a Au(111) substrate to the remarkable result of a cluster-photoelectron signal above the FERMI energy defined by the ground level of the sample holder (see sec. 5.1.1.3, pp .139). We presented a qualitative interpretation of the observed effects based on the change of the reference energy for the cluster spectra that, according to PAX (see sec. 2.2.3.1, pp .49), is no longer the FERMI

energy but the vacuum energy of the substrate (see figure 5.61). In this sense, we called the clusters decoupled by rare gas layers *free clusters on substrate*.

In addition, in section 3.2 (pp 78) we presented the setup of a new cluster deposition machine developed and constructed by C. YIN and B. V. ISSENDORFF in Freiburg within the cooperation in the DFG priority project SPP 1152 [5]. We used this new apparatus to extend our studies of clusters produced by metal island growth to the investigation of size-selected clusters. In particular, we used the cluster source [116] and the mass selector [117] for the generation and deposition of mass-selected Ag_n clusters (n = 40, 55, 80, 147, 309, 561, 923, and 2130) onto different sample substrates.

We presented first results of STM studies of small size-selected Ag_n clusters deposited with a rather high kinetic energy on HOPG (n=40, 55, and 80) in section 5.2 (pp 146). In accordance to the results of CARROLL et al. [104], we could verify the threshold behavior for cluster pinning to their defects. In our investigation, we observed that no cluster pinning took place below deposition energies of 15 eV per atom. In these first experiments, we noticed the curious role of the geometrically magic Ag_{55} clusters due to the observed cluster height relation

$$h_{Ag_{55}} < h_{Ag_{40}} < h_{Ag_{80}}.$$

We could give a possible interpretation regarding the high stability due to the closed geometric shell structure of the Ag_{55} cluster. Finally, we got from these experiments further evidence for the high mobility [158] of clusters on HOPG due to the preferred position of Ag_{80} clusters only at multiple step edges (see figure 5.70).

Moreover, we presented first UPS results of large size-selected clusters on Xe on HOPG in section 5.3 (pp 156). We were able to show in these experiments the high performance of the mass-selector even for large cluster sizes around 2130 atoms. We observed a rounded cluster FERMI edge of partly immersed Ag_{2130} clusters into the Xe film. This suggests a future repetition of such experiments with slightly modified experimental conditions. On the one hand, we will use substrates, which exhibit a better thermal cou-

pling to the sample holder, *e.g.*, a Au(111) crystal, to adsorb more than 10 ML Xe. On the other hand, we will continue to improve the vacuum conditions (in both, the preparation chamber and the mass selector chamber), due to the extremely sensitive surface of these samples at cold temperatures. We are convinced, that in future experiments with mass-selected clusters on, *e.g.*, 60 ML Xe we will be able to verify the qualitative results of the free clusters grown on surfaces. Moreover, we expect to be able to derive more quantitative results for, *e.g.*, the charging energy E_C (see also 2.2.3.3, pp 53) due to the exactly defined cluster size. Furthermore, we will compare these results with the charging energy of clusters in a free beam (see COULOMB staircases in figure 1.2).

Finally, yet importantly, we investigated mass-selected geometric magic silver clusters deposited on a C_{60} functionalized gold surface. The results we presented in section 5.4.1 (pp 160) show extremely interesting outcomes. In spite of five different cluster sizes between 55 atoms and 923 atoms, we observed for all samples clusters with almost the same average cluster height of about 1.7 nm (see previous sec. 5.4.2, pp 179). This observation differs significantly from the constantly increasing calculated cluster heights (see plot in figure 2.19, p. 62). In addition, we observed for Ag_{561} and Ag_{923} larger clusters that roughly agree with the expected cluster sizes. For Ag_{561} two maxima in the size distribution were revealed with good statistics. We showed exemplarily for Ag_{55} clusters, that areas with different cluster densities (see figure 5.74) exhibit clusters with the same cluster height of about 1.7 nm (see figure 5.75) and conclude that no cluster island growth takes places.

In an additional experiment, we investigated the long-term stability at room temperature of the silver clusters on C_{60}. We observed that after 12 hours at room temperature the cluster height remains constant, while the cluster density decreases significantly (see figure 5.86 and figure 5.87 in the previous sec.).

We considered the deposition energy of the clusters as reason for the constant height, but could show that the results are independent of the energy for less than 0.1 eV per atom,

because we observed identical cluster heights for the two different deposition energies 0.03 eV per atom and 0.16 eV per atom.

Our present hypothesis for the interpretation of these results is that the clusters, deposited at room temperature, exhibit a rather metastable than an equilibrium shape. Nevertheless, we have not produced the final experimental evidence yet, which is left to ongoing and future experiments. In planned experiments we will use cold samples and study the temperature dependency of the same Ag_n clusters (n=55, 147, 309, 561, 923, and maybe 1415) on a C_{60} functionalized surface. We will try to prevent the change into a metastable state due to the decreased temperature. Under these conditions, we predict different cluster heights for different cluster sizes.

In a future collaboration with the group of M. MOSELER, we will get theoretical support by simulations of the cluster-C_{60}-Au(111)-sample system.

Furthermore, we will measure STS spectra for size-selected clusters. Figure 6.89 shows first experimental results of STS spectra of individual clusters of the three different cluster sizes Ag_{55}, Ag_{309}, and Ag_{923} on the C_{60} functionalized surface. The STS spectra of the same cluster show reproducibility and a noise level. STS spectra of different individual clusters present similar features if the cluster height is the same within the narrow height distribution.

The scientific results of this thesis offer a broad range of new experiments. Beside the aforementioned scheduled experiments different cluster materials like, *e.g.*, Au, Pt, or Cu, are imaginable as well as other buffer layers and sample substrates. The investigation of the quantized electronic structure of electronically magic metal clusters could become reality by preparing almost *free* clusters on a surface due to an extremely weak coupling to the surface using combinations of rare gas and / or C_{60} layers. It will be extremely interesting to compare these results with the results of cluster in a free beam (see 2.4.2, pp 62), where v. ISSENDORFF *et a*l. nicely observed and explained the quantized electronic structure.

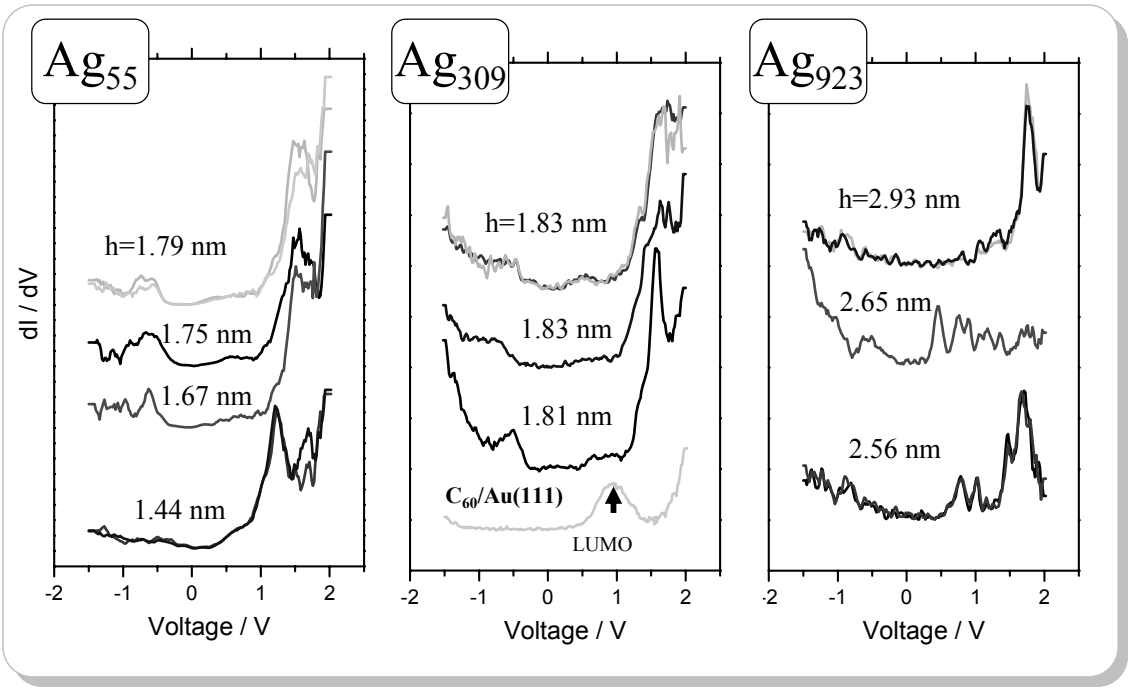

Figure 6.89 STS spectra of Ag_{55}, Ag_{309}, and Ag_{923} clusters measured at 77 K.

Clusters of similar height exhibit similar STS spectra. A full interpretation will be possible, after the repetition of these experiments at T = 5 K and the use of the lock in technique (see 2.2.1.3, p 44).

Chapter 7

APPENDICES

7.1 Cluster Machine Drawings

In the following section, we show some enlarged drawings.

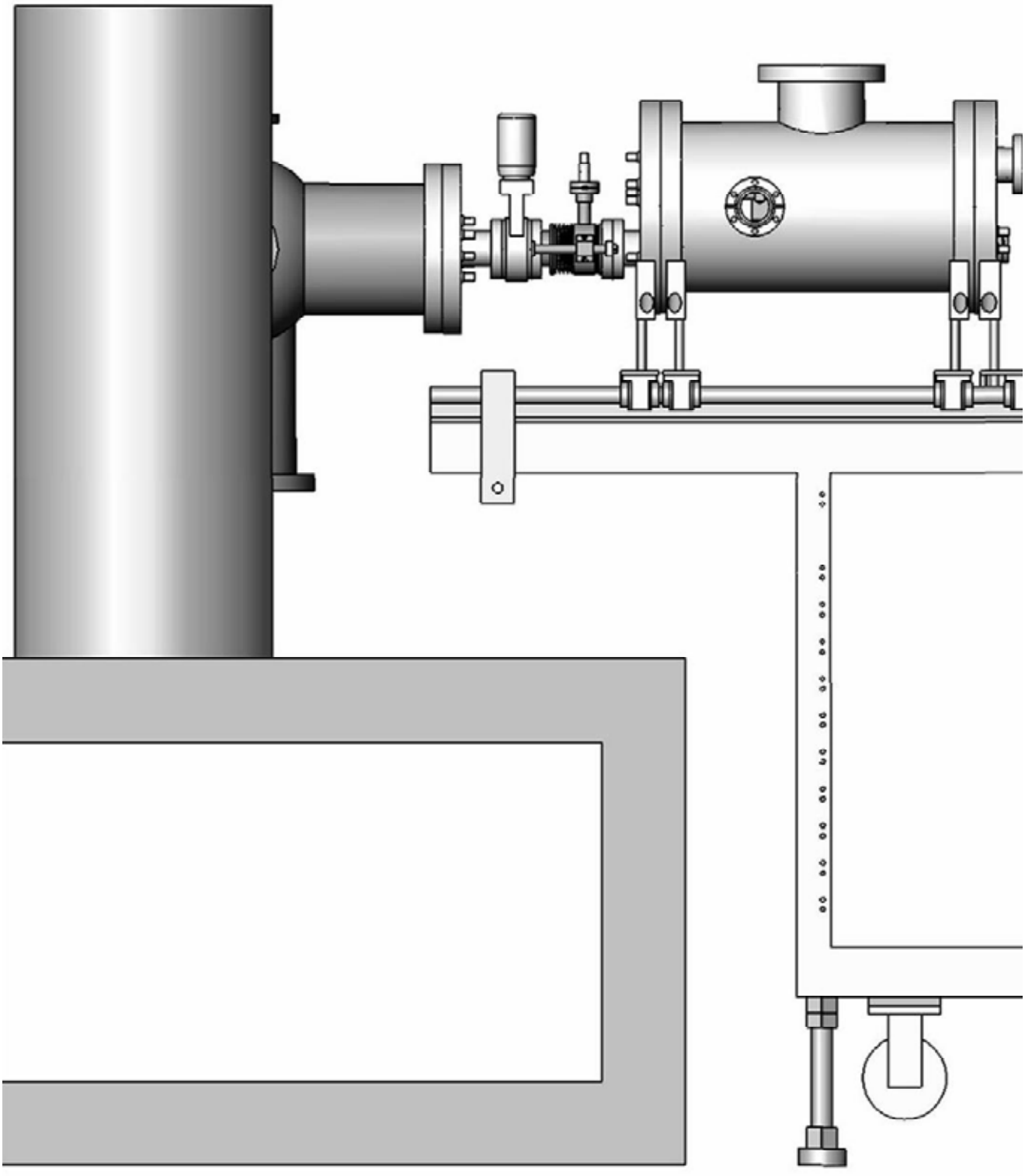

Figure 7.90 Full-size drawing of the cluster deposition machine.

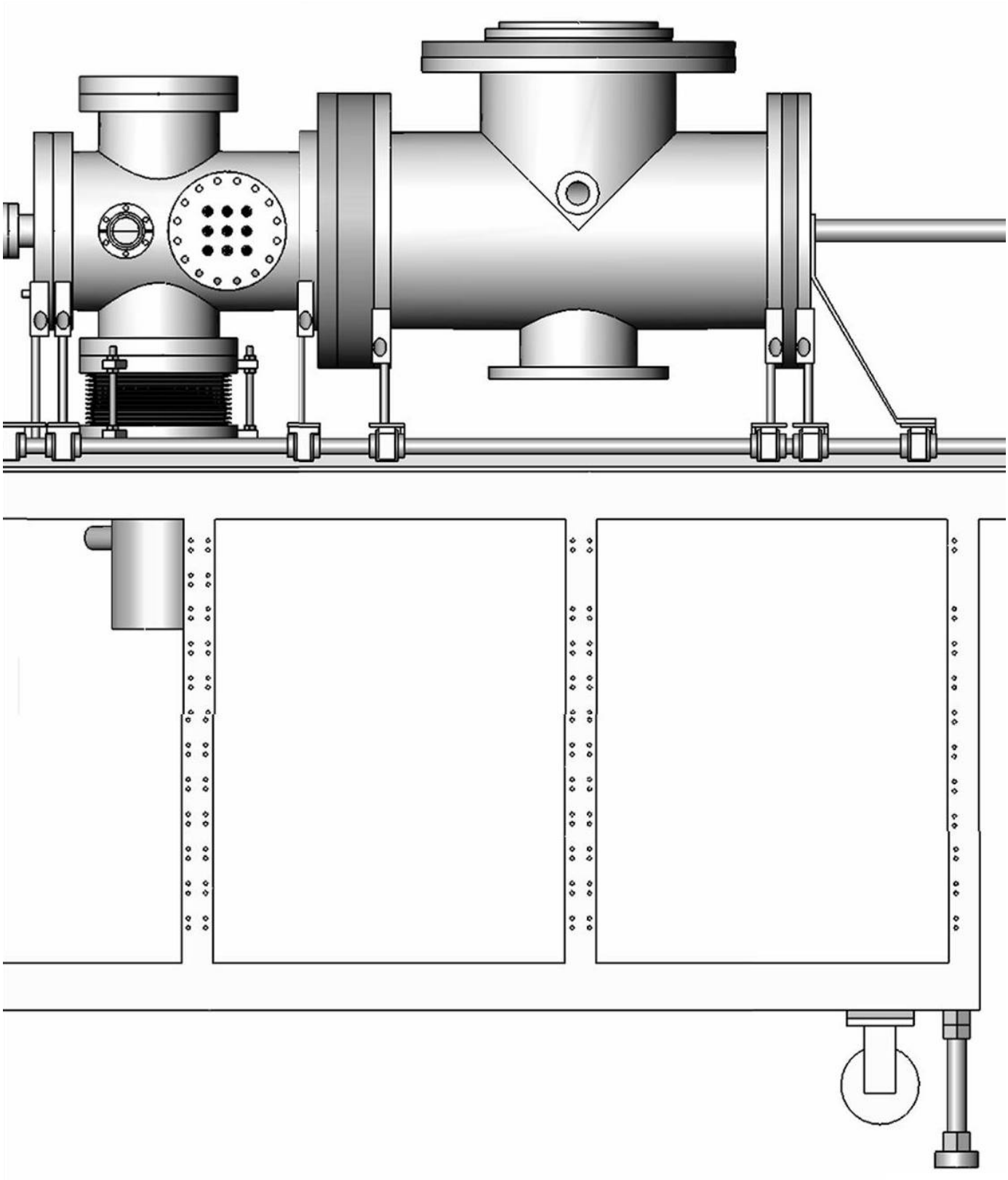

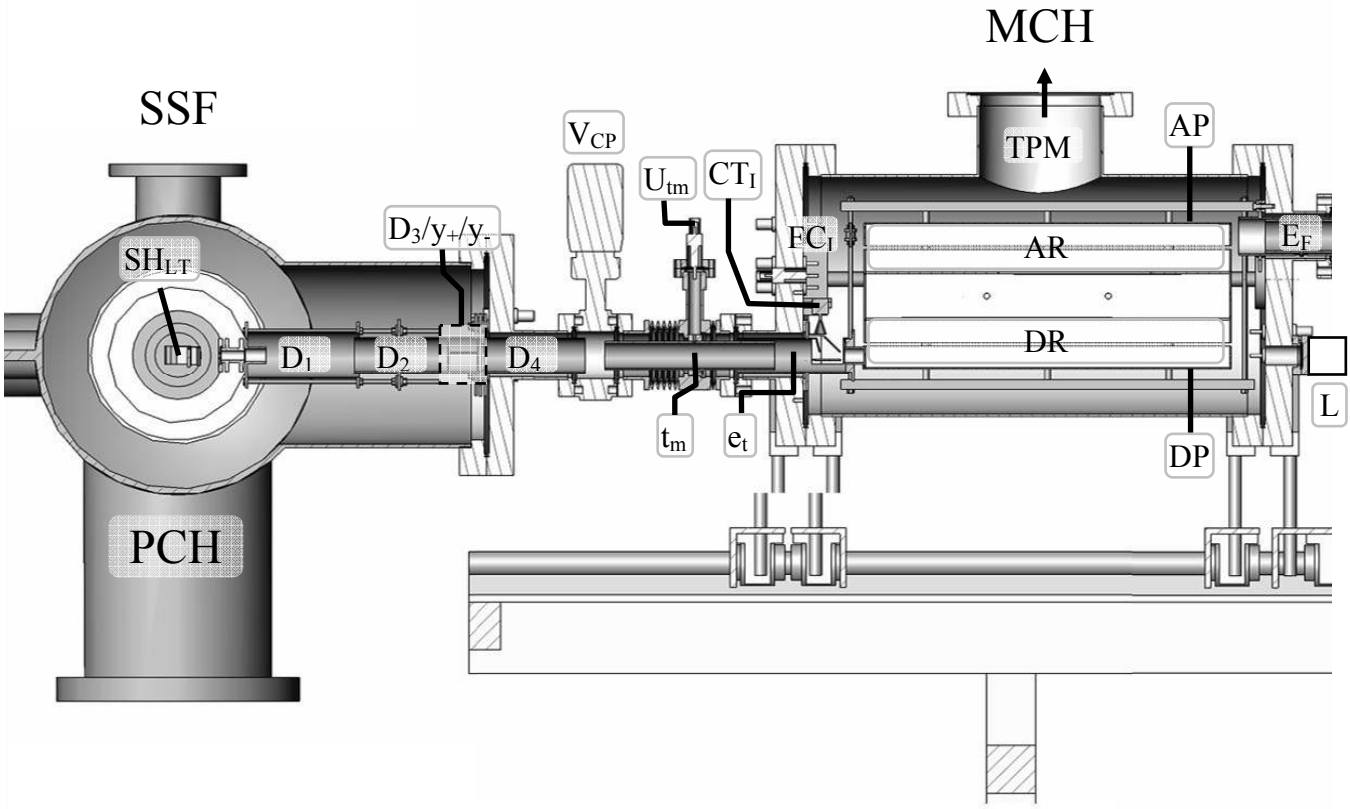

Figure 7.91 Cross-sectional full-size drawing of the cluster deposition machine.

SSF: Surface Science Facility, SH_{LT}: LT-Sample Holder, PCH: Preparation Chamber, D_1, D_2, and D_4: Deposition Optics, D_3 and y_+/y_-: y-deflector electrode combination, MCH: mass-selector chamber, V_{CP}: connection valve between SSF and MCH., t_m: movable tube, U_{tm}: high voltage connector of the movable tube, e_t: exit tube (of the mass-selector), CT_I: channeltron I, FC_I: FARADAY Cup I, AR: acceleration region, AP: acceleration plate, DR: deceleration region, DP: deceleration plate TPM: turbo pump of the mass-selector chamber, E_F: focusing electrode, L: Laser.

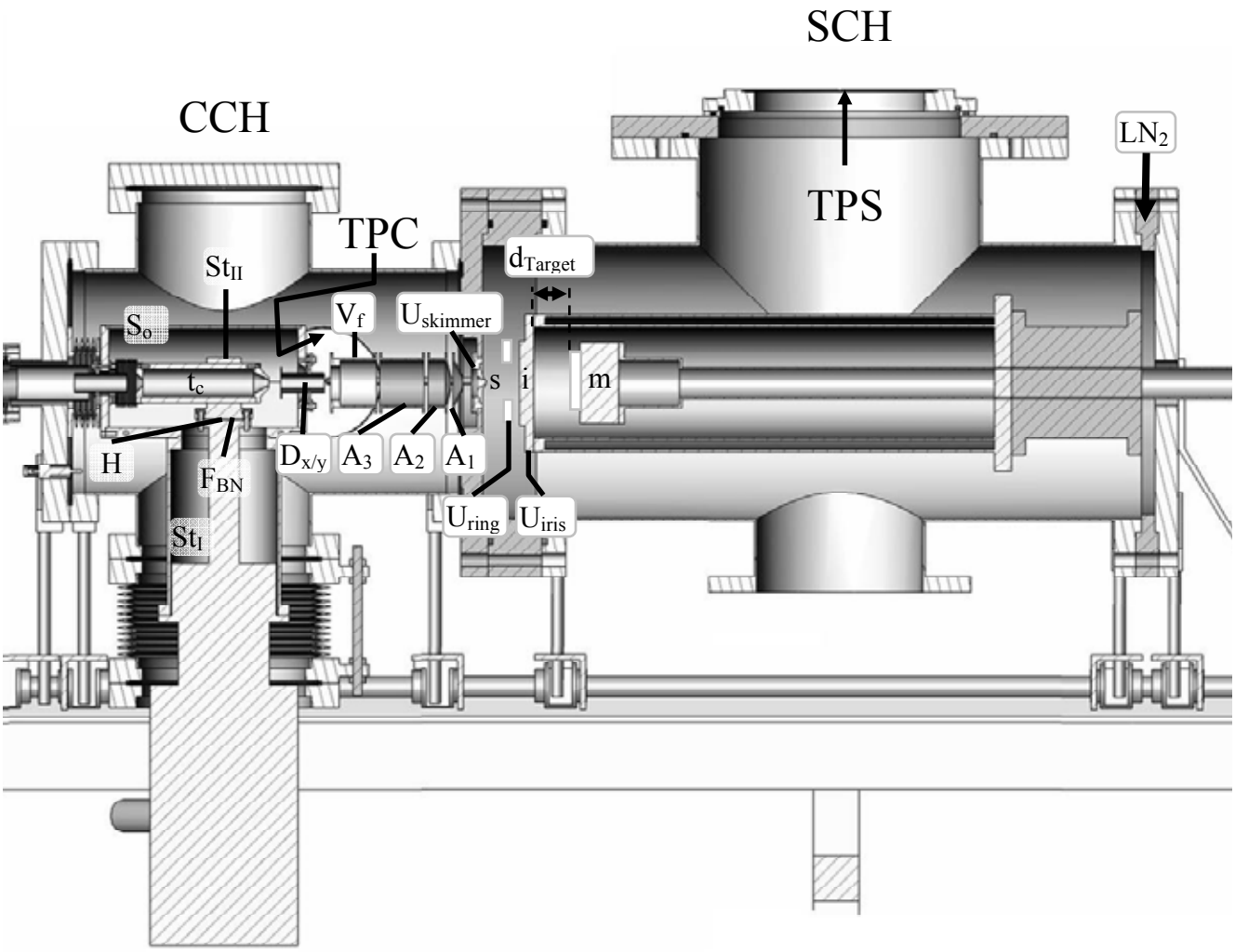

CCH: cryo-pump chamber, H: cryo cold head, S_o: outer shielding, t_C: cryo tube, ST_I: 1st stage of H, ST_{II}: 2nd stage of H, F_{BN}: Boron Nitride foil, $D_{x/y}$: x-y-deflector plates, TPC: turbo pump of the cryo-pump chamber, V_f: floating voltage, A_3, A_2 and A_1: acceleration electrodes, SCH: cluster source chamber s: skimmer, i: iris, m: magnetron sputter discharge head, d_{Target}: distance between target and iris, TPS: turbo pump of the cluster source chamber. LN_2: liquid nitrogen cooling cycle.

7.2 Gifford-McMahon cool head *Coolpower 5/100T*

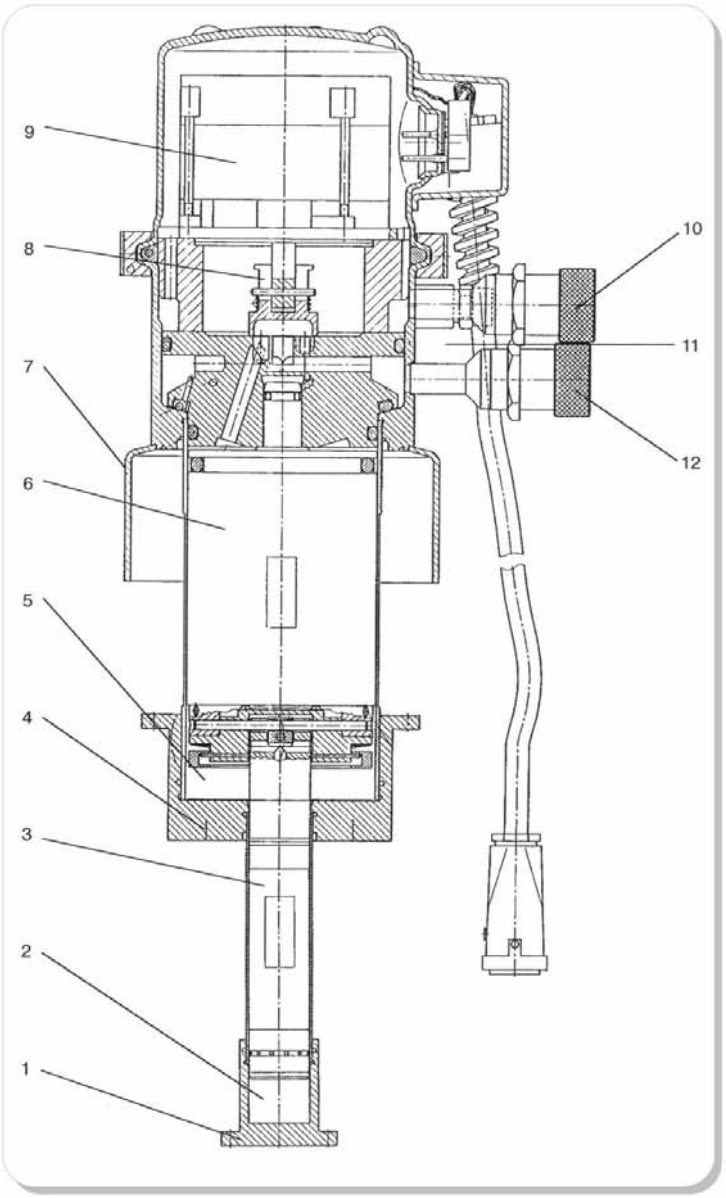

Figure 7.92 Schematic depiction of the Two-stage Gifford-McMahon cool head *Coolpower 5/100T*. (1) 2nd (refrigeration) stage, cooper flange, (2) Expansion volume, 2nd stage, (3) Displacer piston, 2nd stage, (4) 1st (refrigeration) stage, copper flange, (5) Expansion volume, 1st stage, (6) Displacer piston, 1st stage, (7) Weld-on pipe, (8) Control valve, (9) Synchronous motor, (10) He high-pressure connection, (11) Safety valve, (12) He low-pressure connection [118].

7.3 Deposition Parameter Sets for Size-Selected Clusters

7.3.1 Deposition No. 3: Ag_{40} / HOPG

3RD DEPOSITION – AG_{40} CLUSTERS / HOPG			
Deposition time t_D [min.]	20	Power P_{source} [Watt]	5
Sample bias U_{sample} [V]	-800	Temperature T_{sample} [°C]	RT
Frequency f [Hz]	223569.70	Waiting time t_w [µs]	2
Mass m [amu]	4126	Cluster current I_{bd} (before deposition) [pA]	6.3
Flux Φ Ar / He [sccm/sccm]	160 / 200	Cluster current I_{ad} (after deposition) [nA]	2.8
d_{Target} [cm]	11.5	U_{focus} [V]	-239.3
U_{Ring} [V]	0	U_{tm} [V]	-648
U_{Iris} [V]	0	$U_{deflector\ top}$ [V]	-474
A_1 [V]	-132.2	$U_{deflector\ down}$ [V]	$U_{Float.\ V.}$
A_2 [V]	-450.6	U_{D1} [V]	-438
A_3 [V]	-12.6	U_{D2} [V]	-149.8
$U_{skimmer}$ [V]	-16.61	U_{D3} [V]	-231.1
U_{Y-} [V]	-502	U_{D4} [V]	-648
U_{Y+} [V]	-494	U_{Y-} [V]	-239.8
U_{X+} [V]	-493	U_{Y+} [V]	-225.8
U_{X-} [V]	-503	$U_{Float.\ V.}$	-500

Table 7.16 Deposition Parameters for Ag_{40} / HOPG.

7.3.2 Deposition No. 13: Ag_{55}/ C_{60}/Au

13TH DEPOSITION - Ag_{55} CLUSTERS / 1 ML C_{60} / Au(111)			
Deposition time t_D [min.]	10	Power P_{source} [Watt]	14
Sample bias U_{sample} [V]	- 5	Temperature T_{sample} [°C]	40
Frequency f [Hz]	185924,4	Waiting time t_w [µs]	3
Mass m [amu]	5980	Cluster current I_{bd} (before deposition) [pA]	67
Flux Φ Ar / He [sccm/sccm]	81.6 / 384	Cluster current I_{ad} (after deposition) [nA]	N/A
d_{Target} [cm]	13	U_{focus} [V]	-213,573
U_{Ring} [V]	25.596	U_{tm} [V]	-579,19
U_{Iris} [V]	10,2816	$U_{deflector\ top}$ [V]	-481,43
A_1 [V]	-48,002	$U_{deflector\ down}$ [V]	Float. V.
A_2 [V]	-306,20	U_{D1} [V]	-0,0501
A_3 [V]	-12,7095	U_{D2} [V]	-145,534
$U_{skimmer}$ [V]	-17,3375	U_{D3} [V]	-240,08
U_{Y-} [V]	-496,36	U_{D4} [V]	-579,24
U_{Y+} [V]	-499,26	U_{Y-} [V]	-240,75
U_{X+} [V]	-495,82	U_{Y+} [V]	-231,373
U_{X-} [V]	-499,80	$U_{Float.\ V.}$	- 500 V

Table 7.17 Deposition Parameters for Ag_{55} on 1 ML C_{60}.

7.3.3 Deposition No. 18: $Ag_{147}/C_{60}/Au$

18TH DEPOSITION – Ag_{147} CLUSTERS / 1 ML C_{60} / AU(111)			
Deposition time t_D [min.]	5	Power P_{source} [Watt]	9
Sample bias U_{sample} [V]	-26	Temperature T_{sample} [°C]	RT
Frequency f [Hz]	113962.30	Waiting time t_w [µs]	4
Mass m [amu]	15915	Cluster current I_{bd} (before deposition) [pA]	92
Flux Φ Ar / He [sccm/sccm]	100 / 500	Cluster current I_{ad} (after deposition) [nA]	74
d_{Target} [cm]	16.5	U_{focus} [V]	-192.642
U_{Ring} [V]	25.094	U_{tm} [V]	-651.54
U_{Iris} [V]	21.922	$U_{deflector\ top}$ [V]	-488
A_1 [V]	-127.988	$U_{deflector\ down}$ [V]	$U_{Float.\ V.}$
A_2 [V]	-145.937	U_{D1} [V]	-486.77
A_3 [V]	-13.725	U_{D2} [V]	-99.551
$U_{skimmer}$ [V]	-11.94	U_{D3} [V]	-237.99
U_{Y-} [V]	-494.19	U_{D4} [V]	-652.26
U_{Y+} [V]	-501.04	U_{Y-} [V]	-241.41
U_{X+} [V]	-496.67	U_{Y+} [V]	-222.640
U_{X-} [V]	-499.11	$U_{Float.\ V.}$	-499.9

Table 7.18 Deposition Parameters for Ag_{147} on 1 ML C_{60}.

7.3.4 Deposition No. 19: $Ag_{309}/C_{60}/Au$

19TH DEPOSITION – AG_{309} CLUSTERS / 1 ML C_{60} / AU(111)			
Deposition time t_D [min.]	7	Power P_{source} [Watt]	9
Sample bias U_{sample} [V]	-50	Temperature T_{sample} [°C]	53.17
Frequency f [Hz]	78650.13	Waiting time t_w [µs]	6
Mass m [amu]	33412	Cluster current I_{bd} (before deposition) [pA]	70
Flux Φ Ar / He [sccm/sccm]	100 / 435	Cluster current I_{ad} (after deposition) [nA]	70
d_{Target} [cm]	N/A	U_{focus} [V]	N/A
U_{Ring} [V]	N/A	U_{tm} [V]	N/A
U_{Iris} [V]	N/A	$U_{deflector\ top}$ [V]	N/A
A_1 [V]	N/A	$U_{deflector\ down}$ [V]	$U_{Float.\ V.}$
A_2 [V]	N/A	U_{D1} [V]	N/A
A_3 [V]	N/A	U_{D2} [V]	N/A
$U_{skimmer}$ [V]	N/A	U_{D3} [V]	N/A
U_{Y-} [V]	N/A	U_{D4} [V]	N/A
U_{Y+} [V]	N/A	U_{Y-} [V]	N/A
U_{X+} [V]	N/A	U_{Y+} [V]	N/A
U_{X-} [V]	N/A	$U_{Float.\ V.}$	N/A

Table 7.19 Deposition Parameters for Ag_{309} on 1 ML C_{60} (depo 19).

7.3.5 Deposition No. 21: $Ag_{309}/C_{60}/Au$

21TH DEPOSITION – Ag_{309} CLUSTERS / 1 ML C_{60} / AU(111)			
Deposition time t_D [min.]	15	Power P_{source} [Watt]	9
Sample bias U_{sample} [V]	10	Temperature T_{sample} [°C]	RT
Frequency f [Hz]	78650.13	Waiting time t_w [µs]	6
Mass m [amu]	33412	Cluster current I_{bd} (before deposition) [pA]	60
Flux Φ Ar / He [sccm/sccm]	100 / 318	Cluster current I_{ad} (after deposition) [nA]	60
d_{Target} [cm]	N/A	U_{focus} [V]	N/A
U_{Ring} [V]	N/A	U_{tm} [V]	N/A
U_{Iris} [V]	N/A	$U_{deflector\ top}$ [V]	N/A
A_1 [V]	N/A	$U_{deflector\ down}$ [V]	$U_{Float.\ V.}$
A_2 [V]	N/A	U_{D1} [V]	N/A
A_3 [V]	N/A	U_{D2} [V]	N/A
$U_{skimmer}$ [V]	N/A	U_{D3} [V]	N/A
U_{Y-} [V]	N/A	U_{D4} [V]	N/A
U_{Y+} [V]	N/A	U_{Y-} [V]	N/A
U_{X+} [V]	N/A	U_{Y+} [V]	N/A
U_{X-} [V]	N/A	$U_{Float.\ V.}$	N/A

Table 7.20 Deposition Parameters for Ag_{309} on 1 ML C_{60} (depo 21).

7.3.6 Deposition No. 23: $Ag_{561}/C_{60}/Au$

23RD DEPOSITION – AG_{561} CLUSTERS / 1 ML C_{60} / AU(111)			
Deposition time t_D [min.]	15	Power P_{source} [Watt]	9
Sample bias U_{sample} [V]	-2	Temperature T_{sample} [°C]	RT
Frequency f [Hz]	583687.2	Waiting time t_w [µs]	9
Mass m [amu]	60628	Cluster current I_{bd} (before deposition) [pA]	56
Flux Φ Ar / He [sccm/sccm]	80.8 / 413	Cluster current I_{ad} (after deposition) [nA]	50
d_{Target} [cm]	N/A	U_{focus} [V]	N/A
U_{Ring} [V]	N/A	U_{tm} [V]	N/A
U_{Iris} [V]	N/A	$U_{deflector\ top}$ [V]	N/A
A_1 [V]	N/A	$U_{deflector\ down}$ [V]	$U_{Float.\ V.}$
A_2 [V]	N/A	U_{D1} [V]	N/A
A_3 [V]	N/A	U_{D2} [V]	N/A
$U_{skimmer}$ [V]	N/A	U_{D3} [V]	N/A
U_{Y-} [V]	N/A	U_{D4} [V]	N/A
U_{Y+} [V]	N/A	U_{Y-} [V]	N/A
U_{X+} [V]	N/A	U_{Y+} [V]	N/A
U_{X-} [V]	N/A	$U_{Float.\ V.}$	N/A

Table 7.21 Deposition Parameters for Ag_{561} on 1 ML C_{60}.

7.3.7 Deposition No. 20: $Ag_{923}/C_{60}/Au$

20TH DEPOSITION – Ag_{923} CLUSTERS / 1 ML C_{60} / AU(111)			
Deposition time t_D [min.]	30	Power P_{source} [Watt]	9
Sample bias U_{sample} [V]	-1	Temperature T_{sample} [°C]	RT
Frequency f [Hz]	45525.32	Waiting time t_w [µs]	11
Mass m [amu]	99729	Cluster current I_{bd} (before deposition) [pA]	30
Flux Φ Ar / He [sccm/sccm]	100 / 319	Cluster current I_{ad} (after deposition) [nA]	30
d_{Target} [cm]	15	U_{focus} [V]	-197.351
U_{Ring} [V]	17.685	U_{tm} [V]	-671.93
U_{Iris} [V]	14.705	$U_{deflector\ top}$ [V]	-487
A_1 [V]	-79.147	$U_{deflector\ down}$ [V]	$U_{Float.\ V.}$
A_2 [V]	-172.644	U_{D1} [V]	-1.461
A_3 [V]	-9.798	U_{D2} [V]	-106.902
$U_{skimmer}$ [V]	-10.322	U_{D3} [V]	-236.04
U_{Y-} [V]	-497.93	U_{D4} [V]	-671.91
U_{Y+} [V]	-497.77	U_{Y-} [V]	-241.40
U_{X+} [V]	-497.94	U_{Y+} [V]	-227.495
U_{X-} [V]	-497.79	$U_{Float.\ V.}$	-500

Table 7.22 Deposition Parameters for Ag_{923} on 1 ML C_{60}.

7.3.8 Deposition No. 9: Ag_{2130}/10 ML Xe /Au

9TH DEPOSITION – AG_{2130} CLUSTERS / 10 ML XE / AU(111)			
Deposition time t_D [min.]	30	Power P_{source} [Watt]	8
Sample bias U_{sample} [V]	-50	Temperature T_{sample} [K]	30
Frequency f [Hz]	30092.9	Waiting time t_w [µs]	17
Mass m [amu]	230000	Cluster current I_{bd} (before deposition) [pA]	0.98
Flux Φ Ar / He [sccm/sccm]	85.8 / 136	Cluster current I_{ad} (after deposition) [nA]	0.88
d_{Target} [cm]	N/A	U_{focus} [V]	N/A
U_{Ring} [V]	N/A	U_{tm} [V]	N/A
U_{Iris} [V]	N/A	$U_{deflector\ top}$ [V]	N/A
A_1 [V]	N/A	$U_{deflector\ down}$ [V]	N/A
A_2 [V]	N/A	U_{D1} [V]	N/A
A_3 [V]	N/A	U_{D2} [V]	N/A
$U_{skimmer}$ [V]	N/A	U_{D3} [V]	N/A
U_{Y-} [V]	N/A	U_{D4} [V]	N/A
U_{Y+} [V]	N/A	U_{Y-} [V]	N/A
U_{X+} [V]	N/A	U_{Y+} [V]	N/A
U_{X-} [V]	N/A	$U_{Float.\ V.}$	N/A

Table 7.23 Deposition Parameters for Ag_{2130} on 1 ML C_{60}.

Chapter 8

PUBLICATIONS

List of already published results of this thesis and further results.

8.1 Published Papers

T. IRAWAN, I. BARKE and H. HÖVEL: *Size-dependent morphology of gold clusters grown on nanostructured graphite*, Appl. Phys. A **80**, 929 (2005).
http://dx.doi.org/10.1007/s00339-004-3118-8 or
http://e1.physik.uni-dortmund.de/T_Irawan_Appl_Phys_A_80_929_2005.pdf

T. IRAWAN, D. BOECKER, F. GHALEH, C. YIN, B. V. ISSENDORFF, and H. HÖVEL: *Metal Clusters on Rare Gas Layers – Growth and Spectroscopy*, Appl. Phys. A **82**, 81 (2006).
http://e1.physik.uni-dortmund.de/T_Irawan_Appl_Phys_A_82_081_2006.pdf

8.2 Conference Visits and Contributions

1	10.03. - 21.03.2003	-	34th IFFSpring School 2003, *Fundamentals of Nanoelectronics*, FZ-Jülich.
2	24.03. - 28.03.2003	talk	I. BARKE, T. IRAWAN, H. HÖVEL: *Morphologie und quantisierte elektronische Struktur von Goldclustern auf Graphit*, DPG Frühjahrstagung, Dresden.
3	15.09. – 16.09.2003	talk	I. BARKE, T. IRAWAN, H. HÖVEL: *Spektroskopie an Goldclustern unterschiedlicher Größe auf Graphit*, 13. NRW Treffen Oberflächenphysik, Münster.
4	5.10. - 10.10.2003	poster	T. IRAWAN, I. BARKE, H. HÖVEL: *Goldcluster in Nanogruben: Wachstumsprozess und Morphologie*, 312. Wilhelm und Else Heraeus-Seminar über freie und deponierte Cluster, Brand (Österreich).
5	7.11.2003	poster	T. IRAWAN, I. BARKE, H. HÖVEL: *Goldcluster in Nanogruben: Wachstumsprozess und Morphologie*, 3. Materialwissenschaftliches Forum, Wuppertal.
6	18.11.2003	talk	T. IRAWAN, I. BARKE und H. HÖVEL: *Morphologie von Goldclustern, Seminar für Beschleunigerphysik und Synchrotronstrahlung*, Anwendung in der Festkörperphysik, Dortmund.
7	4.03. - 6.03.2004	talk	T. IRAWAN, I. BARKE und H. HÖVEL: *Gold clusters in nanopits: growth process and morphology*, DPG Frühjahrstagung, Regensburg.

8	4.03. - 6.03.2004	talk	I. BARKE, T. IRAWAN und H. HÖVEL: *Spectroscopy of gold clusters on graphite for a broad range of cluster sizes*, DPG Frühjahrstagung, Regensburg
9	8.05. - 13.05.2004	poster	T. IRAWAN, I. BARKE und H. HÖVEL: *Size-dependent morphology of gold clusters on graphite*, EURESCO Conference: Cluster – Surface Interactions, Giens (near Toulon,) Frankreich.
10	17.06. - 19.06.2004	talk	D. BOECKER, T. IRAWAN, I. BARKE, H. HÖVEL und C. YIN, B. V. ISSENDORFF: *Metallinseln auf Edelgaschichten: Photoemission und Rastertunnelmikroskopie*, DFG Kolloquium im SPP 115, Bad Honnef.
11	20.07.2004	talk	T. IRAWAN, D. BOECKER, F. Ghaleh, I. BARKE und H. HÖVEL: *Metallinseln auf Oberflächen als Modellsysteme für Einzelelektronen-Transport*, Seminar zum Graduiertenkolleg 726: Materialeigenschaften und Konzepte zur Quanteninformationsverarbeitung, Dortmund
12	06.09.- 10.09.2004	poster	C. YIN, D. BOECKER, T. IRAWAN, I. BARKE, H. HÖVEL, and B. V. ISSENDORFF: *Spectroscopy of free clusters and clusters on surfaces*, ISSPIC12 (12th International Symposium on Small Particles and Inorganic Clusters), Nanjing, P. R. China.
13	07.10.- 08.10.2004	poster	C. YIN, D. BOECKER, T. IRAWAN, I. BARKE, H. HÖVEL, and B. V. ISSENDORFF: *Spectroscopy of free clusters and clusters on surfaces*, 13th Internal FMF (Freiburger Materialforschungszentrum) Colloquium, Titisee.
14	29.11. – 3.12.2004	poster	T. IRAWAN, D. BOECKER, F. GHALEH, I. BARKE, H. HÖVEL und C. YIN, B. V. ISSENDORFF: *Metal clusters on rare gas layers: growth and spectroscopy*, International Workshop on ATOMIC PHYSICS Max-Planck-Institut für Physik Komplexer Systeme, Dresden.

15	24.02. – 25.02.2005	poster	T. IRAWAN, D. BOECKER, F. GHALEH, I. BARKE, H. HÖVEL und C. YIN, B. V. ISSENDORFF: *Metal clusters on rare gas layers: growth and spectroscopy*, DFG-Kolloquium 1153 *Cluster in Kontakt mit Oberflächen: Elektronenstruktur und Magnetismus,* Antragskolloquium Physikzentrum Bad Honeff.
16	24.02. – 25.02.2005	talk	H. HÖVEL, T. IRAWAN, D. BOECKER, F. GHALEH und C. YIN, B. V. ISSENDORFF: *Ladungstransport*, DFG-Schwerpunktsprogramm 1153 *Cluster in Kontakt mit Oberflächen: Elektronenstruktur und Magnetismus,* Antragskolloquium Physikzentrum Bad Honeff.
17	28.02.- 03.03.2005	poster	C. YIN, D. BOECKER, T. IRAWAN, I. BARKE, H. HÖVEL, and B. V. ISSENDORFF: *Spectroscopy of free clusters and clusters on surfaces*, Symposium on Size Selected Clusters, Brand, Austria.
18	4.03. – 9.03.2005	poster	F. GHALEH, T. IRAWAN, D. BOECKER, I. BARKE, H. HÖVEL and C. YIN, B. V. ISSENDORFF: *Study of metal cluster growth on rare gas layers using STM and UPS*, DPG Frühjahrstagung, Berlin.
19	4.03. – 9.03.2005	poster	I. BARKE, T. IRAWAN, and H. HÖVEL: *Photoelectron spectra of quantized states on cluster facets,* DPG Frühjahrstagung, Berlin.
20	4.03. – 9.03.2005	talk	T. IRAWAN, D. BOECKER, F. GHALEH, I. BARKE, H. HÖVEL, C. YIN, and B. V. ISSENDORFF: *Photoelectron spectroscopy of free clusters on surfaces*, DPG Frühjahrstagung, Berlin.
21	14.06.2005	talk	T. IRAWAN, F. GHALEH, S. KRAUSE, H. HÖVEL, and C. YIN, B. V. ISSENDORFF: *Experiments with Mass-selected Clusters*, Dortmund.

22	11.09. – 16.09.2005	poster	T. IRAWAN, D. BOECKER, F. GHALEH, S. KRAUSE, M. Bieletzki, H. HÖVEL and C. YIN, B. V. ISSENDORFF: E*xperiments for Deposition of Clusters on Rare Gas Layers*, CFN Symposium: Cluster als molekulare Nanostrukturen, Bad Herrenalb.
23	22.09. – 25.09.2005	talk	T. IRAWAN, F. GHALEH, S. KRAUSE, M. Bieletzki, H. HÖVEL and C. YIN, B. V. ISSENDORFF: *Experiments with mass-selected Clusters*, 2nd Workshop GK726 Materials and Concepts of Quantum Information Processing, Hirschegg/Kleinwalsertal.
24	06.10.- 07.10.2005	poster	C. YIN, D. BOECKER, T. IRAWAN, I. BARKE, H. HÖVEL and B. V. ISSENDORFF: *Experiments for Depostion of Clusters on Rare Gas Layers*, 14th internal FMF (Freiburg Materials Research Center) Colloquium, Titisee.
25	24.10. – 25.10.2005	talk	T. IRAWAN, D. BOECKER, F. GHALEH, I. BARKE, H. HÖVEL, C. YIN and B. V. ISSENDORFF: *Metallcluster auf Edelgasschichten – Wachstum und Spektroskopie*, NRW-Mitarbeitertreffen Oberflächenphysik und -chemie, Bonn.
26	24.10. – 25.10.2005	talk	S. KRAUSE, T. IRAWAN, M. Bieletzki, H. HÖVEL, C. YIN, B. V. ISSENDORFF: *Experimente zur Deposition massenselektierter Cluster*, NRW-Mitarbeitertreffen Oberflächenphysik und -chemie, Bonn.
27	10.01.2006	talk	S. KRAUSE, T. IRAWAN, M. Bieletzki, H. HÖVEL, C. YIN, B. V. ISSENDORFF: *Setup for the Study of Mass Selected Clusters at Surfaces*, Seminar für Beschleunigerphysik und Synchrotronstrahlung; Anwendung in der Festkörperphysik, Dortmund.
28	7.02.2006	talk	M. Bieletzki, T. IRAWAN, S. KRAUSE, H. HÖVEL, C. YIN, B. V. ISSENDORFF: *STM - Messungen von Clustern auf Oberflächen*, Seminar für Beschleunigerphysik und Synchrotronstrahlung; Anwendung in der Festkörperphysik, Dortmund.

29	13.03. – 17.03.2006	talk	T. IRAWAN, S. KRAUSE, M. Bieletzki, H. HÖVEL, C. YIN, B. V. ISSENDORFF: *Clusters at Surfaces Studied with Low-Temperature STM and UPS*, APS Marchmeeting, Baltimore (USA).
30	27.03. – 31.03.2006	poster	M. Bieletzki, T. IRAWAN, S. KRAUSE, H. HÖVEL, C. YIN, B. V. ISSENDORFF: *Scanning Tunneling Microscopy and Photoemission of Clusters at Surfaces*, DPG Frühjahrstagung, Dresden.
31	27.03. – 31.03.2006	talk	S. KRAUSE, T. IRAWAN, M. BIELETZKI, H. HÖVEL, C. YIN, B. V. ISSENDORFF: *Setup for the Study of Mass Selected Clusters at Surfaces with Low Temperature STM and UPS*, DPG Frühjahrstagung, Dresden.
32	28.05.- 02.06.2006	poster	T. IRAWAN, S. KRAUSE, M. BIELETZKI, T. RICHTER, H. HÖVEL, C. YIN, B. V. ISSENDORFF: *Mass Selected (Magic?!) Silver Clusters on Surfaces*, ICCS (International Conference on Clusters at Surfaces, Rostock.
33	28.05.- 02.06.2006	talk	H. HÖVEL, T. IRAWAN, S. KRAUSE, M. BIELETZKI, C. YIN, B. V. ISSENDORFF: *Electronic Structure of supported clusters as observed by STM/STS and photoemission*, ICCS (International Conference on Clusters at Surfaces, Rostock.
34	11.07.2006	talk	T. IRAWAN, S. KRAUSE, M. BIELETZKI, T. RICHTER, H. HÖVEL, C. YIN, B. V. ISSENDORFF: *Mass Selected (Magic?!) Silver Clusters on Surfaces*, Seminar of the PhD Program (726) in Materials and Concepts for Quantum Information Processing, Dortmund.
35	23.07- 28.07.2006	poster	H. HÖVEL, T. IRAWAN, S. KRAUSE, M. Bieletzki, T. RICHTER, C. YIN, B. V. ISSENDORFF: I*ndividual mass-selected silver clusters observed by STM/STS and photoemission*, International Symposium on Small Particles and Inorganic Clusters - ISSPIC XIII, Göteborg (Sweden)

Chapter 9

REFERENCES

[001] C. R. HENRY: *Surface studies of supported model catalysts,* Surf. Sci. Rep. **31,** 231 (1998).

[002] P. JENSEN: *Growth of nanostructures by cluster deposition: Experiments and simple models,* Rev. Mod. Phys. **71,** 1695 (1999).

[003] W. HARBICH: *Collision of Clusters with Surfaces* in *Metal Clusters at Surfaces,* ed. K.-H. MEIWES-BROER (Springer, Berlin Heidelberg, 2000).

[004] M. SCHMIDT, R. KUSCHE, W. KRONMÜLLER, B. V. ISSENDORFF, and H. HABERLAND: *Experimental Determination of the Melting Point and Heat Capacity for a Free Cluster of 139 Sodium Atoms,* Phys. Rev. Lett. **79,** 99 (1997).

[005] DFG priority program SPP 1153: *Clusters in Contact with Surfaces – Electronic Structure and Magnetism,* website: .....

[006] F. FURCHE, R. AHLRICHS, P. WEIS, C. JACOB, S. GILB, T. BIERWEILER and M. M. KAPPES: *The structures of small gold cluster anions as determined by a combination of ion mobility measurements and density functional calculations,* J. Chem. Phys. **117,** 6982 (2002).

[007] A. KIRILYUK, K. DEMYK, G. V. HELDEN, G. MEIJER, A. I. POTERYAEV and A. I. LICHTENSTEIN: *Atomic clusters of magnetic oxides: Structure and phonons,* J. Appl. Phys **93,** 7379 (2003).

[008] H. P. BONZEL: *3D equilibrium crystal shapes in the new light of STM and AFM*, Phys. Rep. **385**, 1 (2003).

[009] H. HÄKKINEN, M. MOSELER, O. KOSTKO, M. ASTRUC HOFFMANN, N. MORGNER, and B. V.ISSENDORFF: *Symmetry and structure of noble metal nanoparticles and the role of relativity,* Phys. Rev. Lett. **93,** 093401 (2004).

[010] H. HABERLAND, T. HIPPLER, J.DONGES, O. KOSTKO, M. SCHMIDT, and B. V. ISSENDORFF: *Melting of Sodium Cluster: where do the Magic Numbers come from,* Phys. Rev. Lett. **94,** 035701 (2005).

[011] M. ASTRUC HOFFMANN, G. WRIGGE, and B. v. ISSENDORFF: *Photoelectron spectroscopy of Al32000-: Observation of a "Coulomb staircase" in a free cluster,* Phys. Rev. B **66,** 041404 (2002).

[012] W. P. HALPERIN: *Quantum size effects in metal particles,* Rev. Mod. Phys. **58,** 533 (1986).

[013] W. A. DE HEER: *The physics of simple metal clusters: experimental aspects and simple models,* Rev. Mod. Phys. **65,** 611 (1993).

[014] *Metal Clusters at Surfaces* ed. K.-H. MEIWES-BROER (Springer, Berlin Heidelberg, 2000).

[015] P. A. TIPLER AND R. A. LLEWELLYN, *Moderne Physik* (Oldenburg München Wien, 2003).

[016] J. L. MARTINS, J. BUTTET, and R. CAR: *Electronic and structural properties of sodium clusters,* Phys. Rev. B **31,** 1804 (1985).

[017] B. K. RAO, P. JENA, M. MANNINEN, and R. M. NIEMINEN: *Spontaneous fragmentation of multiply charged metal clusters,* Phys. Rev. Lett. **58,** 1188 (1987).

[018] G. V. HELDEN, M.-T. HSU, N. GOTTS, and M. T. BOWERS: *Carbon cluster cations with up to 84 atoms: structures, formation mechanism, and reactivity,* J. Phys. Chem. **97,** 8182 (1993).

[019] H. HÖVEL, T. BECKER, D. FUNNEMANN, B. GRIMM, C. QUITMANN and B. REIHL: *High-resolution photoemission combined with low-temperature STM,* J. Electron Spectros. Rel. Phenom. **88,** 1015 (1998).

[020] H.-J. GÜNTHERODT and R. WIESENDANGER: *Scanning Tunneling Microscopy I* (Springer Berlin Heidelberg New York, 1994).

[021] F. BESENBACHER: *Scanning Tunneling Microscopy Studies of Metal Surfaces,* Rep. Prog. Phys. **59,** 1737 (1996).

[022] G. BINNING, H. ROHRER, CH. GERBER, and E. WEIBEL: *Surface Studies by Scanning Tunneling Microscopy,* Phys. Rev. Lett. **49,** 57 (1982).

[023] G. BINNIG and H. ROHRER: *Scanning Tunneling Microscopy,* Hel. Phys. Acta, **55,** 726 (1982).

[024] G. BINNIG and H. ROHRER: *Scanning Tunneling Microscopy,* IBM J. Res. Develop. **30,** 4 (1986).

[025] T. MAYER KUCKUK, Kernphysik, (Teubner-Verlag, Stuttgart, 1985).

[026] E. U. CONDON and R. W. GURNEY: *Wave mechanics and radioactive disintegration,* Nature **122,** 439 (1928).

[027] R. W. GURNEY and E. U. CONDON: *Quantum Mechanics and Radioactive Disintegration,* Phys. Rev. **33,** 127 (1929).

[028] A. ANDREEFF: *Tunnel-Effekt,* in *Effekte der Physik und ihre Anwendungen,* ed. M. V. ARDENNE, G. MUSIOL, and U. KLEMRADT, (Verlag Harri Deutsch, Frankfurt, 2005).

[029] P. EBERT: *Rastersondenmikroskopie,* in *Effekte der Physik und ihre Anwendungen,* ed. M. V. ARDENNE, G. MUSIOL, and U. KLEMRADT, (Verlag Harri Deutsch, Frankfurt, 2005).

[030] T. IRAWAN: *Morphologie und elektronische Struktur von Edelmetallclustern hergestellt durch gesteuertes Wachstum auf HOPG,* Diploma Thesis, University of Dortmund (2003).

[031] H. HÖVEL, T. BECKER, A. BETTAC, B. REIHL, M. TSCHUDY and E. J. WILLIAMS: *Controlled cluster condensation into preformed nanometer-sized pits,* J. Appl. Phys. **81,** 154 (1997).

[032] M. HENZLER and W. GÖPEL: *Oberflächenphysik des Festkörpers* (B. G. Teubner, Stuttgart, 1991).

[033] J. BARDEEN: *Tunneling from A Many-Particle Point of View,* Phys. Rev. Lett. **6,** 57 (1961).

[034] J. TERSOFF and D. R. HAMANN: *Theory of the Scanning Tunneling Microscope,* Phys. Rev. B **31,** 805 (1985).

[035] J. TERSOFF and D. R. HAMANN: *Theory and Application for the Scanning Tunneling Microscope,* Phys. Rev. Lett. **50,** 1998 (1983).

[036] B. GRIMM: *Tunnelspektroskopie und Photoemission bei tiefen Temperaturen an Edelgas-Modellsystemen und Nanostrukturen,* Dissertation, University of Dortmund (2000).

[037] A. SELLONI, P. CARNEVALI, E. TOSSATTI and C. D. CHEN: *Voltage-Dependent Scanning-Tunneling Microscopy of a Crystal Surface: Graphite,* Phys. Rev. B **31,** 2602 (1985), *idem* **34,** 7406 (1986).

[038] J. A. STROSCIO, R. M. FEENSTRA and A. P. FEIN: *Electronic Structure of the Si(111)2 × 1 Surface by Scanning-Tunneling Microscopy,* Phys. Rev. Lett. **57,** 2579 (1986).

[039] C. J. CHEN: *Theory of Scanning Tunneling Spectroscopy,* J. Vac. Sci. Technol. A **6,** 319 (1988).

[040] I. BARKE: *Morphology and Electronic Structure of Gold Clusters on Graphite,* Dissertation, University of Dortmund (2004).

[041] H. R. HERTZ: *Über einen Einfluß des ultravioletten Lichtes auf die electrische Entladung,* Ann. Phys. u. Chem. **31,** 983 (1887).

[042] W. HALLWACHS: *Über den Einfluß des Lichtes auf electrostatisch geladene Körper,* Ann. Phys. u. Chem. **33,** 301 (1888).

[043] P. LENARD: *Erzeugung von Kathodenstrahlen durch ultraviolettes Licht,* Ann. Phys. **2,** 359 (1900).

[044] A. EINSTEIN: *Über einen die Erzeugung und Verwandlung des Lichtes betreffenden heuristischen Gesichtspunkt,* Ann. Phys. **17,** 132 (1905).

[045] S. HÜFNER: *Photoelectron spectroscopy* (Springer, Berlin Heidelberg New York, 1995).

[046] F. REINERT and S. HÜFNER: *Photoemission spectroscopy – from early days to recent applications,* New. J. Physics **7,** 97 (2005).

[047] C. N. BERGLUND and W. E. SPICER: *Photoemission Studies of Copper and Silver - Theory,* Phys. Rev. **136,** A1030 (1964).

[048] J. B. PENDRY: *Theory of photoemission,* Surf. Sci. **57,** 679 (1976).

[049] P. DOLLE, K. MARKERT, W. HEICHLER, N. R. ARMSTRONG, K. WANDELT, K. S. KIM AND, and R. A. FIATO: *Characterization of Pt/TiO2 surfaces by means of photoelectron spectroscopy of adsorbed xenon,* J. Vac. Sci. Technol. A **4,** 1465 (1986).

[050] A. JABLONSKI and K. WANDELT: *Quantitative aspects of ultraviolet photoemission of adsorbed xenon - a review,* Surface and Interface Analysis **17,** 611 (1991).

[051] K. WANDELT: *Surface characterization by photoemission of adsorbed xenon (PAX),* J. Vac. Sci. Technol. A **2,** 802 (1984).

[052] T. SCHMITZ-HÜBSCH, K. OSTER, J. RADNIK and K. WANDELT: *Photoemission from Quantum-Well States in Ultrathin Xe crystals,* Phys. Rev. Lett. **74,** 2595 (1995).

[053] A. SHNIRMAN and G. SCHÖN: *Quantum measurements performed with a single-electron transistor,* Phys. Rev. B **57,** 15400 (1998).

[054] R. WILKINS, E. BEN-JACOB, and R. C. JAKLEVIC: *Scanning-tunneling-microscope observations of Coulomb blockade and oxide polarization in small metal droplets,* Phys. Rev. Lett. **63,** 801 (1989).

[055] H. HÖVEL and I. BARKE: *Morphology and electronic structure of gold clusters on graphite: Scanning-tunneling techniques and photoemission*, Prog. Surf. Sci. **81**, 53 (2006).

[056] H. HÖVEL, B. GRIMM, M. POLLMANN, and B. REIHL: *Cluster-Substrate Interaction on a Femtosecond Time Scale Revealed by a High-Resolution Photoemission Study of the FERMI-LEVEL Onset,* Phys. Rev. Lett. **81,** 4608 (1998).

[057] H. HÖVEL, B. GRIMM, M. POLLMANN, and B. REIHL: *Femtosecond dynamics of final-state effects in the valence band photoemission of silver clusters,* The European Physical Journal D **9,** 595 (1999) .

[058] D. BOECKER: *Wachstum von Metallclustern auf Edelgasschichten und Analyse der elektronischen Wechselwirkung mit Hilfe von Ultravioletter Photoelektron Spektroskopie,* Diploma Thesis, University of Dortmund (2004).

[059] J. J. MÉTOIS, J. C. HEYRAUD, and R. KERN: *Surface decoration: Localization of crystallites along the steps,* Surf. Sci. **78,** 191 (1978).

[060] H. HÖVEL: *Clusters on surfaces: high-resolution spectroscopy at low temperatures,* Appl. Phys. A **72,** 295 (2001).

[061] H. HÖVEL, T. BECKER, A. BETTAC, B. REIHL, M. TSCHUDY, and E. J. *Williams: Crystalline structure and orientation of gold clusters grown in preformed nanometer-sized* pits, Appl. Surf. **Sci.** 115, 124 (1997).

[062] V. N. ANTONOV, J. S. PALMER, A. S. BHATTI and J. H. WEAVER: *Nanostructure diffusion and aggregation on desorbing rare-gas solids: Slip on an incommensurate lattice*, Phys. Rev. B **68**, 205418 (2003).

[063] R. ANTON and P. KREUTZER: *In situ TEM evaluation of the growth kinetics of Au particles on highly oriented pyrolytic graphite at elevated temperatures,* Phys. Rev. B **61,** 16077 (2000).

[064] J. A. VENABLES, G. D. T. SPILLER, and M. HANBÜCKEN: *Nucleation and growth of thin films,* Rep. Prog. Phys. **47,** 399 (1984).

[065] K. FIEGER: *Wachstum und Morphologie von Goldclustern auf Oberflächen untersucht mit STM und UPS,* Diploma Thesis, University of Dortmund (1999).

[066] C. J. BOXLEY, H. S. WHITE, T. E. LISTER, and P. J. PINHERO: *Electrochemical Deposition and Reoxidation of Au at Highly Oriented Pyrolytic Graphite. Stabilization of Au Nanoparticles on the Upper Plane of Step Edges,* J. Phys. Chem. B **107,** 451 (2003).

[067] NG. K. H. LIU, and R. M. PENNER: *Subnanometer Silver Clusters Exhibiting Unexpected Eletrochemical Metastability on Graphite,* Langmuir **16,** 4016 (2000).

[068] J. V. ZOVAL, P. R. BIERNACKI, and R. M. PENNER: *Implementation of Electrochemically Synthesized Silver Nanocrystallites for the Preferential SERS Enhancement of Defect Modes on Thermally Etched Graphite Surfaces,* Anal. Chem. **68,** 1585 (1996).

[069] H. MARTIN, P. CARRO, A. HERNANDEZ CREUS, S. GONZALES, R. C. SALVAREZZA, and A. J. ARVIA: *Growth Mode Transition Involving a Potential-Dependent Isotropic to Anisotropic Surface Atom Diffusion Change. Gold Electrodeposition on HOPG followed by STM,* Langmuir **13,** 100 (1997).

[070] J. V. ZOVAL, R. M. STIGER, P. R. BIERNACKI, and R. M. PENNER: *Electrochemical Deposition of Silver Nanocrystallites on the Atomically Smooth Graphite Basal Plane,* J. Phys. Chem. 100, **837** (1996).

[071] S. A. Hendricks, Y. Kim, A. J. Bard: *Imaging of the In Situ Deposition of Lead on Highly Oriented Pyrolytic Graphite by Scanning Tunneling and Atomic Force Microscopies,* J. Electrochem. Soc. **139,** 2818 (1992).

[072] J. D. MCBRIDE, B. V. TASSELL, R. C. JACHMANN, and T. P. BEEBE, JR.: *Molecule Corrals as Templates for the Formation of Metal and Silicon Nanostructures,* J. Phys. Chem. B, **105,** 3972 (2001).

[073] R. T. YANG, and C. WONG: *Etch decoration—scanning electron microscopy technique for measuring carbon gasification rates,* Rev. Sci. Instrum. **53,** 1488 (1982).

[074] A. WAWRO, A. KASUYA, R. CZAJKA, N. HORIGUCHI, and Y. NISHINA: *Gold Clusters Deposited on Si(111) and Graphite Surfaces,* Surf. Coat. Technol. **67,** 173 (1994).

[075] T. IRAWAN, I. BARKE, and H. HÖVEL: *Size-dependent morphology of gold clusters grown on nanostructured graphite,* Appl. Phys. A **80,** 929 (2005).

[076] K. FAUTH, M. HEßLER, D. BATCHELOR, G. SCHÜTZ: *Strong influence of defects on the electronic structure of Pt adatoms and clusters on graphite,* Surf. Sci. **529,** 397 (2003).

[077] T. R. OHNO, J. C. PATRIN, U. S. AYYALA, and J. H. *Weaver: Ag deposition onto Xe - Clustering, incorporation, and surface* attraction, Phys. Rev. **B** 44, 1891 (1991).

[078] G. D. WADDILL, I. M. VITOMIROV, C. M. ALDAO, and J. H. WEAVER: *Cluster deposition on GaAs(110): Formation of abrupt, defect-free interfaces,* Phys. Rev. Lett. **62,** 1568 (1989).

[079] L. HUANG, S. J. CHEY, and J. H. WEAVER: *Buffer-Layer-Assisted Growth of Nanocrystals - Ag-Xe-Si(111),* Phys. Rev. Lett. **80,** 4095 (1998).

[080] C. KITTEL: Einführung in die Festkörperphysik, Oldenbourg Verlag, München Wien, 1998.

[081] H. HABERLAND: *Cluster,* in *Lehrbuch der Experimentalphysik,* W. Raith, de Gruyter, 1992.

[082] U. HEIZ and W.-D. SCHNEIDER: *Physical Chemistry of supported Clusters,* in *Metal Clusters at Surfaces* ed. K.-H. MEIWES-BROER (Springer, Berlin Heidelberg, 2000).

[083] C. BRÉCHIGNAC, PH. CAHUZAC, J. LEYGNIER, and J. WEINER: *Dynamics of uni-molecular dissociation of sodium cluster ions*, J. Chem. Phys. **90**, 1492 (1989).

[085] *Lexikon der Physik,* website: http://www.wissenschaft-online.de/.

[086] M. M. KAPPES, R. W. KUNZ and E. SCHUMACHER: *Production of large sodium clusters (Nax,x≤65) by seeded beam expansions,* Chem. Phys. Lett **91,** 413 (1982).

[084] A. L. MACKAY: *A dense non-crystallographic packing of equal spheres,* Acta Crystallographia **15,** 916 (1962).

[087] J. JORTNER: *Level structure dynamics of clusters,* Bericht der Bunsengesellschaft für Physikalische Chemie **88,** 188 (1984).

[088] M. R. HOARE: *Structure and Dynamics of Simple Microclusters,* Adv. Chem. Phys. **40,** 49 (1979).

[089] H. A. JAHN and E. TELLER: *Stability of Polyatomic Molecules in Degenerate Electronic States. I. Orbital Degeneracy,* Proceedings of the Royal Society of London. Series A, Mathematical and Physical Sciences, **161,** 220 (1937).

[090] D. F. SHRIVER and P. W. ATKINS: *Inorganic Chemistry,* (3rd ed.), 235, (Oxford University Press).

[091] K. CLEMENGER: *Ellipsoidal shell structure in free-electron metal clusters,* Phys. Rev. B **32,** 1359 (1985).

[092] I. GALANAKIS, G. BIHLMAYER, V. BELLINI, N. PAPANIKOLAOU, R. ZELLER, S. BLÜGEL, and P. H. DEDERICHS: *Broken-Bond Rule for the Surface Energies of Noble Metals,* Europhys. Lett. **58,** 751 (2002).

[093] M. METHFESSEL, D. HENNING, and M. SCHEFFLER: *Trends of the surface relaxations, surface energies, and work functions of the 4d transition metals:* Phys. Rev. B **46,** 4816 (1992).

[094] J. C. HEYRAUD and J. J. METOIS: *Equilibrium Shape of Gold Crystallites on a Graphite Cleavage Surface: Surface Energies and Interfacial Energy,* Acta Metall. **28,** 1789 (1980).

[095] Z. WANG and P. WYNBLATT: *The equilibrium form of pure gold crystals,* Surf. Sci. **398,** 259 (1998).

[096] C. BOMBIS, A. EDMUNDTS, M. NOWICKI, and H. P. BONZEL: *Absolute surface free energies of Pb,* Surf. Sci. 511, **83** (2002).

[097] A. EDMUNDTS, M. NOWICKI, and H.P. BONZEL: *Experimental absolute step and kink formation energies on Pb(111) vicinal surfaces,* Surf. Sci. **496,** 35 (2002).

[098] F. A. NICHOLS and W. W. MULLINS: *Surface- (Interface-) And Volume-Diffusion Contributions to Morphological Changes Driven by Capillarity,* Trans. Met. Soc. AIME **233,** 1840 (1965).

[99] H. HÄKKINEN and M. MANNINEN: *How "Magic" is a Magic Metal Cluster?,* Phys. Rev. Lett. **76,** 1599 (1996).

[100] A. SANCHEZ, S. ABBET, U. HEIZ, W.D. SCHNEIDER, H. HÄKKINEN, R. N. BARNETT, and U. LANDMAN: *When Gold Is Not Noble: Nanoscale Gold Catalysts,* J. Phys. Chem. A **103,** 9573 (1999).

[101] W. L. WINTERBOTTOM: *Equilibrium shape of a small particle in contact with a foreign substrate,* Acta Metall. **15,** 303 (1967).

[102] K. H. HANSEN, T. WORREN, S. STEMPEL, E. LÆNGSGAARD, M. BÄUMER, H.-J. FREUND, F. BESENBACHER, and I. STENSGAARD: *Palladium Nanocrystals on Al2O3: Structure and Adhesion Energy,* Phys. Rev. Lett. **83,** 4120 (1999).

[103] H. HÖVEL and I. BARKE: *Large noble metal clusters: electron confinement and band structure effects,* New J. Phys. **5,** 31 (2003).

[104] S. J. CARROLL, S. PRATONTEP, M. STREUN, R. E. PALMER, S. HOBDAY and R. SMITH: *Pinning of size-selected Ag clusters on graphite surfaces,* J. Chem. Phys. 18, **113,** 7723 (2000).

[105] K. BROMANN, C. FELIX, H. BRUNE, W HARBICH, R. MONROT, J. BUTTET, and K. KERN: *Controlled Deposition of Size-Selected Silver Nanoclusters,* Science **274,** 956 (1996).

[106] S. FEDERIGO, W. HARBICH, and J. BUTTET: *Soft landing and fragmentation of small clusters deposited in noble-gas films,* Phys. Rev. B **58,** 7428 (1998).

[107] H. CHENG and U. LANDMAN: *Controlled Deposition, Soft Landing, and Glass Formation in Nanocluster-Surface Collisions,* Science **260,** 1304 (1993).

[108] L. K. ZANG, Y. X. WANG, Z. Y. PAN, L. ZHOU, T. J. LIU, J. ZHU, and X. M. JIANG: *Ar-buffer-assisted deposition of Cu13 on Cu(111) surfaces,* Surf. Sci. **600,** 527 (2006).

[109] M. BIELETZKI: *Rastertunnelmikroskopie an massenselektierten Clustern auf C60,* Diploma Thesis, University of Dortmund (2006).

[110] T. BECKER, H. HÖVEL, M. TSCHUDY, and B. REIHL: *Applications with a new low-temperature UHV STM at 5 K,* Appl. Phys. A **66,** 27 (1998).

[111] OMICRON NanoTechnology GmbH Germany, website: http://www.omicron.de/

[112] R. GAISCH, J. K. GIMZEWSKI, B. REIHL, R. R. SCHLITTLER, M. TSCHUDY and W. D. SCHNEIDER: *Low-temperature ultra-high-vacuum scanning tunneling microscope,* Ultramicroscopy **42,** 1621 (1992).

[113] I. BARKE: *Edelgasschichten auf der Au(111)-Oberfläche: Präparation und lokale Tunnelspektroskopie Massenselektierte Cluster deponiert auf Oberflächen,* Diploma Thesis, University of Dortmund (2001).

[114] O. ALBREKTSEN, H. W. M. SALEMINK, K. A. Mørch, AND A. R. *Thölen: Reliable tip preparation for high-resolution scanning tunneling* microscopy, J. Vac. Sci. Technol. **B** 12, 3187 (1994).

[115] H. HÖVEL, professorial dissertation: *Geometric and Electronic Structure of Nanoscale Systems on Surfaces,* University of Dortmund (2000).

[116] H. HABERLAND, M. MALL, M. MOSELER, Y. QIANG, Th. REINERS, and Y. THURNER: *Filling of micron-sized contact holes with copper by energetic cluster impact,* J. Vac. Sci. Technol. A **12,** 2925 (1994).

[117] B. v. ISSENDORFF and R. E. PALMER: *A new high transmission infinite range mass selector for cluster and nanoparticle beams,* Review of Scientific Instruments **70,** 4497 (1999).

[118] LEYBOLD Vacuum GmbH, website: http://www.leybold.com/ .

[119] U. S. Department of the Treasury, website: http://www.usmint.gov/mint_programs/index.cfm?flash=yes&action=american_eagles

[120] S. KRAUSE: *Massenselektierte Cluster deponiert auf Oberflächen,* Diploma Thesis, University of Dortmund (2006).

[121] VARIAN, Inc., website: http://www.varianinc.com/ .

[122] SIMION®, website: .

[123] KERAFOL®, website: http://www.kerafol.de/ .

[124] BURLE, website: http://www.burle.com/ .

[125] EFM 3, *Omicron* NanoTechnology GmbH [111]

[126] M. WUTZ, H. ADAM, and W. WALCHER: *Theorie und Praxis der Vakuumtechnik* (Vieweg, Braunschweig Wiesbaden, 1992).

[127] MATERIALS AND ELELCTROCHEMICAL RESEARCH (MER) Corporation, website: http://www.mercorp.com/

[128] T. ANDREEV: *Herstellung und Untersuchung von Edelgas-Adsorbatschichten: Einfluss auf die geometrische und elektronische Struktur der Oberfläche,* Diploma Thesis, University of Dortmund (2003).

[129] I. BARKE and H. HÖVEL: *Confined Shockley Surface States on the (111) Facets of Gold Clusters,* Phys. Rev. Lett. **90,** 166801 (2003).

[130] CH. WÖLL, S. CHIANG, R. J. WILSON, and P. H. LIPPEL: *Determination of atom positions at stacking-fault dislocations on Au(111) by scanning tunneling microscopy,* Phys. Rev. B **39,** 7988 (1989).

[131] J. CHLADEK and G. BETZ: *Radiation Effects and Defects in Solids,* **142** (1997).

[132] 3M®, website: http://www.3m.com/ .

[133] L. Pauling: *The Nature of the Chemical Bond,* p. 235, 3rd. Edition 1960.

[134] http://www.2spi.com/.

[135] G. KAINDL, T. C. CHIANG, D. E. EASTMAN, and F.J. HIMPSEL: *Distance-Dependent Relaxation Shifts of Photoemission and Auger Energies for Xe on Pd(001),* Phys. Rev. Lett. **45,** 1808 (1980).

[136] E. I. ALTMANN and R. J. COLTAN: *Nucleation, Growth and Structure of Fullerene Films on Au(111),* Surf. Sci. **279,** 49 (1992).

[137] E. I. ALTMANN and R. J. COLTAN: *The interaction of C60 with noble metal surfaces,* Surf. Sci. **295,** 13 (1993).

[138] E. I. ALTMAN and R. J. COLTON: *Determination of the orientation of C60 adsorbed on Au(111) and Ag(111),* Phys. Rev. B **48,** 18244 (1993).

[139] C. RETTIG: *Bleinanostrukturen auf mit Wasserstoff passiviertem Silizium (111): Elektrochemische Abscheidung und Vakuumaufdampfverfahren,* Dissertation, University of Dortmund (2000).

[140] S. L. QIU, X. PAN, M. STRONGIN, and P. H. CITRIN: *Photoemission from supported metal clusters: The problem of the support,* Phys. Rev. B **36,** 1292 (1987).

[141] P. H. CITRIN, G. K. WERTHEIM, and Y. BAER: *Core-Level Binding Energy and Density of States from the Surface Atoms of Gold,* Phys. Rev. Lett. **41,** 1425 (1978).

[142] B. RICHTER, H. KUHLENBECK, H. J. FREUND, and P. S. BAGUS: *Cluster Core-Level Binding-Energy Shifts: The Role of Lattice Strain,* Phys. Rev. Lett. **93,** 026805 (2004).

[143] G. K. WERTHEIM, S.B. DICENZO, and S. E. YOUNGQUIST: *Unit Charge on Supported Gold Clusters in Photoemission Final State*, Phys. Rev. Lett. **51**, 2310 (1983).

[144] T. ANDREEV, I. BARKE, and H. HÖVEL: *Adsorbed rare-gas layers on Au(111): Shift of the Shockley surface state studied with ultraviolet photoelectron spectroscopy and scanning tunneling* spectroscopy, Phys. Rev. **B** 70, 205426 (2004).

[145] R. J. BEHM, C. R. BRUNDLE, and K. WANDELT: *The underlayer influence on photoemission and thermal desorption of xenon adsorbed on Ag(111),* J. Chem Phys **85,** 1061 (1986).

[146] M. L. KLEIN and J. A. VENABLES (eds.): *Rare gas solids,* Vol. II, (Academic Press, London, New York, San Francisco, 1977).

[147] N. SCHWENTNER: *Mean-free path of electrons in rare-gas solids derived from vacuum-uv photoemission data,* Phys. Rev. B **14,** 5490 (1976).

[148] H. G. BOYEN, G. KASTLE, F. WEIGL, B. KOSLOWSKI, C. DIETRICH, P. ZIEMANN, J. P. SPATZ, S. RIETHMULLER, C. HARTMANN, M. MOLLER, G. SCHMID, M. G. GARNIER, and P. OELHAFEN: Oxidation-Resistant Gold-55 Clusters, Science **297,** 1533 (2002).

[149] R. L. SCHWOEBEL: *Step Motion on Crystal Surfaces. II,* Appl. Phys. **40,** 614 (1969).

[150] G. EHRLICH and F. G. *Hudda: Atomic View of Surface Self-Diffusion: Tungsten on* Tungsten, New York J. Chem. **Phys.** 44, 1039 (1966).

[151] R. L. SCHWOEBEL and E. J. SHIPSEY: *Step Motion on Crystal Surfaces,* J. Appl. Phys. **37,** 3682 (1966).

[152] S. C. WANG and G. EHRLICH: *Atom incorporation at surface clusters: An atomic view,* Phys. Rev. Lett **67,** 2509 (1991).

[153] R. FERRANDO and G. TRÉGLIA: *High-Temperature Study of the Schwoebel Effect in Au(111),* Phys. Rev. Lett. **76,** 2109 (1996).

[154] G. K. WERTHEIM and D. N. E. BUCHANAN: *Interfacial reaction of C60 with silver,* Phys. Rev. B **50,** 11070 (1994).

[155] H. WANG, J. G. HOU, O. TAKEUCHI, Y. FUJISUKU and A. KAWAZU: *STM observations of Ag-induced reconstruction of C60 thin films,* Phys. Rev. B. **61,** 2199 (2000).

[156] D. D. CHAMBLISS and R. J. WILSON: *Relaxed diffusion limited aggregation of Ag on Au(111) observed by scanning tunneling microscopy,* J. Vac. Sci. Technol. B **9,** 928 (1999).

[157] L. BARDOTTI, P. JENSEN, A. HOAREAU, M. TREILLEUX, and B. CABAUD: *Experimental Observation of Fast Diffusion of Large Antimony Clusters on Graphite Surfaces,* Phys. Rev. Lett. **74,** 4694 (1995).

[158] M. COUILLARD, S. PRATONTEP, and R. E. PALMER: *Metastable ordered arrays of size-selected Ag clusters on graphite,* Appl. Phys. Lett. **81,** 2595 (2003).

[159] Landolt-Börnstein, New Series, Group III: Condensed Matter, Volume **42,** Subvolume A2, Chapter 4.4.7 (Springer, Heidelberg, 2002).

[160] M. SCHAFFHÖFER: *Untersuchungen an nanostrukturierten Oberflächen mittels Rastertunnelmikroskopie,* Diploma Thesis, University of Dortmund (1997).

[161] I. BESZEDA, I. A. SZABO, and E. G. GONTIER-MOYA: Morphological evolution of **thin** gold films studied by Auger electron spectroscopy in beading conditions, Appl. Phys. A **78,** 1079 (2004).

[162] H. J. WEISS: *Diffusion,* in *Effekte der Physik und ihre Anwendungen,* eds. M. v. ARDENNE, G. MUSIOL, and U. KLEMRADT, (Verlag Harri Deutsch, Frankfurt, 2005).

[163] R. FERRANDO and G. TRÉGLIA: *Tight-binding molecular dynamics study of diffusion on Au and Ag(111),* Surf. Sci. **331,** 920 (1995).

[164] J. R. SMITH, T. HONG, and D. J. SROLOVITZ: *Metal-Ceramic Adhesion and the Harris Functional,* Phys. Rev. Lett. **72,** 4021 (1994).

Chapter 10

GLOSSARY

F

G

H

I

J

L

M

N

P

R

S

T

U

V

W

ACKNOWLEDGEMENTS

Writing this dissertation would not have been possible without the support of many people.

First, I would like to thank Prof. Dr. METIN TOLAN for the opportunity to carry out this PhD at his chair *Experimentelle Physik I* and for the good spirit within our group due to his sense of humor and friendly manner. Furthermore, it was also always a pleasure to discuss several physical, sportive, or general topics, such as the important things of leadership and career perspectives, in particular after a long day of writing.

Special thanks go to my supervisor Priv. Doz. Dr. HEINZ HÖVEL. He made the most important contribution to this thesis, due to his outstanding support from the beginning of my diploma thesis to the end of my PhD time. I learned most from innumerable fruitful discussions, helpful suggestions, scientific advices, and his impressive knowledge in Physics and beyond. Moreover, I would like to thank him for his enormous helpfulness, unresting engagement, and for teaching me the *scientific way*. It was always a pleasure to spend my PhD time under such optimal conditions, regarding the interesting topic, several interesting and instructive conference visits, and the friendly way he led our STM group.

Furthermore, I am much obliged to both of them for the support concerning my (rather unusual) preparation for my future career.

I would like to thank Prof. Dr. THOMAS WEIS for his interest in my work, the friendly agreeing to referee this thesis, and the good collaboration within the *Physik A1/B1* course.

Special thanks go also to HD Dr. BERND VON ISSENDORFF of the University of Freiburg for the fruitful cooperation within the priority program SPP 1153. I have learned several interesting technical and physical details about the cluster deposition machine and size-selected clusters in general during the time in Freiburg and during the *deposition sessions* in our lab in Dortmund. Moreover, I thank him for the very quick and precise answers of several questions during setting up the cluster machine and writing the manuscript.

Many thanks go to Dipl. Phys. CHUNRONG YIN from the University of Freiburg for the personal, telephonic, and virtual support, including e-mailing, video conferencing, and remote desktop accessing.

The BLAG experiments presented within this thesis have been done in close cooperation with Dipl. Phys. DANIEL BOECKER and Dipl. Phys. FARHAD GHALEH, as well as the deposition experiments with Dipl. Phys. STEFANIE KRAUSE and Dipl. Phys. MARKUS BIELETZKI. Several results are part of their diploma thesises. I would like to thank all of them for the very fruitful contributions and the always-friendly teamwork.

I would like to thank Dr. INGO BARKE for guiding me at the beginning of my diploma thesis until the first year of my PhD thesis, teaching me several technical and physical matters and being such a nice colleague, in particular while working in the lab and traveling to conferences.

Moreover, I would like to thank the present STM Group for being one of the best colleagues I ever had. I am especially grateful for the wonderful time I had together with STEFANIE KRAUSE, MARKUS BIELETZKI, and ROBERT KÖSTER at the ICCS conference in Rostock, the nice working atmosphere we shared and for becoming good friends. Thanks to THORSTEN RICHTER for his caring words and asking after me (usually) very early in the morning.

Special thanks go to my uncle Dr. CHRISTOPH KÖPPEN for promoting my scientific interests, already in the early childhood and for the proofreading of the manuscript. Due to his several linguistic, stylistic, and physical advices, I was able to increase the readability of the thesis significantly.

Sincere thanks go to assistant Prof. Dr. JENNIFER L. SCHUH, CATHERINE DOUGLAS BA (hons.), and VINCENT W. NG for their many useful hints and advices from a *native speaker's* point of view.

Many thanks go to all the people sharing my office, namely, RECHID AZAD, Dipl. Phys. MARKUS KRÄMER, Dipl. Phys. HENNING STERNEMANN, DIRK SCHULZ, and ROLF GREGORI. It was a daily pleasure to be together with all of you, and talk about the *world and his brother*.

Many thanks go to my fellow students and friends Dr. THOMAS ANDREEV and PATRICK CHUDZIAN, who challenged together with me all courses at the University.

Thanks to our technical staff THORSTEN WITT and GEORG JÜLICHER for numerous technical workings and solving computer problems. Thanks to GISELA PIKE and DIRK SCHEMIONEK of the preparation laboratory for providing everything, we need in our lab.

I would like to thank our secretaries MONIKA VOITS-BESLI and MANUELA LINKE for helping me with all administrative problems.

I would like to thank all other members of EIa for the nice atmosphere and the good time in our group.

Thanks to Mrs. SUSANNE FRICKE and the whole team of the mechanic workshop, as well as Mr. KÖPPEN and his team of the electronic workshop for manufacturing everything we need for the cluster machine.

Furthermore, I would like to thank Mr. GALL and Mr. WIDYNSKI for providing liquid nitrogen and helium.

I would like to acknowledge the *Deutsche Forschungsgemeinschaft* (DFG) for the financial support within the priority program SPP 1153 and the PhD program GK 726.

I am deeply thankful to all of my friends and my whole family, in particular to my parents Dr. GISELA IRAWAN and Prof. *h.c.* Dr. PAUL IRAWAN, my sisters ANNETTE IRAWAN and CLAUDIA IRAWAN, and my grandmother JUTTA KÖPPEN, as well as my parents and grand mother-in-law BEATRIX BÜCHEL, HERBERT BÜCHEL and HILDE GÜNTHER, who always encouraged and supported me. Especially the nice phone calls after a long day help me to get away from it all.

Finally, I am sincerely grateful for the loving care of my wife KATRIN, who is the most important person in my life. I would like to thank her for understanding and supporting every decision I made in the past 13 years and the sympathetic way she is managing our life, despite the very less spare time we had together, especially in the last three years.

Endnotes http://dx.doi.org/ - Hyperlink to the reference via The Digital Object Identifier (DOI®).[7] or URL.

---

1 C. R. HENRY: *Surface studies of supported model catalysts*, Surf. Sci. Rep. **31**, 231 (1998). http://dx.doi.org/10.1016/S0167-5729(98)00002-8

2 P. JENSEN: *Growth of nanostructures by cluster deposition: Experiments and simple models*, Rev. Mod. Phys. **71**, 1695 (1999). http://dx.doi.org/10.1103/RevModPhys.71.1695

3 W. HARBICH: *Collision of Clusters with Surfaces* in *Metal Clusters at Surfaces,* ed. K.-H. MEIWES-BROER (Springer, Berlin Heidelberg, 2000).

4 M. SCHMIDT, R. KUSCHE, W. KRONMÜLLER, B. V. ISSENDORFF, and H. HABERLAND: *Experimental Determination of the Melting Point and Heat Capacity for a Free Cluster of 139 Sodium Atoms*, Phys. Rev. Lett. **79**, 99 (1997). http://dx.doi.org/10.1103/PhysRevLett.79.99

5 DFG priority program SPP 1153: *Clusters in Contact with Surfaces – Electronic Structure and Magnetism*, website: http://www.ieap.uni-kiel.de/surface/ag-berndt/spp/index.html.

6 F. FURCHE, R. AHLRICHS, P. WEIS, C. JACOB, S. GILB, T. BIERWEILER and M. M. KAPPES: *The structures of small gold cluster anions as determined by a combination of ion mobility measurements and density functional calculations*, J. Chem. Phys. **117**, 6982 (2002). http://dx.doi.org/10.1063/1.1507582

7 A. KIRILYUK, K. DEMYK, G. V. HELDEN, G. MEIJER, A. I. POTERYAEV and A. I. LICHTENSTEIN: *Atomic clusters of magnetic oxides: Structure and phonons*, J. Appl. Phys **93**, 7379 (2003). http://dx.doi.org/10.1063/1.1558252

---

[7] **What is a DOI?** As defined by the http://www.doi.org/, "the Digital Object Identifier (DOI®) is a system for identifying and exchanging intellectual property in the digital environment. Developed by the International DOI Foundation, it provides a framework for managing intellectual content, for linking customers with content suppliers, for facilitating electronic commerce, and enabling automated copyright management for all types of media."

8 H. P. BONZEL: *3D equilibrium crystal shapes in the new light of STM and AFM*, Phys. Rep. **385**, 1 (2003). http://dx.doi.org/10.1016/S0370-1573(03)00273-4

9 H. HÄKKINEN, M. MOSELER, O. KOSTKO, M. ASTRUC HOFFMANN, N. MORGNER, and B. V.ISSENDORFF: *Symmetry and structure of noble metal nanoparticles and the role of relativity*, Phys. Rev. Lett. **93**, 093401 (2004). http://dx.doi.org/10.1103/PhysRevLett.93.093401

10 H. HABERLAND, T. HIPPLER, J.DONGES, O. KOSTKO, M. SCHMIDT, and B. V. ISSENDORFF: *Melting of Sodium Cluster: where do the Magic Numbers come from,* Phys. Rev. Lett. **94**, 035701 (2005). http://dx.doi.org/10.1103/PhysRevLett.94.035701

11 M. ASTRUC HOFFMANN, G. WRIGGE, and B. v. ISSENDORFF: *Photoelectron spectroscopy of Al_{32000}^-: Observation of a "Coulomb staircase" in a free cluster*, Phys. Rev. B **66**, 041404 (2002). http://dx.doi.org/10.1103/PhysRevB.66.041404

12 W. P. HALPERIN: *Quantum size effects in metal particles*, Rev. Mod. Phys. **58**, 533 (1986). http://dx.doi.org/10.1103/RevModPhys.58.533

13 W. A. DE HEER: *The physics of simple metal clusters: experimental aspects and simple models*, Rev. Mod. Phys. **65**, 611 (1993). http://dx.doi.org/10.1103/RevModPhys.65.611

14 *Metal Clusters at Surfaces* ed. K.-H. MEIWES-BROER (Springer, Berlin Heidelberg, 2000).

15 P. A. TIPLER AND R. A. LLEWELLYN, *Moderne Physik* (Oldenburg München Wien, 2003).

16 J. L. MARTINS, J. BUTTET, and R. CAR: *Electronic and structural properties of sodium clus*ters, Phys. Rev. B **31**, 1804 (1985). http://dx.doi.org/10.1103/PhysRevB.31.1804

17 B. K. RAO, P. JENA, M. MANNINEN, and R. M. NIEMINEN: *Spontaneous fragmentation of multiply charged metal clusters*, Phys. Rev. Lett. **58**, 1188 (1987). http://dx.doi.org/10.1103/PhysRevLett.58.1188

18 G. v. HELDEN, M.-T. HSU, N. GOTTS, and M. T. BOWERS: *Carbon cluster cations with up to 84 atoms: structures, formation mechanism, and reactivity*, J. Phys. Chem. **97**, 8182 (1993). http://dx.doi.org/10.1021/j100133a011

19 H. HÖVEL, T. BECKER, D. FUNNEMANN, B. GRIMM, C. QUITMANN and B. REIHL: *High-resolution photoemission combined with low-temperature STM*, J. Electron Spectros. Rel. Phenom. **88**, 1015 (1998). http://dx.doi.org/10.1016/S0368-2048(97)00114-X

20 H.-J. GÜNTHERODT and R. WIESENDANGER: *Scanning Tunneling Microscopy I* (Springer Berlin Heidelberg New York, 1994).

21 F. BESENBACHER: *Scanning Tunneling Microscopy Studies of Metal Surfaces*, Rep. Prog. Phys. **59**, 1737 (1996).

22 G. BINNING, H. ROHRER, CH. GERBER, and E. WEIBEL: *Surface Studies by Scanning Tunneling Microscopy*, Phys. Rev. Lett. **49**, 57 (1982). http://dx.doi.org/10.1103/PhysRevLett.49.57

23 G. BINNIG and H. ROHRER: *Scanning Tunneling Microscopy*, Hel. Phys. Acta, **55**, 726 (1982).

24 G. BINNIG and H. ROHRER: *Scanning Tunneling Microscopy*, IBM J. Res. Develop. **30**, 4 (1986). http://www.research.ibm.com/journal/rd/441/binnig.pdf

25 T. MAYER KUCKUK, *Kernphysik*, (Teubner-Verlag, Stuttgart, 1985).

26 E. U. CONDON and R. W. GURNEY: *Wave mechanics and radioactive disintegration*, Nature **122**, 439 (1928).

27 R. W. GURNEY and E. U. CONDON: *Quantum Mechanics and Radioactive Disintegration*, Phys. Rev. **33**, 127 (1929). http://dx.doi.org/10.1103/PhysRev.33.127

28 A. ANDREEFF: *Tunnel-Effekt*, in *Effekte der Physik und ihre Anwendungen*, ed. M. v. ARDENNE, G. MUSIOL, and U. KLEMRADT, (Verlag Harri Deutsch, Frankfurt, 2005).

29 P. EBERT: *Rastersondenmikroskopie*, in *Effekte der Physik und ihre Anwendungen*, ed. M. v. ARDENNE, G. MUSIOL, and U. KLEMRADT, (Verlag Harri Deutsch, Frankfurt, 2005).

30 T. IRAWAN: *Morphologie und elektronische Struktur von Edelmetallclustern hergestellt durch gesteuertes Wachstum auf HOPG*, Diploma Thesis, University of Dortmund (2003). http://e1.physik.uni-dortmund.de/hovel/hovel-Dateien/irawan_diplom.pdf

31 H. HÖVEL, T. BECKER, A. BETTAC, B. REIHL, M. TSCHUDY and E. J. WILLIAMS: *Controlled cluster condensation into preformed nanometer-sized pits*, J. Appl. Phys. **81**, 154 (1997). http://dx.doi.org/10.1063/1.364003

32 M. HENZLER and W. GÖPEL: *Oberflächenphysik des Festkörpers* (B. G. Teubner, Stuttgart, 1991).

33 J. BARDEEN: *Tunneling from A Many-Particle Point of View*, Phys. Rev. Lett. **6**, 57 (1961). http://dx.doi.org/10.1103/PhysRevLett.6.57

34 J. TERSOFF and D. R. HAMANN: *Theory of the Scanning Tunneling Microscope*, Phys. Rev. B **31**, 805 (1985). http://dx.doi.org/10.1103/PhysRevB.31.805

35 J. TERSOFF and D. R. HAMANN: *Theory and Application for the Scanning Tunneling Microscope*, Phys. Rev. Lett. **50**, 1998 (1983). http://dx.doi.org/10.1103/PhysRevLett.50.1998

36 B. GRIMM: *Tunnelspektroskopie und Photoemission bei tiefen Temperaturen an Edelgas-Modellsystemen und Nanostrukturen*, Dissertation, University of Dortmund (2000). http://e1.physik.uni-dortmund.de/hovel/hovel-Dateien/grimm_diss.pdf

37 A. SELLONI, P. CARNEVALI, E. TOSSATTI and C. D. CHEN: *Voltage-Dependent Scanning-Tunneling Microscopy of a Crystal Surface: Graphite*, Phys. Rev. B **31**, 2602 (1985), *idem* **34**, 7406 (1986). http://dx.doi.org/10.1103/PhysRevB.31.2602

38 J. A. STROSCIO, R. M. FEENSTRA and A. P. FEIN: *Electronic Structure of the Si(111)2 × 1 Surface by Scanning-Tunneling Microscopy*, Phys. Rev. Lett. **57**, 2579 (1986). http://dx.doi.org/10.1103/PhysRevLett.57.2579

39 C. J. CHEN: *Theory of Scanning Tunneling Spectroscopy*, J. Vac. Sci. Technol. A **6**, 319 (1988). http://dx.doi.org/10.1116/1.575444

40 I. BARKE: *Morphology and Electronic Structure of Gold Clusters on Graphite*, Dissertation, University of Dortmund (2004). http://e1.physik.uni-dortmund.de/hovel/hovel-Dateien/barke_diss.pdf

41 H. R. HERTZ: *Über einen Einfluß des ultravioletten Lichtes auf die electrische Entladung*, Ann. Phys. u. Chem. **31**, 983 (1887).

42 W. HALLWACHS: *Über den Einfluß des Lichtes auf electrostatisch geladene Körper*, Ann. Phys. u. Chem. **33**, 301 (1888).

43 P. LENARD: *Erzeugung von Kathodenstrahlen durch ultraviolettes Licht*, Ann. Phys. **2**, 359 (1900).

44 A. EINSTEIN: *Über einen die Erzeugung und Verwandlung des Lichtes betreffenden heuristischen Gesichtspunkt*, Ann. Phys. **17**, 132 (1905). http://www3.interscience.wiley.com/cgi-bin/abstract/112477431/ABSTRACT

45 S. HÜFNER: *Photoelectron spectroscopy* (Springer, Berlin Heidelberg New York, 1995).

46 F. REINERT and S. HÜFNER: *Photoemission spectroscopy – from early days to recent applications*, New. J. Physics **7**, 97 (2005). http://dx.doi.org/10.1088/1367-2630/7/1/097

47 C. N. BERGLUND and W. E. SPICER: *Photoemission Studies of Copper and Silver - Theory*, Phys. Rev. **136**, A1030 (1964). http://dx.doi.org/10.1103/PhysRev.136.A1030

48 J. B. PENDRY: *Theory of photoemission*, Surf. Sci. **57**, 679 (1976). http://dx.doi.org/10.1016/0039-6028(76)90355-1

49 P. DOLLE, K. MARKERT, W. HEICHLER, N. R. ARMSTRONG, K. WANDELT, K. S. KIM AND, and R. A. FIATO: *Characterization of Pt/TiO2 surfaces by means of photoelectron spectroscopy of adsorbed xenon*, J. Vac. Sci. Technol. A **4**, 1465 (1986). http://dx.doi.org/10.1116/1.573538

50 A. JABLONSKI and K. WANDELT: *Quantitative aspects of ultraviolet photoemission of adsorbed xenon - a review*, Surface and Interface Analysis **17**, 611 (1991). http://dx.doi.org/10.1002/sia.740170902

51 K. WANDELT: *Surface characterization by photoemission of adsorbed xenon (PAX),* J. Vac. Sci. Technol. A **2**, 802 (1984). http://dx.doi.org/10.1116/1.572509

52 T. SCHMITZ-HÜBSCH, K. OSTER, J. RADNIK and K. WANDELT: *Photoemission from Quantum-Well States in Ultrathin Xe crystals*, Phys. Rev. Lett. **74**, 2595 (1995). http://dx.doi.org/10.1103/PhysRevLett.74.2595

53 A. SHNIRMAN and G. SCHÖN: *Quantum measurements performed with a single-electron transistor*, Phys. Rev. B **57**, 15400 (1998).

54 R. WILKINS, E. BEN-JACOB, and R. C. JAKLEVIC: *Scanning-tunneling-microscope observations of Coulomb blockade and oxide polarization in small metal droplets*, Phys. Rev. Lett. **63**, 801 (1989). http://dx.doi.org/10.1103/PhysRevLett.63.801

55 H. HÖVEL and I. BARKE: *Morphology and electronic structure of gold clusters on graphite: Scanning-tunneling techniques and photoemission*, Prog. Surf. Sci. **81**, 53 (2006). http://dx.doi.org/10.1016/j.progsurf.2006.01.002

56 H. HÖVEL, B. GRIMM, M. POLLMANN, and B. REIHL: *Cluster-Substrate Interaction on a Femtosecond Time Scale Revealed by a High-Resolution Photoemission Study of the FERMI-Level Onset*, Phys. Rev. Lett. **81**, 4608 (1998). http://dx.doi.org/10.1103/PhysRevLett.81.4608

57 H. HÖVEL, B. GRIMM, M. POLLMANN, and B. REIHL: *Femtosecond dynamics of final-state effects in the valence band photoemission of silver clusters*, The European Physical Journal D **9**, 595 (1999) http://dx.doi.org/10.1007/s100530050507

58 D. BOECKER: *Wachstum von Metallclustern auf Edelgasschichten und Analyse der elektronischen Wechselwirkung mit Hilfe von Ultravioletter Photoelektron Spektroskopie*, Diploma Thesis, University of Dortmund (2004). http://e1.physik.uni-dortmund.de/hovel/hovel-Dateien/boecker_diplom.pdf

59 J. J. MÉTOIS, J. C. HEYRAUD, and R. KERN: *Surface decoration: Localization of crystallites along the steps,* Surf. Sci. **78**, 191 (1978). http://dx.doi.org/10.1016/0039-6028(78)90220-0

60 H. HÖVEL: *Clusters on surfaces: high-resolution spectroscopy at low temperatures*, Appl. Phys. A **72**, 295 (2001). http://dx.doi.org/10.1007/s003390100768

61 H. HÖVEL, T. BECKER, A. BETTAC, B. REIHL, M. TSCHUDY, and E. J. WILLIAMS: *Crystalline structure and orientation of gold clusters grown in preformed nanometer-sized pits*, Appl. Surf. Sci. **115**, 124 (1997). http://dx.doi.org/10.1016/S0169-4332(97)80194-8

62 V. N. ANTONOV, J. S. PALMER, A. S. BHATTI, and J. H. WEAVER: *Nanostructure diffusion and aggregation on desorbing rare-gas solids: Slip on an incommensurate lattice*, Phys. Rev. B **68**, 205418 (2003). http://dx.doi.org/10.1103/PhysRevB.68.205418

63 R. ANTON and P. KREUTZER: *In situ TEM evaluation of the growth kinetics of Au particles on highly oriented pyrolytic graphite at elevated temperatures*, Phys. Rev. B **61**, 16077 (2000). http://dx.doi.org/10.1103/PhysRevB.61.16077

64 J. A. VENABLES, G. D. T. SPILLER, and M. HANBÜCKEN: *Nucleation and growth of thin films*, Rep. Prog. Phys. **47**, 399 (1984). http://dx.doi.org/10.1088/0034-4885/47/4/002

65 K. FIEGER: *Wachstum und Morphologie von Goldclustern auf Oberflächen untersucht mit STM und UPS*, Diploma Thesis, University of Dortmund (1999). http://e1.physik.uni-dortmund.de/hovel/hovel-Dateien/fieger_diplom.pdf

66 C. J. BOXLEY, H. S. WHITE, T. E. LISTER, and P. J. PINHERO: *Electrochemical Deposition and Reoxidation of Au at Highly Oriented Pyrolytic Graphite. Stabili-*

zation of Au Nanoparticles on the Upper Plane of Step Edges, J. Phys. Chem. B **107**, 451 (2003). http://dx.doi.org/10.1021/jp026496j

67 NG. K. H. LIU, and R. M. PENNER: *Subnanometer Silver Clusters Exhibiting Unexpected Eletrochemical Metastability on Graphite*, Langmuir **16**, 4016 (2000). http://dx.doi.org/10.1021/la9914716

68 J. V. ZOVAL, P. R. BIERNACKI, and R. M. PENNER: *Implementation of Electrochemically Synthesized Silver Nanocrystallites for the Preferential SERS Enhancement of Defect Modes on Thermally Etched Graphite Surfaces*, Anal. Chem. **68**, 1585 (1996). http://dx.doi.org/10.1021/ac951114+

69 H. MARTIN, P. CARRO, A. HERNANDEZ CREUS, S. GONZALES, R. C. SALVAREZZA, and A. J. ARVIA: *Growth Mode Transition Involving a Potential-Dependent Isotropic to Anisotropic Surface Atom Diffusion Change. Gold Electrodeposition on HOPG followed by STM*, Langmuir **13**, 100 (1997). http://dx.doi.org/10.1021/la960700a

70 J. V. ZOVAL, R. M. STIGER, P. R. BIERNACKI, and R. M. PENNER: *Electrochemical Deposition of Silver Nanocrystallites on the Atomically Smooth Graphite Basal Plane*, J. Phys. Chem. 100, **837** (1996). http://dx.doi.org/10.1021/jp952291h

71 S. A. Hendricks, Y. Kim, A. J. Bard: *Imaging of the In Situ Deposition of Lead on Highly Oriented Pyrolytic Graphite by Scanning Tunneling and Atomic Force Microscopies,* J. Electrochem. Soc. **139**, 2818 (1992). http://dx.doi.org/10.1149/1.2068986

72 J. D. MCBRIDE, B. V. TASSELL, R. C. JACHMANN, and T. P. BEEBE, JR.: *Molecule Corrals as Templates for the Formation of Metal and Silicon Nanostructures*, J. Phys. Chem. B, **105**, 3972 (2001). http://dx.doi.org/10.1021/jp003214b

73 R. T. YANG, and C. WONG: *Etch decoration—scanning electron microscopy technique for measuring carbon gasification rates*, Rev. Sci. Instrum. **53**, 1488 (1982). http://dx.doi.org/10.1063/1.1137168

74 A. WAWRO, A. KASUYA, R. CZAJKA, N. HORIGUCHI, and Y. NISHINA: *Gold Clusters Deposited on Si(111) and Graphite Surfaces*, Surf. Coat. Technol. **67**, 173 (1994). http://dx.doi.org/10.1016/0257-8972(94)90117-1

75 T. IRAWAN, I. BARKE, and H. HÖVEL: *Size-dependent morphology of gold clusters grown on nanostructured graphite,* Appl. Phys. A **80**, 929 (2005). http://dx.doi.org/10.1007/s00339-004-3118-8

76 K. FAUTH, M. HEßLER, D. BATCHELOR, G. SCHÜTZ: *Strong influence of defects on the electronic structure of Pt adatoms and clusters on graphite*, Surf. Sci. **529**, 397 (2003). http://dx.doi.org/10.1016/S0039-6028(03)00333-9

77 T. R. OHNO, J. C. PATRIN, U. S. AYYALA, and J. H. WEAVER: *Ag deposition onto Xe - Clustering, incorporation, and surface attraction*, Phys. Rev. B **44**, 1891 (1991). http://dx.doi.org/10.1103/PhysRevB.44.1891

78 G. D. WADDILL, I. M. VITOMIROV, C. M. ALDAO, and J. H. WEAVER: *Cluster deposition on GaAs(110): Formation of abrupt, defect-free interfaces*, Phys. Rev. Lett. **62**, 1568 (1989). http://dx.doi.org/10.1103/PhysRevLett.62.1568

79 L. HUANG, S. J. CHEY, and J. H. WEAVER: *Buffer-Layer-Assisted Growth of Nanocrystals - Ag-Xe-Si(111)*, Phys. Rev. Lett. **80**, 4095 (1998). http://dx.doi.org/10.1103/PhysRevLett.80.4095

80 C. KITTEL: *Einführung in die Festkörperphysik*, Oldenbourg Verlag, München Wien, 1998.

81 H. HABERLAND: *Cluster*, in *Lehrbuch der Experimentalphysik*, W. Raith, de Gruyter, 1992.

82 U. HEIZ and W.-D. SCHNEIDER: *Physical Chemistry of supported Clusters*, in *Metal Clusters at Surfaces* ed. K.-H. MEIWES-BROER (Springer, Berlin Heidelberg, 2000).

83 C. BRÉCHIGNAC, PH. CAHUZAC, J. LEYGNIER, and J. WEINER: *Dynamics of unimolecular dissociation of sodium cluster ions*, J. Chem. Phys. **90**, 1492 (1989). http://dx.doi.org/10.1063/1.456675

84 A. L. MACKAY: *A dense non-crystallographic packing of equal spheres*, Acta Crystallographia **15**, 916 (1962). http://dx.doi.org/10.1107/S0365110X6200239X

85 *Lexikon der Physik*, website: http://www.wissenschaft-online.de/.

86 M. M. KAPPES, R. W. KUNZ and E. SCHUMACHER: *Production of large sodium clusters (Nax,x≤65) by seeded beam expansions*, Chem. Phys. Lett **91**, 413 (1982). http://dx.doi.org/10.1016/0009-2614(82)83080-7

87 J. JORTNER: *Level structure dynamics of clusters*, Bericht der Bunsengesellschaft für Physikalische Chemie **88**, 188 (1984). http://chemport.cas.org/cgi-bin/sdcgi?APP=ftslink&action=reflink&origin=aps&version=1.0&coi=1:CAS:528:DyaL2cXhvVSiu7k%3D&md5=e7317c444929a15b627438d1c8796d0d

88 M. R. HOARE: *Structure and Dynamics of Simple Microclusters*, Adv. Chem. Phys. **40**, 49 (1979). http://chemport.cas.org/cgi-bin/sdcgi?APP=ftslink&action=reflink&origin=aps&version=1.0&coi=1:CAS:528:DyaL3cXot1GltQ%3D%3D&md5=591b53b166753910fdf521c3ff11be9d

89 H. A. JAHN and E. TELLER: *Stability of Polyatomic Molecules in Degenerate Electronic States. I. Orbital Degeneracy*, Proceedings of the Royal Society of London. Series A, Mathematical and Physical Sciences, **161**, 220 (1937). http://adsabs.harvard.edu/abs/1937RSPSA.161..220J

90 D. F. SHRIVER and P. W. ATKINS: *Inorganic Chemistry*, (3rd ed.), 235, (Oxford University Press).

91 K. CLEMENGER: *Ellipsoidal shell structure in free-electron metal clusters*, Phys. Rev. B **32,** 1359 (1985). http://dx.doi.org/10.1103/PhysRevB.32.1359

92 I. GALANAKIS, G. BIHLMAYER, V. BELLINI, N. PAPANIKOLAOU, R. ZELLER, S. BLÜGEL, and P. H. DEDERICHS: *Broken-Bond Rule for the Surface Energies of No-*

ble Metals, Europhys. Lett. **58**, 751 (2002). http://dx.doi.org/10.1209/epl/i2002-00413-7

93 M. METHFESSEL, D. HENNING, and M. SCHEFFLER: *Trends of the surface relaxations, surface energies, and work functions of the 4d transition metals*: Phys. Rev. B **46**, 4816 (1992). http://dx.doi.org/10.1103/PhysRevB.46.4816

94 J. C. HEYRAUD and J. J. METOIS: *Equilibrium Shape of Gold Crystallites on a Graphite Cleavage Surface: Surface Energies and Interfacial Energy*, Acta Metall. **28**, 1789 (1980). http://dx.doi.org/10.1016/0001-6160(80)90032-2

95 Z. WANG and P. WYNBLATT: *The equilibrium form of pure gold crystals*, Surf. Sci. **398**, 259 (1998). http://dx.doi.org/10.1016/S0039-6028(98)80029-0

96 C. BOMBIS, A. EDMUNDTS, M. NOWICKI, and H. P. BONZEL: *Absolute surface free energies of Pb*, Surf. Sci. 511, **83** (2002). http://dx.doi.org/10.1016/S0039-6028(02)01554-6

97 A. EDMUNDTS, M. NOWICKI, and H.P. BONZEL: *Experimental absolute step and kink formation energies on Pb(111) vicinal surfaces*, Surf. Sci. **496**, 35 (2002). http://dx.doi.org/10.1016/S0039-6028(01)01614-4

98 F. A. NICHOLS and W. W. MULLINS: *Surface- (Interface-) And Volume-Diffusion Contributions to Morphological Changes Driven by Capillarity*, Trans. Met. Soc. AIME **233**, 1840 (1965). http://portal.isiknowledge.com/portal.cgi?DestApp=WOS&DestParams=%3F%26CustomersID%3DAIP%26CustomersIP%3D129.217.168.246%26Func%3DLinks%26ImgLogo%3Dhttp%253A%252F%252Fimages.isiknowledge.com%252FWoK3%252FImages%252FLinks%252FAIP_Ret.gif%26PointOfEntry%3DFull

99 H. HÄKKINEN and M. MANNINEN: *How "Magic" is a Magic Metal Cluster?*, Phys. Rev. Lett. **76**, 1599 (1996). http://dx.doi.org/10.1103/PhysRevLett.76.1599

100 A. SANCHEZ, S. ABBET, U. HEIZ, W.D. SCHNEIDER, H. HÄKKINEN, R. N. BARNETT, and U. LANDMAN: *When Gold Is Not Noble: Nanoscale Gold Catalysts*, J. Phys. Chem. A **103**, 9573 (1999). http://dx.doi.org/10.1021/jp9935992

101 W. L. WINTERBOTTOM: *Equilibrium shape of a small particle in contact with a foreign substrate*, Acta Metall. **15**, 303 (1967). http://dx.doi.org/10.1016/0001-6160(67)90206-4

102 K. H. HANSEN, T. WORREN, S. STEMPEL, E. LÆNGSGAARD, M. BÄUMER, H.-J. FREUND, F. BESENBACHER, and I. STENSGAARD: *Palladium Nanocrystals on Al_2O_3: Structure and Adhesion Energy*, Phys. Rev. Lett. **83**, 4120 (1999). http://dx.doi.org/10.1103/PhysRevLett.83.4120

103 H. HÖVEL and I. BARKE: *Large noble metal clusters: electron confinement and band structure effects*, New J. Phys. **5**, 31 (2003). http://dx.doi.org/10.1088/1367-2630/5/1/331

104 S. J. CARROLL, S. PRATONTEP, M. STREUN, R. E. PALMER, S. HOBDAY and R. SMITH: *Pinning of size-selected Ag clusters on graphite surfaces*, J. Chem. Phys. 18, **113**, 7723 (2000). http://dx.doi.org/10.1063/1.1322657

105 K. BROMANN, C. FELIX, H. BRUNE, W HARBICH, R. MONROT, J. BUTTET, and K. KERN: *Controlled Deposition of Size-Selected Silver Nanoclusters*, Science **274**, 956 (1996). http://dx.doi.org/10.1126/science.274.5289.956

106 S. FEDERIGO, W. HARBICH, and J. BUTTET: *Soft landing and fragmentation of small clusters deposited in noble-gas films*, Phys. Rev. B **58**, 7428 (1998). http://dx.doi.org/10.1103/PhysRevB.58.7428

107 H. CHENG and U. LANDMAN: *Controlled Deposition, Soft Landing, and Glass Formation in Nanocluster-Surface Collisions*, Science **260**, 1304 (1993). http://chemport.cas.org/cgi-bin/sdcgi?APP=ftslink&action=reflink&origin=aps&version=1.0&coi=1:CAS:528:DyaK3sXksFKrurc%3D&md5=4153a79a0d1e7970a30793ca726c2b36

108 L. K. ZANG, Y. X. WANG, Z. Y. PAN, L. ZHOU, T. J. LIU, J. ZHU, and X. M. JIANG: *Ar-buffer-assisted deposition of Cu_{13} on Cu(111) surfaces*, Surf. Sci. **600**, 527 (2006). http://dx.doi.org/10.1016/j.susc.2005.11.002

109 M. BIELETZKI: *Rastertunnelmikroskopie an massenselektierten Clustern auf C_{60}*, Diploma Thesis, University of Dortmund (2006).

110 T. BECKER, H. HÖVEL, M. TSCHUDY, and B. REIHL: *Applications with a new low-temperature UHV STM at 5 K,* Appl. Phys. A **66**, 27 (1998). http://dx.doi.org/10.1007/s003390051093

111 OMICRON NanoTechnology GmbH Germany, website: http://www.omicron.de/ . http://www.omicron.de/

112 R. GAISCH, J. K. GIMZEWSKI, B. REIHL, R. R. SCHLITTLER, M. TSCHUDY and W. D. SCHNEIDER: *Low-temperature ultra-high-vacuum scanning tunneling microscope*, Ultramicroscopy **42**, 1621 (1992). http://dx.doi.org/10.1016/0304-3991(92)90495-6

113 I. BARKE: *Edelgasschichten auf der Au(111)-Oberfläche: Präparation und lokale Tunnelspektroskopie Massenselektierte Cluster deponiert auf Oberflächen*, Diploma Thesis, University of Dortmund (2001). http://e1.physik.uni-dortmund.de/hovel/hovel-Dateien/barke_diplom.pdf

114 O. ALBREKTSEN, H. W. M. SALEMINK, K. A. MØRCH, and A. R. THÖLEN: *Reliable tip preparation for high-resolution scanning tunneling microscopy*, J. Vac. Sci. Technol. B **12**, 3187 (1994). http://dx.doi.org/10.1116/1.587497

115 H. HÖVEL, professorial dissertation: *Geometric and Electronic Structure of Nano-scale Systems on Surfaces*, University of Dortmund (2000).

116 H. HABERLAND, M. MALL, M. MOSELER, Y. QIANG, Th. REINERS, and Y. THURNER: *Filling of micron-sized contact holes with copper by energetic cluster impact*, J. Vac. Sci. Technol. A **12**, 2925 (1994). http://dx.doi.org/10.1116/1.578967

117 B. v. ISSENDORFF and R. E. PALMER: *A new high transmission infinite range mass selector for cluster and nanoparticle beams*, Review of Scientific Instruments **70**, 4497 (1999). http://dx.doi.org/10.1063/1.1150102

118 LEYBOLD Vacuum GmbH, website: http://www.leybold.com/ .

119 U. S. Department of the Treasury, website: http://www.usmint.gov/mint_programs/index.cfm?flash=yes&action=american_eagles

120 S. KRAUSE: *Massenselektierte Cluster deponiert auf Oberflächen*, Diploma Thesis, University of Dortmund (2006).

121 VARIAN, Inc., website: http://www.varianinc.com/ .

122 SIMION®, website: http://www.simion.com/ .

123 KERAFOL®, website: http://www.kerafol.de/ .

124 BURLE, website: http://www.burle.com/ .

125 EFM 3, *Omicron* NanoTechnology GmbH [111]

126 M. WUTZ, H. ADAM, and W. WALCHER: *Theorie und Praxis der Vakuumtechnik* (Vieweg, Braunschweig Wiesbaden, 1992).

127 MATERIALS AND ELELCTROCHEMICAL RESEARCH (MER) Corporation, website: http://www.mercorp.com/ .

128 T. ANDREEV: *Herstellung und Untersuchung von Edelgas-Adsorbatschichten: Einfluss auf die geometrische und elektronische Struktur der Oberfläche*, Diploma Thesis, University of Dortmund (2003). http://e1.physik.uni-dortmund.de/hovel/hovel-Dateien/andreev_diplom.pdf

129 I. BARKE and H. HÖVEL: *Confined Shockley Surface States on the (111) Facets of Gold Clusters*, Phys. Rev. Lett. **90**, 166801 (2003). http://dx.doi.org/10.1103/PhysRevLett.90.166801

130 CH. WÖLL, S. CHIANG, R. J. WILSON, and P. H. LIPPEL: *Determination of atom positions at stacking-fault dislocations on Au(111) by scanning tunneling micros-*

copy, Phys. Rev. B **39**, 7988 (1989). http://dx.doi.org/10.1103/PhysRevB.39.7988

131 J. CHLADEK and G. BETZ: *Radiation Effects and Defects in Solids,* **142** (1997).

132 3M®, website: http://www.3m.com/ .

133 L. Pauling: *The Nature of the Chemical Bond*, p. 235, 3rd. Edition 1960.

134 http://www.2spi.com/.

135 G. KAINDL, T. C. CHIANG, D. E. EASTMAN, and F.J. HIMPSEL: *Distance-Dependent Relaxation Shifts of Photoemission and Auger Energies for Xe on Pd(001)*, Phys. Rev. Lett. **45**, 1808 (1980). http://dx.doi.org/10.1103/PhysRevLett.45.1808

136 E. I. ALTMANN and R. J. COLTAN: *Nucleation, Growth and Structure of Fullerene Films on Au(111)*, Surf. Sci. **279**, 49 (1992). http://dx.doi.org/10.1016/0039-6028(92)90741-N

137 E. I. ALTMANN and R. J. COLTAN: *The interaction of C_{60} with noble metal surfaces*, Surf. Sci. **295**, 13 (1993). http://dx.doi.org/10.1016/0039-6028(93)90181-I

138 E. I. ALTMAN and R. J. COLTON: *Determination of the orientation of C_{60} adsorbed on Au(111) and Ag(111)*, Phys. Rev. B **48**, 18244 (1993). http://dx.doi.org/10.1103/PhysRevB.48.18244

139 C. RETTIG: *Bleinanostrukturen auf mit Wasserstoff passiviertem Silizium (111): Elektrochemische Abscheidung und Vakuumaufdampfverfahren*, Dissertation, University of Dortmund (2000). http://e1.physik.uni-dortmund.de/hovel/hovel-Dateien/rettig_diplom.pdf

140 S. L. QIU, X. PAN, M. STRONGIN, and P. H. CITRIN: *Photoemission from supported metal clusters: The problem of the support*, Phys. Rev. B **36**, 1292 (1987). http://dx.doi.org/10.1103/PhysRevB.36.1292

141 P. H. CITRIN, G. K. WERTHEIM, and Y. BAER: *Core-Level Binding Energy and Density of States from the Surface Atoms of Gold*, Phys. Rev. Lett. **41**, 1425 (1978). http://dx.doi.org/10.1103/PhysRevLett.41.1425

142 B. RICHTER, H. KUHLENBECK, H. J. FREUND, and P. S. BAGUS: *Cluster Core-Level Binding-Energy Shifts: The Role of Lattice Strain*, Phys. Rev. Lett. **93**, 026805 (2004). http://dx.doi.org/10.1103/PhysRevLett.93.026805

143 G. K. WERTHEIM, S. B. DICENZO, and S. E. YOUNGQUIST: *Unit Charge on Supported Gold Clusters in Photoemission Final State*, Phys. Rev. Lett. **51**, 2310 (1983). http://dx.doi.org/10.1103/PhysRevLett.93.026805

144 T. ANDREEV, I. BARKE, and H. HÖVEL: *Adsorbed rare-gas layers on Au(111): Shift of the Shockley surface state studied with ultraviolet photoelectron spectroscopy and scanning tunneling spectroscopy*, Phys. Rev. B **70**, 205426 (2004). http://dx.doi.org/10.1103/PhysRevB.70.205426

145 R. J. BEHM, C. R. BRUNDLE, and K. WANDELT: *The underlayer influence on photoemission and thermal desorption of xenon adsorbed on Ag(111)*, J. Chem Phys **85**, 1061 (1986). http://dx.doi.org/10.1063/1.451299

146 M. L. KLEIN and J. A. VENABLES (eds.): *Rare gas solids*, Vol. II, (Academic Press, London, New York, San Francisco, 1977).

147 N. SCHWENTNER: *Mean-free path of electrons in rare-gas solids derived from vacuum-uv photoemission data*, Phys. Rev. B **14**, 5490 (1976). http://dx.doi.org/10.1103/PhysRevB.14.5490

148 H. G. BOYEN, G. KASTLE, F. WEIGL, B. KOSLOWSKI, C. DIETRICH, P. ZIEMANN, J. P. SPATZ, S. RIETHMULLER, C. HARTMANN, M. MOLLER, G. SCHMID, M. G. GARNIER, and P. OELHAFEN: Oxidation-Resistant Gold-55 Clusters, Science **297**, 1533 (2002). http://dx.doi.org/10.1126/science.1076248

149 R. L. SCHWOEBEL: *Step Motion on Crystal Surfaces. II,* Appl. Phys. **40**, 614 (1969). http://dx.doi.org/10.1063/1.1657442

150 G. EHRLICH and F. G. HUDDA: *Atomic View of Surface Self-Diffusion: Tungsten on Tungsten*, New York J. Chem. Phys. **44**, 1039 (1966). http://dx.doi.org/10.1063/1.1726787

151 R. L. SCHWOEBEL and E. J. SHIPSEY: *Step Motion on Crystal Surfaces*, J. Appl. Phys. **37**, 3682 (1966). http://dx.doi.org/10.1063/1.1707904

152 S. C. WANG and G. EHRLICh: *Atom incorporation at surface clusters: An atomic view,* Phys. Rev. Lett **67**, 2509 (1991). http://dx.doi.org/10.1103/PhysRevLett.67.2509

153 R. FERRANDO and G. TRÉGLIA: *High-Temperature Study of the Schwoebel Effect in Au(111)*, Phys. Rev. Lett. **76**, 2109 (1996). http://dx.doi.org/10.1103/PhysRevLett.76.2109

154 G. K. WERTHEIM and D. N. E. BUCHANAN: *Interfacial reaction of C_{60} with silver*, Phys. Rev. B **50**, 11070 (1994). http://dx.doi.org/10.1103/PhysRevB.50.11070

155 H. WANG, J. G. HOU, O. TAKEUCHI, Y. FUJISUKU and A. KAWAZU: *STM observations of Ag-induced reconstruction of C_{60} thin films*, Phys. Rev. B. **61**, 2199 (2000). http://dx.doi.org/10.1103/PhysRevB.61.2199

156 D. D. CHAMBLISS and R. J. WILSON: *Relaxed diffusion limited aggregation of Ag on Au(111) observed by scanning tunneling microscopy*, J. Vac. Sci. Technol. B **9**, 928 (1999). http://dx.doi.org/10.1116/1.585497

157 L. BARDOTTI, P. JENSEN, A. HOAREAU, M. TREILLEUX, and B. CABAUD: *Experimental Observation of Fast Diffusion of Large Antimony Clusters on Graphite Surfaces*, Phys. Rev. Lett. **74**, 4694 (1995). http://dx.doi.org/10.1103/PhysRevLett.74.4694

158 M. COUILLARD, S. PRATONTEP, and R. E. PALMER: *Metastable ordered arrays of size-selected Ag clusters on graphite*, Appl. Phys. Lett. **81**, 2595 (2003). http://dx.doi.org/10.1063/1.1568165

159 LANDOLT-BÖRNSTEIN, New Series, Group III: *Condensed Matter*, Volume **42**, Subvolume A2, Chapter 4.4.7 (Springer, Heidelberg, 2002).

160 M. SCHAFFHÖFER: *Untersuchungen an nanostrukturierten Oberflächen mittels Rastertunnelmikroskopie*, Diploma Thesis, University of Dortmund (1997). http://e1.physik.uni-dortmund.de/hovel/hovel-Dateien/schaffhoefer_diplom.pdf

161 I. BESZEDA, I. A. SZABO, and E. G. GONTIER-MOYA: *Morphological evolution of thin gold films studied by Auger electron spectroscopy in beading conditions*, Appl. Phys. A **78**, 1079 (2004).

162 H. J. WEISS: *Diffusion*, in *Effekte der Physik und ihre Anwendungen*, eds. M. V. ARDENNE, G. MUSIOL, and U. KLEMRADT, (Verlag Harri Deutsch, Frankfurt, 2005).

163 R. FERRANDO and G. TRÉGLIA: *Tight-binding molecular dynamics study of diffusion on Au and Ag(111)*, Surf. Sci. **331**, 920 (1995). http://dx.doi.org/10.1016/0039-6028(95)00276-6

164 J. R. SMITH, T. HONG, and D. J. SROLOVITZ: *Metal-Ceramic Adhesion and the Harris Functional*, Phys. Rev. Lett. **72**, 4021 (1994). http://dx.doi.org/10.1103/PhysRevLett.72.4021